THE UNIVERSITY *of* EDINBURGH

Time evolution of the electric field by the rapid expansion method in controlled-source electromagnetic (CSEM) applications

Yikuo Liu

School of GeoSciences
The University of Edinburgh

Thesis submitted for the degree of
Doctor of Philosophy

August 2020

Abstract

I address the problem of modelling the low-frequency, time-domain controlled-source electromagnetic (CSEM) data by the rapid expansion method (REM). The CSEM method is an active EM exploration method that is recognized as complementary to the seismic method, with the focus on determining subsurface electric resistivity. Interpretation of CSEM data relies on an iterative forward modelling process to search for the model that best fits the data. Therefore, forward modelling is an essential part of the interpretation process. REM is an explicit time-domain forward modelling method that solves the diffusive EM field based on a Chebyshev expansion of the time operator. The temporal estimator is accurate to the Nyquist frequency and temporal numerical dispersion can be mitigated.

I present several extensions of the REM algorithm to generalize its use in various environments. I show the response from the Earth-air interface can be modelled by solving the air field explicitly in the Chebyshev domain. I show that transverse isotropic anisotropy can be included in the modelling with the manipulation of the conductivity tensor. I show that by introducing another fictitious series of Chebyshev polynomials, the updating of Chebyshev terms is equivalent to coupled EM wave equations in a vacuum. EM wavefield modelling techniques can therefore be transferred to the Chebyshev domain, and I show the use of perfectly matched layers, a well-established absorbing boundary condition designed for EM waves, to solve the numerical boundary problems in the Chebyshev method.

I have made two improvements to the numerical efficiency of REM modelling of CSEM data. First, I develop a workflow to solve the 3D electric field by REM but with a 2D model. If the earth model can be simplified to 2D structures, the computational cost to achieve a 3D solution can be reduced by an order of magnitude. Secondly, the code has been parallelized by graphic processing units (GPU), and the performance can be improved by a factor of over 100, compared with the serial REM code implemented in C.

The developed new functionalities make the REM algorithm an accurate forward modeller that solves the time-domain electric field efficiently in various environments. Subsequent CSEM inversion studies can therefore benefit from the method to extract resistivity model from full-bandwidth CSEM field data, which should bring us closer to the true subsurface.

Lay summary

I address the problem of modelling the low-frequency, time-domain electromagnetic (CSEM) data by the rapid expansion method (REM). The CSEM method is an active EM exploration method that is recognized as complementary to the seismic method, with the focus on determining subsurface electric resistivity. Interpretation of CSEM data relies on an iterative forward modelling process to search for the model that best fits the data. Therefore, forward modelling is an essential part of the interpretation process. REM is a time-domain forward modelling method that solves the diffusive EM field based on a specific series of polynomials. It is accurate in estimating temporal derivatives.

I present several extensions of the REM algorithm to generalize its use in various environments. I show the response from the Earth-air interface can be modelled by solving the air field explicitly. I show the directional variation of subsurface conductivity can be included in the modelling by handling the conductivity as a tensor. I show that by introducing another series of polynomials, the updating of the polynomial terms is equivalent to coupled EM wave equations in a vacuum. EM wavefield modelling techniques can therefore be used by the proposed method, and I show how to solve the numerical boundary problems of the method.

I have made two improvements to the numerical efficiency of REM modelling of CSEM data. First, I develop a workflow to solve the 3D electric field by REM but with a 2D model. If the earth model can be simplified to 2D structures, the computational cost to achieve a 3D solution can be reduced by an order of magnitude. Secondly, the code has been accelerated by graphic processing units (GPU), and the performance can be improved by a factor of over 100, compared with the serial REM code implemented in C.

The developed new functionalities make the REM algorithm an accurate forward modeller that solves the time-domain electric field efficiently in various environments. Subsequent CSEM interpretation studies can therefore benefit from the method to extract resistivity model from time-domain CSEM field data, which should bring us closer to the true subsurface.

Declaration

I declare that except where specific reference is made to the work of others, the contents of this thesis are original and have not been submitted in whole or in part for consideration for any other degree or qualification in this, or any other university. Except where otherwise acknowledged, the work presented is entirely my own.

Yikuo Liu
August 2020

Acknowledgements

It is my pleasure to thank those who made this thesis possible. I would like to express my deepest gratitude to my supervisors Anton Ziolkowski and Magnus Hagdorn. Anton is always supportive throughout my research, with his patience, enthusiasm and his immense knowledge. I thank him for all the great times and for all the great discussions. He has taught me a great deal regarding electromagnetic methods, seismic methods, and the scientific methods in general. Magnus is always helpful whenever I come to him. He is a real expert. He has taught me a lot in programming and has helped me overcome many research difficulties that inevitably occur when developing new methods.

I would like to thank Paul Stoffa for his generous sharing of his code as well as many constructive suggestions throughout the project. His research work and his code form the fundamentals and the guidelines for my research. I want to thank Andrew Curtis, for being my advisor as well as his useful comments when reviewing my work.

My sincere thanks also goes to all my friends, colleagues and staff here in Edinburgh, who made my three years a great pleasure.

Most importantly I would like to thank my family for their support and understanding throughout this adventure.

Table of contents

List of figures

Symbols and Abbreviations

Symbols

SI and SI-derived units are used throughout the thesis as specified in the following list.

These variables and subscripts are repeatedly used for various purposes: x, y, z, a, b, c, i, j, k, p, n, d, m, v, h, s, θ, ϕ, λ; similarly the functions f and g. I list only the most common variables and subscripts.

Symbol	Description	Units
A	a vector field	
B	magnetic induction field	Tesla
D	a matrix	
E	electric field	V/m
F	a matrix	
f	frequency	Hz
G	a matrix	
H	magnetic field	A/m
I	identity matrix	
I	electric current	A
i	imaginary unit, $i = \sqrt{-1}$	_
J	electric current density	A/m^2
L	a fictitious wavefield	_
P	a fictitious wavefield	_
p	equivalent time in the Chebyshev domain	$\sqrt{s}$
Q	a fictitious wavefield	_
R	a matrix	
t	time	s
u	directional unit vector	
ε	electrical permittivity	F/m

Symbol	Description	Units
μ	magnetic permeability	H/m
ω	angular frequency	rad/s
ρ	electrical resistivity	Ω m
σ	electrical conductivity	S/m
$\sim$	tilde that denotes change of domain after Fourier transform.	

Functions

Dirac delta function

$$\delta(t) = 0 \quad \text{if} \quad t \neq 0 \quad \text{and} \quad \int_{-\infty}^{\infty} \delta t dt = 1$$

Fourier transform pair

$$\tilde{f}(\omega) = \int_{-\infty}^{\infty} f(t)\exp(-i\omega t)dt$$
$$f(t) = \frac{1}{2\pi}\int_{-\infty}^{\infty} \tilde{f}(\omega)\exp(i\omega t)d\omega$$

Error function and complementary error function

$$\text{erf}(x) = \frac{2}{\sqrt{\pi}}\int_0^x \exp(-t^2)dt$$
$$\text{erfc}(x) = 1 - \text{erf}(x)$$

Abbreviations

1D	1 dimensional
2D	2 dimensional
2.5D	2.5 dimensional
3D	3 dimensional
ABC	absorbing boundary condition
CFL	Courant-Friedrichs-Lewy
CPU	central processing unit

CSEM	controlled source electromagnetic
CUDA	Compute Unified Device Architecture
cuFFT	CUDA fast Fourier transform
DC	direct current
EAGE	European Association of Geoscientists and Engineers
Eddie	The Edinburgh Compute and Data Facility Linux Compute Cluster
EM	electromagnetic
EMmod	electromagnetic modelling (program)
FD	finite-difference
FDTD	finite-difference time-domain
FEM	frequency-domain electromagnetic
FFT	fast Fourier transform
GPU	graphics processing unit
IFFT	inverse fast Fourier transform
MPI	Message Passing Interface
MTEM	multi-channel electromagnetic
MUMPS	Multifrontal Massively Parallel Sparse direct Solver
NMO	normal moveout
OBN	ocean bottom node
OpenMP	Open Multi-Processing
PGS	Petroleum Geo-Services
PML	perfectly matched layers
PRBS	pseudo-random binary sequence
PS	pseudospectral
REM	rapid expansion method
SEG	Society of Exploration Geophysicists
TEM	time-domain electromagnetic
TTI	tilted transverse isotropy
VFSA	very fast simulated annealing
VTI	vertical transverse isotropy

Chapter 1

Introduction

1.1 Review

The electromagnetic (EM) field and the electrical conductivity are connected by Maxwell's equations, and therefore EM exploration methods have the ability to explore for contrasts in electrical conductivity. It leads to geophysical exploration for subsurface conductive anomalies and resistive anomalies. For decades EM surveys have been used by the mining industry to search for onshore conductive ore bodies. The work of EM exploration is described comprehensively by "Electromagnetic methods in applied geophysics" (Nabighian 1987; Nabighian 1991), a two-volume book published by the Society of Exploration Geophysicists (SEG) Mining Committee.

The marine controlled-source electromagnetic method (CSEM) was developed by academics to as a conductivity mapping method for the seafloor (e.g., Edwards and Chave 1986; Cheesman et al. 1987; Chave et al. 1991), as well as analyzing the resistivity and fluids of oceanic lithosphere (e.g., Cox et al. 1986, Constable and Cox 1996). It was developed to replace marine magnetotelluric (MT) method (e.g., Vozoff 1972; Wannamaker et al. 1984) which can be severely limited in deep water by the attenuation in the water of the Earth's natural external magnetic field. The term "controlled-source" is used because it is an active EM method using a man-made source signal, which is different from passive MT methods, which rely on naturally occurring EM fields that originate in the Earth's ionosphere as the source signal. For the oil & gas industry the use of CSEM was discussed by, e.g., Nekut and Spies (1989), more than three decades ago. Nevertheless, a recent commercial use of CSEM in 2002 has particularly drawn the industry's interests, where Ellingsrud et al. (2002) showed the application of CSEM method to detect and assess a hydrocarbon-bearing reservoir in offshore Angola. A big attraction is the ability of CSEM to de-risk very expensive deep water exploration wells. The success marked the start of a shift from academia to industry,

where CSEM methods have been adopted and evolved rapidly over the last two decades. The CSEM method exploits the resistivity difference between a reservoir saturated with highly resistive hydrocarbons and one saturated with conductive saline fluids. Therefore it has the ability to assess a potential reservoir before drilling test wells. It is now becoming a powerful tool in hydrocarbon exploration, appraisal and reservoir monitoring and characterization, as a complementary tool to seismic methods. The advantage of the CSEM method over the seismic method is its sensitivity to subsurface resistive bodies, such as the hydrocarbon-saturated reservoirs. The drawback of the CSEM method is its low imaging resolution compared with the seismic method. The review of the recent CSEM industry development has been discussed by, e.g., Constable (2010), Zhdanov (2010), and Ziolkowski and Wright (2012). Ziolkowski and Slob (2019) present the book "Introduction to controlled-source electromagnetic methods", covering most of the essential theories and many real-world CSEM examples, which can be a very good starting point for a geophysicist coming into the CSEM world.

CSEM methods can be divided into several categories. First, there are land CSEM and marine CSEM. Marine CSEM can be further divided into shallow water and deep water cases. The distinction is that in shallow water we assume the acquired EM data still contain a significant amount of response that has interacted with the Earth-air interface (i.e., the sea surface), whereas in deep water surveys the water layer should be deep enough to attenuate such signals (with the source and receivers located near the seabed) so that the air response can be negligible. As discussed in Ziolkowski and Slob (2019), for water of conductivity 3 S/m, the skin depth at 0.25 Hz is about 580 m. Considering the two-way travelling of the field, a water depth of 500 m can be a reference to understand the nature of a marine CSEM survey.

Marine CSEM survey has mainly two types of acquisition. Conventional marine survey layout uses a deep-towed source and ocean-bottom node (OBN) receivers in both shallow and deep water environment. Petroleum Geo-Services (PGS) has developed a towed-source, towed-receiver CSEM acquisition system specifically for the shallow marine environment. The in-line current dipole source is towed about 10 m below the sea surface, and the receiver cable, which measures the in-line electric field, is towed about 100 m below the sea surface. The survey layout is similar to towed-streamer seismic acquisition, and it has been reported in Anderson and Mattson (2010) and Engelmark et al. (2014). The CSEM system with ocean-bottom receivers usually has a lower noise level of the data, whereas the towed-streamer system provides higher acquisition efficiency and therefore reduces the cost. Shallow and deep marine CSEM examples have been given by, e.g., Ellingsrud et al. (2002); Constable (2010); Ziolkowski et al. (2010); Ziolkowski et al. (2011); and Houck et al. (2015).

Land CSEM survey environment owns its convenience and technical difficulties. For instance, land CSEM survey can place the source and receivers much more precisely than the marine case. In addition, the effect of the airwave (i.e., the response from the air layer) can be handled more easily if EM data are processed in the time domain. For example, if the impulse response of the earth can be recovered as proposed and demonstrated in Wright et al. (2002), the air response can be separated from the earth response by processing, as shown in Ziolkowski and Wright (2007). The challenges of land surveys mainly include the surface topography and a generally higher electrical noise level, which are similar to the issues facing with land seismic surveys. Besides, for a land CSEM survey the source and receivers are usually situated on the surface, which can be a much more resistive and heterogeneous medium than seawater. Such considerations raise the requirements for the source strength as well as the ability to reduce the noise during data processing. Land CSEM studies have been shown by, e.g., Wright et al. (2002), Ziolkowski et al. (2007), Streich (2016), and Schaller et al. (2018).

The second principle to consider CSEM methods is the domain for analyzing the EM data. There are frequency-domain CSEM methods and time-domain CSEM methods. The two categories sound equal in theory, as the two domains are related by the Fourier transform, and the frequency-domain EM data are certainly collected in the real-world time domain as well. However, in practice, frequency-domain methods usually use the source signal containing only a few frequencies. For example, a continuous square wave source time function is often used and this has energy only at the fundamental frequency and odd harmonics. When the source time function has only a line spectrum, the impulse response of the Earth cannot be recovered. That is, the interpretation of frequency-domain CSEM data are based on the earth response to a few frequencies, which cannot be transformed to the time domain. In contrast, time-domain CSEM methods in principle allow a huge range of frequencies to be used in the EM data spectrum. Conventional time-domain methods measure the earth response to the switching-off (or on) of a direct current source signal (e.g., Wang and Hohmann 1993; Commer and Newman 2004; Um et al. 2010). Wright et al. (2002) demonstrate the importance of measuring the source time function, and demonstrate that the impulse response of the earth can be recovered by deconvolution with the source measurement. This leads to the multi-channel transient electromagnetic (MTEM) method, and the benefits from recovery of impulse response are demonstrated in Wright et al. (2002); Ziolkowski et al. (2007); Ziolkowski et al. (2010); and Ziolkowski et al. (2011). The aim of time-domain methods is to extract the subsurface model based on full-bandwidth CSEM data. The differences of aims between the two domains lead to different requirements for source time function, data processing procedure, data modelling techniques and so on. The comparison between the

two domains is continued in section 2.2.1 where I review the forward modelling solutions of CSEM data.

Regardless of the environments and the domain of interpreting the data, a major issue with the analysis of CSEM data is the extraction of the subsurface resistivity distribution from the measured data. This process is performed by inversion. Inversion is essentially an iterative forward modelling process. The parameters of an initial, made-up model are adjusted until the modelled response "matches" (according to some misfit criterion) the real data. The resultant best-fit model is then considered to be close to the true model representing the subsurface. The non-uniqueness of the solution is a well-known problem for such inverse processes, that is, there are many equivalent models that can fit the real data to the required misfit level. In a gradient-based local optimization, the resultant best-fit model is highly dependent on the initial model. Due to the diffusive nature of the low-frequency CSEM data, there is currently no ray theory available for CSEM data as there is for seismic data, and therefore there is no explicit way of determining the resistivities of CSEM data comparable to the determination of velocities in seismic data, e.g., normal moveout (NMO) velocity by aligning seismic arrivals. The interpretation of CSEM data purely by inversion raises the requirement that either an accurate initial model can be derived, or a global optimal model can be found during the inversion search. The derivation of an initial model has been discussed by, e.g., Werthmüller et al. (2013) and Mittet and Berre (2018). The global optimization method to interpret CSEM data has been discussed by, e.g., Jaysaval et al. (2019). The discussion is continued in section 8.2. However, among all the different synthetic and field examples, there has not been a unified inversion workflow to interpret CSEM data. This may be the reason that as powerful a tool as CSEM is, Ziolkowski and Slob (2019) state that "Compared with seismic exploration, however, CSEM is still in its infancy ... There is clearly room for development".

In any case, forward modelling is an essential part in the analysis of CSEM data by inversion, that is, to predict the EM response given a known conductivity model and survey configuration. Although the modelling of the EM field always starts with Maxwell's equations, the numerical algorithms to accomplish it can vary. A review of current forward modelling algorithms is given in Chapter 2. Throughout this project I have been particularly interested in an algorithm named the rapid expansion method (REM), which is an explicit time-domain EM modelling method (Stoffa and Ziolkowski 2019). The time evolution of the electric field is solved by a weighted sum of a series of Chebyshev polynomials expanded from the time operator. The method has several appealing features. First, it is a time-domain modelling method which supports the use of full-bandwidth EM data. Secondly, REM yields spectral accuracy in estimating the temporal derivatives and provides the numerical accuracy

up to the Nyquist frequency. Therefore, temporal dispersion can be mitigated during the numerical modelling. Numerical dispersion, however, can be a common issue with low-order finite-difference estimation which degrades the modelling and inversion results. Finally, the Chebyshev method requires only the computation of matrix dot products, which is highly preferable for parallel computing.

REM was introduced by Tal-Ezer (1986) for seismic wavefield modelling. The accuracy and the efficiency of the method have been demonstrated by Tal-Ezer et al. (1987), Kosloff et al. (1989), Tal-Ezer et al. (1990), and Pestana and Stoffa (2010). Carcione (2006) first extends the algorithm to solving low-frequency diffusive EM field in a 2D model considering a magnetic source. Stoffa and Ziolkowski (2019) extend his work to modelling the 3D electric field excited by an electric dipole, which suits the needs for a marine CSEM modelling study. The code is written in FORTRAN and parallelized by Message Passing Interface (MPI). The code is available on Eddie (The Edinburgh Compute and Data Facility Linux Compute Cluster) and is able to carry out a deep-marine CSEM modelling job.

1.2 Claim

The purpose of my research is to contribute to the extraction of the subsurface resistivity configuration from CSEM data. There are two essential components. First, inversion needs an accurate and efficient forward modeller. Second, the inversion algorithm itself should be able to avoid being trapped in a biased local minimum. I have access to the data collected over the North Sea Harding field to demonstrate the concept. The CSEM data were collected in a shallow marine environment with both source and receivers stationary on the sea floor, about 110 m below the sea surface (Ziolkowski et al. 2010). For this Ph.D. project I have been focused on the modelling of CSEM data. The principal aim is to develop a forward modeller that can calculate the propagating EM field with such model configuration.

REM is of particular interest to undertake the forward modelling job, as it solves the time-domain electric field accurately and efficiently. Such a full-bandwidth forward modeller should bring us closer to the true subsurface resistivity model. Previous work by Stoffa and Ziolkowski (2019) demonstrated the use of REM in a 3D isotropic conductive medium. The work described in this thesis explores various aspects of REM, as listed below, to extend its use to both shallow and deep marine environments, and to improve its accuracy and efficiency whenever necessary. A direct use of my work to land CSEM problems, however, requires more specific considerations, for example, the choice of source signal, and the need to model the airwave, etc. Nevertheless, the theory that has been developed is certainly transferable if necessary. This is further discussed in Chapter 8.

I have made four contributions in this work to EM modelling using REM: inclusion of the Earth-air interface, inclusion of anisotropy, absorbing boundary conditions and numerical speed-up by a factor of 100 using GPUs. Inclusion of the Earth-air interface is necessary when the response from the air cannot be attenuated completely by the water. This includes shallow marine CSEM problems, as well as deep water problems with a deep target where lower frequencies are important and not sufficiently attenuated by the water layer. The response from the air is mixed up with the Earth response and needs to be solved. However, the inclusion of the air layer raises an issue for time-domain solutions, as there is a huge velocity difference between the EM fields travelling in the air and in the Earth. For explicit time-stepping solutions it means tiny time steps are required to step the field in the air. In the case of REM it means the convergence of the Chebyshev series is very slow. Previous work discussed by Wang and Hohmann (1993) and Commer and Newman (2004) has shown how the problem can be solved in the space-time domain, by an upward continuation process. That is, the field in the air needs to be solved explicitly based on the field on the surface. I show how the upward continuation process can be extended to the Chebyshev polynomials and how the air modelling problem can be solved in the space-Chebyshev domain. This allows the use of REM in shallow marine CSEM environments.

The second contribution is the inclusion of anisotropy, so that the variation of subsurface conductivities can be described both spatially and directionally. Electrical anisotropy is normal. For example, the grouping together of thin isotropic rock layers of different isotropic resistivities can be treated as anisotropy of an equivalent medium on the numerical scale. I show how the original REM scheme needs to be modified to consider vertical transverse isotropic (VTI) and tilted transverse isotropic (TTI) anisotropy. I solve the eigenvalues of the modified propagation matrix accordingly, to ensure the convergence of the Chebyshev polynomials with the inclusion of TTI anisotropy.

The third contribution is the incorporation of absorbing boundary conditions. There is a numerical requirement found through my research: the development of an accurate absorbing boundary condition (ABC) for REM. The computational mesh has to be truncated, but the Chebyshev polynomials lack an accurate ABC to attenuate the numerical reflections from model edges. The problem can be mitigated by the natural attenuation of a diffusive field, but it can become severe when the medium is less lossy. To solve the problem, I extend the theory of perfectly matched layers (PML), a well-established ABC technique designed for EM waves, to the Chebyshev domain to solve its boundary problem. Inspired by Stoffa and Ziolkowski (2019), I show by introducing another fictitious Chebyshev series, the updating of electric Chebyshev terms can be rearranged into a form similar to EM coupled wave equations. The equivalent time and frequency definitions for the Chebyshev domain

have been found, so that PML, as well as other EM wavefield modelling techniques can be extended to the Chebyshev domain in a similar manner.

The final contribution is numerical efficiency. The ultimate goal of REM is to undertake inversions of field CSEM datasets. I am personally more interested in global optimization methods so that the results can be independent of initial models and also can avoid being trapped in local minima. Such optimization methods often involve a stochastic search over the solution space, and therefore require the forward modeller to be very efficient. I have made two attempts to improve the efficiency of REM. First, I have tried different parallel implementations of the REM code, and have found that the GPU-accelerated C code appears to be attractive. Running on a single K80 GPU, the speed-up factor can be over 100 compared with the serial C code. Although the GPU memory is still a limiting factor for large-scale 3D CSEM datasets, the computational operations required by REM, include mainly the fast Fourier transform (FFT) and matrix dot product. These are found highly suitable for GPU parallel computing. Secondly, I have extended the 3D REM solution to the 2.5D modelling case, which aims to model the 3D electric field but with a 2D conductivity model. The 2.5D modelling is highly efficient if it is reasonable to assume the model contains only 2D structures. Computational efficiency can be improved by an order of magnitude with the same level of accuracy. This functionality should be particularly useful for 2D marine CSEM studies.

Through my research, the REM algorithm has been implemented in several programming languages, including MATLAB, C, and Python, for different needs. The final version of my REM code is a Python-wrapped library, with internal functions parallelized by GPU computing implemented with CUDA (Compute Unified Device Architecture) C. The forward modelling code is accurate, efficient, and easy to be incorporated with other open-source Python libraries. All the code was written from scratch. All the code files are available on Eddie, so that all the figures and results shown in the thesis can be reproduced.

1.3 Agenda

Following this introduction is a review of the fundamental EM theories as well as a review of the existing CSEM forward modellers in Chapter 2. The discussion is continued, comparing the differences between time-domain and frequency-domain CSEM solutions, as well as comparing explicit and implicit numerical solution schemes. The aim is to clarify where REM sits in the CSEM modelling world, and to discuss why the REM algorithm appears to be attractive. Chapter 3 is a review of the development of REM, especially the work

shown by Stoffa and Ziolkowski (2019). A numerical example is given to demonstrate the correctness of my code to reproduce the previous work.

Chapters 4 to 7 summarize my work as discussed in section 1.2. The inclusion of Earth-air interface, anisotropy, PML, and the extension to 2.5D modelling are demonstrated in Chapters 4, 5, 6 and the first half of Chapter 7, respectively. They are all new functionalities developed by me, and they have been demonstrated in the same manner. I first show the derived new theory and discuss how the original solution needs to be modified. I then demonstrate the correctness of the theory and the code by presenting at least one numerical example. The second half of Chapter 7 reports my investigation into the parallel implementation of the REM algorithm. The efficiency of the GPU-accelerated code is encouraging. I discuss the key aspects to achieve this efficiency as well as the current ability of the code regarding the survey size.

Through my research there are several interesting topics which have not been fully studied. In Chapter 8, I give my recommendations for future development of REM functionalities, as well as an outlook for the use of REM in inversions of field CSEM data. I conclude my work in Chapter 9, revisiting the key findings and contributions from my project. All the developed functionalities should have further extended the use of REM, to handle both shallow and deep marine environments, considering both isotropic and anisotropic conductivities, with the option to switch between 2D and 3D model space, etc. The limitations of my work are discussed in Chapters 8 and 9 as well. One major concern is still numerical efficiency if one focuses on global optimization methods as I do.

The results in Chapters 4 and 5, discussing the Earth-air interface and anisotropy, were published in Liu et al. (2019b). The original paper is modified and split into two parts so that the two independent problems can be discussed separately. Chapter 6 is another published paper (Liu 2019) discussing the absorbing boundaries by PML in the Chebyshev domain. The results in Chapter 7 were presented at the European Association of Geoscientists & Engineers (EAGE) annual conference 2019 (Liu et al. 2019a), to report the 2.5D REM modelling and its parallel implementation. The two papers are attached in the Appendix, along with some mathematical work, which does not fit into the main body of the thesis but may be interesting to some readers.

Chapter 2

Fundamental Theory and Review of Existing Solutions

Electromagnetic data obey Maxwell's equations, which form the underlying theory for modelling the electric field propagating in the earth. This chapter consists of two parts. In the first part I review the fundamental theory and show how the governing equation can be derived for the diffusive electric field propagating in a conductive medium. In the second part I review the current forward modellers that can solve the diffusive governing equation. The review is based on two perspectives: time-domain solutions versus frequency-domain solutions; and explicit numerical solutions versus implicit numerical solutions. I show the position where the rapid expansion method (REM) sits in the world of EM forward modellers, and discuss why the method appears to be attractive.

2.1 Fundamental Relations and the Governing Equations

I begin with Maxwell's equations in the space-time domain without the presence of electric and magnetic source:

$$\nabla \cdot \mathbf{E} = \frac{1}{\varepsilon}\rho_f, \tag{2.1}$$

$$\nabla \cdot \mathbf{B} = 0, \tag{2.2}$$

$$\nabla \times \mathbf{E} + \frac{\partial \mathbf{B}}{\partial t} = 0, \tag{2.3}$$

$$\nabla \times \mathbf{B} - \mu\varepsilon\frac{\partial \mathbf{E}}{\partial t} = \mu\mathbf{J}, \tag{2.4}$$

where the vector **E**(x,y,z,t) is the electric field consisting of three components

$$\mathbf{E}(x,y,z,t) = E_x(x,y,z,t)\mathbf{u}_x + E_y(x,y,z,t)\mathbf{u}_y + E_z(x,y,z,t)\mathbf{u}_z \tag{2.5}$$

with unit V/m; the vector **B**(x,y,z,t) is the magnetic induction field

$$\mathbf{B}(x,y,z,t) = B_x(x,y,z,t)\mathbf{u}_x + B_y(x,y,z,t)\mathbf{u}_y + B_z(x,y,z,t)\mathbf{u}_z \tag{2.6}$$

with unit Tesla or Wb/m^2; the vectors $\mathbf{u}_x$, $\mathbf{u}_y$, $\mathbf{u}_z$ are the unit vectors in the x-, y- and z-directions, respectively; the vector **J**(x,y,z,t) is the current density with unit A/m^2; μ is the magnetic permeability (in free space $\mu_0 = 4\pi \times 10^{-7}$N/A^2); ε is the electric permittivity (in free space $\varepsilon_0 = 8.85 \times 10^{-12}$C^2/(Nm^2)); and ρ_f denotes the charge density with unit C/m^3. Equation 2.1 and 2.2 are Gauss's Law for electric and magnetic field, respectively. Equation 2.3 is Faraday's law of induction. Equation 2.4 is Ampère-Maxwell law including the displacement current.

The current density **J** and the electric field **E** are related by Ohm's law as

$$\mathbf{J}(x,y,z,t) = \boldsymbol{\sigma}(x,y,z)\ \mathbf{E}(x,y,z,t), \tag{2.7}$$

where the vector $\boldsymbol{\sigma}$ is the electric conductivity. It is the reciprocal of electrical resistivity. Generally, the electric conductivity $\boldsymbol{\sigma}$ is a tensor, whose value can vary both spatially and directionally, describing the ease with which an electric current passes. Through this thesis I only consider the spatial and directional variation of subsurface conductivity, that is, the conductivity model is a tensor $\boldsymbol{\sigma}(x,y,z)$ that is dependent only on its spatial position x, y, and z. Such a model has made a few assumptions. The electrical conductivity is assumed to be temperature-independent and pressure-independent. In addition, the conductivity is assumed to be frequency-independent, i.e., there is no induced polarisation effects (e.g., Aristodemou and Thomas-Betts 2000; Hördt et al. 2007). The conductivity is assumed to be time-independent, which can be a problem when considering the near-surface, onshore measurements (e.g, Rein et al. 2004). The assumption of the spatial-only dependence of $\boldsymbol{\sigma}(x,y,z)$ should be feasible in most low-frequency (less than 100 Hz) exploration EM problems. Nevertheless, it is always necessary to revisit those assumptions according to the specific problems.

I first discuss a simplified situation in Chapter 2, where the medium is considered as isotropic and $\boldsymbol{\sigma}$ can be simplified as a scalar $\sigma(x,y,z)$. I discuss the treatment of the conductivity as a tensor in Chapter 5.

By taking the curl of equation 2.3, and combining with equations 2.4 and 2.7, the time-domain wave equation of electric field **E**(x,y,z,t) is established as

$$\nabla \times \nabla \times \mathbf{E} + \mu\varepsilon \frac{\partial^2}{\partial t^2}\mathbf{E} + \mu\sigma \frac{\partial}{\partial t}\mathbf{E} = 0. \tag{2.8}$$

Defining the temporal Fourier transform as

$$\tilde{a}(x,y,z,\omega) = \int_{-\infty}^{+\infty} a(x,y,z,t)\exp(-i\omega t)dt, \tag{2.9}$$

with inverse

$$a(x,y,z,t) = \frac{1}{2\pi}\int_{-\infty}^{+\infty} \tilde{a}(x,y,z,\omega)\exp(i\omega t)d\omega, \tag{2.10}$$

the corresponding derivative relation is then derived as

$$\frac{\partial}{\partial t}a(x,y,z,t) = \frac{1}{2\pi}\int_{-\infty}^{+\infty} i\omega\tilde{a}(x,y,z,\omega)\exp(i\omega t)d\omega. \tag{2.11}$$

Using equation 2.11, the frequency-domain wave equation is established as

$$\nabla \times \nabla \times \tilde{\mathbf{E}} - \omega^2\mu\varepsilon\tilde{\mathbf{E}} + i\omega\mu\sigma\tilde{\mathbf{E}} = 0, \tag{2.12}$$

where $\tilde{\mathbf{E}}$ denotes the vector electric field in the frequency domain.

Equations 2.8 and 2.12 have identical form. The first term in each equation, the double curl operator, describes the spatial propagation of the field. The second term, which contains a second-order time derivative, represents an energy conservation term and controls the wave behaviour of the electric field. The third term, which contains a first-order time derivative, controls the diffusive behaviour of the electric field. In applied geophysics, most of the time we are dealing with conductive materials ($\sigma \neq 0$) where the term controlling the diffusive behaviour exists. Therefore the electromagnetic field can be characterized as a lossy wavefield or, alternatively, a diffusive field. Loseth et al. (2006) give the analysis on the ambiguity between these two. They conclude that "one might call low-frequency propagation of EM fields in conductive media what one prefers. But when one characterizes field propagation as diffusion, it might be clearer to add that one is not referring to the random motion usually affiliated with diffusion processes. When field propagation is characterized as wave propagation, one should remember that waves are highly dispersive and strongly attenuated."

The magnetic permeability within the earth and air is assumed to be constant and is set to that of free space($4\pi \times 10^{-7}$H/m). This is assuming no magnetic materials in the earth that

can be important enough to affect the electric field. Again this is an assumption that may need to be revisited according to the specific subsurface problem. Considering low-frequency EM applications such as controlled-source electromagnetic (CSEM) measurements (less than 100 Hz), the inequality

$$\varepsilon << \sigma/\omega \tag{2.13}$$

can be satisfied. This leads to the inequality

$$|\omega^2 \mu_0 \varepsilon \tilde{\mathbf{E}}| << |i\omega\mu_0\sigma\tilde{\mathbf{E}}| \tag{2.14}$$

to be satisfied in the frequency domain and

$$|\mu_0\varepsilon\frac{\partial^2}{\partial t^2}\mathbf{E}| << |\mu_0\sigma\frac{\partial}{\partial t}\mathbf{E}| \tag{2.15}$$

to be satisfied in the time domain. Therefore the second-order derivative term is negligible and can be ignored. The abandonment of this term means, mathematically, neglecting the term of displacement current, and it is also referred as the diffusive approximation. It has been used extensively in low-frequency EM applications such as CSEM. The reason for this is not only for the simplicity, but also for the consideration of numerical stability: the inclusion of weak displacement currents is found to be harmful to step the field in large enough time steps (Wang and Hohmann, 1993). With the diffusive approximation, the governing equations for the time-domain and frequency-domain electric field $\mathbf{E}$ are

$$\nabla\times\nabla\times\mathbf{E}+\mu_0\sigma\frac{\partial}{\partial t}\mathbf{E}=0, \tag{2.16}$$

and

$$\nabla\times\nabla\times\tilde{\mathbf{E}}+i\omega\mu_0\sigma\tilde{\mathbf{E}}=0, \tag{2.17}$$

respectively, without the inclusion of external source.

When EM survey are adopted by the industry for the purpose of exploration, an active man-made EM source is often necessary. Considering the CSEM application for the search of hydrocarbons, with the inclusion of external electrical source $\mathbf{J_s}$, the Ampère-Maxwell equation in the time domain becomes

$$\nabla\times\mathbf{B}-\mu\varepsilon\frac{\partial\mathbf{E}}{\partial t}=\mu(\mathbf{J}+\mathbf{J_s}). \tag{2.18}$$

By taking the curl of equation 2.3, and combining with equations 2.7 and 2.18, the time-domain wave equation of $\mathbf{E}$ considering external electric source $\mathbf{J_s}$ is established as

$$\nabla \times \nabla \times \mathbf{E} + \mu\varepsilon \frac{\partial^2}{\partial t^2}\mathbf{E} + \mu\sigma \frac{\partial}{\partial t}\mathbf{E} + \mu \frac{\partial}{\partial t}\mathbf{J_s} = 0. \tag{2.19}$$

As discussed by equations 2.13, 2.14, and 2.15, considering low-frequency EM applications such as CSEM, we neglect the displacement current term, and assume the magnetic permeability is a constant of that of free space ($\mu_0 = 4\pi \times 10^{-7}$H/m). The governing equation of $\mathbf{E}$ in the time domain can be approximated as

$$\nabla \times \nabla \times \mathbf{E} + \mu_0\sigma \frac{\partial}{\partial t}\mathbf{E} + \mu_0 \frac{\partial}{\partial t}\mathbf{J_s} = 0, \tag{2.20}$$

and the frequency-domain governing equation can be derived as

$$\nabla \times \nabla \times \tilde{\mathbf{E}} + i\omega\mu_0\sigma\tilde{\mathbf{E}} + i\omega\mu_0\tilde{\mathbf{J}}_\mathbf{s} = 0, \tag{2.21}$$

correspondingly. Depending on the choice of electric source being used in the CSEM survey and the choice of the domain of solution, one may need to solve one of the equations from 2.16, 2.17, 2.20, and 2.21, to conduct a forward modelling process given a subsurface conductivity model.

2.2 A Review of Current Solutions

Controlled-source electromagnetic (CSEM) uses a man-made active electric source to excite EM signal and to locate subsurface resistivity variations. Starting from the first commercial test of marine CSEM for hydrocarbon detection as demonstrated by Ellingsrud et al. (2002), however, the acquisition and processing of CSEM data can have different implementations in the current industry. Constable (2010) and Ziolkowski and Slob (2019) give comprehensive reviews of the recent CSEM industry. Accordingly, the EM forward and inverse solutions are various. This section reviews part of the existing forward modelling solutions in the CSEM industry, based on two perspectives. First, there are time-domain solutions and frequency-domain solutions. Secondly, there are explicit modelling solutions and implicit modelling solutions. The aim is to briefly review the commonly used methods, discuss the difference, and indicate the position where the method that we are interested is sitting in the world of EM forward modellers. Note that the solutions reviewed in this section contain only 2D or 3D solutions where numerical discretization is involved. The 1D EM solutions can

often be semianalytical and follow a different manner. Those examples are given by, e.g., Slob et al. (2010); and Hunziker et al. (2015).

2.2.1 The domain of solution: time versus frequency

There are two different approaches to modelling CSEM data: time-domain CSEM (TEM) and frequency-domain CSEM (FEM). As stated by the name, TEM methods perform the modelling and recover the resistivity profile by matching the data in the time domain, whereas FEM methods operate in the frequency domain. The two methods are in theory equal, as the two domains are related by the Fourier transform. However, in practice, the two methods are different in the frequency content of the source signal, and therefore different in the bandwidth of the data.

TEM methods aim to recover the Earth's step response or impulse response. They use a source waveform and record data with the greatest possible bandwidth. The choice of source signal starts from Heaviside function, or step function. Since an impulse is the time derivative of a step, the impulse response can be obtained by differentiating the step response. In practice, the step function is implemented by switching on or off the electric source, including electric dipole, loop or electric line. Forward modelling solutions are demonstrated by, for example, Oristaglio and Hohmann (1984), who solve the response of a homogeneous half-space to the shut-off of a steady line current. The shutting-off of electric source means the source term can be abandoned after the initial time step, as shown in equation 2.16, which reduces the difficulty of forward modelling to some extent. Similar modelling studies utilizing the step function by the shutting-off of electric field can also be found in Wang and Hohmann (1993), Commer and Newman (2004), Um et al. (2010), and Commer et al. (2015).

Despite the simplicity of using a step function as the source signal, the complete step response cannot be fully obtained because it is infinitely long. Ziolkowski and Slob (2019) give a comprehensive analysis on the source time functions in TEM applications. A more precise way to recover the Earth's impulse response is to regard the Earth as a linear filter and the data as a convolution result of the Green's function with the source time function, and therefore the Earth's impulse response can be recovered by deconvolution of the measured data for the measured source time function. Wright et al. (2002) demonstrate the importance of measuring the source time function. The recovery of the earth impulse response is the patented multi-channel transient electromagnetic (MTEM) method (Wright et al. 2005) and the applications have been demonstrated in, for example, Wright et al. (2002); Ziolkowski et al. (2007); Ziolkowski et al. (2010); and Ziolkowski et al. (2011). If the source is measured and the step of deconvolution is included as in the MTEM method, the source time function can be various and not restricted to a step function anymore. Ziolkowski et al. (2011) show

the use of a pseudo-random binary sequence (PRBS) in marine CSEM application. The improvements on broadening the source bandwidth are obvious as demonstrated in the studies listed above. The advantages of PRBS are further demonstrated in Ziolkowski and Slob (2019) by comparing the deconvolution gain among PRBS, square-wave time function and other special periodic functions. They show the use of PRBS is especially preferable when noise is important in the measured data. However, no matter which source time function is used in practice, the forward modelling algorithm is trying to solve the same problem: it aims to solve the impulse response of a given model. Therefore, the forward modelling algorithm only needs to consider an impulsive electric source, e.g., an impulsive electric dipole. Such forward solutions can be found in Stoffa and Ziolkowski (2019); Liu et al. (2019b); and Liu (2019).

FEM methods aim to process and analyze the data in the frequency domain. The conductivity model from an FEM inversion is derived by matching the EM data at certain frequencies. A commonly used source signal is a continuous square wave function, which provides a discrete bandwidth consisting of a fundamental frequency and its odd harmonics. Since a square wave function does not provide energy at all frequencies up to the Nyquist frequency, the impulse response of the model cannot be recovered. This restricts the analysis of the data to the frequency domain, and cannot be transferred to the time domain. Nevertheless, if there is no intention to transform and analyze the data in the time domain, a discrete source bandwidth with the absence of some frequency components may not be a problem. In fact, the continuous square wave function has been widely applied in FEM applications. Recent examples on the analysis of FEM field data can be found in, e.g., Li and Li (2017); and Helwig et al. (2018). In this case, the forward modelling algorithms need to solve the electric field at a given frequency. Such forward solutions are discussed by, e.g., Li and Key (2007); Key and Ovall (2011); Jaysaval et al. (2016); and Li et al. (2018). It is worth pointing out that the choices of source time functions in FEM applications are not limited by a square wave function. A square wave function is used frequently because of its simplicity. More advanced periodic functions are proposed by, e.g., Srnka et al. (2006); Mittet and Schaug-Pettersen (2008); and Mattsson et al. (2012). The aim is to improve the number of frequencies and to improve the power at the selected frequencies. Nevertheless, the source bandwidth is still "discrete" which makes them distinctive as frequency-domain solutions. Again, no matter which source time function is used in an FEM application, the FEM forward modelling method is trying to solve the same problem: it aims to solve the response of the model one frequency at a time. The forward modelling of different frequencies are independent from each other.

It is beyond the scope of the thesis to demonstrate which domain is more appropriate for the analysis of EM data. Such studies are given by, e.g., Helwig et al. (2018); and Connell (2011), although in practice it is difficult to create a completely fair situation to compare the results between two different domains. The advantage of TEM methods is that the source time function covers a broad bandwidth. Based on the experience of seismic data analysis, a broader bandwidth should lead to a better subsurface model as there is more information contained in the data. However, the argument in favour of FEM methods is that the discrete source bandwidth has more energy in the selected frequencies, and does not waste energy in frequencies that are not needed.

I am personally more interested in time-domain EM solutions. There are two reasons. First of all, the transient signal in TEM methods can contain a broad frequency spectrum. The benefits of applying broad bandwidth signal have been demonstrated in seismic exploration, e.g., by Ten Kroode et al. (2013), and the same conclusion is intuitively transferable to EM surveys. As the data contains more information (frequencies), the subsurface model should be less likely trapped in a local minimum during the inversion process and the imaging should achieve better resolution. The current limitation of a transient signal, as discussed by many studies (e.g., Connell 2011), is that it is a relatively low-energy signal because of its broad spectrum. Therefore its advantages are often observed in low noise environments. Nevertheless, this limitation is more related to the energy of the source in practice, and should be countered accordingly in the future when the active man-made source becomes more powerful.

The second reason for my interest in time-domain EM solutions is that there are certain situations where time-domain approaches are preferable. For example, in shallow marine environment or in land survey where the source is close to the Earth-air interface, the response of the air is dominant whereas we are more interested in the response of the earth. The TEM methods can separate the two types of response relatively easily based on their arrival time (e.g., Ziolkowski and Wright 2007), thanks to the huge difference of EM wave velocity between the earth and the air. The FEM methods cannot take such advantage and therefore need to include the full airwave response in the inversion by accurately modelling the water layer.

2.2.2 Solving the governing equation: explicit vs implicit

The governing equation of the EM field is determined by the solution domain and the choice of the source signal, as discussed in section 2.2.1. The numerical formulation of the governing equation often involves many choices, e.g., the spatial discretization of the subsurface; the approximation of the partial derivatives; the handling of the numerical boundaries; etc.

To discretize the 3D subsurface, one may choose between a finite-difference system (e.g., Commer and Newman 2004) and a finite-element system Um et al. 2010. To approximate the spatial derivatives numerically, one may choose between a finite-difference estimator (e.g., Um et al. 2010) and a pseudospectral estimator (e.g., Carcione 2006). To truncate the computational mesh, one may choose between a Dirichlet boundary condition (e.g., Jaysaval et al. 2016) and a perfectly matched layer (e.g., Liu 2019). These options and their comparisons are discussed in detail in the following chapters when I demonstrate our modelling algorithm. This subsection aims to give a higher level of view. That is, after formulating the linear system, how the governing equation can be solved numerically as shown by many studies.

There are two basic numerical solution schemes: explicit and implicit. An explicit scheme solves the unknown quantities of the system based on its previous known state. For example, considering time-domain EM modelling, if $\mathbf{E}(t)$ is the current electric field and $\mathbf{E}(t+\Delta t)$ is the electric field at the later time with Δt defining the time step, an explicit method solves the electric field as

$$\mathbf{E}(t+\Delta t) = \mathbf{G}_{\text{exp}}(\mathbf{E}(t)), \tag{2.22}$$

where $\mathbf{G}_{\text{exp}}$ denotes a function that approximates spatial and temporal derivatives. The electric field at future time $\mathbf{E}(t+n\Delta t)$ can therefore be solved in order by an explicit scheme. In contrast, an implicit scheme needs to construct a linear system containing sets of equations of the electric field $\mathbf{E}$ at different sampling points, as

$$\mathbf{G}_{\text{imp}}\mathbf{E} = \mathbf{s}, \tag{2.23}$$

where $\mathbf{G}_{\text{imp}}$ denotes the system matrix determined by the approximations of the spatial and temporal derivatives; $\mathbf{E}$ is the unknown vector containing the components of $\mathbf{E}$ at different time points (or frequency components if considering frequency-domain EM modelling); and $\mathbf{s}$ is a known vector which often contains the source signal information in EM modelling. The forward modelling of the field $\mathbf{E}$ then becomes the problem of solving the inverse of matrix $\mathbf{G}_{\text{imp}}$, either via a direct matrix solver or via an iterative scheme.

Both numerical solution schemes, explicit and implicit, have been demonstrated successful in the modelling of low-frequency EM data. The advantage of an explicit method is its simplicity: one can avoid solving the inverse of a potentially very large matrix. Nevertheless, one needs to be careful with the stability of an explicit numerical solution because the explicit solution is only conditionally stable. One needs to match the stability condition to ensure the convergence of the solution, that is, the time step Δt needs to be less than a certain time so that the approximation of the temporal derivatives can be valid through the modelling. A

well-known stability condition is Courant–Friedrichs–Lewy (CFL) condition (Courant et al., 1928). For example, in one-dimensional modelling case, the CFL condition becomes

$$C = \frac{u\Delta t}{\Delta x} \leq C_{max}, \tag{2.24}$$

which indicates the maximum time step is related to the wave speed u and the spatial sampling Δx. The dimensionless number C is termed as the Courant number and the value of C_{max} changes with the specific method of being used. For a simple explicit linear solver, the value of C_{max} is 1. However, it is worth pointing out that the CFL condition is not a sufficient condition but a necessary condition to ensure the stability. In practice, the maximum time step may need to be even smaller than the reference provided by the CFL condition.

In contrast, the major advantage of an implicit method over an explicit method is its insensitivity to the numerical time step. The implicit methods are often described as unconditionally stable, because as long as the matrix inverse can be solved, the derived solution is always within the range of the specified error tolerance. The insensitivity of numerical time step is especially important in time-domain diffusive EM modelling, because the electric field may need to be solved over a large range of time, e.g., from 10^{-4} s to 10^{2} s. For such a diffusion problem, a very small numerical time step is required in early time to resolve the broad frequency spectrum of the electric field, and the high frequency components are rapidly attenuated with time and larger time steps are preferable for the consideration of efficiency. An explicit method with stringent stability conditions may be inefficient, and the choice of numerical time steps needs to be carefully designed to avoid numerical dispersion. The implicit methods, however, always try to solve the inverse of the linear system and are therefore more robust to the relatively arbitrary time steps. The time-domain CSEM implicit modelling examples have been shown by, e.g., Um et al. (2010); and the frequency-domain CSEM implicit modelling examples have been given by, e.g., Li and Key (2007); Mulder et al. (2008); and Key and Ovall (2011).

Nevertheless, the robustness to numerical steps does not mean implicit methods are always the panacea. The unconditional stability of implicit methods relies on the assumption that if the inverse of the linear system can be solved. However, in practice, solving the inverse of a linear system can be a difficult problem by itself. In addition to the formulation of the linear system (i.e., equation 2.23), there are two important points to consider: a) by which solver the linear system can be solved efficiently; and b) how the linear system can be preconditioned if the system matrix is ill-conditioned and yielding a slow convergence rate.

The options of linear solvers mainly fall into two categories: direct solvers and iterative solvers. Direct solvers attempt to solve the exact matrix inverse via a finite sequence of

operations, whereas iterative solvers approach to the matrix inverse iteratively following the gradient of the error estimator until it converges. Both types of solvers have been applied and demonstrated successful in CSEM modelling. Direct solvers are used by, for example, Li et al. (2018); and Um et al. (2010). The major advantages of direct solvers are the guarantee to find the exact matrix inverse and the regardless of iterative steps which may lead to slow convergence. A popular choice of direct solvers can be, e.g., MUMPS (MUltifrontal Massively Parallel Sparse direct Solver), as discussed in Amestoy et al. (2001) and a series of their studies. Davis (2006) gives a comprehensive review of direct solvers. On the other hand, the use of iterative solvers in CSEM modelling have been demonstrated by, e.g., Mulder et al. (2008); and Jaysaval et al. (2016). Iterative methods are often preferable when the system matrix is very large, and especially when the computer memory cannot allow the direct access to the entire matrix at once. A popular choice of iterative solvers can be a biconjugate-gradient-type method, e.g., BiCGStab2, as discussed in Van der Vorst (1992) and Gutknecht (1993). The performance of an iterative solver, i.e., the convergence rate of the system, also depends on the choice of parameters in specific problems. The common parameters that need tuning often include the updating step size, the choice of the regularization term, whether or not to apply linear constraints, and the updating direction, etc., although the updating direction is often paired with the choice of the iterative solver itself.

An efficient preconditioner is also necessary when applying iterative implicit methods, because the system matrices in low-frequency EM problems can be poorly conditioned. The poor conditioning of the matrix can be caused by, e.g., the presence of a highly resistive air layer, which gives a null-space to the 3D curl-curl operator; and/or large grid aspect ratios, e.g., the small grids required in the air layer compared with the large grids required in the edge region. Under such situations the inclusion of a preconditioning step is then important to speed up the convergence of the iteration. That is, instead of solving the original equation 2.23, one needs to design a preconditioner $\mathbf{P}_c$ and try to solve the preconditioned system

$$\mathbf{P}_c^{-1}\mathbf{G}_{imp}\mathbf{E} = \mathbf{P}_c^{-1}\mathbf{s}, \tag{2.25}$$

where $\mathbf{P}_c^{-1}\mathbf{G}_{imp}$ has a smaller condition number than $\mathbf{G}_{imp}$. A popular group of $\mathbf{P}_c$ can be the ones based on the multigrid method (Wesseling 1995; Briggs et al. 2000). The numerical solution is iteratively achieved within several cycles of varying the grid size between fine and coarse. The multigrid method can be used as a standalone solver or as a preconditioner for another one, as discussed in Aruliah and Ascher (2002); and Mulder (2006). The examples of utilizing a multigrid preconditioner in CSEM forward modelling are given by, e.g., Mulder et al. (2008); Koldan et al. (2014); and Jaysaval et al. (2016). The three listed examples

demonstrated the use of the multigrid preconditioner in finite-integral, finite-element and finite-difference systems, respectively.

It is not straightforward to conclude whether implicit methods or explicit methods can lead to a better performance in practice. For example, Mulder et al. (2008) discuss the computational complexity and shows the explicit Du Fort-Frankel method (Du Fort and Frankel 1953) has an asymptotic complexity of $\mathcal{O}(n^4)$, where n denotes the number of the grid points in one of the dimensions; and an implicit solver that converges in $\mathcal{O}(1)$ iterations also has the same computational complexity. The actual performances of the two methods still depend on the details of the implementation and the actual constants in the complexity analysis. Low-frequency, time-domain EM modelling is essentially a diffusive problem, which often requires the modelling to be conducted over a large dynamic time range and over an adaptive grid system, and that may be the reason that implicit methods are interested and applied in many studies as listed above. Nevertheless, the dynamic range of time and grid size also imposes difficulty on preconditioning the linear system. Unless an efficient preconditioner and its pairing solver have been found, solving the linear system can be difficult and time consuming. This is the main reason that researchers are exploring explicit methods to model the time-domain EM fields. The simplicity and stability of explicit methods have been demonstrated by, e.g., Wang and Hohmann (1993); Druskin and Knizhnerman (1994); Commer and Newman (2004); Carcione (2006); Commer et al. (2015); Stoffa and Ziolkowski (2019); Liu et al. (2019b); and Liu (2019). Since the bottleneck of an explicit method is its stringent stability condition, research effort has been made to mitigate this stringency and therefore improve the efficiency of the method.

One way to relax the restrictive stability limit is the Du Fort-Frankel method and its modified versions. Examples of the methods in modelling time-domain EM field are given by, e.g., Oristaglio and Hohmann (1984) for the 2D case; and Wang and Hohmann (1993); Commer and Newman (2004); and Commer et al. (2015) for the 3D cases. An artificial light term is introduced to the system, acting as a displacement current term, so that the original Du Fort-Frankel method can also be applied to the first-order equations. As discussed in Wang and Hohmann (1993), the method allows the numerical time step to be proportional to the square root of simulation time, without doing too much harm to the accuracy of the solution. The computational complexity can be reduced from $\mathcal{O}(n^5)$ to $\mathcal{O}(n^4)$ with the use of the method as discussed in Mulder et al. (2008). Commer and Newman (2004) present a parallel implementation of the method to further speed up the performance. Commer et al. (2015) show a more aggressive implementation of the method where by introducing a grid-coarsening step, the required number of time steps can be further reduced by a factor of up to 6.7, compared to the original scheme, without affecting the accuracy too much.

2.2.3 The Krylov method and the Chebyshev method

Section 2.2.1 discusses the domain to solve a CSEM modelling problem. Section 2.2.2 discusses the two numerical schemes to handle the modelling in the time domain. An explicit method solves the field at each numerical time point step by step (equation 2.22), whereas an implicit method solves the field as an inverse problem (equation 2.23). In addition to solving the time-domain field exactly in the time domain, an alternative solution is to utilize spectral methods to handle the time evolution of the field. Hesthaven et al. (2007) give a comprehensive review of using spectral methods to solve time-dependent problems. In general, spectral methods evaluate the solution as a sum of certain "polynomials". For example, considering time-domain EM modelling, a spectral method can solve the field $\mathbf{E}(t)$ in the form of

$$\mathbf{E}(t) = \sum c_n \mathbf{X}_n, \tag{2.26}$$

where $\mathbf{X}_n$ denotes the n-th term of the selected polynomial series, and c_n denotes its corresponding coefficient. The field $\mathbf{E}$ at each time point t is retrieved by a weighted summation of the selected polynomials $\mathbf{X}$. Therefore, the time-dependent field is essentially evaluated in the selected polynomial subspace. The polynomials $\mathbf{X}$ can be obtained following an explicit scheme. For example, the n-th Chebyshev polynomial can be calculated recursively from its $(n-1)$-th term and $(n-2)$-th term by using the Chebyshev recursive relation. Alternatively, the polynomials $\mathbf{X}$ can also be obtained following an implicit scheme as solving an inverse problem, as shown by, e.g., Druskin et al. (2009), and Börner et al. (2015).

Considering the time-domain diffusive EM modelling, there are mainly two types of methods being interested: Krylov methods (Druskin 1988; Druskin and Knizhnerman 1994; Druskin et al. 1999) and Chebyshev methods (Carcione 2006; Stoffa and Ziolkowski 2019; Liu et al. 2019b; Liu 2019). The two methods are based on different polynomial subspace, but they both follow the form of equation 2.26, that is, to retrieve the time-domain field by a weighted summation of the selected polynomials. As shown by Druskin (1988) and Carcione (2006), both methods allow the numerical step to be proportional to the square root of the simulation time, and therefore they are both at least an order of magnitude faster than the conventional explicit time-stepping.

Druskin (1988) show the time-domain diffusive EM solution in Krylov subspace, including a spectral Lanczos decomposition method to handle the matrix exponential in Krylov subspace. The original large sparse matrix is transformed into a much smaller and denser matrix during the iterative computation to enhance the efficiency. The Krylov method is subsequently extended to be applied in either time domain or frequency domain (Druskin and Knizhnerman 1994), and the efficiency and the accuracy appear to be attractive in 3D

applications (Druskin et al. 1999). The explicit Krylov method has then been extended to allow the use of Krylov subspace by an implicit numerical scheme. The rational Krylov subspace methods are demonstrated by, e.g., Druskin et al. (2009); Knizhnerman et al. (2009); Druskin et al. (2010); and Börner et al. (2015). The polynomial and rational Krylov methods form a popular group to solve the diffusive EM equation with spectral accuracy in either time domain or frequency domain.

The Chebyshev method is another spectral method which solves the time-domain EM field by an expansion of the time operator with Chebyshev polynomials. As discussed before, both the Chebyshev and Krylov methods are highly efficient methods (that allow the numerical step to be proportional to the square root of time). The main advantage of the Chebyshev method over the Krylov method is that it does not use inner products, whereas the Krylov method requires a matrix-vector evaluation at each iteration step. This feature makes the Chebyshev method highly attractive in parallel computing.

The Chebyshev method is first proposed by Tal-Ezer (1986) for solving hyperbolic equations. Kosloff et al. (1989) named the Chebyshev method the rapid expansion method (REM) in their study. The accuracy and efficiency of the method were first demonstrated in the modelling of seismic and EM waves (Tal-Ezer et al. 1987; Tal-Ezer et al. 1990; Davydycheva et al. 2003; and Pestana and Stoffa 2010). Carcione (2006) first shows the use of the Chebyshev method to solve the diffusive EM equation, considering a 2D conductive model and a magnetic source. Stoffa and Ziolkowski (2019) show the 3D application and the parallel implementation of the method.

Diffusive EM field modelling by the Chebyshev method is not as extensively studied as the Krylov method. To my knowledge there is no frequency-domain or implicit modelling version. It certainly requires future research to further utilize the benefits of the method. Nevertheless, there are three features that make the Chebyshev method highly attractive. First, it is a highly efficient explicit time-domain EM modelling method. Second, it only computes dot products among matrices during the modelling which is highly preferable in parallel computing. Third, it yields spectral accuracy in estimating the temporal derivatives and provides the numerical accuracy up to the Nyquist frequency. Therefore, temporal dispersion can be mitigated during the numerical modelling. In addition to the features above that make the Chebyshev method an efficient and accurate forward modeller, Stoffa and Ziolkowski (2019) show the Chebyshev polynomials expanded from the diffusive electric field essentially obey a discrete wave equation. This fact provides the potential, to either extend any wavefield modelling techniques to the diffusive electric field, or alternatively, to transform the diffusive electric field into a fictitious wave field. These are the main reasons why I am interested in researching the Chebyshev method.

The Chebyshev method, or more precisely, the rapid expansion method (to refer to the use of Chebyshev polynomials in seismic and EM modelling), are further discussed in detail in the following chapters.

2.3 Summary

The low-frequency electric field propagating in a conductive medium (such as the earth) obeys the diffusive equation where the displacement current can be neglected. The EM diffusion equation is the governing equation that needs to be solved in order to model CSEM data. The governing equation can be solved in the time domain or frequency domain, and can be solved by an explicit numerical scheme or an implicit numerical scheme. Various existing numerical solutions have been reviewed, and the rapid expansion method (REM) appears to be attractive, because of its accuracy, efficiency, and suitability to parallel computing.

Chapter 3

Rapid Expansion Method

The modelling of time-domain electromagnetic (EM) data relies mostly on finite-difference or finite-element methods. The accuracy is limited by the approximations of temporal and spatial derivatives. In this chapter, I review the theory of the rapid expansion method (REM), which uses an explicit scheme that solves the time-domain EM field by a Chebyshev expansion of the time operator. The temporal estimator is accurate to the Nyquist frequency and temporal numerical dispersion can be mitigated. By comparing the modelled synthetic data with the analytic solution, I demonstrate the correctness of the method as well as the code written by myself. The Chebyshev polynomials, expanded from the time-domain EM field, are proved to obey a discrete wave equation in the Chebyshev-space domain, with units of $\sqrt{\text{s}}$-m. The Chebyshev domain therefore provides the bridge to link the modelling of a diffusion field with a wavefield, which has the potential leading to various applications.

3.1 Introduction

Controlled-source electromagnetic (CSEM) data provide insight into how the formation behaves if an electric current is applied, which can be used to determine whether the pore fluids are conductive, for instance brine, or resistive, for instance hydrocarbons. The transient CSEM approach uses an impulsive electric dipole source to acquire the broadband information (Ziolkowski et al., 2011), and it has been applied successfully for detecting hydrocarbons in shallow water (Anderson and Mattson, 2010; Ziolkowski et al., 2010) and on land (Wright et al., 2002; Ziolkowski et al., 2007).

The extraction of subsurface conductivity from CSEM data relies on an iterative forward modelling process. The conductivity model is iteratively modified until it produces synthetic data that are in some sense a best fit to the real data. The resultant model is the model that best represents the subsurface, according to the specified criterion. Through this process,

the heart of the procedure is to model the electric field accurately in the space-time domain, given a known conductivity model.

Most existing modelling methods handle the time evolution of the electric field by a finite-difference scheme (Wang and Hohmann, 1993; Commer and Newman, 2004; Um et al., 2010). However, all finite-difference schemes have accuracy limited by the approximations of temporal derivatives. Low-order approximations of temporal derivatives may introduce numerical errors and dispersion. Such problems degrade the accuracy of the result and may lead to a failure of the modelling (Adhidjaja and Hohmann, 1989).

To address this issue, Tal-Ezer (1986) proposes a spectral method for hyperbolic equations based on a Chebyshev expansion of the time operator. The time evolution of the wavefield is integrated by a summation of the Chebyshev terms in the domain of the eigenvalues of the propagation matrix. Compared with the conventional, second-order finite-difference approximation of the temporal derivative, Tal-Ezer (1986) shows the proposed Chebyshev method can be orders of magnitude more accurate, at the same computational effort, or orders of magnitude more efficient, to achieve the same level of accuracy. Kosloff et al. (1989) named the Chebyshev method the rapid expansion method (REM). The accuracy and efficiency of REM has been demonstrated for the acoustic wave equation (Tal-Ezer et al., 1987; Pestana and Stoffa, 2010), visco-elastic equation (Carcione et al., 1988; Tal-Ezer et al., 1990), and Maxwell's EM wave equation (Raedt et al., 2003). The results are free of temporal discretization errors and accurate to the Nyquist frequency.

Most of the authors mentioned above use the Fourier pseudospectral method to evaluate the spatial derivatives in the wavenumber domain. The applications and advantages of the pseudospectral (PS) method has been widely discussed in previous studies such as Fornberg (1987, 1988); Liu (1997). Fornberg (1987) shows that the pseudospectral evaluation of spatial derivatives is accurate to the Nyquist wavenumber in a locally homogeneous part of the model, and with a 2D elastic wave modelling example he demonstrates the clear advantage of the PS method over the fourth-order finite-difference approximation when internal interfaces are present and P- and S-waves hit the interface with various angles. Liu (1997) uses a time-domain 2D EM wave modelling example to demonstrate that the PS evaluation only requires 2 grids per wavelength, compared with the finite-difference approximation requiring 8-16 grids per wavelength to achieve the same accuracy. Pestana and Stoffa (2010) state "When REM is combined with a pseudospectral method for the spatial derivatives ... we can obtain a well-balanced implementation with infinite accuracy in the time and space directions", which explains why the pseudospectral method is a common choice to be paired with REM to handle spatial and temporal derivatives.

Nevertheless, the pseudospectral method by itself is not panacea. It requires additional computational effort to transform between space and wavenumber domain, and the appearance of irregular internal interfaces reduces the benefits that it is expected to obtain. Fornberg (1988) describes the pseudospectral method "produced especially accurate results when interfaces were straight and located halfway between adjacent gridlines", but "with interfaces not aligned with the grid, large errors are unavoidable". He proposes a grid-mapping method to align the curved interface with the mapped grids. Mittet (2017) gives comprehensive analysis on the implementation of sharp internal interface in both finite-difference and pseudospectral situations, and proposes to band-limiting the jump of material properties to reduce the staircase diffraction generated by a sharp internal slope. For more complex model configurations, the finite-element method may be necessary (Um et al., 2010). However, the evaluation of spatial derivatives and the implementation of internal interface are independent of REM, which is concerned only with the time-stepping of the field in the Chebyshev domain. The reduction of temporal dispersion can be achieved anyway by using the Chebyshev expansion of the time operator, no matter which method is used to handle the spatial propagation of the field.

Carcione (2006) first extends the use of REM to solve a parabolic equation, considering the low-frequency, diffusive EM field in a 2D conductive section excited by a magnetic source. Stoffa and Ziolkowski (2019) extend Carcione (2006)'s work to 3D time-domain CSEM modelling. The implications of their work are twofold. First, they show how the REM can time-step a 3D diffusive electric field excited by an impulsive electric dipole, which is a common type of source used in marine and land CSEM (Wright et al., 2002; Anderson and Mattson, 2010), and therefore demonstrates the feasibility of using REM to solve a CSEM modelling problem. Second, they first observe that by expanding the time-domain diffusive electric field into the Chebyshev domain, the resultant Chebyshev terms exhibit wave-like characteristics, which is then shown to obey a discrete wave equation. This discovery provides the linkage between the modelling of a diffusive field and a wavefield, which opens up huge potential developments in the interpretation of time domain CSEM data.

I first review the work of Stoffa and Ziolkowski (2019) to describe the solution of the 3D diffusive electric field by REM in section 3.2. Then, in section 3.3, I provide numerical tests to demonstrate the accuracy of REM and the correctness of my code. Finally, the wave-like characteristics of the Chebyshev terms are revisited, with implications discussed in section 3.4.

3.2 Rapid Expansion Method

In conductive media where the displacement current can be neglected, the electric field **E**(x,y,z,t) satisfies the diffusion equation

$$\frac{\partial}{\partial t}\mathbf{E} = -\frac{1}{\mu_0}\boldsymbol{\sigma}^{-1}\nabla\times\nabla\times\mathbf{E} - \boldsymbol{\sigma}^{-1}\frac{\partial}{\partial t}\mathbf{J}_s, \tag{3.1}$$

where **E** is the vector electric field $\mathbf{E}(x,y,z,t) = (E_x(x,y,z,t), E_y(x,y,z,t), E_z(x,y,z,t))^T$ with units V/m; $\mathbf{J}_s$ (A/m^2) is the source current density and $\boldsymbol{\sigma}$ (S/m) is the conductivity tensor.

I present the derivation of the algorithm closely following the notation discussed in Stoffa and Ziolkowski (2019). They consider an isotropic conductive subsurface, where $\boldsymbol{\sigma}$ can be treated as a scalar σ, and the source term $\mathbf{J}_s$ is an impulsive electric dipole. Section 3.2.1 and 3.2.2 describe the handling of temporal and spatial derivatives, respectively. Section 3.2.3 gives the solution of the maximum absolute eigenvalue to ensure the convergence of Chebyshev expansion. Section 3.2.4 shows the solution of the initial field excited by the impulsive dipole to incorporate the source.

3.2.1 Time evolution of the field by REM

Considering an isotropic conductive subsurface, the two curl operators in equation 3.1 can be combined and equation 3.1 can be written as

$$\frac{\partial}{\partial t}\mathbf{E} = -\frac{1}{\mu_0\sigma}\begin{pmatrix} -(\partial_y{}^2+\partial_z{}^2) & \partial_x\partial_y & \partial_x\partial_z \\ \partial_y\partial_x & -(\partial_x{}^2+\partial_z{}^2) & \partial_y\partial_z \\ \partial_z\partial_x & \partial_z\partial_y & -(\partial_x{}^2+\partial_y{}^2) \end{pmatrix}\mathbf{E} + \mathbf{s}, \tag{3.2}$$

where σ is the conductivity matrix and can have a different value at every grid point, describing the 3D conductivity variations, and **s** denotes the source term in 3.1. The left-hand side of equation 3.2 describes the temporal variation of the field **E**, whereas the right-hand side of equation 3.2 describes the spatial variation of the field **E**. The spatial derivatives of **E** need to be evaluated numerically. I use a matrix **D** to define the numerical evaluation of the spatial derivatives inside the double curl operator,

$$\begin{pmatrix} -(\partial_y{}^2+\partial_z{}^2) & \partial_x\partial_y & \partial_x\partial_z \\ \partial_y\partial_x & -(\partial_x{}^2+\partial_z{}^2) & \partial_y\partial_z \\ \partial_z\partial_x & \partial_z\partial_y & -(\partial_x{}^2+\partial_y{}^2) \end{pmatrix}\mathbf{E} \approx \mathbf{DE}, \tag{3.3}$$

and equation 3.2 can be written in the matrix form as

$$\frac{\partial}{\partial t}\mathbf{E} = -\frac{1}{\mu_0\sigma}\mathbf{D}\mathbf{E} + \mathbf{s}, \tag{3.4}$$

or more compactly,

$$\frac{\partial}{\partial t}\mathbf{E} = \mathbf{G}\mathbf{E} + \mathbf{s}, \tag{3.5}$$

where $\mathbf{G}$ is termed as the propagation matrix

$$\mathbf{G} = -\frac{1}{\mu_0\sigma}\mathbf{D}. \tag{3.6}$$

The propagation matrix $\mathbf{G}$ consists of two parts: a numerical differential matrix $\mathbf{D}$, and the term related to the 3D conductivity model σ. Depending on the numerical method to evaluate the spatial derivatives, matrices $\mathbf{D}$ and $\mathbf{G}$ can have various forms. This is specified in section 3.2.2.

Since we are considering an impulsive electric source, immediately after the impulse there is no source term, but there is an initial field $\mathbf{E}_0$ generated by the impulsive source. With the absence of source, the temporal variation of the electric field becomes

$$\frac{\partial}{\partial t}\mathbf{E} = \mathbf{G}\mathbf{E}, \tag{3.7}$$

which essentially describes an exponential relaxation of $\mathbf{E}$ with time. The field $\mathbf{E}$ at time t can be solved from the initial field $\mathbf{E}_0$, as

$$\mathbf{E}(t) = \exp(\mathbf{G}t)\mathbf{E}_0. \tag{3.8}$$

Rapid expansion method evaluates the matrix exponential term $\exp(\mathbf{G}t)\mathbf{E}_0$ by a Chebyshev expansion of the exponential term truncated to order M

$$\mathbf{E}(t) \approx \sum_{k=0}^{M} b_k \mathbf{Q}_k, \tag{3.9}$$

where $\mathbf{Q}$ denotes the Chebyshev terms,

$$\mathbf{Q}(x,y,z) = Q_x(x,y,z)\mathbf{u}_x + Q_y(x,y,z)\mathbf{u}_y + Q_z(x,y,z)\mathbf{u}_z \tag{3.10}$$

and the weights b_k are given by

$$b_k = c_k \exp(-bt) I_k(bt), \tag{3.11}$$

where $c_0 = 1$, $c_k = 2$, for $k \geq 1$, I_k is the modified Bessel function and b is the maximum absolute eigenvalue of the propagation matrix $\mathbf{G}$. The choice of M in equation 3.9 is related to the value of b to ensure the convergence (discussed later). The Chebyshev terms $\mathbf{Q}$ are updated by the Chebyshev recursion as

$$\mathbf{Q}_0 = \mathbf{E}_0, \tag{3.12}$$

$$\mathbf{Q}_1 = \mathbf{F}\mathbf{E}_0, \tag{3.13}$$

$$\mathbf{Q}_{k+1} = 2\mathbf{F}\mathbf{Q}_k - \mathbf{Q}_{k-1}, \tag{3.14}$$

with the numerical operator $\mathbf{F}$ defined as

$$\mathbf{F} = \frac{1}{b}\mathbf{G} + \mathbf{I}, \tag{3.15}$$

where $\mathbf{I}$ is the identity matrix.

The evolution of the field exactly follows equations 3.12, 3.13 and 3.14 to obtain the required number of Chebyshev terms in order. The time-domain electric field is then retrieved by a weighted summation of the Chebyshev terms, as defined in equation 3.9.

3.2.2 Spatial propagation of the field

The recursive updating of Chebyshev terms needs the calculation of the propagation matrix $\mathbf{G}$ at every step. This section shows the solution of the spatial derivatives inside the matrix $\mathbf{G}$ by a pseudospectral method in the 3D wavenumber domain. Similarly to the temporal Fourier transform defined in equations 2.9 and 2.10, define the spatial Fourier transforms along directions x, y and z as

$$\mathrm{FT}_x[a(x,y,z,t)] = \tilde{a}(k_x,y,z,t) = \int_{-\infty}^{+\infty} a(x,y,z,t) \exp(-ik_x x) dx, \tag{3.16}$$

$$\mathrm{FT}_y[a(x,y,z,t)] = \tilde{a}(x,k_y,z,t) = \int_{-\infty}^{+\infty} a(x,y,z,t) \exp(-ik_y y) dy, \tag{3.17}$$

$$\mathrm{FT}_z[a(x,y,z,t)] = \tilde{a}(x,y,k_z,t) = \int_{-\infty}^{+\infty} a(x,y,z,t) \exp(-ik_z z) dz, \tag{3.18}$$

respectively, with the corresponding inverse transforms as

$$\mathrm{FT}_x^{-1}[\tilde{a}(k_x,y,z,t)] = a(x,y,z,t) = \frac{1}{2\pi}\int_{-\infty}^{+\infty}\tilde{a}(k_x,y,z,t)\exp(ik_x x)dk_x, \tag{3.19}$$

$$\mathrm{FT}_y^{-1}[\tilde{a}(x,k_y,z,t)] = a(x,y,z,t) = \frac{1}{2\pi}\int_{-\infty}^{+\infty}\tilde{a}(x,k_y,z,t)\exp(ik_y y)dk_y, \tag{3.20}$$

$$\mathrm{FT}_z^{-1}[\tilde{a}(x,y,k_z,t)] = a(x,y,z,t) = \frac{1}{2\pi}\int_{-\infty}^{+\infty}\tilde{a}(x,y,k_z,t)\exp(ik_z z)dk_z, \tag{3.21}$$

respectively. The 1-D spatial Fourier transforms can be combined in any order to give the transformed field in the desired wavenumber domain, for example, the 3-D spatial Fourier transform is given as

$$\begin{aligned}\mathrm{FT}^3_{(x,y,z)}[a(x,y,z,t)] &= \mathrm{FT}_x[\mathrm{FT}_y[\mathrm{FT}_z[a(x,y,z,t)]]]\\ &= \tilde{a}(k_x,k_y,k_z,t),\end{aligned} \tag{3.22}$$

with the inverse

$$\begin{aligned}\mathrm{FT}^{-3}_{(x,y,z)}[\tilde{a}(k_x,k_y,k_z,t)] &= \mathrm{FT}_x^{-1}[\mathrm{FT}_y^{-1}[\mathrm{FT}_z^{-1}[\tilde{a}(k_x,k_y,k_z,t)]]]\\ &= a(x,y,z,t).\end{aligned} \tag{3.23}$$

The partial derivatives in the spatial domain become multiplications in the corresponding wavenumber domain, as

$$\frac{\partial}{\partial x}a(x,y,z,t) = \mathrm{FT}_x^{-1}[ik_x\tilde{a}(k_x,y,z,t)], \tag{3.24}$$

$$\frac{\partial}{\partial y}a(x,y,z,t) = \mathrm{FT}_y^{-1}[ik_y\tilde{a}(x,k_y,z,t)], \tag{3.25}$$

$$\frac{\partial}{\partial z}a(x,y,z,t) = \mathrm{FT}_z^{-1}[ik_z\tilde{a}(x,y,k_z,t)], \tag{3.26}$$

respectively. By transforming the differential matrix $\mathbf{D}$ defined in equation 3.3 into the 3-D wavenumber domain (k_x,k_y,k_z)

$$\tilde{\mathbf{D}} = \mathrm{FT}^3_{(x,y,z)}[\mathbf{D}] = \begin{pmatrix} {k_y}^2+{k_z}^2 & -k_xk_y & -k_xk_z \\ -k_yk_x & {k_x}^2+{k_z}^2 & -k_yk_z \\ -k_zk_x & -k_zk_y & {k_x}^2+{k_y}^2 \end{pmatrix}, \tag{3.27}$$

the calculation of the propagation matrix **G** at every step by a pseudospectral method is then given as

$$\mathbf{GQ}_k = -\frac{1}{\mu_0\sigma}\mathrm{FT}^{-3}_{(x,y,z)}[\tilde{\mathbf{D}}\cdot\mathrm{FT}^{3}_{(x,y,z)}[\mathbf{Q}_k]]. \tag{3.28}$$

The 3-D forward and inverse Fourier transforms of the Chebyshev terms **Q** are numerically implemented using the Fast Fourier transform (FFT) algorithm. All the components of **Q** are collocated with the conductivity σ at the same position without any grid staggering, so that the material properties are not altered during modelling. Averaging the material property is, however, a standard treatment in staggered grids used by finite difference methods. It results in ambiguous definitions of boundaries and creates transition layer effects (Feise et al., 2004).

3.2.3 Eigenvalue of the propagation matrix

In the 3-D wavenumber domain (k_x, k_y, k_z), the propagation matrix is

$$\tilde{\mathbf{G}} = -\frac{1}{\mu_0\sigma}\tilde{\mathbf{D}}, \tag{3.29}$$

with the differential matrix $\tilde{\mathbf{D}}$ defined in equation 3.27. The eigenvalues of $\tilde{\mathbf{G}}$ satisfying equation

$$\tilde{\mathbf{G}} - \lambda\mathbf{I} = 0 \tag{3.30}$$

can be solved as

$$\begin{aligned}
\lambda_1 &= 0, \\
\lambda_2 &= -\frac{1}{\mu_0\sigma}({k_x}^2 + {k_y}^2 + {k_z}^2), \\
\lambda_3 &= -\frac{1}{\mu_0\sigma}({k_x}^2 + {k_y}^2 + {k_z}^2),
\end{aligned} \tag{3.31}$$

and therefore they are all real and negative, which is important for the convergence. The maximum absolute eigenvalue, b, corresponds with the minimum conductivity (i.e., the highest speed) and the maximum wavenumber components. The maximum wavenumber components are the Nyquist wavenumbers, i.e., the highest wavenumber of the spatial Fourier transform. For the use of FFT and the grid spacings of Δx, Δy and Δz, the Nyquist wavenumbers are

$$\begin{aligned}
k_{x,Nq} &= \pi/\Delta x, \\
k_{y,Nq} &= \pi/\Delta y, \\
k_{z,Nq} &= \pi/\Delta z, f
\end{aligned} \tag{3.32}$$

respectively. Hence, combining equations 3.31 and 3.32, the maximum absolute eigenvalue, b, is

$$b = \frac{\pi^2}{\mu_0 \sigma_{\min}} \left(\frac{1}{\Delta x^2} + \frac{1}{\Delta y^2} + \frac{1}{\Delta z^2} \right), \tag{3.33}$$

with the unit of s^{-1} (Stoffa and Ziolkowski, 2018). Tal-Ezer (1989) shows the polynomial order should be $O(\sqrt{bt})$. Carcione (2006) finds that

$$M = \beta \sqrt{bt} \tag{3.34}$$

is sufficient to obtain stability and accuracy with β in the range of 5-6.

3.2.4 Solution to initial condition

The REM modelling can be initiated either by a source or by an initial condition (Carcione, 2006). Stoffa and Ziolkowski (2019) give the analytic expression of the initial condition $\mathbf{E}_0$ excited by an impulsive dipole. The solution is derived by taking the time-derivative of the analytic solution for the switch-on step response of an x-directed current dipole at the origin of a full space, given by Ward and Hohmann (1987). The source function of an x-directed impulsive dipole is

$$\mathbf{J}_s = Ids\,\delta(x)\delta(y)\delta(z)\delta(t)\mathbf{u}_x, \tag{3.35}$$

in which I is the current and Ids is the dipole moment (amp-m), $\delta(t)$ is the Dirac delta function, and $\mathbf{u}_x$ is the unit vector in the x-direction. Considering the dipole located at the origin $(0,0,0)$, the three components of the initial field $\mathbf{E}_0$ at position (x,y,z) and time t is solved as

$$E_x(x,y,z,t) = \frac{Ids\theta^3}{\pi^{3/2}\sigma t} \exp\left(-\theta^2 r^2\right)\left(1 - \theta^2(y^2+z^2)\right), \tag{3.36}$$

$$E_y(x,y,z,t) = \frac{Ids\theta^5}{\pi^{3/2}\sigma t} \exp\left(-\theta^2 r^2\right) xy, \tag{3.37}$$

$$E_z(x,y,z,t) = \frac{Ids\theta^5}{\pi^{3/2}\sigma t} \exp\left(-\theta^2 r^2\right) xz, \tag{3.38}$$

in which

$$\theta = \left(\frac{\mu_0 \sigma}{4t}\right)^{1/2}, \tag{3.39}$$

and

$$r = (x^2 + y^2 + z^2)^{1/2}. \tag{3.40}$$

Therefore the initial field $\mathbf{E}_0$ can be established at any grid point and at any initial time. The analytical solution of $\mathbf{E}_0$ treats σ as a constant, which implies the source region to be

homogeneous. The value of the initial time, t_0, cannot be too large to violate this assumption. It can neither be too small with respect to the grid spacing, otherwise it creates a singularity at the source position. An empirical choice of t_0 is given by Stoffa and Ziolkowski (2019) as

$$t_0 \approx 2.5\mu\sigma(\Delta l)^2, \tag{3.41}$$

where Δl is the smallest of Δx, Δy, and Δz.

The assumption of a homogeneous source region can be valid in many practical examples, e.g., a towed electric dipole source in the sea water. But it is not always true. To consider an arbitrary conductivity variation within the source region, one may need to solve a 3D Poisson problem, as discussed in Commer and Newman (2004). Alternatively, one can introduce irregular grids to establish the model, and use fine enough grids around the source and compute the initial field at a early enough t_0 until the partial homogeneous assumption can be valid.

To summarize, the numerical structure of REM follows the updating of Chebyshev terms explicitly. First an initial field needs to be established at an appropriate time. This initial field is the first Chebyshev term. Then the rest of the Chebyshev terms are computed recursively, as shown in equations 3.13 and 3.14. The evaluation of the propagation matrix $\mathbf{G}$ is undertaken in the wavenumber domain by a pseudospectral method, as shown in equation 3.28. The updating of Chebyshev terms is truncated at a finite order, where the order to ensure the convergence is related to the eigenvalue of $\mathbf{G}$ and given in equation 3.34. The obtained Chebyshev terms are weighted and summed to retrieve the electric field in the time domain, as shown in equation 3.9.

3.3 Numerical Example: A Homogeneous Full Space

In this section, I present numerical tests to demonstrate the accuracy of the REM solution. I check the code in a homogeneous full space against the analytical solution given by Slob et al. (2010). I use the same model configuration as shown in Stoffa and Ziolkowski (2019). The REM algorithm has been written in a parallel FORTRAN code (Stoffa and Ziolkowski, 2019), a parallel C code (Liu et al., 2019a), and an alternative MATLAB code. For the tests below with a computationally small model, I reproduce the published results by my MATLAB code, running on a desktop machine with a single core (3.20 GHz), to demonstrate the correctness of the algorithm and the code.

For the results shown below I do not apply an absorbing boundary. The default numerical boundary condition of the pseudospectral REM algorithm is a periodic boundary condition,

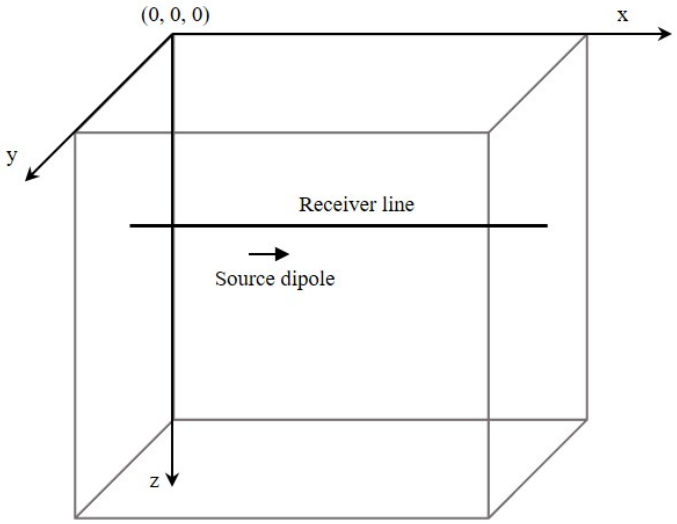

Fig. 3.1 Configuration of the model. The full-space modelling cube is constructed by $128\times128\times128$ nodes with a constant grid spacing of 20 m along x-, y-, and z-direction. The origin of the Cartesian coordinates is placed at one corner of the cube; axes are coincident with three edges. The 1 amp-m source dipole is at (1010, 1010, 1010) m, and the receivers are along the line parallel to the x-axis with $y = 1000$ m and $z = 900$ m.

because the use of FFT implicitly assumes the periodicity of the signal. Since the diffusive EM field decays naturally in a conductive medium, a practical option is to extend the model to be large enough for the desired simulation time. The use of the periodic boundary condition is proved adequate to avoid most edge effects except for the very late arrival times near the edge of the model as shown in Figure 3.2 and 3.3. A more accurate and complicated absorbing boundary condition, perfectly matched layers, is discussed in Chapter 6.

Figure 3.1 shows the configuration of the model, constructed by 128 × 128 × 128 nodes with a constant grid spacing of 20 m in the x-, y- and z-directions, respectively. The conductivity is 1 S/m everywhere. The origin (0, 0, 0) of the Cartesian coordinates is placed at one corner of the model cube. The source is located at (1010, 1010, 1010) m, halfway between the computational nodes close to the centre of the cube. I use a unit dipole moment $Ids = 1$ amp-m. The initial field is computed with $t_0 = 1$ ms after some preliminary tests. The simulation time is 200 ms with a sample interval $\Delta t = 2$ ms, which needs about 540 Chebyshev terms to converge and takes approximately 20 minutes on the single-core desktop.

Figure 3.2 compares all the three components of the **E** field at two receiver positions, (500, 1000, 900) m and (1520, 1000, 900) m, which are symmetric for the x-coordinate of the source. The modelling results show an excellent agreement with the analytic solution with no observable difference. The two selected receivers have exactly the same y- and z-coordinates, but the opposite x-offset with respect to the source. Therefore the component E_x should be

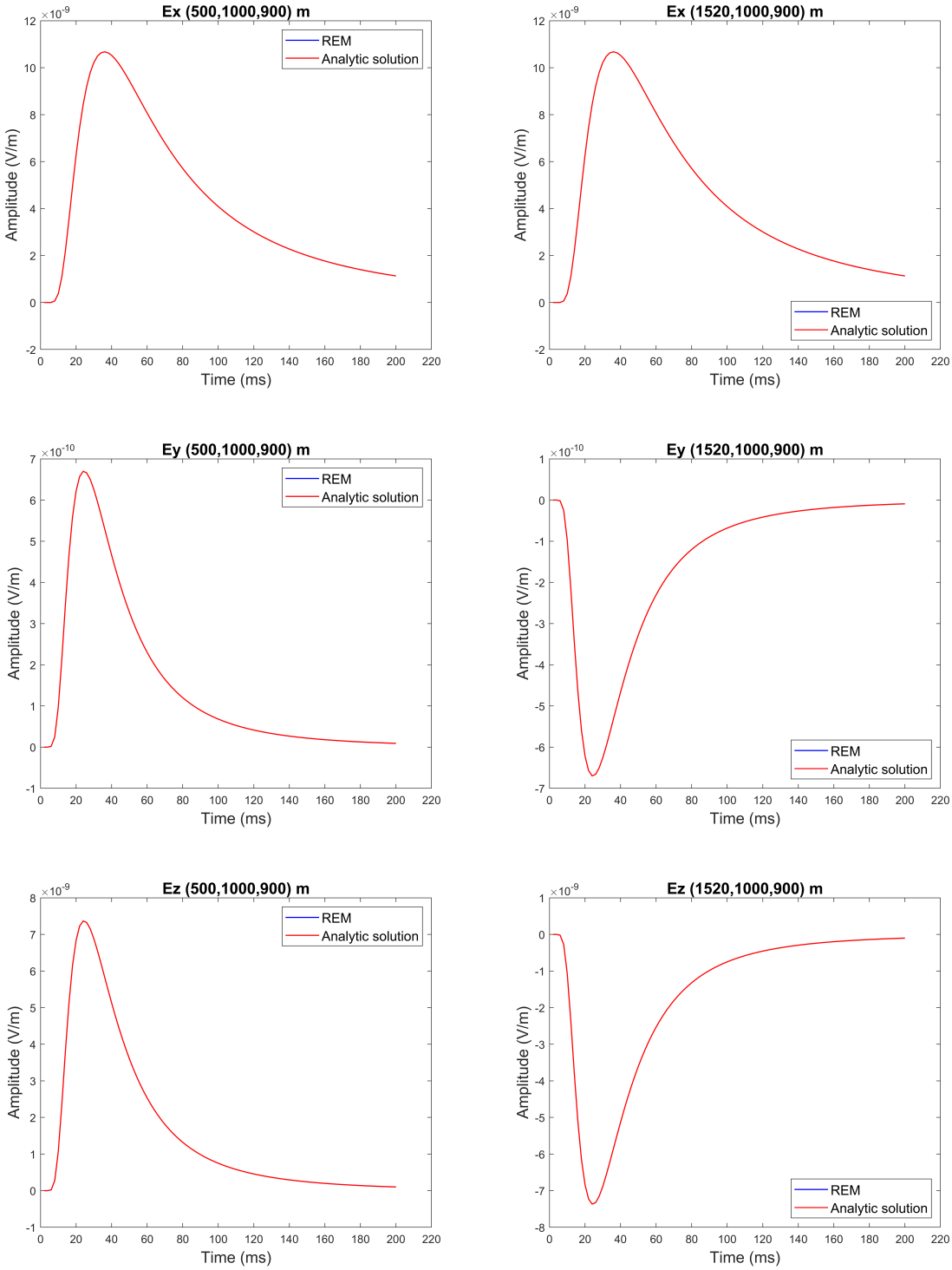

Fig. 3.2 Comparison of the three components of the electric field in the time domain. The REM and analytic solution are denoted by blue and red lines, respectively. Two receiver positions are shown: (500, 1000, 900) m (left column) and (1520, 1000, 900) m (right column).

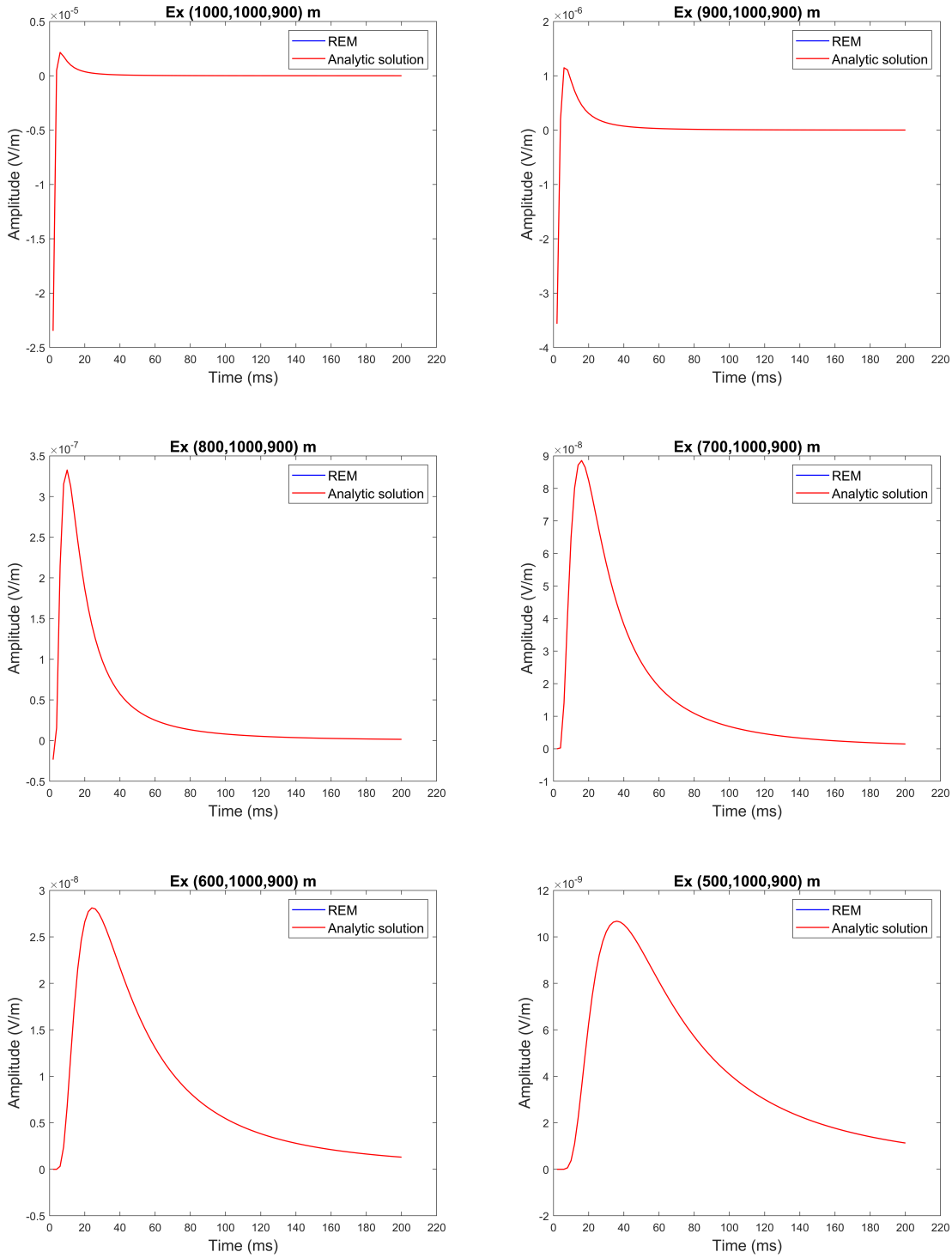

Fig. 3.3 Comparison of the inline electric field along the receiver line. The REM and analytic solutions are denoted by blue and red lines, respectively.

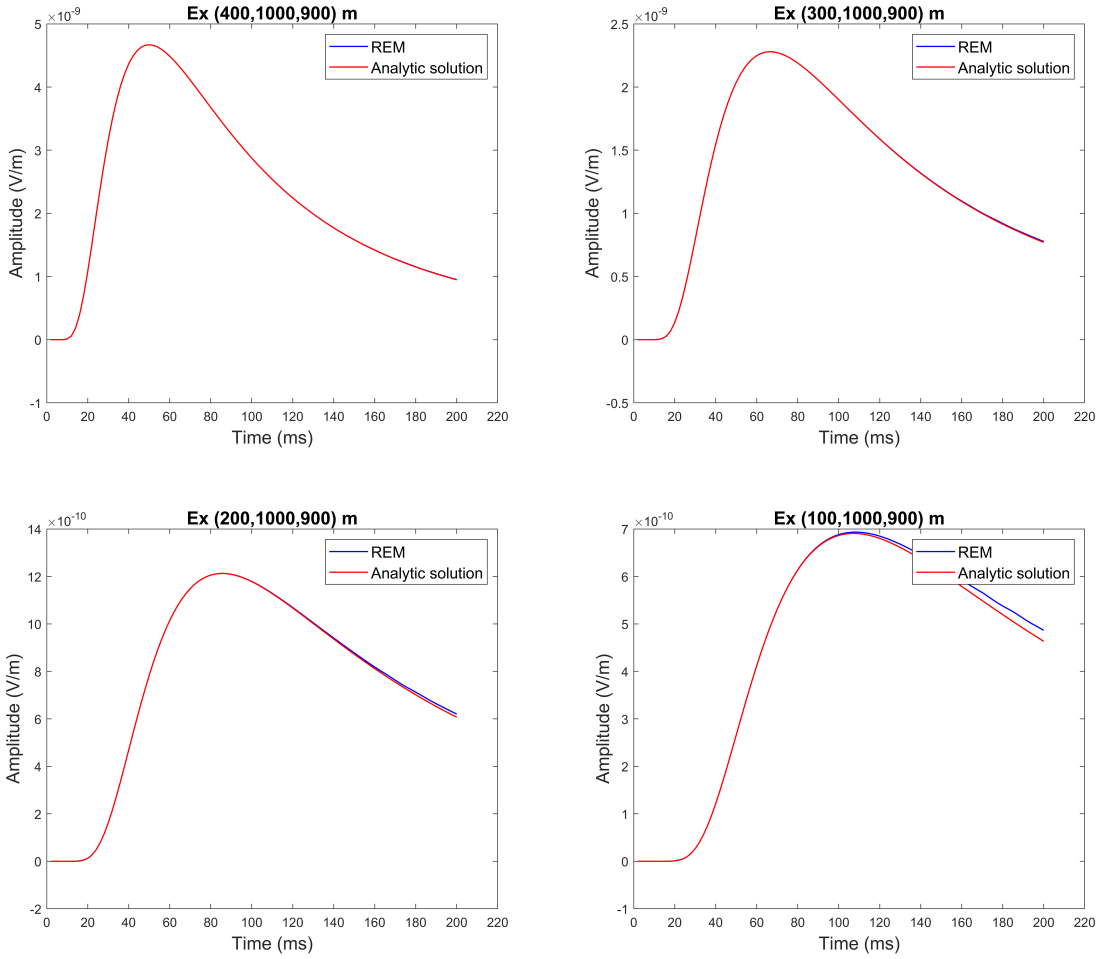

Fig. 3.3 Comparison of the inline electric field along the receiver line (cont.). The REM and analytic solutions are denoted by blue and red lines, respectively.

symmetrical, and it is; the components E_y and E_z should be antisymmetrical, and they are. Since the receiver line is placed vertically above the source with a small crossline offset (10 m), the amplitude of the crossline component, E_y, is the smallest among the three: it is an order of magnitude smaller than E_z, and two orders of magnitude smaller than E_x.

The inline component E_x is then examined along the receiver line as shown in Figure 3.3. Because of the established symmetry, only half of the receivers are shown, with the x-offset 10 m, 110 m, 210 m, ..., until 910 m, approximately reaching to the side of the cube. Almost all of the plots show exactly the correct modelling response. The only exceptions are the far-offset, late-time response, where the effect of numerical boundaries becomes more severe. For a model using the Dirichlet boundary condition or periodic boundary condition,

distortions from the boundaries are inevitable. For these boundary conditions, the model needs to be sufficiently large for a given propagation time.

Figure 3.4 shows the relative percentage error at three positions, considering near-, mid- and far-offset results: x = 900 m (offset = 110 m), x = 500 m (offset = 510 m), and x = 100 m (offset = 910 m). For the near offset (x = 900 m), the relative difference is less than 0.01% for all times to 200 ms. For the mid offset (x = 500 m), the relative difference is less than 0.1% for most of the time, except for the very early time (less than 10 ms) where the maximum difference reaches to less than 1%. The amplitude of the signal is very small during the early time, as shown in Figure 3.3, and the calculated relative difference is easily affected by numerical rounding errors. For the far offset (x = 100 m), the relative difference increases up to 3% during the early times before the main peak arrives, and decreases down to below 0.01% at approximately 60 ms during the main peak of the signal, and then increases steadily to approximately 5% at 200 ms. This error is attributed to the periodic boundary condition being used in this case, as discussed before. The level of accuracy presented in this 3D example (Stoffa and Ziolkowski, 2019) is similar to the 2D example presented in Carcione (2006) with a magnetic source.

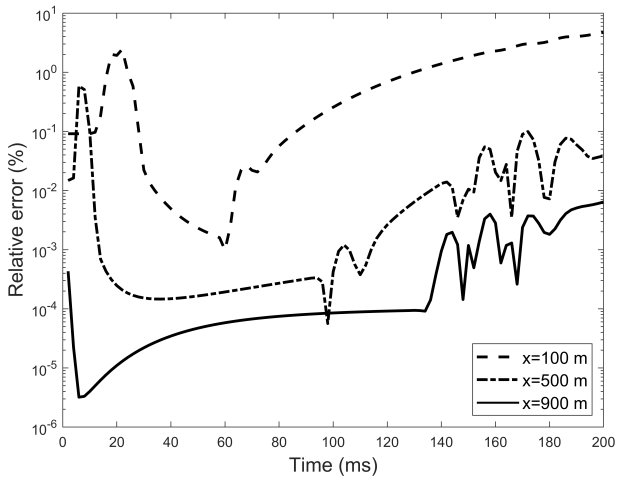

Fig. 3.4 Relative difference plot for the inline electric field at three receivers, x = 100, 500 and 900 m, considering far-, mid- and near-offset, respectively.

To summarise, the comparison between the pseudospectral REM modelling code and the analytic solution for a homogeneous full space indicates that the method is very accurate and produces synthetic data that match the analytic solution almost perfectly in the main part of the model. Numerical dispersion is hardly observed. No filtering is applied to the signal in either space or time. The edge effects shown in the example can be reduced by either enlarging the model in space, or by improving the numerical boundary condition.

3.4 Discussion: the wave-like Chebyshev polynomials

Stoffa and Ziolkowski (2019) first observed the wave-like characteristics in snapshots of the Chebyshev terms **Q**. Figure 3.5 shows the x-z plane snapshots of the 60th, 120th, 180th Chebyshev terms from the simulation of a homogeneous full space presented in section 3.3. Although the first Chebyshev term $\mathbf{Q}_0$ is in fact a diffusive field, the rest of the Chebyshev terms exhibit a propagating wave with the increase of polynomial order. After the integration weighted by the modified Bessel function (equation 3.9) the wave-like characteristics disappear and the field **E** propagates as a diffusive field in conductive media. Figure 3.6 shows the snapshots of **E** on the same plane.

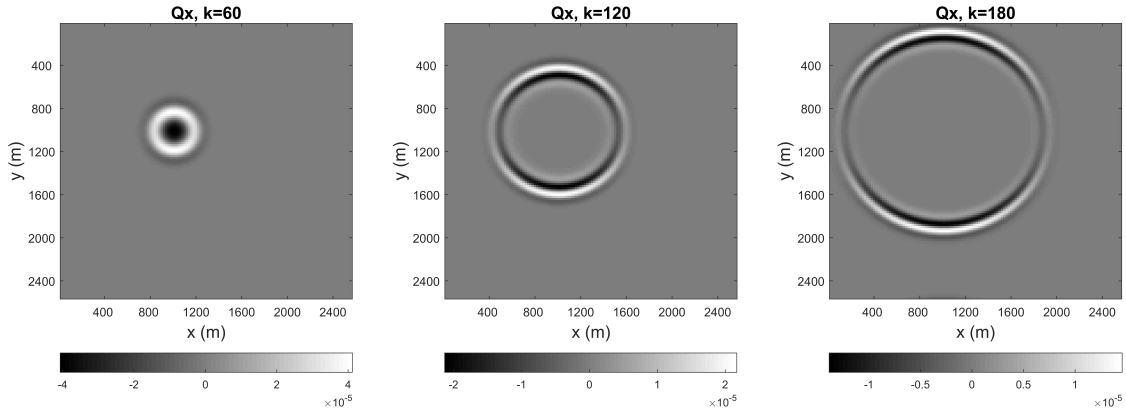

Fig. 3.5 Snapshots of Q_x. The x-z plane is located on $y = 1000$ m.

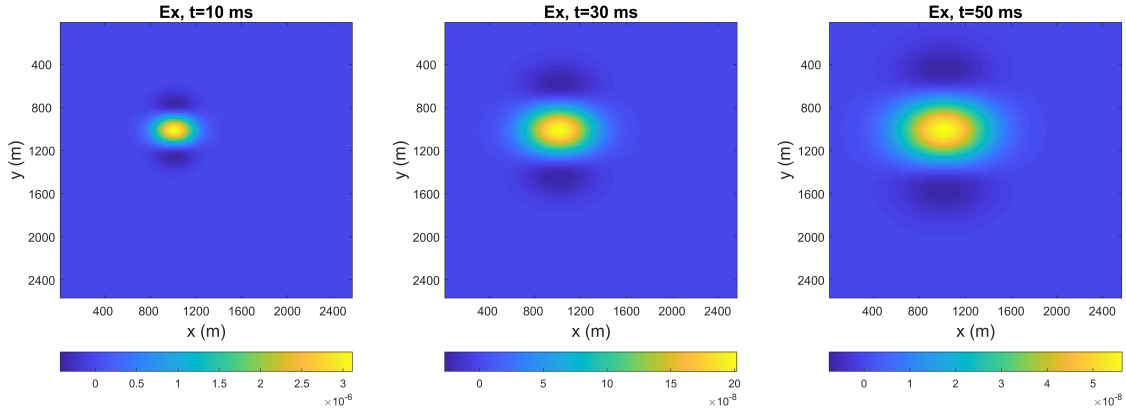

Fig. 3.6 Snapshots of E_x. The x-z plane is located on $y = 1000$ m.

The wave-like characteristics of the Chebyshev terms are proved mathematically by Stoffa and Ziolkowski (2019). By combining equations 3.6, 3.14 and 3.15, the recursive

updating of Chebyshev polynomials can be written as a discrete wave equation

$$\frac{\mathbf{Q}_{k+1} - 2\mathbf{Q}_k + \mathbf{Q}_{k-1}}{\Delta p^2} = -\frac{1}{\mu\sigma}\nabla \times \nabla \times \mathbf{Q}_k, \tag{3.42}$$

where

$$\Delta p = \sqrt{2/b}, \tag{3.43}$$

which can be seen as the equivalent time step in the Chebyshev domain. The maximum eigenvalue b, as given in equation 3.33, has units in s^{-1}. Thus the Chebyshev time step Δp has units in the square root of time, $\sqrt{\mathrm{s}}$. The corresponding 'velocity' in the Chebyshev-space domain is $\sqrt{1/\mu\sigma}$ and has units in $\mathrm{m}/\sqrt{\mathrm{s}}$. Therefore, the updating of Chebyshev polynomials is essentially equivalent to the propagation of a wavefield in Chebyshev domain, where the Chebyshev time interval Δp is dependent on the maximum eigenvalue of the propagation matrix. Equation 3.42 explains the wave-like characteristics being observed in the snapshots of Chebyshev terms.

It is not the first time that one can relate the diffusive EM field to a fictitious wavefield domain. As discussed in Stoffa and Ziolkowski (2019), the closest relation to their work would be the q-transform and its related applications (e.g., Lee et al., 1989; Lee and Xie, 1993; Wilson, 1997; Lee and Uchida, 2005; Li et al., 2017). The q-transform is based on the Laplace transform of the electric field, so that the diffusive field can be related to an equivalent wavefield with a transformation of variables. The equivalent wavefield derived from the q-transform shares the same units for the time-like variable and velocity with the Chebyshev domain: $\sqrt{\mathrm{s}}$ and $\mathrm{m}/\sqrt{\mathrm{s}}$, respectively. As indicated by Stoffa and Ziolkowski (2019), "it is shown that the integral transformation (equation 11) of Lee et al. (1989) and our summation with modified Bessel function weights are in fact the analog and discrete equivalents of each other". When simulating the wavefield in the fictitious domain, the q-transform methods use Courant-Friedrichs-Lewy (CFL) stability condition to choose the numerical step, whereas the Chebyshev method determines the step based on an eigenvalue analysis. While considering the diffusion-to-wavefield mapping, both methods are facing an ill-posed problem to transform the diffusive electric field into an equivalent fictitious wavefield. Attempts of diffusion-to-wavefield mapping have been shown by, e.g., Wilson (1997), Lee and Uchida (2005), Ziolkowski and Stoffa (2019). Other diffusion-wavefield transformation methods, as presented in de Hoop (1996), Mittet (2010), serve a similar purpose, but the dimension of the time-like variable remain in time, instead of the square root of time, and therefore are clearly different from the wavefield presented in the Chebyshev domain.

The bridge between a diffusive field and a wavefield can certainly lead to various interesting applications. First, there are many efficient wave modelling algorithms readily available. Those algorithms can be transferred to the fictitious wavefield domain, which is the Chebyshev domain in this case, and they should work successfully. Therefore the modelling of a diffusive EM field has the potential to be realised from both a diffusion-based algorithm and a wave-based algorithm. The Chebyshev domain provides the option. An example is given in Chapter 6 for further discussion. Second, as discussed in Stoffa and Ziolkowski (2019), the use of the Chebyshev domain can go beyond the realm of modelling. Since the wavefield **Q** and the diffusive field **E** are related by the Bessel function weighting (equation 3.9), in theory, the wavefield **Q** should be able to be recovered from the diffusive field **E**. In that case, EM data can be transformed and then processed and interpreted as waves, just like seismic data. Nevertheless, the extraction of the **Q** field from the **E** field involves the deconvolution of a sparse matrix, which can be unstable especially when the actual field **E** is collected with noise. Whether we can recover the field **Q** from real data remains a topic for future consideration.

3.5 Summary

This chapter reviews the theory of the rapid expansion method for modelling transient electromagnetic data in conductive media. The time evolution of the EM field is handled by a weighted sum of Chebyshev polynomials. The spatial derivatives are solved in the wavenumber domain by a pseudospectral method. The modelling is initiated by an initial condition excited by an impulsive dipole, and truncated at a sufficient degree to ensure convergence. The method is accurate to the Nyquist frequency and temporal numerical dispersion is hardly observed. The correctness of the method and the code are demonstrated with a homogeneous isotropic full-space example.

The updating of Chebyshev polynomials is proved to obey a discrete wave equation. The Chebyshev polynomials can be seen as a fictitious wavefield. After transforming into the Chebyshev domain, the modelling of a diffusive electric field is undertaken by the modelling of a wavefield. The Chebyshev domain provides the bridge to link a diffusive field with a wave field, which can lead to various potential applications in modelling, and presumably, processing and interpretation of electromagnetic data.

Chapter 4

Inclusion of the Earth-Air Interface

In the air, the electromagnetic (EM) field travels as a wave at the speed of light, which is orders of magnitude faster than the speed of EM diffusion propagating in the earth. The huge velocity difference makes the Earth-air interface a special internal interface requiring extra consideration in numerical modelling. In this chapter, I show how the Earth-air interface can be included in the rapid expansion method (REM) to solve a low-frequency, time-domain electric field. For each Chebyshev term, the field in the air needs to be determined explicitly based on the field in the earth, following a process named upward continuation, to avoid a direct simulation with the air conductivity. I introduce a new series of Chebyshev polynomials, pairing with the original ones, to undertake the upward continuation and to ensure the stability of the modelling. I present numerical tests against the analytical solution for a homogeneous half space to demonstrate the accuracy of the approach and the correctness of the code.

4.1 Introduction

The Earth-air interface is the interface that separates the earth and the air. The propagation of the EM field in the earth is a diffusive process, whereas in the air the EM field travels as a wave at the speed of light. The velocity contrast can be several orders of magnitude. I start with considering a homogeneous half space, where the electric field can be solved in an analytic form (e.g., Bannister, 1984; Slob et al., 2010; King et al., 2012), and it may provide some insight into how the air response behaves. For example, Slob et al. (2010) give the explicit Green's tensors for the diffusive electric field excited by an electric dipole buried in a half space. They use the diffusive approximation (i.e., the air conductivity is treated as zero) and show the air term can be separated from the earth response. The behavior can be understood physically as the diffusive electric field decays in the conductive medium and refracts at the Earth-air interface, and propagates as a wave with an infinite speed along the

interface with only lateral spreading, and continuously diffuses down into the subsurface with a finite speed in the vertical direction. If considering a 1D-layered model, the total response is therefore an interference effect between the air layer and all the other subsurface layers. The 1D modelling problems are not new, and have been well discussed in, e.g., Chave (2009); Key (2009); and Hunziker et al. (2015). Most of the 1D solutions are derived in the frequency domain and based on a reflection-coefficient scheme.

Considering 3D time-domain CSEM modelling, the huge velocity contrast between the air and the earth leads to a difficulty. A direct simulation of the air field requires very small numerical time steps, which can be four orders of magnitude smaller than the time steps required to model the field in the earth. It is therefore computationally too onerous and practically infeasible, which requires extra consideration.

There are mainly three types of scheme developed to handle the response from the Earth-air interface. The first type is to model the air field independently and then remove it from the data during processing (e.g., Amundsen et al., 2006; Madsen, 2006; Nordskag and Amundsen, 2007; Ziolkowski and Wright, 2007). The removal methods usually require some preliminary knowledge to estimate the air field, e.g., a simplified earth model so that the air field can be derived analytically (Nordskag and Amundsen, 2007), or a long-offset measurement where the air field dominates and can be used to estimate the shape of the air field in the entire survey (Ziolkowski and Wright, 2007). Nevertheless, as commented by Constable (2010), "the method presumably holds no advantage if the data are being modeled or inverted using code that includes the air layer". In addition, most of these methods are developed considering the land CSEM problems only where the source is placed on the surface. If considering a shallow-marine problem where the source is buried in the subsurface, since the response from the Earth-air interface is coupled to all other interfaces in the model, the removal of the air response can only be truly achieved if the full subsurface is already known. The effect of the Earth-air interface in a shallow-marine environment has been discussed by, e.g., Hunziker et al. (2011), and Wright (2015).

The second type of scheme is to use a reasonably small value to replace the actual conductivity of the air. For example, Commer et al. (2015) state that using the conductivity contrast between the air and the earth "ranging from 1:100 to 1:500 is a compromise between accuracy and computing effort". Many numerical examples set the air conductivity to be 10^{-4} S/m (Hördt and Müller, 2000; Um et al., 2010; Commer et al., 2015; Hu et al., 2017), comparing with its actual value which can range from 10^{-13} to 10^{-9} S/m (Seran et al., 2017). It can be a practical option in some problems, especially for land surveys where surface topography can be complex, making it difficult to apply other solutions. However,

the accuracy of this approximation decreases with increasing offset. It may also introduce unnecessary time steps.

The third type of scheme is to use zero to replace the actual conductivity of the air. As will be shown later, replacing the conductivity with zero results in Laplace's equation in the air and the electric field in the air is then treated as a potential field. It is probably the closest approximation to reality. Oristaglio and Hohmann (1984) first show how the air field satisfying Laplace's equation can be solved simultaneously with the earth field satisfying the diffusive EM equation. They describe the solution process by the term "upward continuation", since at every time step the air field is solved explicitly based on the earth field, as the field is continued upwardly from the earth to the air. Upward continuation is now a well-known boundary condition to handle the Earth-air interface in time-domain EM modelling, such as Wang and Hohmann (1993), Commer and Newman (2004), Wang (2006), etc. All these examples are based on finite-difference schemes.

There is no previous literature showing how the pseudospectral REM method can handle the Earth-air interface, although there is no extra difficulty to apply the removal methods during processing, or alternatively, using a reasonably small conductivity to represent the air layer. Carcione (2006) states "in principle, air can be modeled as a very-low-conductivity medium". Nevertheless, it remains a strong interest to develop a workflow to handle the air layer directly and accurately within the REM scheme, as the upward continuation does to finite-difference time-domain methods. If successful, the developed method should enhance the accuracy of modelling the Earth-air interface. It should be particularly useful for solving shallow-water CSEM problems, in which the signal reflected and refracted by the air layer is usually mixed up with the signal responded from the subsurface, making them indistinguishable and often requiring the capability of the modelling algorithm to solve the air field directly.

In this chapter I show that the response of the Earth-air interface can be modelled with REM via upward continuation of the time derivative of the magnetic induction decomposed in the Chebyshev domain. I first review the theory of upward continuation in section 4.2.1. I then demonstrate how it can be extended to the Chebyshev domain in section 4.2.2, with details of numerical implementation explained in section 4.2.3. I use a homogeneous half space example to demonstrate the correctness of the theory and the code in section 4.3. The theory and the results presented in this chapter were published in Liu et al. (2019b). I modified the original text, figures, layout, and symbols to fit the style of the thesis.

4.2 Theory

4.2.1 Laplace's equation and an artificial light speed

Wang and Hohmann (1993) and Commer and Newman (2004) present the implementation of the upward continuation in 3D EM modelling by finite difference in the time domain. The conductivity of the air is replaced by zero, and, under the quasi-static approximation, the magnetic field and its time derivative obey the equation

$$\nabla \times \nabla \times \mathbf{A} = 0, \tag{4.1}$$

where $\mathbf{A}$ is a vector field which can be the magnetic induction $\mathbf{B}$ or its time derivative $\dot{\mathbf{B}}$. Since the potential field $\mathbf{A}$ satisfies the divergence free condition (equation 2.2),

$$\nabla \cdot \mathbf{A} = 0, \tag{4.2}$$

combining equations 4.1 and 4.2 can show that the field $\mathbf{A}$ obey Laplace's equation

$$\frac{\partial^2}{\partial x^2}\mathbf{A} + \frac{\partial^2}{\partial y^2}\mathbf{A} + \frac{\partial^2}{\partial z^2}\mathbf{A} = 0, \tag{4.3}$$

in the air.

The use of Laplace's equation means a potential field is used to represent the speed of light of the physical airwave. It is probably the closest approximation to reality. Equation 4.3 can be solved in many ways. I discuss the solution in the horizontal wavenumber domain as shown in Wang and Hohmann (1993) and Commer and Newman (2004). Take the 2D Fourier transform of $\mathbf{A}$ with respect to the horizontal axes

$$\tilde{\mathbf{A}}(k_x, k_y, z) = \mathrm{FT}^2_{(x,y)}[\mathbf{A}(x, y, z)], \tag{4.4}$$

and rewrite equation 4.3 with the help of the derivative theorem ($\partial/\partial x \rightarrow ik_x$; $\partial/\partial y \rightarrow ik_y$) as

$$\frac{\partial^2}{\partial z^2}\tilde{\mathbf{A}} = ({k_x}^2 + {k_y}^2)\tilde{\mathbf{A}}, \tag{4.5}$$

any component of $\tilde{\mathbf{A}}$ at any height in the air can be instantaneously determined by the continuation of its surface field, as

$$\tilde{A_n}(k_x, k_y, z < 0) = \tilde{A_n}(k_x, k_y, z = 0) \exp\left(\sqrt{{k_x}^2 + {k_y}^2}\, z\right), \tag{4.6}$$

where subscript n denotes component x, y or z. Wang and Hohmann (1993) use the continuation of field $\mathbf{B}$ and Commer and Newman (2004) use the continuation of field $\dot{\mathbf{B}}$. At every time step, the field in the air is explicitly determined from the field on the surface, following equation 4.6. It avoids a direct simulation of the air field, which would require many tiny time steps and is computationally too onerous.

4.2.2 Upward Continuation in the Chebyshev domain

The implementation of the Earth-air interface in the Chebyshev domain should follow a similar approach. An immediate thought could be to exploit the upward continuation of the Chebyshev terms $\mathbf{Q}$. However, in the case of REM, after many trials, I found that direct continuation of the Chebyshev terms $\mathbf{Q}$ fails to produce accurate and stable results. The Chebyshev terms $\mathbf{Q}$, as part of $\mathbf{E}$, share the same continuity conditions as the electric field. During the simulation, the vertical electric component E_z and its Chebyshev terms Q_z are discontinuous across the Earth-air interface. This leads to two difficulties applying the upward continuation: 1) a direct modification of Q_z in the air layer intensifies the Gibbs phenomenon and eventually generates a non-physical source on the boundary and 2) calculation of Q_z exactly on the surface is problematic because of the discontinuity.

I have found that these problems can be avoided if we use the continuation of the time derivative of the magnetic induction $\dot{\mathbf{B}}$. Faraday's law states that $\dot{\mathbf{B}}$ is the negative the curl of $\mathbf{E}$. To exploit the use of $\dot{\mathbf{B}}$, I introduce the Chebyshev pair $\mathbf{Q}$ and $\mathbf{P}$, where the Chebyshev terms $\mathbf{P}$ satisfy Faraday's law

$$\mathbf{P} = -\nabla \times \mathbf{Q}, \tag{4.7}$$

and $\mathbf{P}$ has the same relation to $\mathbf{Q}$ as $\dot{\mathbf{B}}$ to $\mathbf{E}$. By taking the curl of equation 3.9, the magnetic induction time derivative $\dot{\mathbf{B}}$ can be written as a weighted summation of Chebyshev terms $\mathbf{P}$

$$\dot{\mathbf{B}}(t) \approx \sum_{k=0}^{M} b_k \mathbf{P}_k. \tag{4.8}$$

As can be shown by mathematical induction, the field $\mathbf{P}$ shares the same continuity condition with the field $\dot{\mathbf{B}}$. In the air layer, in which the conductivity is treated as zero, they both propagate their information instantaneously without any decay.

We first look at the vertical component $\dot{B}_z$ and its Chebyshev term P_z, which has the largest magnitude when the source is a horizontal dipole. The term $\dot{B}_z$ and $\partial_z \dot{B}_z$ are continuous across the Earth-air interface (Weir, 1980). Therefore, P_z and $\partial_z P_z$ are also continuous, which

allows P_z to be interpolated at the surface and supports the continuation of it into the air, as

$$\tilde{P}_z(k_x, k_y, z < 0) = \tilde{P}_z(k_x, k_y, z = 0) \exp\left(\sqrt{{k_x}^2 + {k_y}^2}\, z\right), \tag{4.9}$$

where $\tilde{P}_z$ is the field P_z after a 2D Fourier transform along the horizontal axes. The horizontal components of a potential field satisfying equation 4.3 can be calculated from its vertical component on the same horizontal plane (Macnae, 1984; Wang and Hohmann, 1993), and P_x and P_y can be obtained from P_z as

$$\tilde{P}_x(k_x, k_y, z) = -\frac{ik_x}{\sqrt{{k_x}^2 + {k_y}^2}} \tilde{P}_z(k_x, k_y, z), \tag{4.10}$$

and

$$\tilde{P}_y(k_x, k_y, z) = -\frac{ik_y}{\sqrt{{k_x}^2 + {k_y}^2}} \tilde{P}_z(k_x, k_y, z), \tag{4.11}$$

where $\tilde{P}_x$ and $\tilde{P}_y$ are the fields P_x and P_y after a 2D Fourier transform along the horizontal axes. Therefore, the modelling of P_x and P_y can also benefit from P_z. The air is included as a special layer through the modelling. I use at least two nodes to define the air layer. It is simulated together with the earth grids under the REM structure except that for each Chebyshev term, the values in the air layer need to be updated explicitly by the upward continuation.

4.2.3 Implementation

The numerical implementation of the Earth-air interface in REM is summarized as follows. In order to implement the upward continuation in the Chebyshev domain, for each Chebyshev term $\mathbf{Q}$, whenever the propagation matrix $\mathbf{G}$ needs to be applied, I replace this one-step, double-curl computation with a two-step, single-curl computation. Define $\mathbf{d}$ and $\tilde{\mathbf{d}}$ as the differential matrix evaluating the single curl in the space domain and the wavenumber domain, respectively,

$$\tilde{\mathbf{d}} = \mathrm{FT}^3_{(x,y,z)}[\mathbf{d}] = \begin{pmatrix} 0 & -ik_z & ik_y \\ ik_z & 0 & -ik_x \\ -ik_y & ik_x & 0 \end{pmatrix}, \tag{4.12}$$

and define a phase shift operator

$$\mathbf{s}^{\pm} = \exp(\pm ik_x \Delta x/2) \exp(\pm ik_y \Delta y/2) \exp(\pm ik_z \Delta z/2) \tag{4.13}$$

to make the field staggered by half of the grid spacing in all directions, the evaluation of $\mathbf{GQ}_k$ now takes three steps to include the upward continuation:

1. Apply the phase shift operator $\mathbf{s}^+$ to the electric field $\tilde{\mathbf{Q}}_k$ and compute the curl of it in the wavenumber domain, as

$$\tilde{\mathbf{P}_k} = \tilde{\mathbf{d}}\mathbf{s}^+ \mathrm{FT}^3_{(x,y,z)}[\mathbf{Q}_k]. \tag{4.14}$$

   The obtained Chebyshev term $\tilde{\mathbf{P}_k}$ is staggered to $\tilde{\mathbf{Q}_k}$ and corresponds to the time derivative of the magnetic induction.

2. Take the surface field of $\tilde{P_z}$ and update the values of $\tilde{\mathbf{P}}$ in the air layer, where $\tilde{P_z}$ is updated by the upward continuation (equation 4.9) and $\tilde{P_x}$ and $\tilde{P_y}$ are obtained from $\tilde{P_z}$ (equations 4.10 and 4.11).

3. Apply the opposite phase shift operator $\mathbf{s}^-$ to the updated $\tilde{\mathbf{P}_k}$ and compute the curl of it, and multiply the result by $-{\mu_0}^{-1}\sigma^{-1}$, as

$$\mathbf{GQ}_k = -\frac{1}{\mu_0\sigma}\mathrm{FT}_{(}x,y,z)^{-3}[\tilde{\mathbf{d}}\mathbf{s}^-\tilde{\mathbf{P}_k}]. \tag{4.15}$$

For the earth grids that are only subject to steps 1 and 3, the combination of equations 4.14 and 4.15 is equivalent to computing the propagation matrix $\mathbf{G}$ in a conductive model (equation 3.28), without violating any results discussed in the previous chapter, except now the Earth-air interface has been included by the addition of an air layer. The additional computational cost mainly comes from the upward continuation itself and the required forward and inverse Fourier transforms.

As shown by equations 4.14 and 4.15, the conductivity σ and the Chebyshev terms $\mathbf{Q}$ are always defined at the same position, whereas the field $\mathbf{Q}$ and $\mathbf{P}$ are staggered by half of the grid spacing. The reason for applying a staggered operator is two-fold. First, the computation of the first-order derivatives $\tilde{\mathbf{d}}$ in the wavenumber domain requires staggered grids. Bale (2002) and Corrêa et al. (2002) give comprehensive analysis on the benefits of using staggered grids. The inclusion of a staggered operator, as shown in equation 4.13, can keep the continuity of the phase at the Nyquist wavenumbers, and therefore reduces the numerical ringing effects effectively. They indicate that for the consideration of accuracy, one should choose staggered grids to compute first-order derivatives, and choose centered grids to compute second-order derivatives. Second, upward continuation of the component P_z requires its surface field to be known (equation 4.9), and the surface, i. e. the Earth-air

interface, is located halfway between the earth grids ($\sigma > 0$) and the air grids ($\sigma = 0$). The use of staggered grids makes the surface field of **P** available for each Chebyshev time step.

4.3 Numerical Results

In this section, I present numerical tests to demonstrate the correctness of the theory and the code. I check the results in a homogeneous half space with the Earth-air interface, against the analytical solution given by Slob et al. (2010). As discussed before, the algorithm has been written in a parallel C code (Liu et al., 2019a) and an alternative MATLAB code. For the tests in this section with synthetic data and a computationally small model, I show the results from the MATLAB code, running on a desktop machine with a single core (3.20 GHz). The model is constructed using $128 \times 128 \times 128$ nodes. The initial field is built with $t_0 = 10^{-3}$ s after some preliminary tests. The numerical boundary condition is the default periodic boundary condition, because of the use of FFT, as discussed in Chapter 3. No extra absorbing boundary is applied.

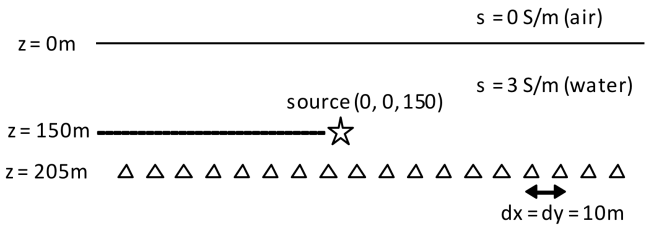

Fig. 4.1 Model configuration: a homogeneous half-space model. The air-water interface is defined as $z = 0$ m. The node spacing is 10 m and is arranged such that the first layer of nodes is 5 m below the air-water interface. The dipole source is located 150 m below the air-water interface in the centre with coordinates $x = y = 0$. The receivers are located 55 m below the source, on nodes.

I set the conductivity of the medium to be 3 S/m to consider a marine CSEM case. Figure 4.1 shows the model configuration, with the Earth-air interface at $z = 0$ m. The nodes in the earth are at $z = 5$, 15, 25 m, etc. The source, an x-directed impulsive dipole, is placed at $z = 150$ m below the Earth-air interface in the center of the model with coordinates $x = y = 0$ m. The receivers are located 55 m below the source; that is, the receivers are on nodes. The grid spacing is 10 m along each direction, and I use nine grids (nodes) to represent the air layer.

Figure 4.2 examines the half-space modelling results in the space domain. The absolute amplitudes of three electric components are compared with the explicit Green's tensors given by Slob et al. (2010) along all the inline receivers with coordinates $y = 5$ m. The REM results

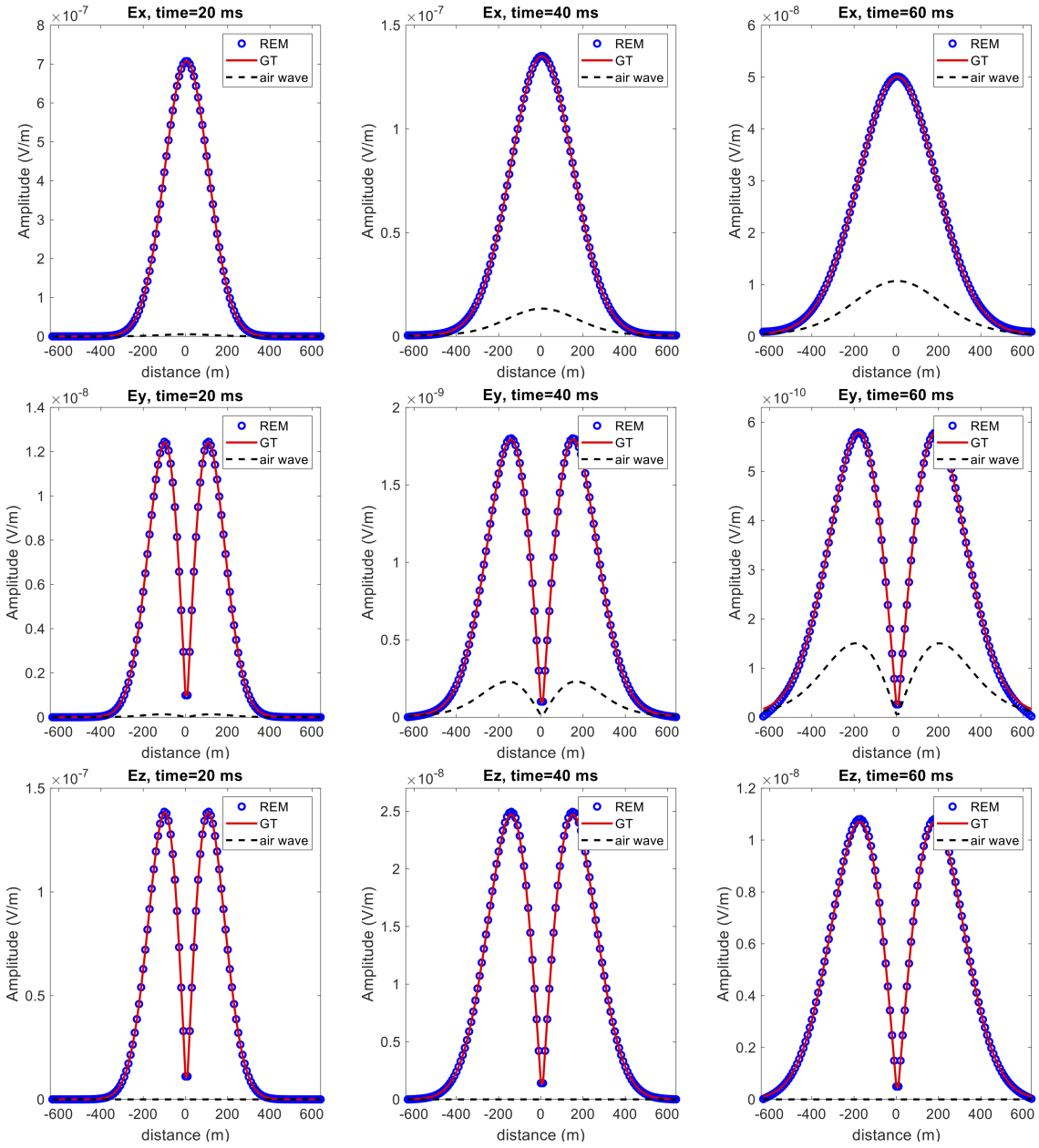

Fig. 4.2 Homogeneous half-space results: comparison of the absolute amplitude of three electric components in the space domain. The REM solutions are denoted by the circles, and the Green's tensors (analytical solution) are denoted by the solid lines. The airwave (analytical solution) is shown in the dashed lines. From left to right, the graphs show the electric field E_x of 20, 40, and 60 ms after constructing the initial field. The source (0, 0, 150) m is located in the center of the horizontal plane and 150 m below the air-water interface. The inline receivers are located 55 m below the source with coordinate $y = 5$ m

.

show excellent agreement with the analytical solution. For a duration of 60 ms, the sum of relative difference along 128 grids is calculated as 0.75% for E_x, 0.75% for E_y, and 1.08%for E_z. This level of accuracy is similar to the 2D full-space example shown in Carcione (2006), and the 3D full-space example shown in the last chapter. Because the source is an x-directed dipole, the magnitude of E_x is usually larger than the magnitude of E_y and E_z, and the inline electric field is usually more robust in the presence of actual or numerical noise.

It is worth noting that for an inline electric source, there is no airwave component in E_z, as shown in Figure 4.2. This is the reason that there are attempts in conducting CSEM surveys with vertical source and receiver (e.g., Holten et al., 2009; Hunziker et al., 2011; Helwig et al., 2013; Singer and Atramonova, 2013). The advantage of using vertical sources and receivers is mainly the complete absence of the airwave component. In addition, Holten et al. (2009) claim that the vertical electric field is more sensitive to deep resistive targets. Nevertheless, acquisition with vertical sources and receivers also has disadvantages. The complete absence of the airwave can only be achieved if the sources and receivers can keep vertical perfectly. Hunziker et al. (2011) investigate the effects of imperfect verticality, and show that in their numerical test, a dip of 0.05 °of the source results in a contribution of the airwave of 20% with respect to the total response. As soon as the source is dipped slightly, the airwave component appears. Besides, acquisition with vertical sources and receivers can be less efficient compared to the towed-streamer system (e.g., Anderson and Mattson, 2010), because a vertical source cannot be dragged behind a boat. The research is still ongoing to investigate the effects of various source and receiver antenna orientations.

Figure 4.3 compares the half-space modelling results in the time domain. I use 90 time samples distributed logarithmically from 0.001 to 0.5 s. Because the electric field in time is reconstructed from the Chebyshev terms, we have the flexibility to choose a linear or a logarithmic time scale and the computational cost depends only on the maximum time of the response. The three receivers shown below are located on the same inline $y = 5$ m, but with three difference source receiver offsets 105, 255, and 405 m, respectively, in the x-direction, considering the near, mid and far offsets. The REM solution fits well with the analytical solution, which again demonstrates the accuracy of this method. If I move the receiver further away from the source, the accuracy starts to decrease as the effect of numerical boundaries becomes more severe. For a model using the Dirichlet boundary condition or periodic boundary condition, distortions from the boundaries are inevitable. For these boundary conditions, the model needs to be sufficiently large for a given propagation time.

The airwave refers to the electric field refracted at the Earth-air interface, travelling through the air at the speed of light and propagating vertically downward into the earth. I

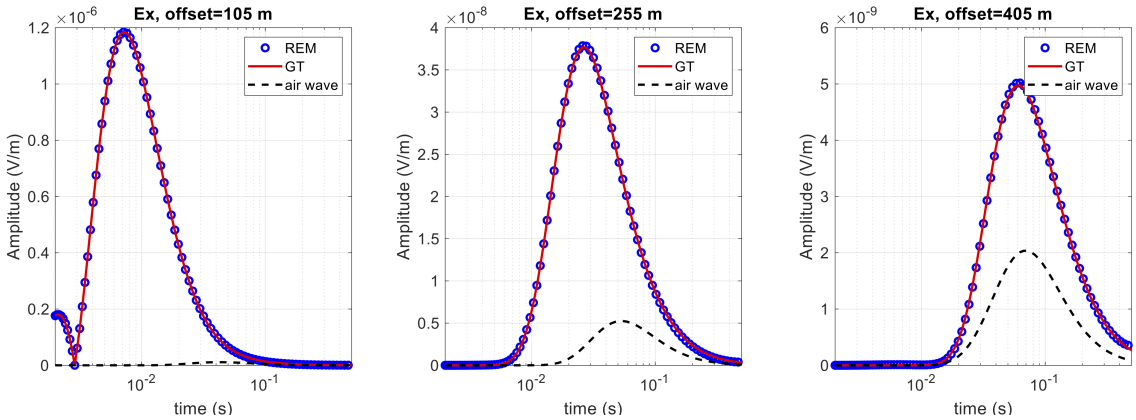

Fig. 4.3 Homogeneous half-space results: comparison of the absolute amplitude of the inline electric field in the time domain. The REM solutions are denoted by the circles, and the Green's tensors (analytical solution) are denoted by the solid lines. The airwave (analytical solution) is shown in the dashed lines. From left to right, the graphs show the response at inline receivers ($y = 5$ m) with offsets of 105, 255, and 405 m in the x-direction, respectively. The source is located in the center of the horizontal plane and 150 m below the air-water interface

.

calculate the airwave using the analytic solution (Slob et al., 2010) and show it in dashed lines in Figure 4.2 and 4.3 to compare the strength of it with the total electric field. Because the source and the receivers are buried in the conductive medium, the total field is the airwave and the direct field plus scattering of both. In this shallow-water example (with the depth of receivers around 200 m), the airwave is mixed up with the earth response, and the two responses are indistinguishable from each other. It is neither small enough to be negligible as in a deep-water example (e.g., Jaysaval et al., 2016), nor distinguishable enough to be extracted and removed from the recorded data as in a land example (e.g., Ziolkowski and Wright, 2007). Therefore for solving shallow-water problems, the inclusion of a direct modelling of the air field is particularly important as shown by this case.

Figure 4.4 and 4.5 show the x-z plane snapshots of the Chebyshev terms Q_x and the electric field E_x. The wavefront reflected by the Earth-air interface is clearly observed in Figure 4.4. Numerical dispersion and noise are hardly observed. No filtering has been applied, even though the conductivity contrast between the earth and the air is almost always the sharpest one in low-frequency EM problems and implementing sharp internal interfaces without any band limitation can be problematic (Mittet, 2017). The snapshots of the Chebyshev terms, as well as the comparison against the analytic solution in space and time, have demonstrated the proposed method and the code to include the Earth-air interface

into REM, by an upward continuation of the time derivative of the magnetic induction decomposed in the Chebyshev domain.

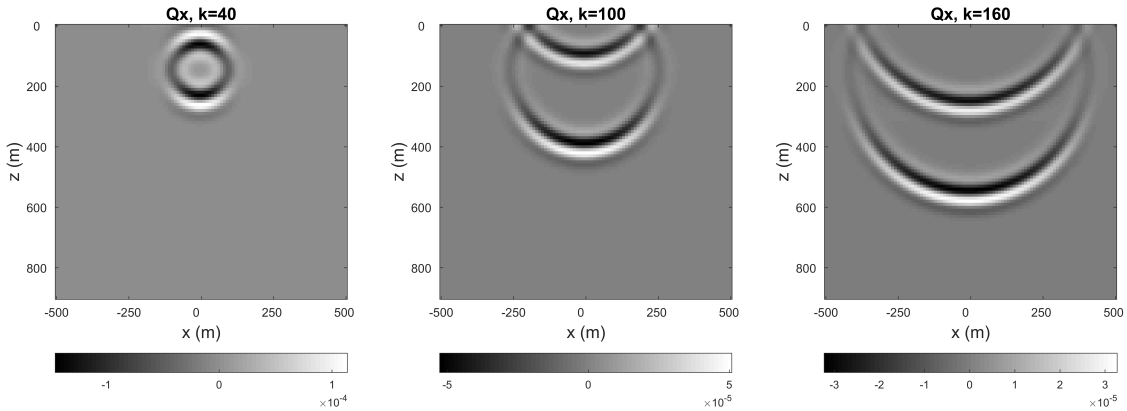

Fig. 4.4 Snapshots of Q_x. The x-z plane is located on $y = 1000$ m.

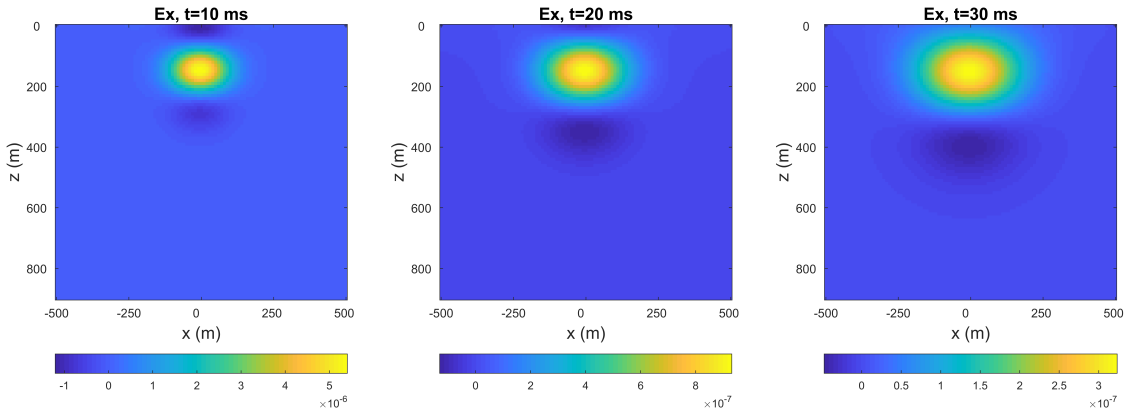

Fig. 4.5 Snapshots of E_x. The x-z plane is located on $y = 1000$ m.

The results of Figure 4.2 (time duration 60 ms) use $M = 340$ Chebyshev terms, and the results of Figure 4.3 (time duration 500 ms) use $M = 1000$. The required number of Chebyshev term is proportional to the square root of the maximum time. And REM has the option to produce a logarithmic time scale of modelled results to save storage (because it only updates the Chebyshev terms). This is one advantage of this method in EM modelling of long time traces. The execution time took approximately 300 s for the first example and 1800 s for the second example with a single processor.

4.4 Discussion

The REM structure without considering the Earth-air interface, shown in Chapter 3, has the Chebyshev terms following a one-step, second-order wave equation. After the inclusion of the Earth-air interface, as shown in section 4.2, the governing equation has been modified to a set of two-step, first-order wave equations, because of the introducing of the Chebyshev polynomials **P**. Extra Fourier transforms and staggered grids are then applied accordingly, making the presented algorithm more computationally expensive than simply including an upward continuation. However, due to the continuity of the fields as discussed before, the use of the Chebyshev terms **P** and the change of numerical structure are necessary if we want to include the Earth-air interface into the REM scheme.

Throughout the work of Stoffa and Ziolkowski (2019) and my study, we use regular spacing because of the numerical efficiency of the FFT and we can apply the PS method to obtain accurate spatial derivatives. In some situations, however, this may not be the best parameterization of the model. Certain model configurations pose problems for regular grids, and irregular grids may be more appropriate, e.g., considering the towed streamer and towed shallow source system for marine EM surveying (Anderson and Mattson, 2010). Tests using 1D modelling by REM show that a source with depth 20-40 m requires the spatial interval to be approximately 2 m to propagate the field successfully. For an explicit time-domain modelling method, the use of very fine grids is inevitable when modelling a shallow source, no matter what modelling method is used: finite difference, finite element, or REM. I want to emphasize that the problem of spatial sampling has nothing to do with REM, which is concerned only with the time-stepping component of the evolution. REM, and the upward continuation presented in this chapter, can doubtless cope with irregular grids: An eigenvalue analysis will be required for the limiting case, and the time stepping interval will be determined by the lowest conductivity (fastest speed) and the smallest spatial grid block.

4.5 Summary

To include the Earth-air interface into finite-difference, time-domain EM modelling, a well-known solution is to exploit an upward continuation process, which essentially treats the EM field in the air as a potential field, so that the air field can be determined by the field in the earth instantaneously and explicitly.

To include the Earth-air interface into REM, applying the upward continuation of the Chebyshev terms **Q** fails to produce stable and accurate results because of the discontinuity of Q_z across the interface. The problem has been solved by introducing a new series of

Chebyshev terms **P** pairing with **Q**, where **P** is essentially the time derivative of the magnetic induction decomposed in the Chebyshev domain. By using the upward continuation of the Chebyshev terms **P**, the Earth-air interface can be included in the REM scheme. Numerical tests against analytical solutions, along with the snapshots of the Chebyshev terms and the electric field, have demonstrated the correctness of the proposed method and the code.

Chapter 5

Inclusion of Anisotropy

Anisotropy is the variation of a material property with direction. If the electrical resistivity of a rock is direction dependent, electrical anisotropy is present. It is an important property that alters the propagation of EM fields and influences the interpretation of CSEM measurements, and it is normal. For example, the grouping together of thin isotropic rock layers of different isotropic resistivities can be treated as anisotropy in an equivalent medium. In this chapter, I show how transverse isotropic anisotropy can be included in the REM modelling by manipulation of the conductivity tensor. I present numerical tests considering vertical transverse isotropic (VTI) conductivity and tilted transverse isotropic (TTI) conductivity, to demonstrate the accuracy of the approach and the correctness of the code.

5.1 Introduction

Anisotropy is the variation of a material property with direction. If the electrical resistivity of a rock is direction dependent, electrical anisotropy is present. It is normal. It can be caused by many different mechanisms, such as variation of lithology, fractures, bedding or stratification, etc. For example, fractured formations with voids filled with conductive fluids often display higher conductivities in the directions parallel to the fractured planes than the directions perpendicular to them. For another example, the grouping together of thin isotropic rock layers of different isotropic resistivities can be treated as anisotropy of equivalent medium (Edwards et al., 1984).

Anisotropy has been recognized as having a significant influence on electromagnetic (EM) responses (e.g., Edwards et al., 1984; Ellis et al., 2009; Werthmüller, 2009; Bhattacharya, 2012; Fanavoll et al., 2014; Løseth et al., 2014; Jaysaval et al., 2016). Inversion studies of synthetic CSEM data can provide some insight into how it affects the interpretation. For example, Werthmüller (2009) compares the 1D isotropic and anisotropic inversion results of

various 1D anisotropic models. Given an interface in the resistivity model, the horizontal and vertical resistivity can vary differently, and he shows that an isotropic modelling and inversion which requires an averaging of the directional resistivities can cause significant errors in estimating the depth of targets. For another example, Jaysaval et al. (2016) show that in their numerical tests, it is necessary to include TTI anisotropy in the modelling and inversion, to consider the effects of the tilting of subsurface. The resistive target cannot be observed in the VTI inversion results. The consideration and use of anisotropy in real-world CSEM problems have been discussed by various studies, e.g., recent applications from the Barents Sea (e.g., Fanavoll et al., 2014; Løseth et al., 2014). Løseth et al. (2014) show that the resistive reservoir is more detectable in the inverted vertical resistivity model, rather than the horizontal resistivity. Fanavoll et al. (2014) show that by using the ratio between the vertical and horizontal resistivity, which essentially quantifies how anisotropic the medium it is, the appearance of a thin resistor can be well resolved from the background. Therefore, the inverted anisotropy model can also be a useful attribute in the interpretation of CSEM data.

The consideration of anisotropy is surely not new, and the numerical modelling algorithms can be various, implementing anisotropy to different levels of complexities. However, they share the same principle. An isotropic medium makes a simplification to Ohm's law where the current density $\mathbf{J}$ and the electric field $\mathbf{E}$ are related by a scalar σ as

$$\begin{pmatrix} J_x \\ J_y \\ J_z \end{pmatrix} = \begin{pmatrix} \sigma & 0 & 0 \\ 0 & \sigma & 0 \\ 0 & 0 & \sigma \end{pmatrix} \begin{pmatrix} E_x \\ E_y \\ E_z \end{pmatrix}. \tag{5.1}$$

An anisotropic medium requires the conductivity to be described by a tensor $\boldsymbol{\sigma}$, and $\mathbf{J}$ and $\mathbf{E}$ are related as

$$\begin{pmatrix} J_x \\ J_y \\ J_z \end{pmatrix} = \begin{pmatrix} \sigma_{xx} & \sigma_{xy} & \sigma_{xz} \\ \sigma_{yx} & \sigma_{yy} & \sigma_{yz} \\ \sigma_{zx} & \sigma_{zy} & \sigma_{zz} \end{pmatrix} \begin{pmatrix} E_x \\ E_y \\ E_z \end{pmatrix}, \tag{5.2}$$

that is, any component of $\mathbf{E}$ can contribute to any component of $\mathbf{J}$ with an independent proportion σ_{ij}. In equation 5.1, the subsurface conductivity is only dependent on spatial location. For each grid point, only 1 value is necessary to define the conductivity (e.g., theory and results shown in chapter 3). In equation 5.2, for each grid point, up to 9 elements are required to define the directional dependence of an anisotropic conductivity. The generalization from equation 5.1 towards equation 5.2 is the principle that most algorithms follow to model the conductivity when it is not isotropic.

A frequently used simplification of the conductivity tensor shown in equation 5.2 is to assume the medium is transversely isotropic, i.e., the medium property is the same

in all directions parallel to planes of isotropy and is different perpendicular to planes of isotropy. The perpendicular direction is an axis of rotational symmetry. The transverse isotropic system can be very representative of the subsurface anisotropy caused by many geological factors, such as bedding, fractures, and stratification. Two types are commonly considered to represent the layered anisotropic earth: vertical transverse isotropy (VTI), and tilted transverse isotropy (TTI), where the axis of rotational symmetry is vertical, and tilted, respectively. For each grid point, to define a VTI anisotropy, the conductivity tensor requires 2 values: a conductivity σ_p parallel to the plane of isotropy (horizontal conductivity) and a conductivity σ_n normal to the plane of isotropy (vertical conductivity). For TTI anisotropy, the tensor requires 2 more values at each grid point. These 2 values define the rotation of the tilted system with respect to the Cartesian coordinate system in which the electric field is propagating.

There are many examples that consider the inclusion of anisotropy in EM modelling. For example, the semi-analytical solution of the electric field in 1D VTI media given by Wait (1966), Hunziker et al. (2015), and Werthmüller (2017). The 3D finite-difference (FD) solution of the electric field in VTI or TTI media has been discussed by Wang and Fang (2001), Weiss and Newman (2002), Davydycheva et al. (2003), Liu and Yin (2014), and Jaysaval et al. (2016). Nevertheless, to my knowledge, there is no published example showing how to handle anisotropy with the REM scheme. Compared with the FD solutions listed above, the pseudospectral-REM algorithm has at least two distinguishable differences: 1) it uses collocated grids to discretize the earth whereas previous FD solutions use Yee's grids (Yee, 1966) or Lebedev's grids (Lebedev, 1964); and 2) a stability analysis is required to find the maximum eigenvalue to ensure the convergence of the Chebyshev polynomials when VTI or TTI anisotropy is included in the propagation matrix.

In this chapter I show how VTI and TTI anisotropy can be included in the REM modelling with the manipulation of the conductivity tensor. In section 5.2, I extend the original theory by considering conductivity as a tensor. I solve the eigenvalues of the propagation matrix which can ensure the convergence of the Chebyshev terms when anisotropy is included. I discuss the collocated grid, which is a distinguishable feature of the pseudospectral REM algorithm, and compare it with other grids used by FD solutions. I then demonstrate the correctness of the theory and the code in section 5.3, with various models including 1D and 3D, VTI and TTI anisotropic conductivities. The theory and the results presented in this chapter are published in Liu et al. (2019b). I modified the original text, figures, layout, and symbols to fit the style of the thesis.

5.2 Inclusion of Anisotropy in REM

5.2.1 The conductivity tensor

Section 3.2.1 shows the time evolution of the electric field by REM when the conductivity is isotropic, and therefore can be treated as a scalar σ. To consider an anisotropic conductivity, first of all, the conductivity needs to be generalized to a tensor

$$\boldsymbol{\sigma} = \begin{pmatrix} \sigma_{xx} & \sigma_{xy} & \sigma_{xz} \\ \sigma_{yx} & \sigma_{yy} & \sigma_{yz} \\ \sigma_{zx} & \sigma_{zy} & \sigma_{zz} \end{pmatrix}, \tag{5.3}$$

and the original theory shown in section 3.2.1 needs to be derived again with the conductivity tensor $\boldsymbol{\sigma}$. The numerical structure does not change: the Chebyshev terms are obtained in order by the Chebyshev recursion, and the time-domain electric field is then obtained by a weighted summation of the Chebyshev terms. However, with the inclusion of the conductivity tensor, the propagation matrix $\mathbf{G}$ that is evaluated at every step in the Chebyshev recursion, has been modified to

$$\mathbf{G}\mathbf{Q}_k = -\frac{1}{\mu_0}\boldsymbol{\sigma}^{-1}\mathrm{FT}^{-3}_{(x,y,z)}[\tilde{\mathbf{D}} \cdot \mathrm{FT}^{3}_{(x,y,z)}[\mathbf{Q}_k]], \tag{5.4}$$

where $\tilde{\mathbf{D}}$ is the differential matrix in the wavenumber domain as defined in equation 3.27. The spatial derivatives are evaluated in the wavenumber domain as a pseudospectral method accompanied by 3D forward and inverse Fast Fourier Transforms (FFTs), as described previously. The matrix $\boldsymbol{\sigma}^{-1}$ is evaluated in the space domain considering the spatial and directional variation of conductivities.

Because the spatial derivatives are solved by a pseudospectral method, the electric field components E_x, E_y and E_z can be defined at the same positions as the conductivity tensor $\boldsymbol{\sigma}$. This grid discretization (collocated grid) allows the current density $\mathbf{J}$ and the electric field $\mathbf{E}$ to be connected directly via $\boldsymbol{\sigma}$, without any interpolation or averaging of material properties (further discussed in section 5.4). The only remaining difficulty left in equation 5.4 is the evaluation of $\boldsymbol{\sigma}^{-1}$. I consider transverse isotropic anisotropy, where the inverse of $\boldsymbol{\sigma}$ can be written as

$$\boldsymbol{\sigma}^{-1} = \mathbf{R}^T \begin{pmatrix} \sigma_p & 0 & 0 \\ 0 & \sigma_p & 0 \\ 0 & 0 & \sigma_n \end{pmatrix}^{-1} \mathbf{R}, \tag{5.5}$$

where σ_p and σ_n are the conductivities parallel and normal to the transverse isotropic plane, respectively, and $\mathbf{R}$ is the rotation matrix

$$\mathbf{R} = \begin{pmatrix} \cos\theta\cos\phi & \cos\theta\sin\phi & -\sin\theta \\ -\sin\phi & \cos\phi & 0 \\ \sin\theta\cos\phi & \sin\theta\sin\phi & \cos\theta \end{pmatrix}, \tag{5.6}$$

with its elements defined by two Euler angles, the strike ϕ and the dip θ, to describe the rotation between the Cartesian coordinate system and the tilted coordinate system where the transverse isotropic anisotropy can be described by a diagonal matrix (Jaysaval et al., 2016). For the isotropic and the vertical transverse isotropy (VTI) cases, $\mathbf{R}$ is an identity matrix with $\phi = \theta = 0$, and $\boldsymbol{\sigma}$ reduces to a diagonal matrix with two values σ_p, σ_n defined per node. Up to this point the inclusion of anisotropy does not increase the computational cost. For a tilted transverse isotropy (TTI) case, four values are defined per node, two conductivities σ_p and σ_n and two Euler angles ϕ and θ, and extra computation is needed to carry out the forward and backward rotation of the coordinates.

5.2.2 Eigenvalue of the propagation matrix

The Chebyshev domain can be seen as the domain of the eigenvalues of the propagation matrix (equation 3.42), and the eigenvalue analysis is important when anisotropy is included. First, it is necessary to prove that with the inclusion of anisotropy, the eigenvalues are still all real and negative, which ensures stability. Second, the maximum absolute eigenvalue needs to be found. The value determines the equivalent 'time' step in the Chebyshev domain (equation 3.43), as well as the polynomial order to which the Chebyshev series are sufficient to be truncated (equation 3.34).

In the 3-D wavenumber domain (k_x, k_y, k_z), with the inclusion of anisotropy, the propagation matrix is

$$\tilde{\mathbf{G}} = -\frac{1}{\mu_0}\boldsymbol{\sigma}^{-1}\tilde{\mathbf{D}}, \tag{5.7}$$

with $\boldsymbol{\sigma}^{-1}$ defined in equation 5.5. The eigenvalues of $\tilde{\mathbf{G}}$ satisfying equation

$$\tilde{\mathbf{G}} - \lambda\mathbf{I} = 0 \tag{5.8}$$

can be solved as (Appendix A)

$$\begin{aligned}
\lambda_1 =& 0, \\
\lambda_2 =& -\frac{1}{\mu_0\sigma_p}({k_x}^2+{k_y}^2+{k_z}^2), \\
\lambda_3 =& -\frac{1}{\mu_0\sigma_p}(k_x\sin\theta\cos\phi+k_y\sin\theta\sin\phi+k_z\cos\theta)^2 \\
&-\frac{1}{\mu_0\sigma_n}[(k_x\sin\theta\sin\phi-k_y\sin\theta\cos\phi)^2+(k_x\cos\theta-k_z\sin\theta\cos\phi)^2 \\
&+(k_y\cos\theta-k_z\sin\theta\sin\phi)^2].
\end{aligned} \tag{5.9}$$

As shown by equation 5.9, the eigenvalues are all on the negative real axis, and therefore the system is still stable with the inclusion of anisotropy. When $\sigma_p = \sigma_n$ and $\phi = \theta = 0$, the expression of λ_3 is simplified to be the same as λ_2, and they are actually the eigenvalues of the isotropic propagation matrix as given in equation 3.31. In an anisotropic case, the maximum absolute eigenvalue should consider the spatial variation as well as the directional variation of the conductivity. Defining quantity a as the maximum value of the inverse of the parallel and normal conductivities times μ_0^{-1}, that is, $a = max(\frac{1}{\mu_0\sigma_p}, \frac{1}{\mu_0\sigma_n})$, the absolute value of λ_3 always satisfies the inequality

$$\begin{aligned}
|\lambda_3| \leqslant& a[(k_x\sin\theta\cos\phi+k_y\sin\theta\sin\phi+k_z\cos\theta)^2+(k_x\sin\theta\sin\phi-k_y\sin\theta\cos\phi)^2 \\
&+(k_x\cos\theta-k_z\sin\theta\cos\phi)^2+(k_y\cos\theta-k_z\sin\theta\sin\phi)^2] \\
=& a({k_x}^2+{k_y}^2+{k_z}^2),
\end{aligned} \tag{5.10}$$

and the right side value of equation 5.10 is also always greater than or equal to $|\lambda_2|$. The maximum wavenumber components are the Nyquist wavenumbers, which for grid spacings Δx, Δy, and Δz are $k_x = \pi/\Delta x$, $k_y = \pi/\Delta y$, and $k_z = \pi/\Delta z$, to consider the highest harmonics of the spatial Fourier transform. Therefore the maximum absolute eigenvalue b, considering transverse isotropic anisotropy, is given as

$$b = a\pi^2(\frac{1}{\Delta x^2}+\frac{1}{\Delta y^2}+\frac{1}{\Delta z^2}). \tag{5.11}$$

This expression is similar to the one solved in an isotropic case, given in equation 3.33, but now it has accounted for transverse isotropic anisotropy. Since the value of a takes the maximum between $(\mu_0\sigma_p)^{-1}$ and $(\mu_0\sigma_n)^{-1}$, the expression for b derived in equation 5.11 is always sufficiently large to ensure convergence and accuracy. Alternatively, one can calculate the eigenvalues from equation 5.9 based on the knowledge of σ_p, σ_n, ϕ and θ, to decide the

order of the Chebyshev terms. Another choice is to observe the value of $I_k(bt)$, as discussed in Stoffa and Ziolkowski (2019).

The theory of including the anisotropy, developed in section 5.2.1 and 5.2.2, can be extended to include the Earth-air interface with no extra difficulty. To do so, the evaluation of the propagation matrix **G** needs to follow the two-step, single-curl computation with an extra step of upward continuation, as discussed in section 4.2.3. The only modification is that in equation 4.15, instead of multiplying by the scalar σ^{-1}, we need to multiply by the inverse of the conductivity tensor, as

$$\mathbf{GQ}_k = -\frac{1}{\mu_0}\boldsymbol{\sigma}^{-1}\mathrm{FT}_{(}x,y,z)^{-3}[\tilde{\mathbf{d}}\mathbf{s}^{-}\tilde{\mathbf{P}}_k], \tag{5.12}$$

and the evaluation of $\boldsymbol{\sigma}^{-1}$ follows the same steps as discussed in the previous sections (equations 5.5 and 5.6).

5.2.3 Collocated grid discretization

An important feature of the presented pseudospectral REM algorithm is to use regular and collocated grids to discretize the subsurface. Regular collocated grid is probably the easiest one to implement numerically: the 3D subsurface box is divided into many unit cubic cells, and each node is defined with a conductivity tensor to describe its variation. Because all the three components of the electric field are always defined at the same location with the conductivity tensor, the implementation of anisotropy is very straightforward, without any interpolation or averaging of material properties, as discussed in the previous sections. The interface of conductivities is exactly defined half-way between the grids. This is an advantage over the conventional Yee's grid used extensively by finite-difference solutions (e.g., Wang and Hohmann, 1993; Wang and Fang, 2001; Weiss and Newman, 2002; Commer and Newman, 2004; Liu and Yin, 2014). Figure 5.1(a) shows the discretization of Yee's grid for a unit cell. The conductivity tensors, defined at positions (x_i, y_j, z_k) and $(x_{i+1}, y_{j+1}, z_{k+1})$, are not collocated with the components of the EM field. Averaging the material property, or other types of interpolation, is therefore a standard treatment. It results in ambiguous definitions of boundaries and creates transition layer effects (Feise et al., 2004). In addition, when the medium is anisotropic, as discussed in Davydycheva et al. (2003), the inverse of Ohm's law implemented by Yee's grid can be troublesome: the inverse of a local interpolation operator cannot be local, and the duality (symmetry) between the electric and magnetic fields is lost in an anisotropic medium.

An alternative finite difference solution is to use the Lebedev grid (Lebedev, 1964) to discretize the earth. The Lebedev grid is illustrated in Figure 5.1(b). The Lebedev grid

provides two features to satisfy the modelling of anisotropy by finite difference: 1) the electric field and the magnetic field are always staggered in any direction, and 2) the three components of each field are always collocated. Since the components are always collocated, the implementation of anisotropy is straightforward, as shown in Davydycheva et al. (2003); Nauta et al. (2013); and Jaysaval et al. (2016). Nevertheless, the computational cost of using the Lebedev grid increases fourfold compared to Yee's grid. For each unit cell, Yee's grid requires 6 components to be defined, and the Lebedev grid requires 24 components to be defined (each component on the corner counts one eighth to the unit cell as it is shared by eight cells; each component on the edge counts one fourth to the unit cell; each component on the surface counts one half to the unit cell), although the Lebedev grid allows the use of coarser cell sizes (Davydycheva et al., 2003).

The regular collocated grids used by the pseudospectral REM algorithm, are illustrated in Figure 5.1(c) and 5.1(d), considering the model without and with the air layer, respectively. Without the inclusion of the air, the proposed REM algorithm requires 3 components to be defined per cell. With the consideration of the air, it requires 6 components per cell, because of the introduction of another series of Chebyshev terms. As the components are always collocated with the conductivity tensor, it does not suffer from the problems that Yee's grid does, and it is 4 to 8 times cheaper computationally than the Lebedev grid. Therefore, the use of a collocated grid is clearly an appealing feature of the proposed pseudospectral REM algorithm, especially when considering the inclusion of anisotropy. It is numerically efficient, simple to implement, and very accurate because of the pseudospectral evaluation of the spatial derivatives, as discussed previously. The only function lacking here, is probably the inclusion of irregular grids. These can be useful when considering complex geometries. Nevertheless, I want to emphasize that the spatial implementation is completely independent of REM, which only concerns the time evolution of the field in the Chebyshev domain. The REM algorithm itself can be combined with any method to consider the spatial implementation, including finite difference, finite element or a pseudospectral method, as I present here.

5.3 Numerical Results

In this section, I present numerical tests to demonstrate the accuracy of the REM solution and the correctness of the code. I use the same homogeneous half space presented in Chapter 4 and add anisotropy to it. First I add VTI layers to the half space and check the solution against published 1D EM modelling code EMmod (Hunziker et al., 2015). Then, I test the performance of the REM algorithm when TTI anisotropy and 3D resistive anomalies are present. For the tests in this section where the models are computationally small, I show

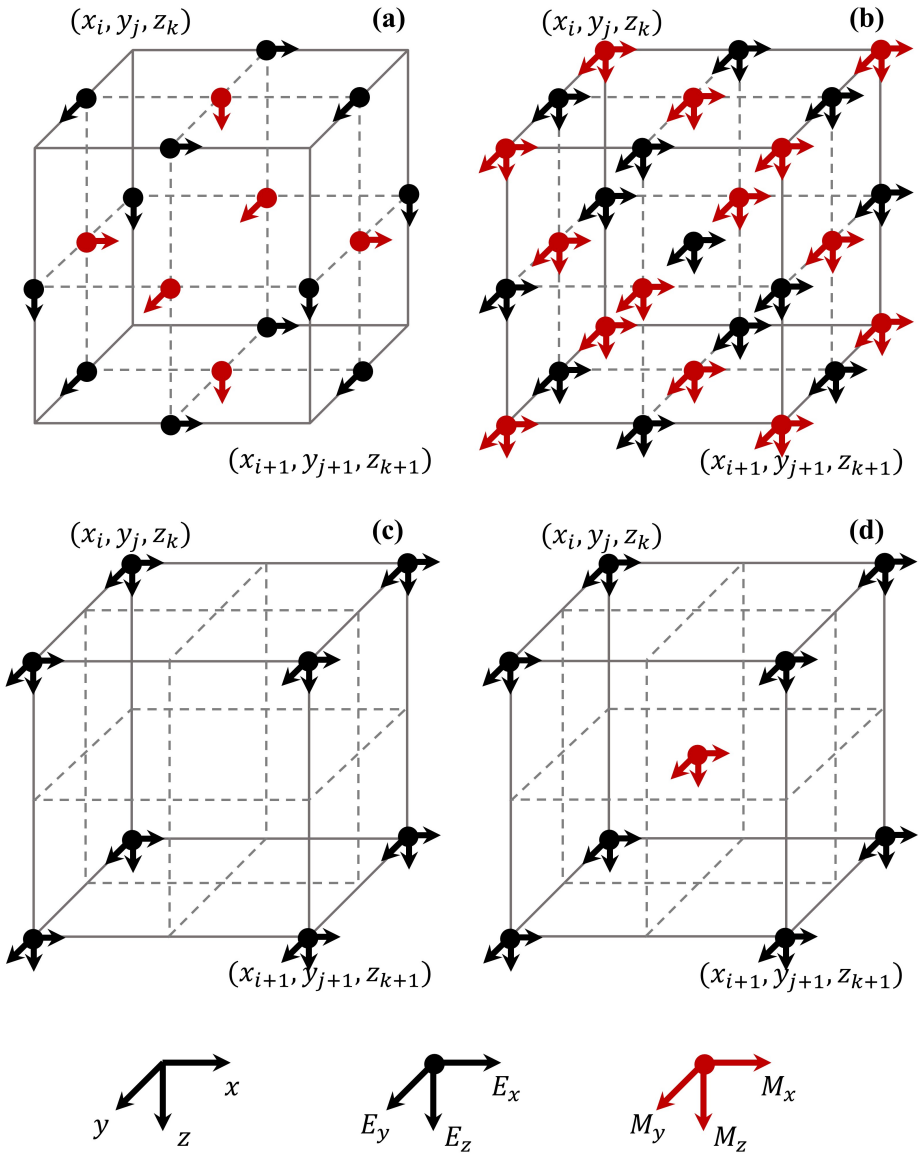

Fig. 5.1 Grid discretization. The graphs show a unit cubic cell when the subsurface is discretized by (a) standard Yee's grid; (b) Lebedev grid; (c) collocated grid (components of electric field only); and (d) collocated grid (components of electric and magnetic fields). The subsurface conductivities are defined at positions (x_i, y_j, z_k) and $(x_{i+1}, y_{j+1}, z_{k+1})$, etc. The electric and magnetic components are denoted by black and red arrows, respectively.

the results from MATLAB code, running on a desktop machine with a single processor (3.20 GHz). The homogeneous half space, as illustrated in Figure 4.1, is constructed using $128 \times 128 \times 128$ nodes. The initial field is built with $t_0 = 10^{-3}$ s after some preliminary tests.

The numerical boundary condition is the default periodic boundary condition, because of the use of FFT, as discussed in Chapter 3. No extra absorbing boundary is applied.

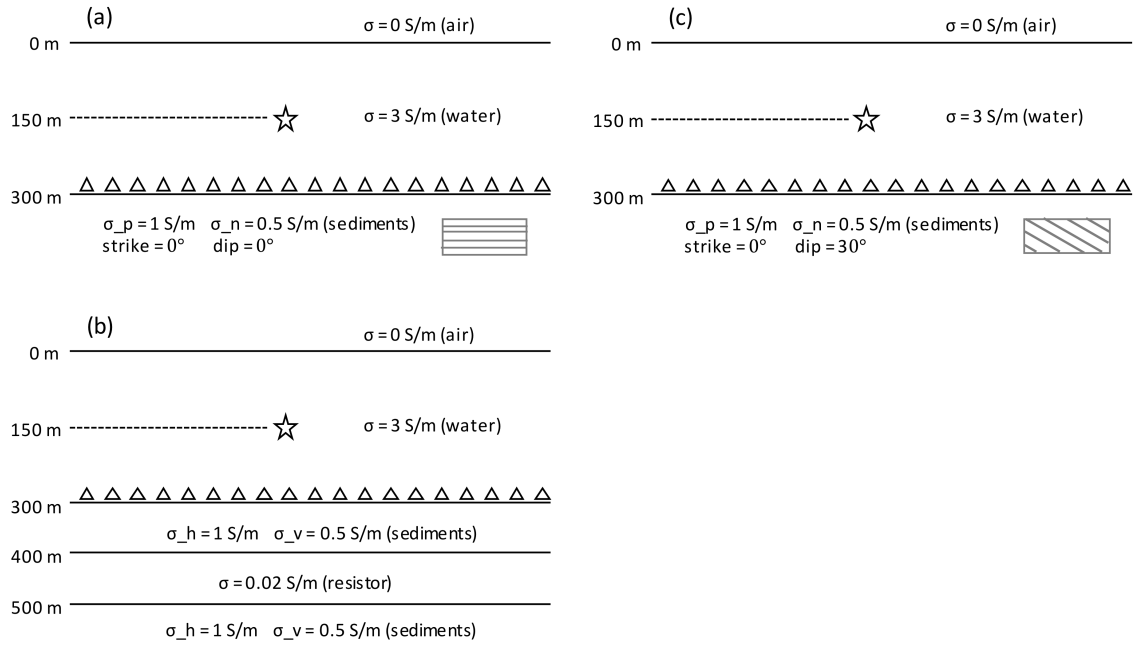

Fig. 5.2 Model configuration: layered anisotropic half-space. The 1D model consists of a 300 m thick water layer beneath the air, and a layer of (a) VTI anisotropic sediments, (b) VTI anisotropic sediments plus a 100 m thick resistive layer, and (c) TTI anisotropic sediments with a 30° dip.

The calibration code, EMmod, simulates the 3D EM field in a 1D earth in the frequency-wavenumber domain, and the results are transformed back to space through a Hankel transformation. I need to select several regularly-sampled frequencies and transform the results back to the time domain via an inverse Fast Fourier transform (IFFT). Because the solution is derived in a 1D model, it does not suffer from the boundary problems like the 3D methods.

I show two examples. First, I put sediments beneath the water layer, as illustrated in Figure 5.2(a). To consider a more realistic situation than the isotropic assumption, I consider mild VTI anisotropy. The vertical ρ_v and horizontal ρ_h resistivities of the sediments are defined as 2 and 1 ohm-m, respectively, with VTI anisotropy $\lambda = \sqrt{\rho_v/\rho_h} = \sqrt{2}$. The dipole source is located 150 m below the air-water interface, and the receivers are located just above the seabed.

Figure 5.3 compares the inline electric field in the time domain. The EMmod results consist of 250 time samples linearly distributed from 2 to 500 ms, and I use a logarithmic time sampling (90 samples from 1 to 500 ms) for REM. In general, the REM results show

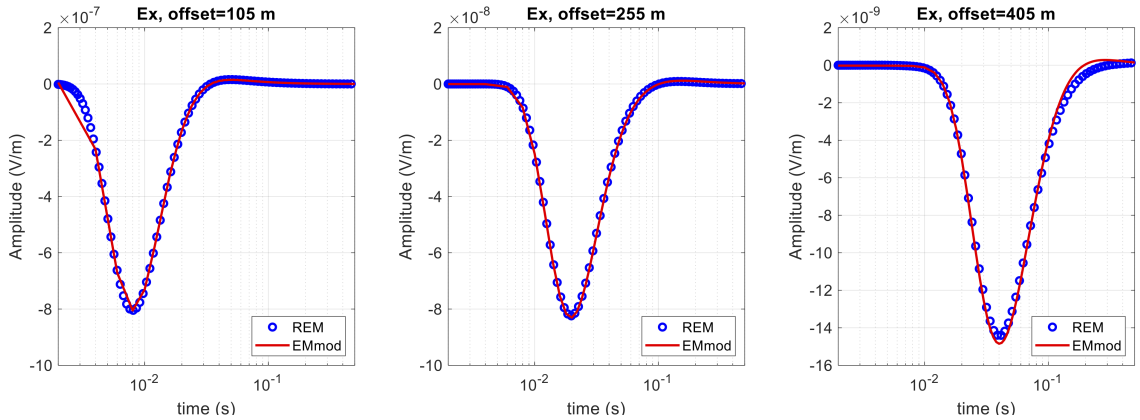

Fig. 5.3 Layered half-space with VTI anisotropy: comparison of the inline electric field in the time domain. The REM and EMmod solutions are denoted by the circles and solid lines. From left to right, the graphs show the responses at crossline receivers ($x = 5$ m) with offsets in the y-direction of 105, 255, and 405 m, respectively. The model configuration is illustrated in Figure 5.2(a).

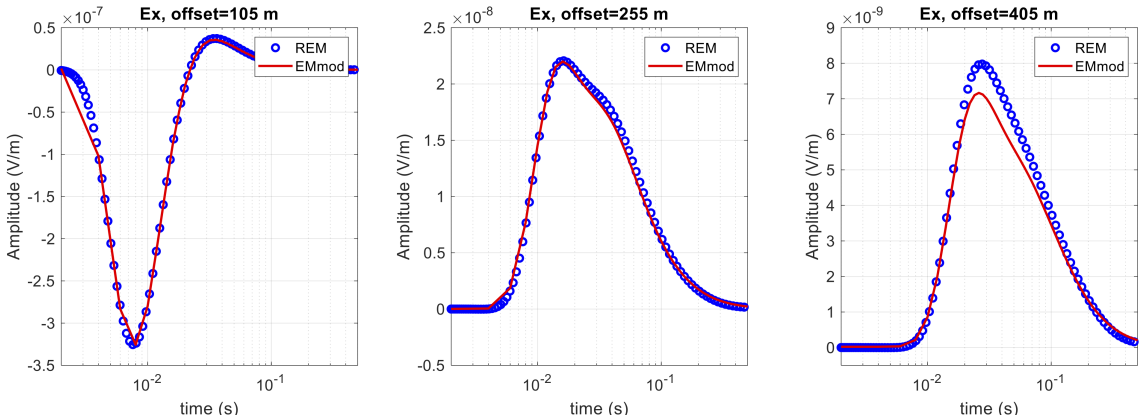

Fig. 5.4 Layered half-space with VTI anisotropy and resistor: comparison of the inline electric field in the time domain. The REM and EMmod solutions are denoted by the circles and solid lines. From left to right, the graphs show the responses at inline receivers ($y = 5$ m) with offsets in the x-direction of 105, 255, and 405 m, respectively. The model configuration is illustrated in Figure 5.2(b).

good agreement with the calibrated solution. At the near offset (105 m), the mismatch at early times (before 0.01 s) is essentially due to the mismatch of the time sampling. REM uses 33 time samples to capture the first peak before 0.01 s, whereas I use 5 time samples with EMmod. For these parameters, the early-time, sharp variation of the electric field is better characterized by the REM results. The very accurate near-offset, early-time modelling results should lead to a confident estimate of the shallow conductivity in the inversion, which is fundamental to the further inversion of deeper sections. A slight divergence of the curves can

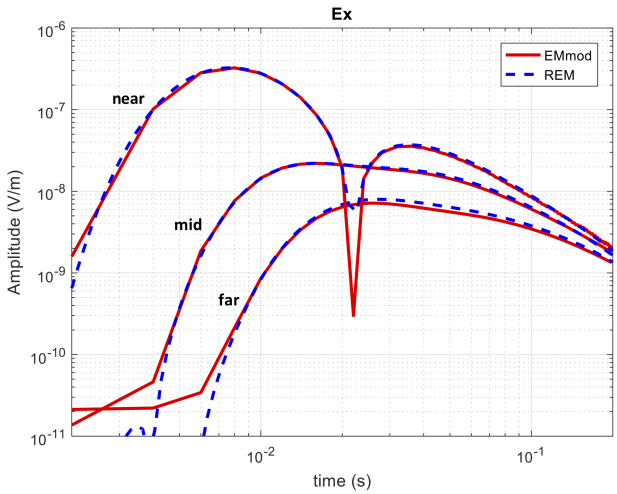

Fig. 5.5 Comparison of the inline electric field with amplitude in logarithmic scale. The same EMmod and REM results of Figure 5.4 are now compared on a logarithmic scale, shown by the solid and dashed lines.

be observed for far-offset (405 m) results. Compared with the half-space modelling results, as shown in Figure 4.3, the late-time, far-offset divergence indicates that distortions from the numerical boundaries arrive earlier in this case, because the diffusive speed in the anisotropic sediment layer is faster. In contrast, the 1D solution is free of numerical boundary problems.

In the next model, I insert a 100 m thick, isotropic 1D resistor into the anisotropic sediments at 100 m beneath the seabed, as shown in Figure 5.2(b). The same time domain comparison is made and shown in Figure 5.4. The near-offset results still show excellent agreement. The mid- and far-offset results are accurate at early times, but they suffer more severe boundary distortion at late times and toward the edge of the model. The maximum signal at any distance d arrives at time $t = \mu\sigma d^2/4$ (Carcione, 2006), and for the resistive layer with $\sigma = 0.02$ S/m it takes only 2.6 ms for the diffusive field to travel from the center to the edge. A time recording of 500 ms is clearly beyond the ability of this 1 km size model. However, in real 3D problems, the boundary effect can be efficiently attenuated with two factors: 1) resistors are usually 3D bodies with finite size surrounded by conductive sediments in which the diffusion can be slowed down and attenuated; and 2) a much larger model is often used in CSEM modelling and such effects can be moved out to later times and larger distances.

Up to this point, I have examined the REM solutions with the amplitudes shown on a linear scale, so that any differences can be clearly observed. In some cases, however, it is the order of magnitude that needs to be determined rather than the amplitude itself. Therefore, it is common to compare the modelling results on a logarithmic scale (e.g., Wang

and Hohmann, 1993; Commer and Newman, 2004). Figure 5.5 shows the results of Figure 5.4 on a logarithmic scale. The maximum relative difference is approximately 11% on the linear scale amplitude, calculated at the peak values of the far-offset results. The same amount of difference reduces to 0.6% after taking the base 10 logarithm of the amplitudes. In terms of determining the order of magnitude, the REM results show good agreement with the calibration code, although contaminated with numerical reflections from the boundaries.

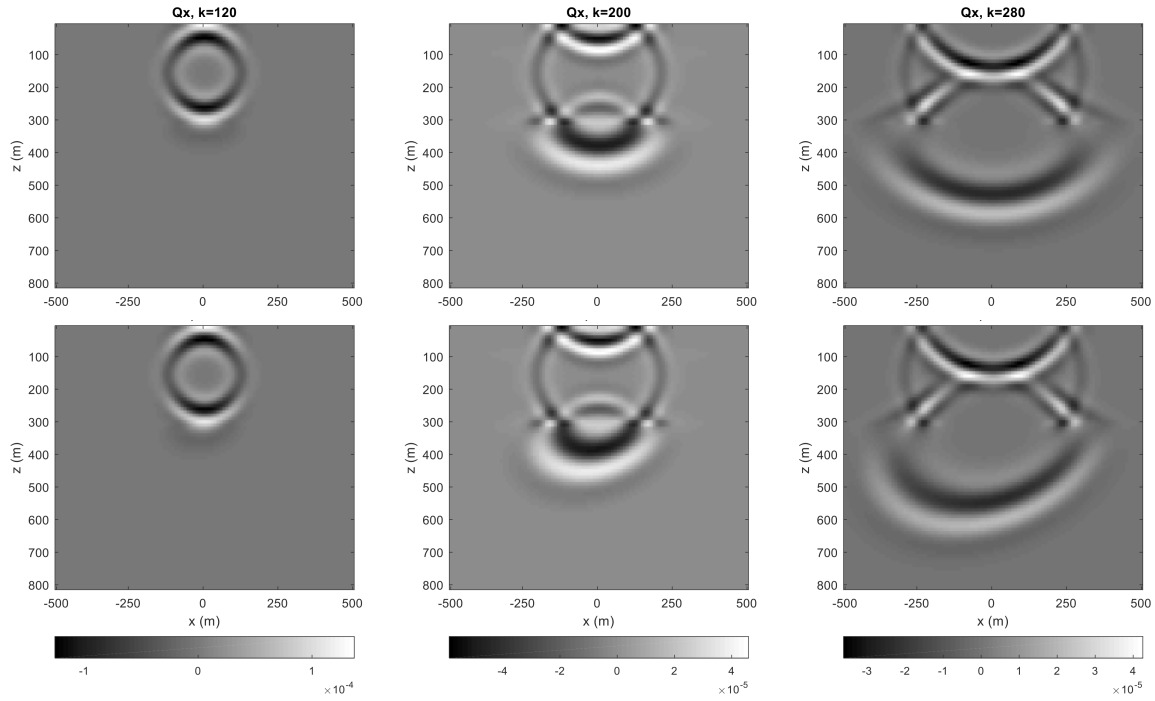

Fig. 5.6 Snapshots of Q_x. The x-z plane locates on $y = 5$ m. The model configurations are shown in Figure 5.2(a) and 5.2(c), for the top and bottom row, to consider the VTI and the TTI sediments, respectively. From left to right, the graphs show the snapshots of the 120th, the 200th, and the 280th Chebyshev term of the x-component electric field, respectively.

In the third model, I rotate the transverse isotropic plane of the anisotropic sediments 30° clockwise around the y-axis, considering a TTI anisotropy case (strike $\phi = 0°$, dip $\theta = 30°$) as shown in Figure 5.2(c). I show the x-z plane snapshots of the Chebyshev terms Q_x in Figure 5.6 to compare the VTI and TTI models. The tilt of the propagation of the wavefield is clearly observed in the TTI sediments. Reflections from the air-water interface and the the water-sediments interface can also be distinguished in both cases. Numerical dispersion is hardly observed. The change of amplitude is plotted in Figure 5.7, comparing the inline electric field at the same receiver position. The amplitude change is noticeable in the mid and far offsets in which the scattered field has a relatively higher contribution than the direct

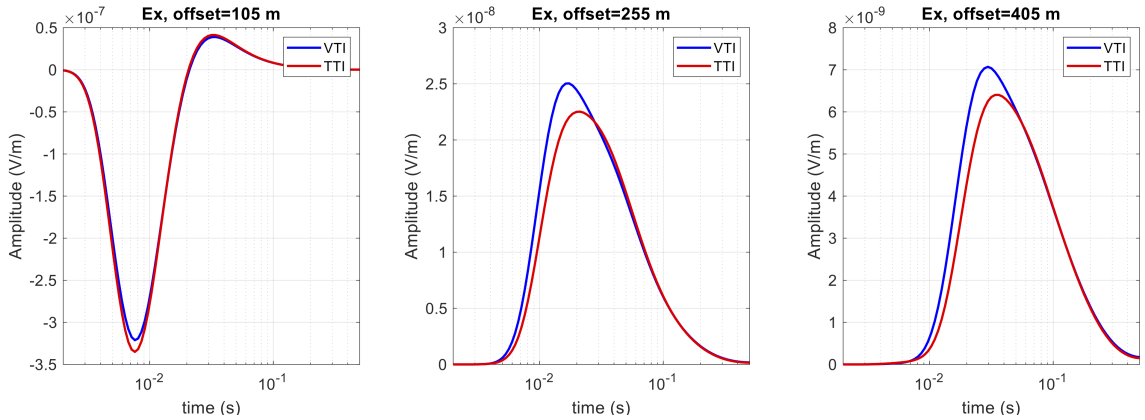

Fig. 5.7 Layered half-space with VTI and TTI anisotropy: comparison of the inline electric field in the time domain. The solutions in the VTI and TTI case are denoted by the blue and red lines, respectively. From left to right, the graphs show the responses at inline receivers ($y = 5$ m) with offsets in the x-direction of 105, 255, and 405 m, respectively. The model configurations are illustrated in Figure 5.2(a) and 5.2(c).

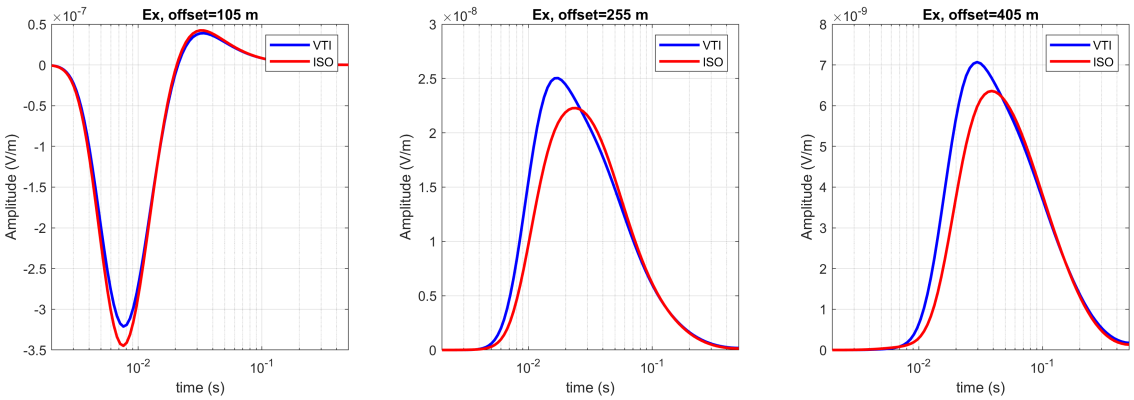

Fig. 5.8 Layered half-space with VTI anisotropic and "equivalent" isotropic conductivity: comparison of the inline electric field in the time domain. The isotropic model has the same configuration as the VTI model (Figure 5.2(a)), but the anisotropic layer has been replaced by an "equivalent" isotropic layer ($\sigma_m = \sqrt{\sigma_p \sigma_h} \approx 0.707$ S/m). The VTI and isotropic results are denoted by the blue and red lines, respectively. From left to right, the graphs show the responses at inline receivers ($y = 5$ m) with offsets in the x-direction of 105, 255, and 405 m, respectively.

field. These examples demonstrate the ability of REM to handle VTI and TTI anisotropic conductivity.

To demonstrate the importance of including anisotropy in the forward modelling, I compare the modelled VTI results to the response from an "equivalent" isotropic model. The model has the same configuration as shown by Figure 5.2(a), but the VTI anisotropic layer has been replaced by an "equivalent" isotropic conductive layer. The "equivalent"

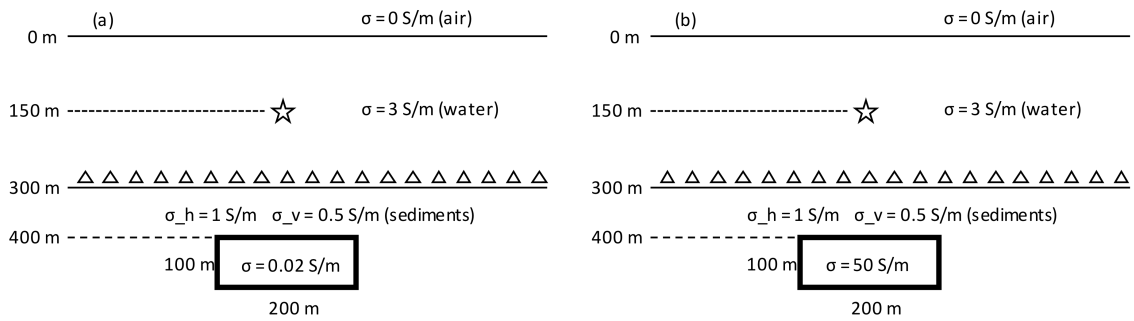

Fig. 5.9 Model configuration: layered half-space with VTI anisotropic sediments and a 3D resistivity anomaly. The 3D anomalous block has a size of $200 \times 200 \times 100$ m. It is put into the background model as shown in Figure 5.2(a), with its center right below the dipole source. The anomalous conductivities are (a) 0.02 Sm and (b) 50 Sm, respectively, to consider the presence of a 3D resistor and a 3D conductor.

conductivity is calculated as $\sigma_m = \sqrt{\sigma_p \sigma_n}$, the same way as used in Werthmüller (2009). That is, $\sigma_m \approx 0.707$ S/m in this case. Figure 5.8 shows the difference between the VTI and the "equivalent" isotropic modelling results. Note that the VTI anisotropy considered here is mild ($\lambda = \sqrt{2}$). As discussed in Werthmüller (2014), in any case, a slight conductivity anisotropy of $\lambda \approx 1.5$ may be more realistic than the isotropic assumption. As shown by Figure 5.8, "equivalent" isotropic model cannot provide perfectly identical results to handle the VTI anisotropy. The noticeable amplitude differences in the mid and far offsets are the reasons that isotropic modelling and inversion can cause errors in estimating the depth of targets (e.g., Werthmüller, 2009). This example shows the importance of anisotropy in the modelling process.

Finally, I test the code with 3D variations of conductivity with a sharp material contrast (a factor of 50). A $200 \times 200 \times 100$ m block, with an anomalous conductivity, is inserted into the background model of Figure 5.2(a). I consider a resistive case (0.02 S/m) and a conductive case (50 S/m). The resulting new models are shown in Figure 5.9(a) and 5.9(b), respectively. Figures 5.10 and 5.11 show the x-z plane snapshots of the inline electric field when the 3D anomalies are included. Sharp variations of the conductivity lead to velocity contrasts of the propagating field, and the boundaries of the anomalous block in both situations are imaged very well by the variation of the electric field when travelling through it, especially the vertical boundaries. Nonphysical noise is hardly seen with the presence of sharp material contrasts. These examples demonstrate the ability of REM to handle 3D problems.

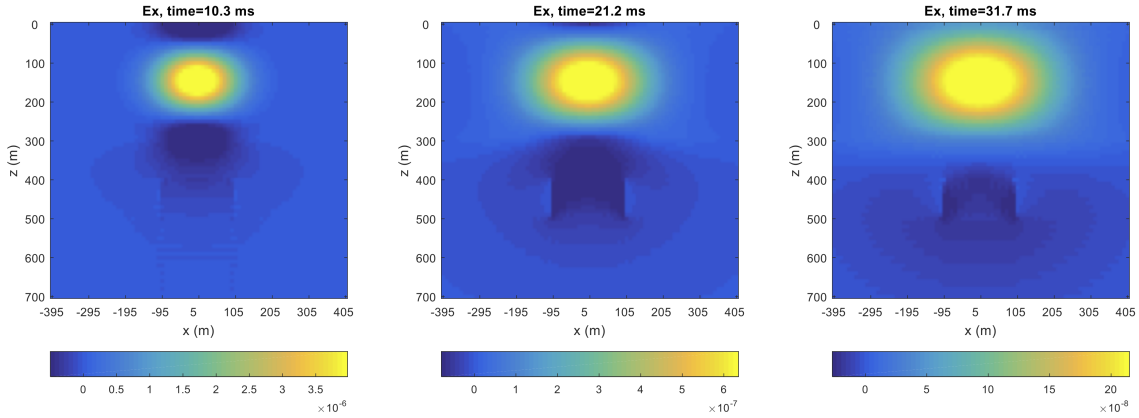

Fig. 5.10 Test of the presence of a 3D resistor: wavefield snapshots. From left to right, the graphs show the x-component snapshots on the x-z plane ($y = 5$ m) at time 10.3, 21.2, and 31.7 ms. The model configuration is illustrated in Figure 5.9(a).

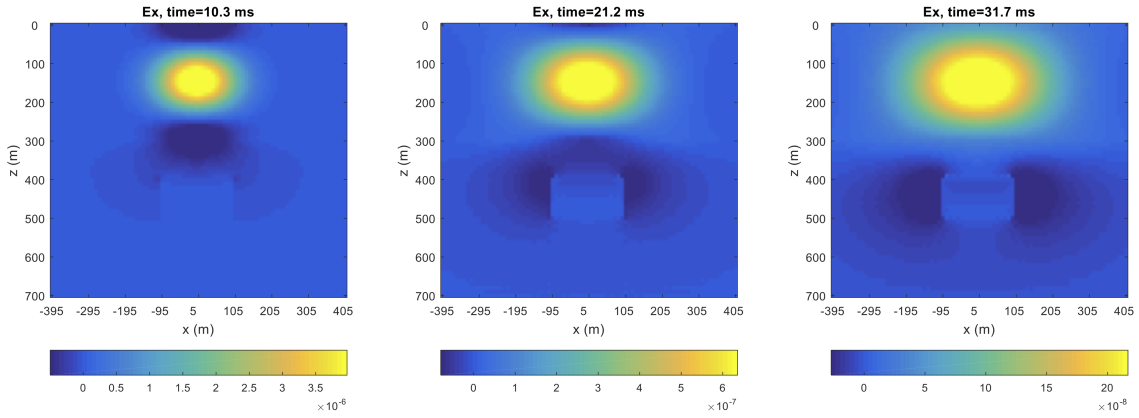

Fig. 5.11 Test of the presence of a 3D conductor: wavefield snapshots. From left to right, the graphs show the x-component snapshots on the x-z plane ($y = 5$ m) at time 10.3, 21.2, and 31.7 ms. The model configuration is illustrated in Figure 5.9(b).

5.4 Discussion

The pseudospectral REM method is an explicit method that solves the time evolution of the diffusive field. Compared with implicit methods, explicit methods are attractive in terms of their simplicity and robustness in the presence of large conductivity contrasts. An explicit method is also found to be reliable to produce accurate results over a large dynamic time range (Commer and Newman, 2004). The major drawback of the explicit method is the stringent stability condition, which leads to a high computational cost. The Chebyshev approach,

however, is an efficient and attractive explicit method for two reasons. First, the number of evaluations of the propagation matrix required by REM is much fewer than the conventional, second-order finite difference in time. For example, considering the 3D example shown in Figure 5.10 with a minimum conductivity of 0.02 S/m, the maximum diffusion time by finite difference (Potter, 1973) is $\Delta t = \mu\sigma\Delta x^2 \approx 6.28 \times 10^{-7}$ s, and a simulation of 1 s requires the propagation matrix $\mathbf{G}$ to be evaluated for $t/\Delta t \approx 1.59 \times 10^6$ times. However, the Chebyshev approach requires approximately 1.7×10^5 evaluations of $\mathbf{G}$, which is about an order of magnitude cheaper. Besides, this efficiency further increases with the length of simulation time, as the number of the Chebyshev terms needed for convergence is proportional to the square root of time (equation 3.34). Second, the Chebyshev method does not require the computation of inner products, which is highly beneficial in parallel computing. This is the advantage of the proposed method over the Krylov approach (Carcione, 2006).

Stoffa and Ziolkowski (2019) show the REM solution to the 3D EM diffusion problem, as discussed in Chapter 3. I extend the work of Stoffa and Ziolkowski (2019) to include the air layer and anisotropy, as discussed in Chapter 4 and 5. Through the development of the theory, I deliberately used a small model that would fit into a standard desktop or laptop machine and compute in a reasonable time, to demonstrate the correctness of the method and the code. There are edge effects that lead to small errors in the far-offset results. One solution to that is to move to a bigger machine and extend the model size. An alternative solution is to improve the absorbing boundary conditions, such as applying perfectly matched layers to the Chebyshev polynomials. This is discussed in Chapter 6.

As discussed in section 5.2.3, we use collocated regular grids because it is simple to implement, numerically efficient, and it is very accurate because of the pseudospectral evaluation of spatial derivatives. When considering anisotropy, the inverse of Ohm's law implemented by Yee's grid can be troublesome, and the use of collocated grids is preferable. The presented results are very accurate, considering VTI and TTI anisotropy, and 3D resistive anomalies. Nevertheless, as discussed in section 4.4, in some situations, irregular grids may be more appropriate, to consider a shallow source or irregular interfaces. Irregular girds can be combined with the pseudospectral method via a mapping function, as discussed in Fornberg (1988). Finite element is also an option in combination with REM in order to consider complex subsurface geometry.

5.5 Summary

I have presented another extension to the pseudospectral REM algorithm that includes anisotropic conductivity. Transverse isotropic anisotropy can be included in the REM

modelling with the manipulation of the conductivity tensor. Eigenvalues of the anisotropic propagation matrix are solved, whose values are important to ensure the stability and the convergence of the Chebyshev recursion. Through the modelling, all the three electric components are sampled at the same location as the conductivity tensor without any averaging of material properties. Numerical tests against the 1D spectral method, along with the snapshots of the Chebyshev terms and the electric field in various anisotropic models, have demonstrated the ability of REM to handle VTI and TTI anisotropic conductivity.

Chapter 6

Application of Perfectly Matched Layers in the Chebyshev Domain

The subsurface where the electric field propagates is often considered as unbounded space, whereas the computational domain is always limited. There must be a way to truncate the computational mesh. Absorbing boundary conditions (ABC) are developed and applied to the numerical boundaries, to minimize the spurious reflections caused by the truncation of the computational space. The domain of Chebyshev polynomials needs an accurate absorbing boundary. In this chapter, I show how the theory of perfectly matched layers, a well-established ABC in electromagnetic modelling, can be extended to the Chebyshev domain to solve its boundary problems. I present numerical tests against the analytic solution and spectral methods to demonstrate the usefulness of the PML absorbing boundary and the correctness of the theory and the code.

6.1 Introduction

Stoffa and Ziolkowski (2019) show how to use the rapid expansion method (REM) to solve the 3D EM diffusion problem. Liu et al. (2019b) extend their work to include the Earth-air interface and anisotropic conductivity into the REM solution. The time evolution of the electric field is integrated by a summation of the Chebyshev terms in the domain of the eigenvalues of the propagation matrix, and the Chebyshev evaluation is accurate to the Nyquist frequency and temporal numerical dispersion can be mitigated, as discussed in Chapter 3, 4 and 5. However, there is a potential issue in this approach that may degrade the accuracy of the REM results: the lack of an accurate and efficient absorbing boundary condition (ABC).

The lack of an accurate ABC in the Chebyshev domain has been known for years. For example, Raedt et al. (2003) show that the Chebyshev method can be orders of magnitude more efficient than finite-difference time-domain (FDTD) methods; however, "FDTD methods can easily handle absorbing boundary conditions but at present, there is no guarantee that the Chebyshev polynomial approximation will still be accurate in these circumstances." Carcione (2006) first applies the pseudospectral REM alogrithm to solve a diffusive EM modelling problem, and he comments "further work is required to improve the absorbing boundary, preferably based on the use of nonperiodic boundary conditions". One possible ABC used in the Chebyshev domain is to manually reduce the amplitude of the Chebyshev terms in the surrounding strips of the mesh (e.g., Tal-Ezer et al., 1987; Carcione, 2006). These boundaries are absorbing, but there are numerical reflections generated by the manual damping, which can degrade the accuracy of the modelling. Alternatively, one can avoid the use of absorbing boundaries by increasing the size of the simulation model. In that case, the default numerical boundary condition is the Dirichlet boundary condition or periodic boundary condition, depending on whether the spatial derivatives are solved by a finite-difference method or by a pseudospectral method. Increasing the size of the computational space is a practical option, especially when simulating the diffusive EM fields, because the diffusive EM fields decay naturally in a conductive medium (e.g., Wang and Hohmann, 1993; Commer and Newman, 2004). However, the appearance of a less-lossy (resistive) medium makes the spurious reflections caused by the numerical boundaries less attenuated, and therefore the modelling results become less reliable if we are unable to truncate the Chebyshev terms with absorption in space.

Therefore, a more advanced ABC is required to solve the numerical boundary problem related to the Chebyshev method. One option is to exploit the use of the perfectly matched layer (PML) in the Chebyshev domain. PML is a well-established ABC technique in time- and frequency-domain EM modelling and is often considered the most effective one to attenuate the EM fields. It was proposed by Berenger (1994), with the idea of matching the impedance of the absorbing layer to make it reflectionless. Gedney (1996) shows that PML can be implemented by introducing uniaxial anisotropic material in the absorbing region. Alternatively, Chew and Weedon (1994) apply the PML absorbing boundary with a modified set of Maxwell's equations as the EM field is stretched in complex coordinates. More advanced versions of PML are further developed, such as complex frequency-shifted PML (Kuzuoglu and Mittra, 1996) and convolutional PML (Roden and Gedney, 2000), to optimize its efficiency in an arbitrary medium and improve the absorption of evanescent waves. It has been a popular choice to truncate finite-difference grids, as shown by recent

studies of 3D magnetotelluric modelling (de la Kethulle de Ryhove and Mittet, 2014) and 3D CSEM modelling (Hu et al., 2017; Li et al., 2018).

In this chapter, I show that the PML technique can be extended to the Chebyshev domain to simulate the 3D time-domain electric field by REM. By transforming the time-domain electric field to the Chebyshev domain, the Chebyshev terms follow a one-step, second-order wave equation, as shown by Stoffa and Ziolkowski (2019). I introduce a fictitious magnetic field in the Chebyshev domain and modify the original governing equation to a set of two-step, first-order wave equations. The new simulation of the Chebyshev terms is very similar to the propagation of EM waves in a lossless medium. The PML technique can be applied to the Chebyshev terms in a straightforward way, and attenuates the Chebyshev terms close to the boundary and therefore correct the electric field so that the boundary problem in the Chebyshev method can be solved.

I first review the work of Stoffa and Ziolkowski (2019) to show that the recursion of Chebyshev polynomials is equivalent to the propagation of a wavefield in the "Chebyshev" domain. Then, I introduce a fictitious field in the Chebyshev domain and describe the modification of the governing equation. I show how the theory of PML based on EM wave modelling can be applied to the Chebyshev terms of the electric field. Finally, I demonstrate the accuracy of the method and the usefulness of absorbing boundary by two numerical examples. The theory and the results presented in this chapter were published in Liu (2019). I modified the original text, figures, layout, and symbols to fit the style of the thesis.

6.2 Theory

6.2.1 Introducing a fictitious magnetic field

As shown in section 3.4, considering isotropic conductivity, Stoffa and Ziolkowski (2019) found that the updating of Chebyshev terms can be written in the form

$$\frac{\mathbf{Q}_{k+1} - 2\mathbf{Q}_k + \mathbf{Q}_{k-1}}{\Delta p^2} = -\frac{1}{\mu\sigma}\nabla \times \nabla \times \mathbf{Q}_k, \tag{6.1}$$

where $\Delta p = \sqrt{2/b}$ is the equivalent 'time' step in the Chebyshev domain with dimensions of square root of time. This equation is a discrete wave equation. For a numerical problem with node spacing Δx, Δy, and Δz, the Chebyshev time step Δp is a constant value

$$\Delta p = \frac{1}{\pi}\sqrt{\frac{2\mu_0\sigma_{min}}{\Delta x^{-2} + \Delta y^{-2} + \Delta z^{-2}}}, \tag{6.2}$$

where σ_{min} denotes the minimum conductivity in the model.

I define $\mathbf{Q}$ as the Chebyshev electric field, and define p as the Chebyshev time. I introduce another field $\mathbf{L}$, such that

$$\mu \frac{\mathbf{L}_{k+\frac{1}{2}} - \mathbf{L}_{k-\frac{1}{2}}}{\Delta p} = -\nabla \times \mathbf{Q}_k, \tag{6.3}$$

$$\sigma \frac{\mathbf{Q}_{k+1} - \mathbf{Q}_k}{\Delta p} = \nabla \times \mathbf{L}_{k+\frac{1}{2}}. \tag{6.4}$$

By taking the curl of equation 6.3 and replacing the curl of $\mathbf{L}$ by the form of equation 6.4, the combination of equations 6.3 and 6.4 is equivalent to equation 6.1, except that in equation 6.1 I use $\{\mathbf{Q}_k, \mathbf{Q}_{k-1}\}$ to update $\mathbf{Q}_{k+1}$, but now in equation 6.3 and 6.4 I use $\{\mathbf{Q}_k, \mathbf{L}_{k-\frac{1}{2}}\}$ to update $\{\mathbf{Q}_{k+1}, \mathbf{L}_{k+\frac{1}{2}}\}$. The fields $\{\mathbf{Q}, \mathbf{L}\}$ propagating in the Chebyshev domain are exactly like the fields $\{\mathbf{E}, \mathbf{H}\}$ propagating in a vacuum where the first-order time derivative has been dropped and EM fields propagate as waves. The numerical simulation of $\{\mathbf{Q}, \mathbf{L}\}$, as shown by equations 6.3 and 6.4, is exactly a finite difference scheme, which is derived based on the Chebyshev recursion relation. For the initial field where $k = 0$, I use

$$\mu \frac{\mathbf{L}_{1/2}}{\Delta p/2} = -\nabla \times \mathbf{Q}_0, \tag{6.5}$$

$$\sigma \frac{\mathbf{Q}_1 - \mathbf{Q}_0}{\Delta p} = \nabla \times \mathbf{L}_{1/2}, \tag{6.6}$$

and again equations 6.5 and 6.6 give

$$\mathbf{Q}_1 = -b^{-1}(\mu\sigma)^{-1} \nabla \times \nabla \times \mathbf{Q}_0 + \mathbf{Q}_0, \tag{6.7}$$

which is equivalent to the Chebyshev relation corresponding to the first term. Therefore the modelling of the diffusive field $\mathbf{E}$ becomes a wave-based scheme in the Chebyshev domain, and any EM wave modelling technique should be easily extended and applied to the Chebyshev terms $\{\mathbf{Q}, \mathbf{L}\}$.

6.2.2 Inclusion of PML in the Chebyshev domain

Chew and Weedon (1994) show that PML can be implemented in the model by stretching the coordinates in the complex domain. The modified Maxwell's equations are

$$i\omega\mu\tilde{\mathbf{H}} = -[\mathbf{s}^{-1}] \nabla \times \tilde{\mathbf{E}}, \tag{6.8}$$

$$i\omega\varepsilon\tilde{\mathbf{E}} = [\mathbf{s}^{-1}] \nabla \times \tilde{\mathbf{H}}, \tag{6.9}$$

where the tilde symbol denotes the fields in the frequency domain, and $[\mathbf{s}^{-1}]$ denotes the coordinate stretching tensor that consists of complex numbers. In the main body of the model there is no PML and $\mathbf{s}$ is an identity matrix, the coordinates are not stretched and the governing equations are Maxwell's equations. In the PML region, the complex tensor $\mathbf{s}$ is designed to match the impedance of the medium but the inclusion of the imaginary part makes the medium lossy to absorb energy.

In this section, I consider an isotropic case to derive the formulas of PML applicable to the Chebyshev domain. Potential future work is discussed in section 6.4. The Chebyshev pairs $\{\mathbf{Q},\mathbf{L}\}$ in the stretched coordinates are defined as

$$i\upsilon\mu\tilde{\mathbf{L}} = -[\mathbf{s}^{-1}]\nabla\times\tilde{\mathbf{Q}}, \tag{6.10}$$

$$i\upsilon\sigma\tilde{\mathbf{Q}} = [\mathbf{s}^{-1}]\nabla\times\tilde{\mathbf{L}}, \tag{6.11}$$

where υ is the angular frequency in the Chebyshev frequency domain that corresponds to the Chebyshev time p, and σ is the conductivity of the medium. With reference to Berenger (2002), I similarly define the complex coordinate stretching factors as

$$s_d = \kappa_d + \frac{\eta_d}{\alpha_d + i\upsilon\sigma}, \tag{6.12}$$

where $d = x, y$ or z denotes the direction, $\eta \geqslant 0$ controls the loss in the PML region, $\alpha \geqslant 0$ controls the shift of the frequency-dependent component and $\kappa \geqslant 1$ acts as a scaling factor.

Equations 6.10, 6.11 and 6.12 are the governing equations to implement a general form of PML in the Chebyshev domain. In this chapter, I show the application of uniaxial PML. Other types of PML can be similarly used by varying the corresponding terms in equations 6.10, 6.11 and 6.12. Following the derivation in Gedney (1996), the curl operator in the stretched coordinates is written as

$$[\mathbf{s}^{-1}]\nabla\times = \begin{pmatrix} 0 & -\frac{s_x}{s_y}\frac{1}{s_z}\frac{\partial}{\partial z} & \frac{s_x}{s_z}\frac{1}{s_y}\frac{\partial}{\partial y} \\ \frac{s_y}{s_x}\frac{1}{s_z}\frac{\partial}{\partial z} & 0 & -\frac{s_y}{s_z}\frac{1}{s_x}\frac{\partial}{\partial x} \\ -\frac{s_z}{s_x}\frac{1}{s_y}\frac{\partial}{\partial y} & \frac{s_z}{s_y}\frac{1}{s_x}\frac{\partial}{\partial x} & 0 \end{pmatrix}, \tag{6.13}$$

with $\kappa = 1$ and $\alpha = 0$ in the stretching factors s_x, s_y and s_z. Combining equations 6.10, 6.11, 6.12 and 6.13, the six components in the Chebyshev frequency domain satisfy

$$i\upsilon\tilde{L_x}(1+\frac{\eta_x}{i\upsilon\sigma})^{-1}(1+\frac{\eta_y}{i\upsilon\sigma})(1+\frac{\eta_z}{i\upsilon\sigma}) = -\frac{1}{\mu}[-\frac{\partial\tilde{Q_y}}{\partial z}+\frac{\partial\tilde{Q_z}}{\partial y}], \tag{6.14}$$

$$i\upsilon\tilde{L_y}(1+\frac{\eta_y}{i\upsilon\sigma})^{-1}(1+\frac{\eta_x}{i\upsilon\sigma})(1+\frac{\eta_z}{i\upsilon\sigma}) = -\frac{1}{\mu}[-\frac{\partial\tilde{Q_z}}{\partial x}+\frac{\partial\tilde{Q_x}}{\partial z}], \tag{6.15}$$

$$i\upsilon\tilde{L_z}(1+\frac{\eta_z}{i\upsilon\sigma})^{-1}(1+\frac{\eta_x}{i\upsilon\sigma})(1+\frac{\eta_y}{i\upsilon\sigma}) = -\frac{1}{\mu}[-\frac{\partial\tilde{Q_x}}{\partial y}+\frac{\partial\tilde{Q_y}}{\partial x}], \tag{6.16}$$

$$i\upsilon\tilde{Q_x}(1+\frac{\eta_x}{i\upsilon\sigma})^{-1}(1+\frac{\eta_y}{i\upsilon\sigma})(1+\frac{\eta_z}{i\upsilon\sigma}) = \frac{1}{\sigma}[-\frac{\partial\tilde{L_y}}{\partial z}+\frac{\partial\tilde{L_z}}{\partial y}], \tag{6.17}$$

$$i\upsilon\tilde{Q_y}(1+\frac{\eta_y}{i\upsilon\sigma})^{-1}(1+\frac{\eta_x}{i\upsilon\sigma})(1+\frac{\eta_z}{i\upsilon\sigma}) = \frac{1}{\sigma}[-\frac{\partial\tilde{L_z}}{\partial x}+\frac{\partial\tilde{L_x}}{\partial z}], \tag{6.18}$$

$$i\upsilon\tilde{Q_z}(1+\frac{\eta_z}{i\upsilon\sigma})^{-1}(1+\frac{\eta_x}{i\upsilon\sigma})(1+\frac{\eta_y}{i\upsilon\sigma}) = \frac{1}{\sigma}[-\frac{\partial\tilde{L_x}}{\partial y}+\frac{\partial\tilde{L_y}}{\partial x}]. \tag{6.19}$$

The Fourier transform derivative relation can be extended to the Chebyshev domain. Taking the L_x component as an example, its derivative with respect to the Chebyshev time p satisfies

$$\frac{\partial}{\partial p}L_x = \frac{1}{2\pi}\int_{-\infty}^{+\infty} i\upsilon\tilde{L_x}\exp(i\upsilon p)d\upsilon. \tag{6.20}$$

Converting equations 6.14 - 6.19 into the Chebyshev time domain, and using the derivative relation given in equation 6.20 to transform the frequency-dependent terms into the corresponding derivatives and integrals with respect to p, yields

$$\begin{aligned}\frac{\partial}{\partial p}L_x+\frac{\eta_y+\eta_z}{\sigma}L_x+\int_{-\infty}^{p}\frac{\eta_y\eta_z}{\sigma^2}L_x(\tau)d\tau = \\ -\frac{1}{\mu}[-\frac{\partial Q_y}{\partial z}+\frac{\partial Q_z}{\partial y}]-\frac{1}{\mu}\int_{-\infty}^{p}\frac{\eta_x}{\sigma}[-\frac{\partial Q_y(\tau)}{\partial z}+\frac{\partial Q_z(\tau)}{\partial y}]d\tau,\end{aligned} \tag{6.21}$$

$$\begin{aligned}\frac{\partial}{\partial p}L_y+\frac{\eta_x+\eta_z}{\sigma}L_y+\int_{-\infty}^{p}\frac{\eta_x\eta_z}{\sigma^2}L_y(\tau)d\tau = \\ -\frac{1}{\mu}[-\frac{\partial Q_z}{\partial x}+\frac{\partial Q_x}{\partial z}]-\frac{1}{\mu}\int_{-\infty}^{p}\frac{\eta_y}{\sigma}[-\frac{\partial Q_z(\tau)}{\partial x}+\frac{\partial Q_x(\tau)}{\partial z}]d\tau,\end{aligned} \tag{6.22}$$

$$\begin{aligned}\frac{\partial}{\partial p}L_z+\frac{\eta_x+\eta_y}{\sigma}L_z+\int_{-\infty}^{p}\frac{\eta_x\eta_y}{\sigma^2}L_z(\tau)d\tau = \\ -\frac{1}{\mu}[-\frac{\partial Q_x}{\partial y}+\frac{\partial Q_y}{\partial x}]-\frac{1}{\mu}\int_{-\infty}^{p}\frac{\eta_z}{\sigma}[-\frac{\partial Q_x(\tau)}{\partial y}+\frac{\partial Q_y(\tau)}{\partial x}]d\tau,\end{aligned} \tag{6.23}$$

$$\begin{aligned}\frac{\partial}{\partial p}Q_x+\frac{\eta_y+\eta_z}{\sigma}Q_x+\int_{-\infty}^{p}\frac{\eta_y\eta_z}{\sigma^2}Q_x(\tau)d\tau = \\ \frac{1}{\sigma}[-\frac{\partial L_y}{\partial z}+\frac{\partial L_z}{\partial y}]+\frac{1}{\sigma}\int_{-\infty}^{p}\frac{\eta_x}{\sigma}[-\frac{\partial L_y(\tau)}{\partial z}+\frac{\partial L_z(\tau)}{\partial y}]d\tau,\end{aligned} \tag{6.24}$$

$$\frac{\partial}{\partial p}Q_y+\frac{\eta_x+\eta_z}{\sigma}Q_y+\int_{-\infty}^{p}\frac{\eta_x\eta_z}{\sigma^2}Q_y(\tau)d\tau= \\ \frac{1}{\sigma}[-\frac{\partial L_z}{\partial x}+\frac{\partial L_x}{\partial z}]+\frac{1}{\sigma}\int_{-\infty}^{p}\frac{\eta_y}{\sigma}[-\frac{\partial L_z(\tau)}{\partial x}+\frac{\partial L_x(\tau)}{\partial z}]d\tau, \tag{6.25}$$

$$\frac{\partial}{\partial p}Q_z+\frac{\eta_x+\eta_y}{\sigma}Q_z+\int_{-\infty}^{p}\frac{\eta_x\eta_y}{\sigma^2}Q_z(\tau)d\tau= \\ \frac{1}{\sigma}[-\frac{\partial L_x}{\partial y}+\frac{\partial L_y}{\partial x}]+\frac{1}{\sigma}\int_{-\infty}^{p}\frac{\eta_z}{\sigma}[-\frac{\partial L_x(\tau)}{\partial y}+\frac{\partial L_y(\tau)}{\partial x}]d\tau. \tag{6.26}$$

The components of **L** and **Q** are collocated in space and staggered in the Chebyshev time. I use central difference to calculate the derivative with respect to p, which is consistent with the governing equation 6.3 and 6.4, such that

$$\frac{\partial}{\partial p}L_{x,k}=\frac{L_{x,k+\frac{1}{2}}-L_{x,k-\frac{1}{2}}}{\Delta p}. \tag{6.27}$$

Equations 6.21 - 6.26 can be approximated numerically as

$$\left(1+\frac{\eta_y+\eta_z}{2\sigma}\Delta p\right)L_{x,k+\frac{1}{2}}=-\frac{\Delta p}{\mu}[-\frac{\partial Q_{y,k}}{\partial z}+\frac{\partial Q_{z,k}}{\partial y}] \\ +\left(1-\frac{\eta_y+\eta_z}{2\sigma}\Delta p\right)L_{x,k-\frac{1}{2}}-\frac{\eta_y\eta_z}{\sigma^2}\sum_{k'=1}^{k'=k}L_{x,k'-\frac{1}{2}}\Delta p^2-\frac{\eta_x}{\mu\sigma}\sum_{k'=0}^{k'=k}[-\frac{\partial Q_{y,k'}}{\partial z}+\frac{\partial Q_{z,k'}}{\partial y}]\Delta p^2, \tag{6.28}$$

$$\left(1+\frac{\eta_x+\eta_z}{2\sigma}\Delta p\right)L_{y,k+\frac{1}{2}}=-\frac{\Delta p}{\mu}[-\frac{\partial Q_{z,k}}{\partial x}+\frac{\partial Q_{x,k}}{\partial z}] \\ +\left(1-\frac{\eta_x+\eta_z}{2\sigma}\Delta p\right)L_{y,k-\frac{1}{2}}-\frac{\eta_x\eta_z}{\sigma^2}\sum_{k'=1}^{k'=k}L_{y,k'-\frac{1}{2}}\Delta p^2-\frac{\eta_y}{\mu\sigma}\sum_{k'=0}^{k'=k}[-\frac{\partial Q_{z,k'}}{\partial x}+\frac{\partial Q_{x,k'}}{\partial z}]\Delta p^2, \tag{6.29}$$

$$\left(1+\frac{\eta_x+\eta_y}{2\sigma}\Delta p\right)L_{z,k+\frac{1}{2}}=-\frac{\Delta p}{\mu}[-\frac{\partial Q_{x,k}}{\partial y}+\frac{\partial Q_{y,k}}{\partial x}] \\ +\left(1-\frac{\eta_x+\eta_y}{2\sigma}\Delta p\right)L_{z,k-\frac{1}{2}}-\frac{\eta_x\eta_y}{\sigma^2}\sum_{k'=1}^{k'=k}L_{z,k'-\frac{1}{2}}\Delta p^2-\frac{\eta_z}{\mu\sigma}\sum_{k'=0}^{k'=k}[-\frac{\partial Q_{x,k'}}{\partial y}+\frac{\partial Q_{y,k'}}{\partial x}]\Delta p^2, \tag{6.30}$$

$$\left(1+\frac{\eta_y+\eta_z}{2\sigma}\Delta p\right)Q_{x,k+1}=\frac{\Delta p}{\sigma}[-\frac{\partial L_{y,k+\frac{1}{2}}}{\partial z}+\frac{\partial L_{z,k+\frac{1}{2}}}{\partial y}]$$
$$+\left(1-\frac{\eta_y+\eta_z}{2\sigma}\Delta p\right)Q_{x,k}-\frac{\eta_y\eta_z}{\sigma^2}\sum_{k'=0}^{k'=k}Q_{x,k'}\Delta p^2+\frac{\eta_x}{\sigma^2}\sum_{k'=0}^{k'=k}[-\frac{\partial L_{y,k'+\frac{1}{2}}}{\partial z}+\frac{\partial L_{z,k'+\frac{1}{2}}}{\partial y}]\Delta p^2, \tag{6.31}$$

$$\left(1+\frac{\eta_x+\eta_z}{2\sigma}\Delta p\right)Q_{y,k+1}=\frac{\Delta p}{\sigma}[-\frac{\partial L_{z,k+\frac{1}{2}}}{\partial x}+\frac{\partial L_{x,k+\frac{1}{2}}}{\partial z}]$$
$$+\left(1-\frac{\eta_x+\eta_z}{2\sigma}\Delta p\right)Q_{y,k}-\frac{\eta_x\eta_z}{\sigma^2}\sum_{k'=0}^{k'=k}Q_{y,k'}\Delta p^2+\frac{\eta_y}{\sigma^2}\sum_{k'=0}^{k'=k}[-\frac{\partial L_{z,k'+\frac{1}{2}}}{\partial x}+\frac{\partial L_{x,k'+\frac{1}{2}}}{\partial z}]\Delta p^2, \tag{6.32}$$

$$\left(1+\frac{\eta_x+\eta_y}{2\sigma}\Delta p\right)Q_{z,k+1}=\frac{\Delta p}{\sigma}[-\frac{\partial L_{x,k+\frac{1}{2}}}{\partial y}+\frac{\partial L_{y,k+\frac{1}{2}}}{\partial x}]$$
$$+\left(1-\frac{\eta_x+\eta_y}{2\sigma}\Delta p\right)Q_{z,k}-\frac{\eta_x\eta_y}{\sigma^2}\sum_{k'=0}^{k'=k}Q_{z,k'}\Delta p^2+\frac{\eta_z}{\sigma^2}\sum_{k'=0}^{k'=k}[-\frac{\partial L_{x,k'+\frac{1}{2}}}{\partial y}+\frac{\partial L_{y,k'+\frac{1}{2}}}{\partial x}]\Delta p^2, \tag{6.33}$$

and equations 6.28 - 6.33 are the ones which are used to update the field components in the PML region. If $\eta_x=\eta_y=\eta_z=0$, equations 6.28 to 6.33 reduce to the normal equations which are used to update the field in the main section.

The interface between the interior region and the PML region is reflectionless, however, there is still an apparent reflection from the outer boundary of the model. For a PML layer with thickness d and decay factor $\eta(\delta)$, with δ denoting the distance from the PML-interior interface, the apparent reflection is a function of the incident angle θ, solved by Berenger (1994),

$$R(\theta)=\exp\left(-\frac{2\cos\theta}{\sigma c}\int_0^d\eta(\delta)d\delta\right), \tag{6.34}$$

where $c=(\mu\sigma)^{-\frac{1}{2}}$ is the propagation speed in the Chebyshev-space domain. For numerical consideration, the value of $\eta(\delta)$ needs to be tapered gradually from its maximum to zero towards the PML-interior interface

$$\eta(\delta)=\eta_{max}\left(\frac{\delta}{d}\right)^m, \tag{6.35}$$

where m can be either 2 or 3. As discussed by Berenger (2002), $m=3$ has a better absorption on the evanescent region whereas $m=2$ has a better absorption on the propagation region. I

use $m = 2$. Substituting equation 6.35 into 6.34, the apparent reflection is

$$R(\theta) = \exp\left(\frac{2d\cos\theta}{m+1}\frac{\eta_{max}}{\sigma c}\right). \tag{6.36}$$

The value of $R(\theta)$ can be used to measure the effectiveness of the absorption. By increasing the decay factor η_{max}, the predicted reflection $R(\theta)$ will continuously decrease. However, there is a lower bound for the realizable $R(\theta)$ in the discrete space since the numerical discretization error increases with the decay factor η_{max}. For example, Gedney (1996) finds that for a ten-node PML the minimum numerical error occurs when $R(0) \approx e^{-16}$ and for a five-node PML the minimum error occurs when $R(0) \approx e^{-8}$. The optimal choice of $R(0)$ is problem-dependent and controlled by η_{max}. I use a modified optimal formulation for η_{max} similar to that in Pan and Habashy (2012) and Li et al. (2018),

$$\eta_{max}(x,y,z) = w\frac{(m+1)\sigma(x,y,z)}{d\Delta p}, \tag{6.37}$$

where w is a constant that determines the magnitude of η_{max} and $R(\theta)$. The inclusion of Δp makes the scale of w less problem-dependent and easier to tune. For an EM modelling problem with node spacing of 20 m, varying w from 1 to 100 gives the normal incidence reflection $R(0)$ varying from about e^{-1} to e^{-40}, which should cover most of the desired range of $R(0)$.

6.3 Numerical Results

I present two numerical examples to demonstrate the use of PML in REM modelling. First I check the code in a homogeneous whole space, against the analytical solution given by Slob et al. (2010). Then I add resistive layers to the model and check the solution against the published 1D modelling code EMmod (Hunziker et al., 2015). The analytical solution and the semi-analytical 1D modelling method are free of boundary problems. I compare the 3D REM modelling results with and without PML, to demonstrate the correctness of the developed theory and to discuss the improvements of the results by improving the absorbing boundary.

The algorithm is written in a parallel C code and in an alternative Matlab code. For the tests below with synthetic data and computationally small models, I show the results from the Matlab code, running on a desktop machine with a single processor (3.20 GHz). The model cube is constructed with 128 nodes along each of the x-, y- and z-direction, with 14 nodes on each side working as the PML absorbing boundary. Therefore the main section of the cube

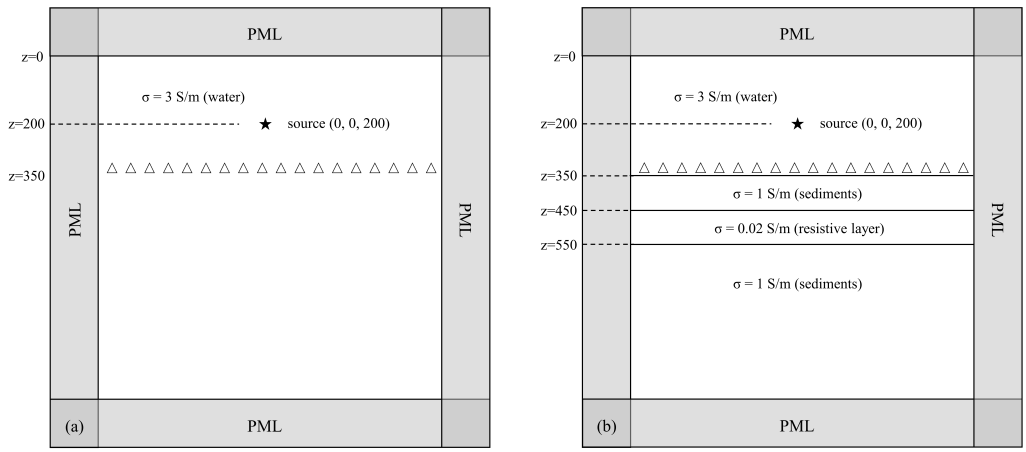

Fig. 6.1 Configuration of the model. PML is implemented with 14 nodes on each side along the x-, y-, and z-directions. The x-directed dipole source is located 200 m below the PML region in the center with coordinates $x = y = 0$. The inline receivers ($y = 5$ m) are 145 m below the source on the nodes. The node spacing is 10 m. (a) A homogeneous model. (b) A 1D layered model.

has $100 \times 100 \times 100$ nodes, excluding the absorbing boundaries. Node spacing is 10 m. The x-directed dipole source is located 200 m below the PML region and the inline receivers are located 145 m below the source on the nodes (Figure 6.1). I use a maximum decay factor η_{max} with $w = 25$ such that the apparent reflection at normal incidence is approximately $R(0) \approx e^{-19}$.

I first compare the snapshots of Q_x in the homogeneous whole space (Figure 6.1a). Since **Q** and **L** are waves in the Chebyshev domain, it is a good place to observe the appearance of any numerical reflections from the boundary. When PML is turned off, the modelling of REM uses periodic boundary condition. This is because the spatial derivatives in the propagation matrix **G** are evaluated in the wavenumber domain and the periodicity of the FFT makes the field periodic. Figure 6.2 shows the propagation of Q_x in an x-z slice. The up-going wave generated from the source and shown on the top of the 80^{th} Chebyshev term eventually appears at the bottom of the model, and interacts with the down-going wave as shown in the 280^{th} Chebyshev term. The up-going wave proves that a problem certainly exists. Then PML is turned on and the new snapshots of Q_x are shown in Figure 6.3. The up-going wave has vanished in the 180^{th} and 280^{th} Chebyshev terms, as the medium is infinite and the wave keeps propagating out of the model. No numerical reflection is observed from the boundary.

The effect of PML is also checked along the horizontal directions. The x-y horizontal slices of Q_x are compared in figure 6.4 and 6.5, without and with PML applied, respectively.

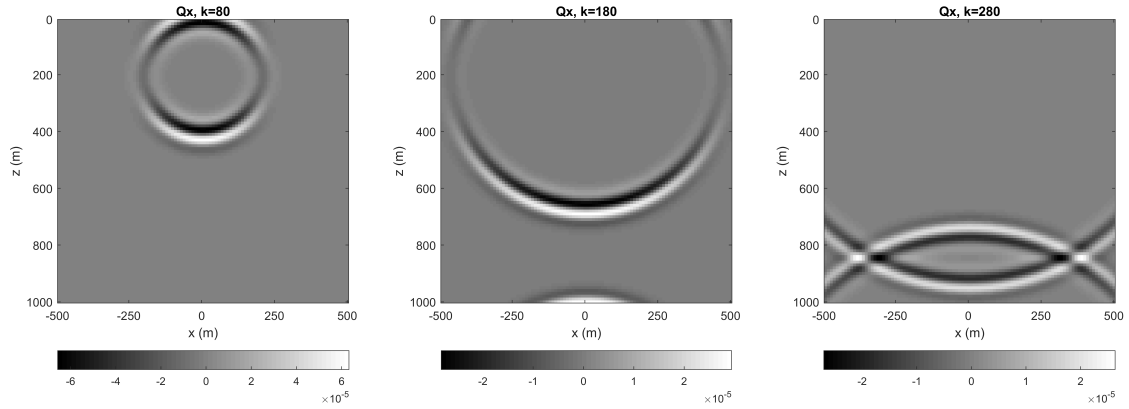

Fig. 6.2 Snapshots of Q_x. The x-z plane is located on $y = 5$ m. The model configuration is shown in Figure 6.1a. PML is OFF. The PML region is not shown.

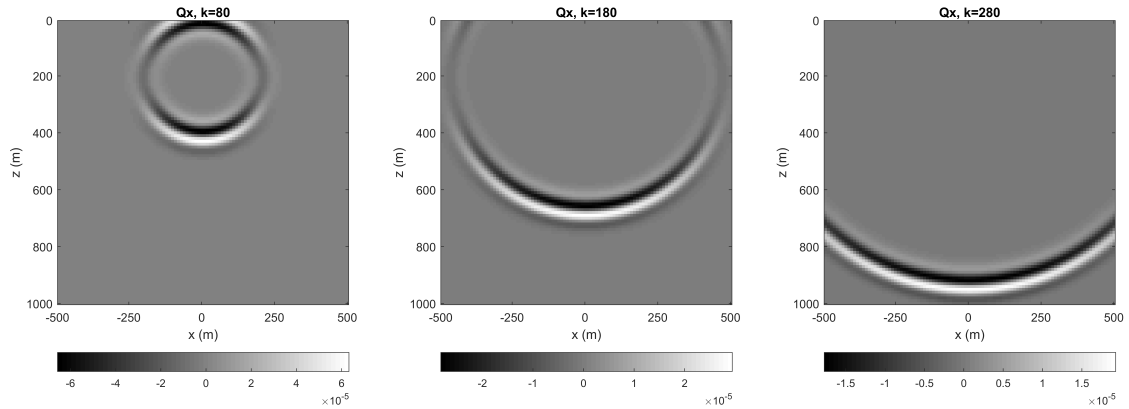

Fig. 6.3 Snapshots of Q_x. The x-z plane is located on $y = 5$ m. The model configuration is shown in Figure 6.1a. PML is ON. The PML region is not shown.

The periodicity of the field is observed again by comparing the 180$^{\text{th}}$ and 380$^{\text{th}}$ Chebyshev term. The energy is trapped in the model without absorbing boundaries. If Dirichlet boundary condition is used, we can expect pseudo-reflections from the numerical boundary instead of periodicity problems. In any case, the boundary effects are clearly illustrated in the Chebyshev domain. When turning on the PML, as shown in Figure 6.5, the scattered energy becomes almost invisible. The comparison of the horizontal and vertical slices of Q_x show that PML is absorbing and reflectionless in all three directions.

The time-domain response of the electric field is a weighted sum of Chebyshev terms, and the wave-like characteristics are smoothed out by the modified Bessel function (equation 3.9). Therefore we cannot observe an extra arrival corresponding to the up-going wave. What

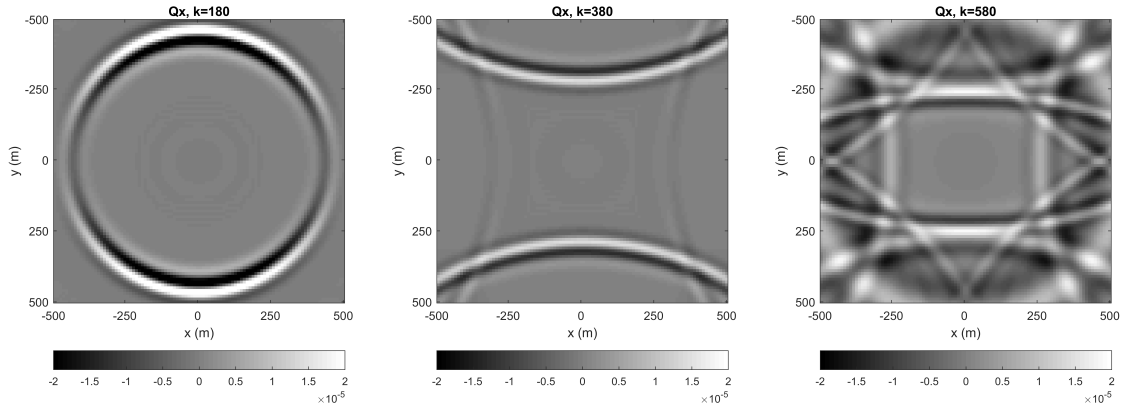

Fig. 6.4 Snapshots of Q_x. The x-y receiver plane is located on $z = 345$ m, 145 m below the source. The model configuration is shown in Figure 6.1a. PML is OFF. The PML region is not shown.

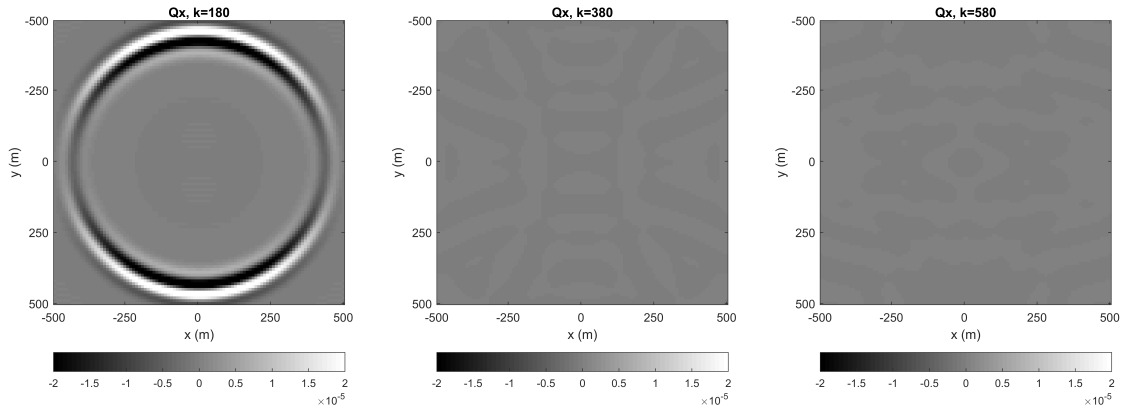

Fig. 6.5 Snapshots of Q_x. The x-y receiver plane is located on $z = 345$ m, 145 m below the source. The model configuration is shown in Figure 6.1a. PML is ON. The PML region is not shown.

we can observe is a slight mismatch of the long tails of the curves at far offset and late times, as shown in Figure 6.6. After turning on the PML, the mismatch vanishes and the REM results show excellent agreement with the analytical solution in Figure 6.7.

The electric field in the conductive medium is naturally attenuative, and in some cases the decay of the field itself is strong enough to absorb the numerical reflections from the boundary. However, the extent of the decay certainly depends on the conductivity of the medium. A resistive layer with a smaller conductivity gives a faster diffusive speed and less attenuation of the field, and under such circumstance the boundary problem can be severe.

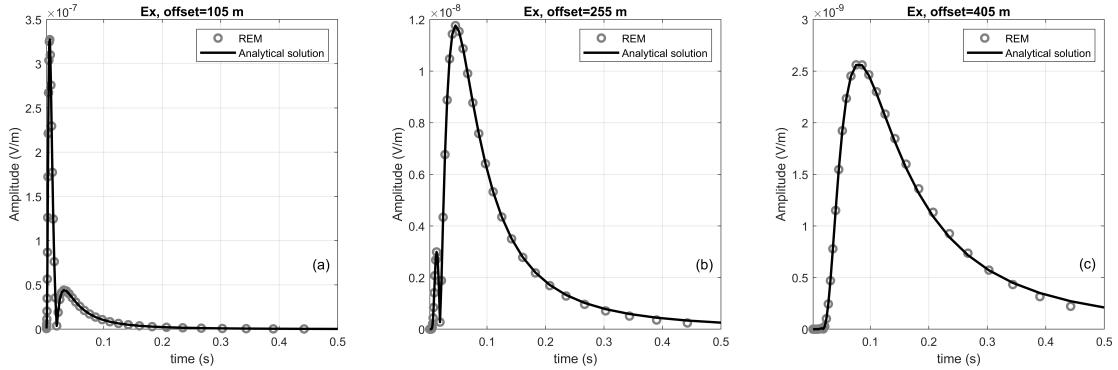

Fig. 6.6 Comparison of the inline electric field in the time domain. The model configuration is shown in Figure 6.1a. PML is OFF. The REM and analytical solution are denoted by the circles and solid lines, respectively. (a-c) The absolute amplitude of E_x at inline receivers ($y = 5$ m) with offsets in the x-direction of 105 m, 255 m, and 405 m, respectively.

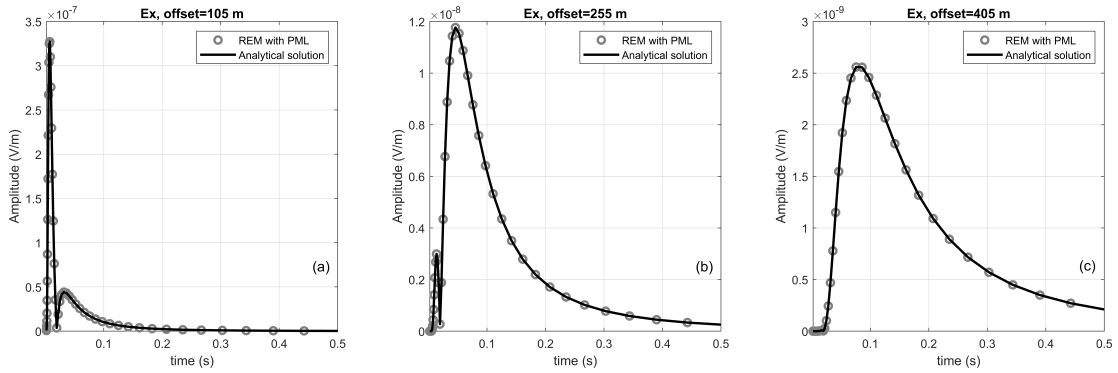

Fig. 6.7 Comparison of the inline electric field in the time domain. The model configuration is shown in Figure 6.1a. PML is ON. The REM and analytical solution are denoted by the circles and solid lines, respectively. (a-c) The absolute amplitude of E_x at inline receivers ($y = 5$ m) with offsets in the x-direction of 105 m, 255 m, and 405 m, respectively.

To demonstrate this, I insert layers into the previous model, with $\sigma = 1$ S/m representing sediments and $\sigma = 0.02$ S/m representing a potential resistive target (Figure 6.1b). The Chebyshev terms Q_x are compared in Figure 6.8. The horizontal axis is the inline offset and the vertical axis is the Chebyshev order k of the term Q_x. By presenting in this way, the Chebyshev terms can be analyzed in a way similar to seismic data. Without PML, the appearance of linear noise and periodic multiples is observed when the order k is greater than 4000. Due to the weighting by the modified Bessel function (equation 3.11), this section has a relatively greater contribution in the late time response rather than the early times. The amplitude of E_x, as examined in Figure 6.9, shows a clear difference from the calibration

curve, both in the peak value and in the long tail. The relative misfit increases towards the edge of the model.

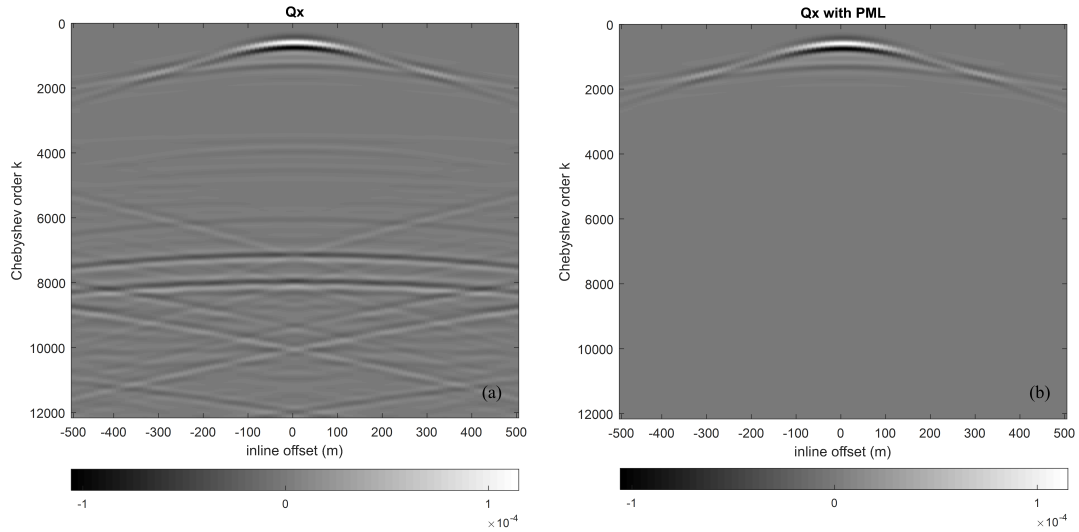

Fig. 6.8 Comparison of Q_x in the 1D layered model. The receiver line is located on $y = 5$ m and $z = 345$ m. Chebyshev terms Q_x are sampled at every 10 terms. (a and b) The Chebyshev terms Q_x with PML turning OFF and turning ON, respectively.

Linear noise and periodic multiples are generated due to the periodicity of the field, and the boundary effect in this example has a severe impact on E_x, since the resistive layer gives relatively small attenuation. After including PML, as shown in Figure 6.8, the unwanted signals are almost invisible in the high-order Q_x terms. As a result, the amplitude of E_x, as examined in Figure 6.10, shows an excellent agreement with the calibration curve.

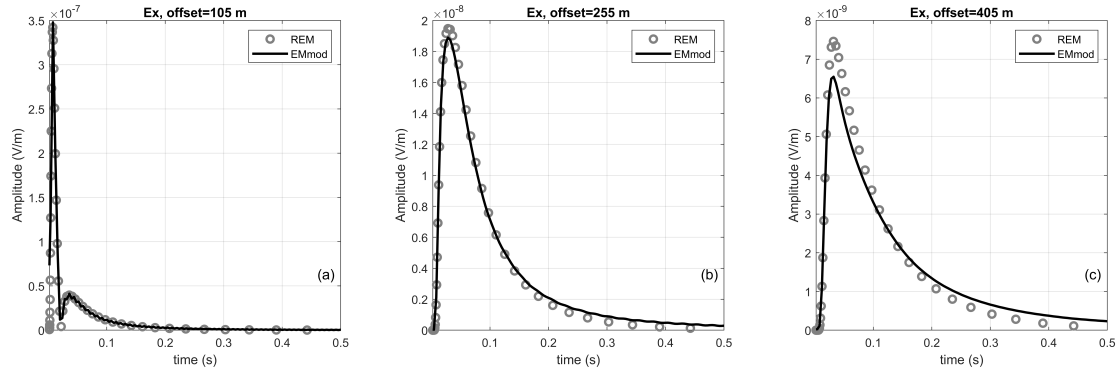

Fig. 6.9 Comparison of the inline electric field in the time domain. The model configuration is shown in Figure 6.1b. PML is OFF. The REM and EMmod solution are denoted by circles and solid lines, respectively. (a-c) The absolute amplitude of E_x at inline receivers ($y = 5$ m) with offsets in the x-direction of 105 m (20%), 255 m (50%), and 405 m (80%), respectively.

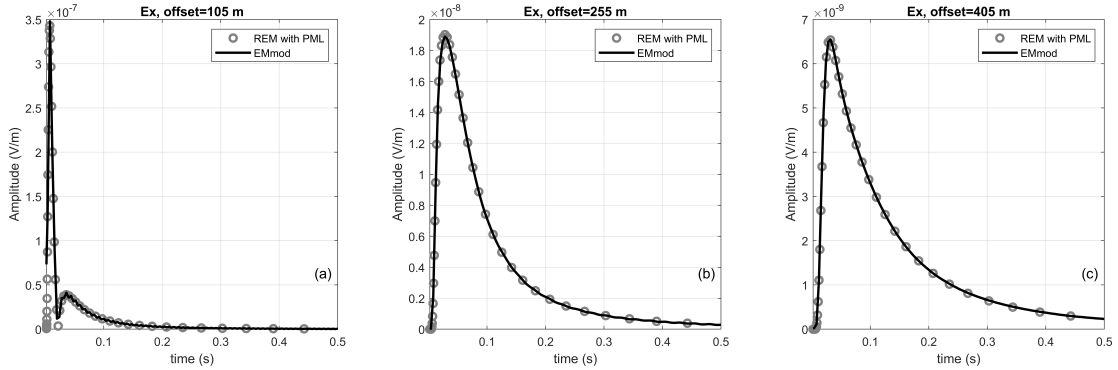

Fig. 6.10 Comparison of the inline electric field in the time domain. The model configuration is shown in Figure 6.1b. PML is ON. The REM and EMmod solution are denoted by circles and solid lines, respectively. (a-c) The absolute amplitude of E_x at inline receivers ($y = 5$ m) with offsets in the x-direction of 105 m (20%), 255 m (50%), and 405 m (80%), respectively.

The relative difference calculated at the far-offset receiver is shown in Figure 6.11. For the homogeneous case, the relative differences between the analytical solution and the REM results reduce to less than 0.1% after incorporating PML, apart from the difference in tiny amplitudes at very early times. For the 1D layered model, the relative differences between the EMmod and the REM results are about 0.1% to 1% for most of the simulation time, slightly larger than in the homogeneous case. The numerical error inevitably increases due to a direct implementation of internal interfaces (Mittet, 2017). The EMmod results also exhibit some numerical errors, as shown by the oscillation observed at the near-offset receiver (Figure 6.10). This may be due to the discrete Hankel transformation from the wavenumber to the space domain, as discussed in Hunziker et al. (2015), as well as the FFT and the spline interpolation managed by myself to match the results at the same time point. Nevertheless, the excellent agreement between the modelling responses delivers a convincing result that demonstrates the accuracy of the Chebyshev method when PML solves the boundary problem.

The number of nodes in the PML region can vary from a few to about twenty nodes to achieve different levels of effectiveness. Figure 6.11 shows the change of relative difference when the thickness of PML is reduced from 14 nodes to 10 nodes and 6 nodes, respectively. For the 6-node PML, the maximum relative difference increases to about 0.5% for the homogeneous model, and to about 4% for the 1D layered model. This level of accuracy may be practically acceptable in some cases. For the purpose of comparison, the values of η_{max} are kept the same for all the three PMLs. Better performance may be achieved for the thinner PMLs after tuning the optimal parameter for each case. A thinner PML usually requires a

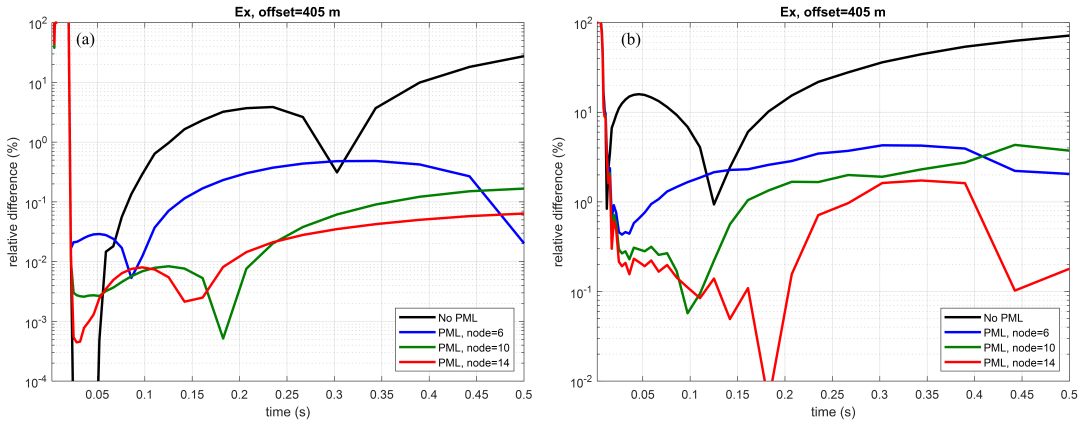

Fig. 6.11 Relative difference of the inline electric field in the time domain. (a and b) The relative difference calculated at the far-offset receiver ($x = 405$ m) for the homogeneous model (Figure 6.1a) and for the 1D layered model (Figure 6.1b), respectively. The calibration methods are the analytical solution (Slob et al., 2010) and the semi-analytical solution EMmod (Hunziker et al., 2015), respectively. Four cases are considered: REM modelling without PML and REM modelling with 6, 10, and 14 nodes acting as the PML region.

smaller decay factor to balance the apparent reflection and the discretization error (Gedney, 1996).

6.4 Discussion

PML itself is a well-studied technique in time-domain and frequency-domain EM wavefield modelling. However, to my knowledge, there is no previous examples showing the implementation of PML in the Chebyshev domain. The major difficulty was that after transforming the time-domain EM field into Chebyshev polynomials, the definitions of time and frequency become ambiguous. The main contributions of this study are 1) to link the recursion of Chebyshev polynomials to a coupled wave equation, which can be used to define explicitly the time and frequency component in the Chebyshev domain based on the eigenvalues of the propagation matrix (equations 6.2 - 6.6); and 2) to derive the theory of uniaxial PML that is applicable to the Chebyshev domain (equation 6.21 - 6.26) and therefore solves its boundary problems. More advanced PML can also be included in the Chebyshev domain following a similar procedure since the Chebyshev time and frequency have been given.

The use of PML gives several advantages. First, the accuracy of the modelling results, especially at far offsets, becomes more reliable and it no longer depends on the size of the simulation and the loss in the medium. Second, the computational cost can be reduced because of the truncation of the simulation region, despite the fact that PML is more expensive than the default, periodic boundary condition. Finally, for joint inversion of seismic and CSEM data (e.g., Hu et al., 2009), an accurate ABC such as PML can avoid enlarging the EM simulation model, which is more convenient for grid matching of the two data sets.

I have derived and demonstrated the inclusion of PML into REM in an isotropic case. To extend the PML theory to incorporate anisotropy, the conductivity needs to be generalized as a tensor, as discussed in Chapter 5, and the PML formulas designed for anisotropic medium should be used (e.g., Liu, 1999; Collino and Tsogka, 2001) and re-derived in the Chebyshev domain. To extend the PML theory to incorporate the air layer, the upward continuation of the field $\mathbf{L}$ should be used, similarly as discussed in Chapter 4, and the PML formulas designed for Laplace's equation should be used (e.g., Dedek et al., 2002) to be applied to the air layer. Future work is needed.

The application of PML only requires modelling the time evolution of the electric field in the Chebyshev domain. The evaluation of the spatial derivatives at every step is, however, independent of that. There are situations where one may want to use the finite-element or finite-difference method in order to consider more complex geometry or to minimize the computational cost. In such cases, the theory developed in this chapter can be directly transferred to a finite-element or finite-difference time-domain modelling to include PML as the absorbing boundary. The only change is to evaluate the propagation matrix $\mathbf{G}$ in the space domain, instead of the wavenumber domain.

The simulation of the time-domain electric field exactly follows a coupled wave equation in the Chebyshev domain. The similarity between the Chebyshev pair $\{\mathbf{Q},\mathbf{L}\}$ and the EM wave $\{\mathbf{E},\mathbf{H}\}$ has been shown in the theory section (equations 6.8-6.11). I have shown that PML can be applied to modelling the diffusive EM field in the Chebyshev domain. Other EM wavefield modelling techniques can be similarly transferred if necessary.

6.5 Summary

I have presented an extension of the pseudospectral REM method to solve the 3D diffusive electric field in the time domain. The original decoupled, one-step governing equation is modified to a coupled, two-step governing equation by introducing a fictitious magnetic field in the Chebyshev domain. The Chebyshev terms of the diffusive electric field exhibit

similarities with EM wave propagation in a lossless medium, and EM wave modelling techniques can be transferred to the Chebyshev domain in a straightforward way.

I have shown a successful application of PML as the absorbing boundaries in REM modelling. PML is directly implemented in the Chebyshev domain, to attenuate the Chebyshev terms in the absorbing region. The boundary effects are almost invisible in the waves propagating in the Chebyshev domain. The modelling results of the electric field show excellent agreement with the calibration code after turning on PML, which demonstrates the accuracy of the algorithm. The improvement of the far-offset result is clear, which demonstrates the usefulness of PML.

Chapter 7

Implementation of REM: The Concern of Numerical Efficiency

Inversion is essentially an iterative forward modelling process. Depending on the inversion algorithm, a forward modeller could be executed $10^2 - 10^4$ times. It raises the computational efficiency requirement for a forward modelling algorithm in solving real-world, geophysical problems. In this chapter, I discuss my investigation into improving the numerical efficiency of the rapid expansion method (REM). It consists of two parts. First, if the model in question can be simplified to 2D or 1D structures, the computational cost to achieve a 3D solution can be reduced by 1 or 2 orders of magnitude, correspondingly, with a loss of accuracy less than 1%. Second, the computationally-heavy tasks are parallelized by graphic processing units (GPU), and the performance of the algorithm can be improved by a factor of over 100, compared with the serial REM code implemented in C. The significant improvement of numerical efficiency should further generalize the use of REM in real-world problems.

7.1 Introduction

A good forward modelling program should be accurate and fast. If the program is accurate but slow, many optimization algorithms, e.g., stochastic optimization algorithms, may not be applicable due to the computational time. My research starts with the issue of the accuracy of REM modelling. The inclusions of Earth-air interface, anisotropy and perfectly matched layers (PML) provide the accuracy of REM modelling in various situations. The next concern is numerical efficiency. The REM program should be written in a compiled programming language with options to utilize parallel computing to accelerate the computational speed to a necessary level.

This chapter discusses the problems related to the practical concern of REM. It consists of two separate parts. First, if the conductivity model consists only of 1D or 2D structures, the 3D modelling program should be able to simplify the solution accordingly. In practice, the EM source emits a 3D initial field. Modelling a 3D field within a 2D model is also known as a 2.5D problem, which has been widely discussed in previous studies (e.g., Lee and Morrison, 1985; Li and Key, 2007; Key and Ovall, 2011). The 2.5D EM modelling itself is an individual topic apart from 3D or 2D EM modelling. Many industry examples interpret the field data by 2.5D modelling and inversion (e.g., Kong et al., 2008), especially when the EM survey is a 2D line. Regardless of its various practical examples, I consider the 2.5D modelling as a simplified version of 3D modelling, and derive the theory and the code to solve the 2.5D modelling problem accordingly. If the model consists only of 1D or 2D structures, the computational effort to solve a 3D field can be reduced by up to two orders of magnitude, with the loss of accuracy less than 1%. In theory, the 2.5D and 3D modelling by REM should provide the same results. For the consideration of numerical efficiency, the option of 2.5D modelling should further generalize the use of REM in 2D problems due to its reduction in computational time as well as the required memory space.

The second part of this chapter discusses the numerical implementation of REM. Stoffa and Ziolkowski (2019) discuss a parallel computing architecture where three components of the electric field are simulated simultaneously. The program is written in FORTRAN and the parallel computing is implemented by Message Passing Interface (MPI). Through my research study, the REM algorithm has further developed several new functionalities, including the modelling of the air field, anisotropic conductivity and PML. The new functionalities require the algorithm to be modified accordingly, as discussed in chapters 4, 5 and 6, and I have written an entirely new version of the code for the ease of developing the theory. Nevertheless, no matter which functionality is necessary for execution, the REM simulation always follows the recursive updating of Chebyshev terms, which is well suited for parallel computing, because this process does not require matrix multiplication. The computationally intensive tasks are the 3D fast Fourier transforms (FFT) and the dot products among matrices. The algorithm has been accelerated with CPU and GPU parallel computing. GPU computing is particularly interesting in this case because we recognise its excellent performance for computing large-scale FFTs and large-scale matrix arithmetic operations. As a result, the performance of the GPU code, running on a single K80 GPU, can be over 100 times faster than the serial C code, and 20 times faster than the multi-threaded C code with 16 CPU processors. Although, for the time being, GPU memory is a limiting factor for large-scale 3D problems, the combination of GPU computing and 2.5D modelling is ready to be used now to solve real-world problems providing both accuracy and efficiency.

Section 7.2 derives the theory of REM modelling of 1D and 2D conductivity structures with a 3D dipole source. Section 7.3 presents a 2.5D numerical example to validate the theory and the code. Section 7.4 summarizes the implemented REM programs and compares different versions of parallel REM modelling. The performance improvements and the flexibility to choose the solution domain should further generalize the use of REM in 1D, 2D and 3D problems. The theory and the results discussed in this chapter were published in Liu et al. (2019a) and presented at the 2019 European Association of Geoscientists and Engineers (EAGE) annual conference. I have modified the original text, figures, layout and symbols to fit the style of the thesis.

7.2 Extension to 1D and 2D Model Space with a 3D Source

7.2.1 Extension to 2D conductivity structure

In certain problems, a 3D conductivity structure can be simplified to 2D model space if one wants to assume the material properties are unchanged along the strike direction. If so, the computational cost of the 3D solution can be reduced correspondingly. The EM source (an impulsive electric dipole being considered throughout the thesis) emits a 3D field. The 2D model space and the 3D EM source add up to a 2.5D problem, which has been discussed extensively by finite-difference and finite-element solutions (e.g., Lee and Morrison, 1985; Li and Key, 2007; Key and Ovall, 2011). Since the conductivity is constant along the strike direction, there is no need to solve all the strike wavenumber components. Instead, a few of them spaced logarithmically from the DC to the Nyquist are sufficient to retrieve the other wavenumbers via interpolation. Therefore the 2.5D model can easily be one order of magnitude faster than the corresponding 3D run, as usually around 30 wavenumbers (Key and Ovall, 2011) are sufficient whereas in a 3D problem hundreds of spatial nodes are required. This section explains the 2.5D transient EM modelling by REM.

The main strategy of 2.5D EM modelling is to simulate a series of 2D wavefield in the strike wavenumber domain, and then interpolate the other required wavenumbers and convert the field back to the spatial domain. The solution generally takes three steps:

1. initialize a series of 2D wavefield $\tilde{\mathbf{E}}(x,k_y,z)$ with a set of k_y values spaced logarithmically covering the wavenumber range from the DC to the Nyquist;

2. solve a series of $x-z$ plane 2D modelling problems by REM;

3. interpolate the values of $\tilde{\mathbf{E}}(x,k_y,z)$ for the rest of the wavenumbers and convert the electric field back to $\mathbf{E}(x,y,z)$.

Modelling by REM is flexible between the space and wavenumber domains, as the evolution of the field in the Chebyshev domain is independent of the domain. The updating of the terms can be carried out in the domains of (k_x, k_y, k_z), or (k_x, k_y, z), or (x, k_y, z) or (x, y, z), to simulate the field considering the conductivity variation in a homogeneous, 1D layered, 2D, or 3D model, respectively, with the propagation matrix $\mathbf{G}$ modified accordingly. For instance, for the 2.5D modelling, the electric field $\tilde{\mathbf{E}}(x, k_y, z, t)$ is approximated by the Chebyshev terms as

$$\tilde{\mathbf{E}}(x, k_y, z, t) \approx \sum_{k=0}^{M} b_k \tilde{\mathbf{Q}}_k(x, k_y, z, t), \tag{7.1}$$

where $\tilde{\mathbf{Q}}$ denotes the Chebyshev terms in the strike wavenumber domain,

$$\tilde{\mathbf{Q}}(x, k_y, z) = \tilde{Q}_x(x, k_y, z)\mathbf{u}_x + \tilde{Q}_y(x, k_y, z)\mathbf{u}_{k_y} + \tilde{Q}_z(x, k_y, z)\mathbf{u}_z \tag{7.2}$$

and the weights b_k are the modified Bessel function as given by equation 3.11. The first Chebyshev term, $\tilde{\mathbf{Q}}_0$, is the initial field $\tilde{\mathbf{E}}_0$ and it needs to be solved analytically in the strike wavenumber domain to incorporate the 3D dipole source. I take the Fourier transform of the initial field in the 3D spatial domain (equations 3.36 - 3.38) along the y-direction, and the initial field $\tilde{\mathbf{E}}_0$ in the strike wavenumber domain (x, k_y, z) is solved as (Appendix B):

$$\tilde{E}_x(x, k_y, z, t) = \frac{Ids}{4\pi\sigma t} \exp\left(-\theta^2(x^2 + z^2) - \frac{{k_y}^2}{4\theta^2}\right)(-4\theta^4 z^2 + 2\theta^2 + {k_y}^2), \tag{7.3}$$

$$\tilde{E}_y(x, k_y, z, t) = -i\frac{Ids\theta^2}{2\pi\sigma t} \exp\left(-\theta^2(x^2 + z^2) - \frac{{k_y}^2}{4\theta^2}\right)xk_y, \tag{7.4}$$

$$\tilde{E}_z(x, k_y, z, t) = \frac{Ids\theta^4}{\pi\sigma t} \exp\left(-\theta^2(x^2 + z^2) - \frac{{k_y}^2}{4\theta^2}\right)xz. \tag{7.5}$$

Therefore the Chebyshev terms can be initialized and recursively updated as

$$\tilde{\mathbf{Q}}_0 = \tilde{\mathbf{E}}_0, \tag{7.6}$$

$$\tilde{\mathbf{Q}}_1 = \frac{1}{b}\tilde{\mathbf{G}}\tilde{\mathbf{Q}}_0 + \tilde{\mathbf{Q}}_0, \tag{7.7}$$

$$\tilde{\mathbf{Q}}_{k+1} = \frac{2}{b}\tilde{\mathbf{G}}\tilde{\mathbf{Q}}_k + 2\tilde{\mathbf{Q}}_k - \tilde{\mathbf{Q}}_{k-1}, \tag{7.8}$$

with the propagation matrix $\tilde{\mathbf{G}}$ defined in the strike wavenumber domain (x, k_y, z) as

$$\tilde{\mathbf{G}}\tilde{\mathbf{Q}}_k = -\frac{1}{\mu_0}\boldsymbol{\sigma}^{-1}\mathrm{FT}^{-2}_{(x,z)}[\tilde{\mathbf{D}} \cdot \mathrm{FT}^{2}_{(x,z)}[\tilde{\mathbf{Q}}_k]]. \tag{7.9}$$

In equation 7.9, the differential matrix $\tilde{\mathbf{D}}$ is the same matrix as given in equation 3.27. The conductivity tensor $\boldsymbol{\sigma}$ contains $n_x \times n_z$ spatial grids, where each grid can have one to four elements defined, to consider the conductivity from isotropic to TTI anisotropic case, as discussed in Chapter 5.

The eigenvalues of the propagation matrix $\tilde{\mathbf{G}}$ in 2.5D modelling can be solved following exactly the same process as in 3D modelling, where the maximum absolute eigenvalue b is given in equations 3.33 and 5.11. Nevertheless, the maximum strike wavenumber k_y in equations 3.33 and 5.11 is dependent on the grid spacing Δy ($k_{y,Nq} = \pi/\Delta y$), whereas now in 2.5D modelling the maximum k_y is defined explicitly. I set the maximum k_y to be the same as the Nyquist wavenumber along the x-direction, that is

$$k_{y,max} = k_{x,Nq} = \pi/\Delta x, \tag{7.10}$$

and compute the corresponding b and M to truncate the Chebyshev terms. As shown by Key and Ovall (2011), a logarithmic spaced set of around 30 ky values from 10^{-4} to the Nyquist is sufficient to retrieve the other required wavenumbers via interpolation. That is, equation 7.1 needs to be evaluated around 30 times, to solve the field $\tilde{\mathbf{E}}_(x,k_y,z,t)$ with different strike wavenumber components. However, each evaluation is totally independent of the others, and all the strike wavenumber components $\tilde{\mathbf{E}}_(x,k_y,z,t)$ can be solved simultaneously. It is an embarrassingly parallel process and highly desirable when parallelizing the code.

The initial field shown in equations 7.3-7.5 considers the impulsive dipole with an infinitesimal length ds. In practice, the dipole source being considered may have a finite length, and the excited initial field needs to be solved again in the space domain and the strike wavenumber domain. Considering an x-directed finite-length dipole source located from X_1 to X_2 on the x-axis, the space-domain electric field is solved by Ziolkowski and Taylor (2010). I solve the strike-wavenumber-domain initial field by taking the Fourier transform of the space-domain solution along the y-axis, as (Appendix B):

$$\begin{aligned}\tilde{E}_x(x,k_y,z,t) = \frac{I}{8\pi^{1/2}\sigma t\theta}\exp(-\theta^2 z^2 - \frac{{k_y}^2}{4\theta^2})(4\theta^4 z^2 - 2\theta^2 - {k_y}^2)[\mathrm{erf}(\theta(x-X_2)) \\ - \mathrm{erf}(\theta(x-X_1))],\end{aligned} \tag{7.11}$$

$$\tilde{E}_y(x,k_y,z,t) = -i\frac{Ik_y}{4\pi\sigma t}\exp(-\theta^2 z^2 - \frac{{k_y}^2}{4\theta^2}))(e^{-\theta^2(x-X_2)^2} - e^{-\theta^2(x-X_1)^2}), \tag{7.12}$$

$$\tilde{E}_z(x,k_y,z,t) = \frac{Iz\theta^2}{2\pi\sigma t}\exp(-\theta^2 z^2 - \frac{{k_y}^2}{4\theta^2}))(e^{-\theta^2(x-X_2)^2} - e^{-\theta^2(x-X_1)^2}). \tag{7.13}$$

Depending on the type of EM data, one can choose the appropriate set of equations to initialize the 2.5D modelling by REM. The inclusion of the Earth-air interface, anisotropy and perfectly matched layers can be extended to the strike wavenumber domain (x,k_y,z) following a procedure similar to that discussed in Chapter 4, 5 and 6.

7.2.2 Extension to 1D conductivity structure

If the conductivity model is considered to be a 1D layered structure, the computational effort to solve the 3D field by REM can be further reduced. Since the conductivity $\boldsymbol{\sigma}$ is invariant in the horizontal directions, the Chebyshev terms can be initialized and updated in the horizontal wavenumber domain (k_x,k_y,z). Following the same procedure for the 2.5D modelling and 3D modelling process, the objective is to approximate the electric field $\tilde{\mathbf{E}}(x,k_y,z)$ by a series of Chebyshev terms

$$\tilde{\mathbf{E}}(k_x,k_y,z,t) \approx \sum_{k=0}^{M} b_k \tilde{\mathbf{Q}}_k(k_x,k_y,z,t), \tag{7.14}$$

where $\tilde{\mathbf{Q}}$ denotes the Chebyshev terms in the horizontal wavenumber domain,

$$\tilde{\mathbf{Q}}(k_x,k_y,z) = \tilde{Q}_x(k_x,k_y,z)\mathbf{u}_{k_x} + \tilde{Q}_y(k_x,k_y,z)\mathbf{u}_{k_y} + \tilde{Q}_z(k_x,k_y,z)\mathbf{u}_z. \tag{7.15}$$

I take the Fourier transform of equations 7.3-7.5 along the x-direction, to solve the initial field $\tilde{\mathbf{E}}_0$ in the horizontal wavenumber domain (k_x,k_y,z) as (Appendix B)

$$\tilde{E}_x(k_x,k_y,z,t) = \frac{Ids}{4\pi^{1/2}\sigma t\theta}\exp\left(-\frac{{k_x}^2}{4\theta^2} - \frac{{k_y}^2}{4\theta^2} - \theta^2 z^2\right)\left(-4\theta^4 z^2 + 2\theta^2 + {k_y}^2\right), \tag{7.16}$$

$$\tilde{E}_y(k_x,k_y,z,t) = -\frac{Ids}{4\pi^{1/2}\sigma t\theta}\exp\left(-\frac{{k_x}^2}{4\theta^2} - \frac{{k_y}^2}{4\theta^2} - \theta^2 z^2\right)k_x k_y, \tag{7.17}$$

$$\tilde{E}_z(k_x,k_y,z,t) = -i\frac{Ids\theta}{2\pi^{1/2}\sigma t}\exp\left(-\frac{{k_x}^2}{4\theta^2} - \frac{{k_y}^2}{4\theta^2} - \theta^2 z^2\right)k_x z. \tag{7.18}$$

The initial field defined in equations 7.16-7.18 allows the updating of Chebyshev terms in the horizontal wavenumber domain (k_x,k_y,z). The updating is the same recursive process as shown in equations 7.6-7.8, except that the propagation matrix $\tilde{\mathbf{G}}$ in the horizontal wavenumber domain (k_x,k_y,z) is defined as

$$\tilde{\mathbf{G}}\tilde{\mathbf{Q}}_k = -\frac{1}{\mu_0}\boldsymbol{\sigma}^{-1}\mathrm{FT}^{-1}_{(z)}[\tilde{\mathbf{D}}\cdot\mathrm{FT}_{(z)}[\tilde{\mathbf{Q}}_k]]. \tag{7.19}$$

Equation 7.14 needs to be solved for a set of horizontal wavenumbers (k_x, k_y), where k_x and k_y are spaced logarithmically. Similar to the 2.5D modelling, each evaluation of $\tilde{\mathbf{E}}(k_x, k_y, z, t)$ is independent, and different wavenumber components can be solved simultaneously and then combined to retrieve the electric field $\mathbf{E}(x, y, z, t)$ in the spatial domain via 2D inverse FFT. Therefore, the time-domain electric field excited by a 3D dipole source is solved in a 1D model, which can give another order of magnitude improvement in numerical efficiency.

7.3 Numerical Results: A 2.5D Example

In this section, I present numerical tests to demonstrate the theory of 2.5D modelling by REM and the correctness of the code. Similar tests demonstrating the 1D solution are not shown to avoid the verbosity. The 2.5D REM solution is implemented in MATLAB and checked against the 3D MATLAB code. The 2D conductivity structure is illustrated in Figure 7.1, with its values invariant along the y-direction. The 3D modelling uses $128 \times 128 \times 128$ nodes with 10 m spacing along the x-, y-, and z-direction, respectively. The 2.5D modelling uses 128×128 nodes along the x- and z-direction, and uses 12~30 nodes along the strike wavenumber direction. The initial field is built with $t_0 = 10^{-3}$ s after some preliminary tests. No extra absorbing boundary is applied in this example.

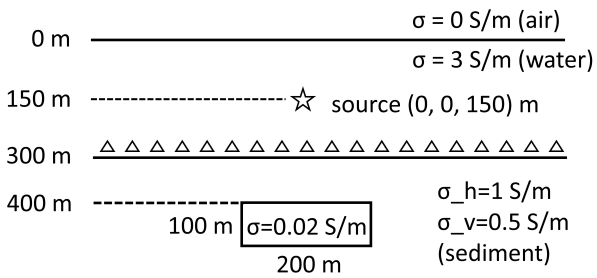

Fig. 7.1 Configuration of the 2D conductivity model. The source is located 150 m below the Earth-air interface and the receiver line is located on the seabed, 145 m below the source. Conductivity is invariant along the y-direction.

The strike wavenumber used by the 3D modelling is a discrete series of k_y values starting from $2\pi/n_y\Delta y$, which is approximately 0.0049 in this case, excluding the direct current (DC) component (where $k_y = 0$). For the 2.5D modelling, I select 12~30 k_y values, spaced logarithmically from 10^{-3} to the Nyquist wavenumber, plus the DC component (where

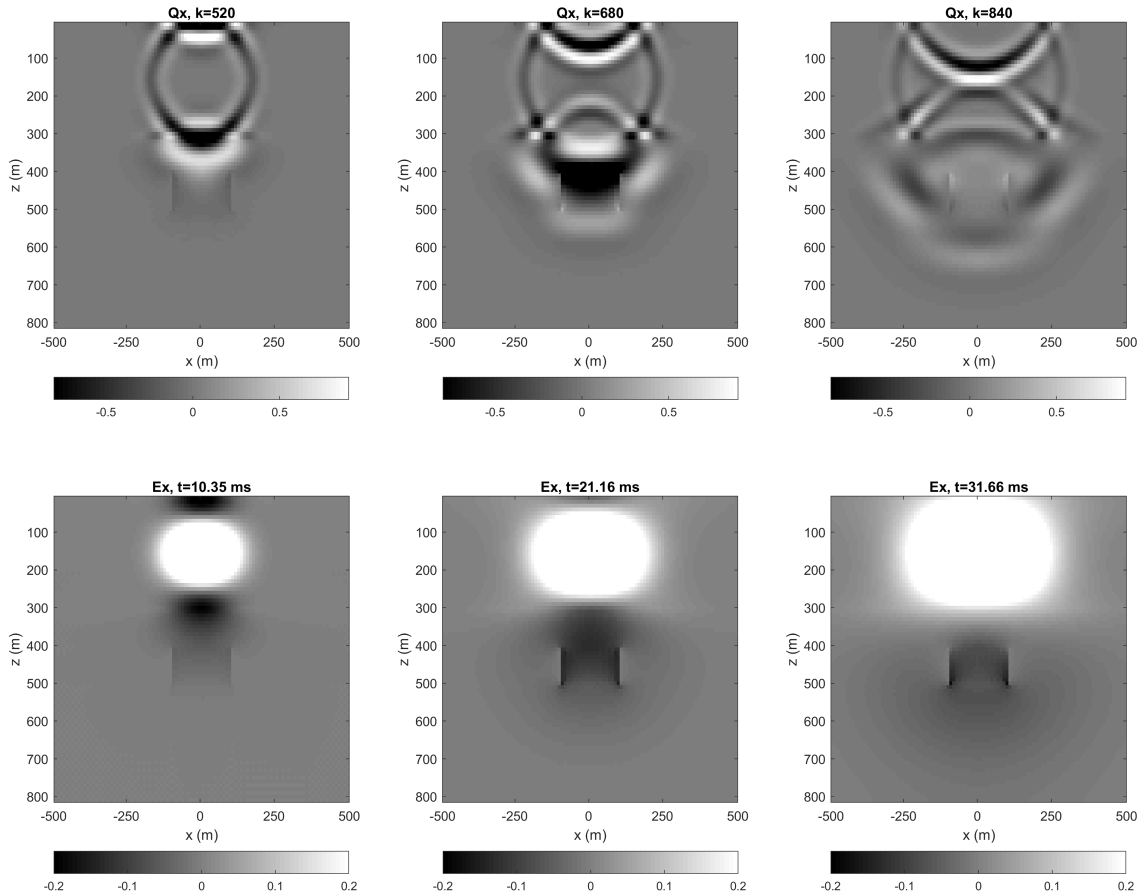

Fig. 7.2 The x-z plane snapshots of Q_x and E_x by 2.5D REM modelling. The top row shows the Chebyshev terms Q_x with the order k = 520, 680, and 840. The bottom row shows the electric field E_x at times t = 10.35, 21.16, and 31.66 ms.

$k_y = 0$), to cover the necessary range of k_y. After the selected $\tilde{\mathbf{E}}$ fields are derived in the strike wavenumber domain (x, k_y, z), the other required strike wavenumbers are obtained by a spline interpolation, and then transformed back to the 3D spatial domain via an inverse Fast Fourier transform (IFFT) along the y-direction. The 2.5D modelling code is examined from two perspectives, the wavefield snapshots and the accuracy of the modelling results.

Figure 7.2 shows the wavefield snapshots generated by the 2.5D modelling code using 30 wavenumbers. In the snapshots of the Chebyshev terms Q_x, the reflections of the wavefield from the air-water interface and the seabed can be clearly observed. The effect of the 3D resistor is illustrated by the sharp variation of the Q_x and E_x field with its boundaries clearly outlined. Numerical dispersion is hardly observed in the 2.5D modelling example.

Figure 7.3 examines the amplitude of E_x along the receiver line. The benchmark is the 3D REM modelling code, the accuracy of which has been demonstrated in the previous

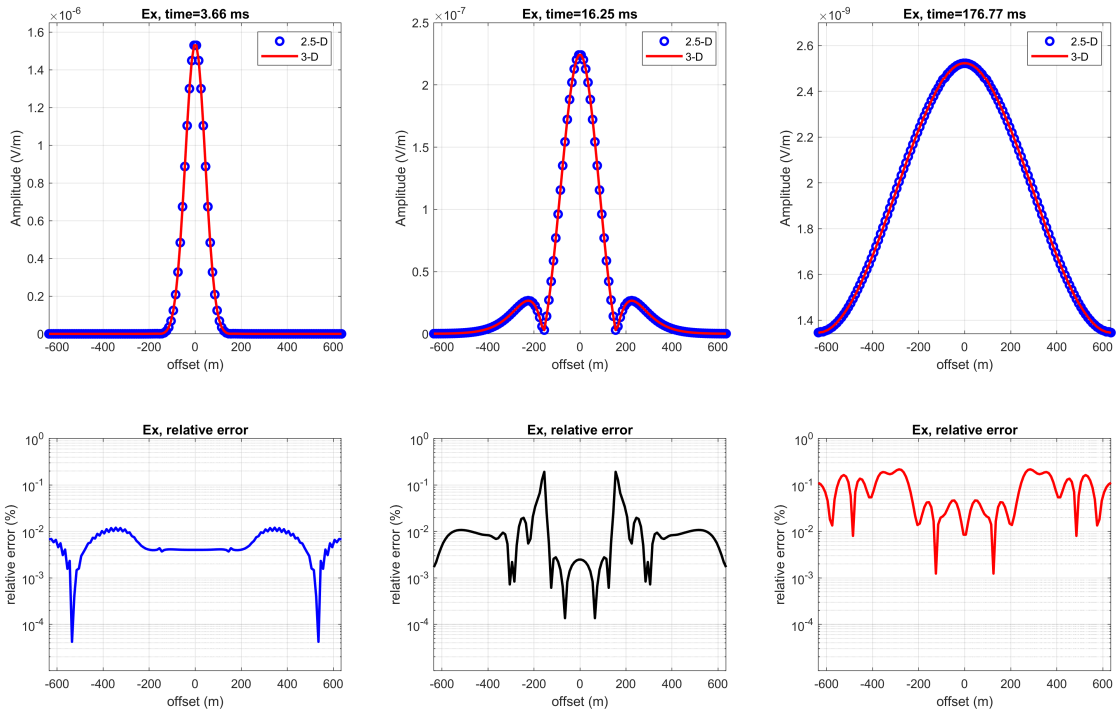

Fig. 7.3 Amplitude comparison between the 2.5D and 3D REM modelling. The top row shows the absolute amplitude of the inline component E_x, and the bottom row shows the relative difference between them along the receiver line. This example uses 30 k_y slices.

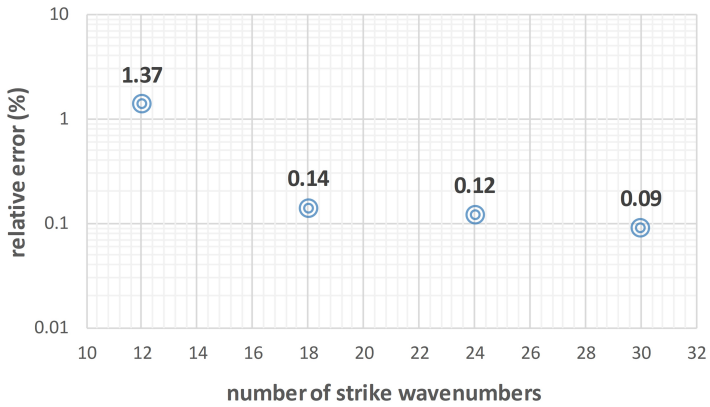

Fig. 7.4 Relative error of the 2.5D modelling results versus the number of k_y being used during the modelling. Relative errors are computed by taking the average along the receiver line at time t = 176.77 ms.

chapters. As shown in Figure 7.3, the 2.5D results show excellent agreement with the 3D code at early, mid and late times with the relative errors all below 1%. The average relative

difference at late times is approximately 0.1%. Figure 7.4 shows the variation of the relative difference versus the strike wavenumber being used during the 2.5D modelling. The average relative error, calculated at the late-time, far-offset results, increases up to 1.4 percent when only 12 k_y values are used for the 2.5D modelling. Based on Figure 7.4, using 18 to 24 strike wavenumbers may be enough to obtain the required accuracy. Comparing with 128 spatial grids in the 3D modelling, the 2.5D modelling reduces the computational effort by a factor of 5 to 7. In addition, the factor of improving the numerical efficiency is expected to grow when a bigger model is considered, since the strike wavenumbers required in the 2.5D modelling are distributed logarithmically. This example demonstrates the correctness of the 2.5D modelling code and the numerical efficiency it can obtain when a 2D conductivity model is used to represent the subsurface.

7.4 Parallel Implementation: the GPU-Accelerated REM Modelling

In this section, I discuss the numerical implementation of the REM algorithm and present tests of its numerical efficiency. The REM algorithm is first written in MATLAB for the convenience of coding during the research phase of the theory. After that, I translate the MATLAB code to an equivalent C code for computational speed. The major computational burden of REM comes from the calculation of the propagation matrix at every step, for example, considering an anisotropic full space 3D modelling,

$$\mathbf{G}\mathbf{Q}_k = -\mu_0^{-1}\boldsymbol{\sigma}^{-1}\mathrm{FT}^{-3}_{x,y,z}[\tilde{\mathbf{D}}\cdot\mathrm{FT}^{3}_{x,y,z}[\tilde{\mathbf{Q}}_k]], \tag{7.20}$$

where $\tilde{\mathbf{D}}$ is the differential matrix containing all the spatial derivatives transformed into the 3D wavenumber domain. The numerical workflow is shown in Algorithm 1 (below). The computational task consists mainly of two parts: 1) the dot products of the 3D matrices and 2) the 3D FFTs. The matrix computation is embarrassingly parallel (also called perfectly parallel), since no inner product of matrices is involved. That is, considering a 3-component field $\mathbf{Q}$ of spatial size $n_x \times n_y \times n_z$ nodes, the tasks are the arithmetic operations on all the $3 \times n_x \times n_y \times n_z$ nodes, and each node is totally independent of all the others. Therefore, there is no extra difficulty to distribute the big problem into a number of parallel tasks. The computation of the multi-dimensional FFT, in contrast, is not embarrassingly parallel. The parallelization of FFT is undertaken by the parallel version of existing FFT libraries to achieve optimal efficiency.

Parallel implementation of REM has been investigated in both CPU and GPU computing. For the parallelization with CPU processors, I have written the algorithm as a multi-threaded C code using Open Multi-Processing (OpenMP). The 3D FFTs are handled by the multi-threaded FFTW package (Frigo and Johnson, 2005). The matrix computation is parallelized whenever necessary along all the dimensions (refer to Table 7.1). The performance of the code is tested in a homogeneous half space ($\sigma = 3$ S/m) with $128 \times 256 \times 256$ nodes and with a 200 ms time period being simulated which requires approximately 650 Chebyshev terms. Figure 7.5 shows the performance of the code as the number of processors is increased. The run time decreases with the number of processors as expected, but the speed-up factor reaches approximately only 4 with 16 processors, i.e., an efficiency of 0.25. The low parallel efficiency is mainly due to the calculation of FFTs, since the task is not embarrassingly parallel, as well as the synchronization of the threads at the barriers between FFTs and matrix dot products. As shown by Algorithm 1, there are 3 barriers for full-space modelling during step 2a to compute the propagation matrix $\mathbf{GQ}_k$. There are 7 barriers for half-space modelling when upward continuation and the complementary Chebyshev series $\mathbf{L}$ are required.

Another approach to solving this problem is to use GPU acceleration to compute the matrix dot products and FFTs. Computation by GPU has been recognised for its advantage of calculating massive parallel jobs (Nickolls and Dally, 2010). In addition, the GPU-accelerated FFT library, CUDA Fast Fourier Transform (cuFFT) developed by NVIDIA, has been reported to have excellent performance especially when computing large-scale FFTs (Abdellah et al., 2012). Therefore, GPU computing can be a highly attractive option in accelerating the REM algorithm. To demonstrate this, I have implemented the algorithm as a CUDA C code, and the numerical flow is shown in Algorithm 2. The computational tasks in both implementations (step 2) are the same. However, the 3D FFTs are now undertaken by the cuFFT library and the spatial grids and the nested loops are distributed to the GPU threads whenever possible (Table 7.1). The GPU-accelerated code is tested on a K80 GPU with different sizes of model and the results are shown in Figure 7.5. For the model size of $256 \times 256 \times 256$ nodes, the performance of the CUDA C code is over 100 times faster than the serial C code, and 20 times faster than the multi-threaded C code with 16 processors. The improvement in speed is very impressive. Furthermore, the speed-up factor increases with the size of the model, which indicates the potential of GPU computing for large-scale problems.

To better understand the improvement of the GPU-accelerated code, Table 7.2 gives a breakdown of functions which have used most of the computational time. As discussed above, the two main computational tasks are the 3D FFTs (and IFFTs) and the 3D matrix operations. Depending on the specific modelling job, the two tasks can occupy over 90% of

time. The serial C code, multi-threaded C code and CUDA C code are compared using the same numerical test (a homogeneous half space ($\sigma = 3$ S/m) with $128 \times 128 \times 128$ nodes and a 200 ms simulation time). The multi-threaded C code is timed using the function *omp_get_wtime*(), and the CUDA C code is timed using the functions *cudaEventRecord*() and *cudaEventElapsedTime*(). As shown in Table 7.2, with running on 16 processors, the multi-threaded C code reaches a speed-up factor of 5.1 for computing the 3D FFTs, and a speed-up factor of 10.7 for the 3D matrix operations. In contrast, given the exactly same computational tasks, the CUDA C code reaches a speed-up factor of 32.2 for the 3D FFTs, and a speed-up factor of 33.3 for the 3D matrix operations. As a result, for this example, the speed of the CUDA C code is about 5 times of the multi-threaded C code, and about 33 times of the serial C code. And this factor is expected to grow with the size of the model, as indicated by Figure 7.5. This example demonstrates again that the performance of the CPU-accelerated code is mainly limited by the 3D FFTs, whereas the GPU-accelerated code performs almost equally well for both parallel computing jobs, which ends up an impressive improvement of speed.

Table 7.1 Parallel implementation of the computational tasks

Parallel Implementation			
steps	computational task	C + OpenMP	CUDA C
2a(i); 2a(iii)	3D FFTs	multi-threaded FFTW	cuFFT
2a(ii); 2a(iv); 2b; 2c	matrix dot product	CPU threads	GPU threads

Note that the computational time and the numerical efficiency shown in Figure 7.5 and Table 7.2 only considers the computation of Chebyshev terms, i.e., step 2 in both algorithms. The time of initializing the program (step 1) is however not included in both cases. Ideally, initializing the program should happen only once during an iterative forward modelling process. It is particularly important to satisfy this condition when using GPU computing, because data transfer between CPU and GPU memory (Algorithm 2, step 1e and 3a), which is an exclusive step for the use of GPU, is very time consuming. In some cases the time to transfer data can be longer than the computational time itself. Therefore, to achieve the improvement of efficiency as shown in Figure 7.5, and to optimize the benefits from GPU computing, expensive transfers (Algorithm 2, step 1e and 3a) should happen only once, no matter how many times the forward model (Algorithm 2, step 2) needs to be called.

Since data transfer between CPU and GPU is not involved in the iteration, all the variables need to be pre-allocated and kept in the GPU cores during the iterative forward modelling. When considering large-scale 3D problems, the GPU memory can be a limiting factor for the time being. Considering the GPU resources I can access from Eddie (The Edinburgh

Algorithm 1 Numerical structure of the REM modelling program.

1. Initialize the program
   (a) specify the 3D conductivity model with the size of $n_x \times n_y \times n_z$ and the node spacings of Δx, Δy, and Δz; specify the time axis t to be recorded; specify the position of the source and receivers;
   (b) allocate memory space of all the variables in CPU;
   (c) compute the initial field $\mathbf{Q}_0$; compute the weights b_k; compute the order M which guarantees the convergence;
2. For the Chebyshev polynomial order $k = 0$ to M:
   (a) Compute $\mathbf{GQ}_k$
      i. 3D FFT of $\mathbf{Q}_k \rightarrow \tilde{\mathbf{Q}}_k$
      ii. For x in $\{1, ..., n_x\}$, For y in $\{1, ..., n_y\}$, For z in $\{1, ..., n_z\}$, For d in $\{1, 2, 3\}$, compute the double curl of $\tilde{\mathbf{Q}}_k \rightarrow \tilde{\mathbf{C}}(x,y,z,d) = \tilde{\mathbf{D}}(x,y,z,d) \cdot \tilde{\mathbf{Q}}(x,y,z,d)$
      iii. 3D IFFT of $\tilde{\mathbf{C}} \rightarrow \mathbf{C}$
      iv. $\mathbf{GQ}_k = -\boldsymbol{\sigma}^{-1}\mathbf{C}/\mu_0$
   (b) Compute the next Chebyshev term by its recursive relation $\rightarrow \mathbf{Q}_{k+1}$
   (c) weighted summation $\mathbf{E}(t) = \mathbf{E}(t) + b_k\mathbf{Q}_k$
3. Output
   (a) Output $\mathbf{E}(t)$;
   (b) Clear the memory space in CPU;

Compute and Data Facility Linux Compute Cluster), a single K80 GPU has a memory limit of 16 GB, and a single Titan-X GPU has 32 GB. In contrast, 3D modelling with $1024 \times 1024 \times 1024$ nodes and a regular node spacing of 10 m in x-, y-, and z-directions, considering roughly a 10km $\times$ 10km $\times$ 10km 3D field, requires approximately 120 GB memory for a half-space, REM modelling program. This is clearly beyond the memory capability of GPU. In that case, a hybrid CPU-GPU parallel computing system is required to distribute the tasks across multiple GPU processors to fit the memory, and the communication among multiple GPUs requires data transfer between CPUs and GPUs during the iteration. Since the time-consuming data transfer becomes inevitable in a hybrid system, there is no evidence for the moment that the GPU computing is still highly beneficial in that case, especially when an elegant parallel implementation purely based on CPU processors has been developed by Stoffa and Ziolkowski (2019). They use Message-Passing Interface (MPI)

Algorithm 2 Numerical structure of the GPU-accelerated REM program.

1. Initialize the program
   (a) specify the 3D conductivity model with the size of $n_x \times n_y \times n_z$ and the node spacings of Δx, Δy, and Δz; specify the time axis t to be recorded; specify the position of the source and receivers;
   (b) allocate memory space of the necessary variables in CPU;
   (c) compute the initial field $\mathbf{Q}_0$; compute the weights b_k; compute the order M which guarantees the convergence;
   (d) allocate memory space of the necessary variables in GPU;
   (e) Transfer the variables from CPU to GPU;
2. For the Chebyshev polynomial order $k = 0$ to M, undertake the same computational tasks as shown in step 2, Algorithm 1 with GPU processors;
3. Output
   (a) Transfer the results from GPU to CPU;
   (b) Clear the memory space in CPU and GPU;

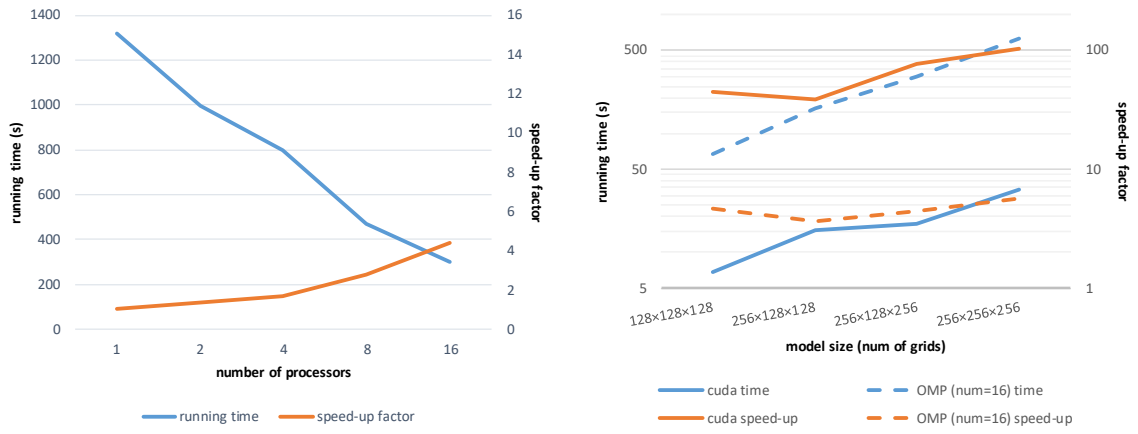

Fig. 7.5 Comparison between the GPU- and CPU-accelerated C code. (Left) Run time and speed-up test with the multi-threaded C code with increasing number of processors. (Right) Comparison between the GPU- and CPU-accelerated C code for different sizes of models. The GPU code runs with a single K80 GPU and the OpenMP C code runs with 16 processors.

and OpenMP to distribute the tasks and simulate the three components of the Chebyshev terms simultaneously. The communication among CPU processors via MPI is much more

efficient and therefore preferable for the moment when considering large-scale, 3D problems which are not easy to fit into the GPU cores.

Table 7.2 Comparison between the GPU- and CPU-accelerated code

	Computational time (s)		
Tasks	serial C	C + OpenMP (16 processors)	CUDA C
3D FFTs	231.98	45.55	7.20
matrix operations	121.46	11.40	3.65
total	353.44	56.95	10.85

Nevertheless, the limitation of GPU memory for the time being cannot deny the fact that GPU computing is highly suitable for the computational tasks of the pseudospectral REM modelling. Although the 3D modelling problem may not be fully ready for the utilization of GPU, the 2.5D modelling problem, however, does not suffer the memory limitation as stringently as the 3D case and therefore can already benefit from the GPU acceleration in many situations. For example, considering a 2.5D modelling problem with the same inline offset as the previous 3D field, it requires 1024×1024 nodes with the same node spacing in x- and z-directions per each strike wavenumber k_y, and in total around 32 k_y values are needed. This results in approximately 6.1 GB memory space, where a single K80 GPU is capable of doing the job. The resultant solution considers a 2D 10km $\times$ 10km variation of conductivity, which should be useful in many real-world applications.

In order to acquire the numerical efficiency from GPU computing, as well as considering the practical usefulness of the code in real-world problems, the 2.5D REM modelling algorithm has been written in a C program and accelerated by GPU computing with CUDA C. The CUDA C code is then wrapped as a Python library with a CPython wrapper, so that the 2.5D REM modelling code is available in Python for the ease of use. More importantly, the access to the platform of Python enables the REM program to be combined with many useful open-source libraries in Python to undertake various geophysical jobs. A non-exhaustive list of potential useful Python libraries includes *segyio* for reading and writing segy files; *scipy* for signal processing and inversion; *numpy* for manipulating the data as matrices; *sklearn* for utilizing machine learning algorithms and *keras* for utilizing neural-network based learning algorithms. The Python library of REM modelling is named *curem* with three functions callable, $curem.cudainit()$, $curem.rem()$, and $curem.remfree()$, executing the jobs as described in Algorithm 2, steps 1, 2, and 3, respectively. During an iterative forward modelling process, the initialization function $curem.cudainit()$ and the clean-up function $curem.remfree()$ only need to be called once, at the start and at the end of the program. The function $curem.rem()$ needs to be called iteratively following the manner of the specific

optimization algorithm, to simulate the electric field based on an iteratively updated, 2D conductivity model.

I have developed the REM modelling algorithm in different programming languages with different functionalities. Most of the theories are derived and validated in MATLAB first due to the ease of coding. Part of the modelling functions are implemented in C for the investigation and optimization of computational speed. The final version of the REM program is a Python-wrapped, CUDA C modelling program which is designed to be fast, easy to use, and easy to be incorporated with other open-source Python libraries. Table 7.3 lists the functions of the REM program available on each programming platform. Due to the limit of time, some functions available on MATLAB have not been transferred to the Python library yet. However, considering a 2D, VTI anisotropic conductivity model as an example, the 3D REM modelling by the MATLAB code can take a few hours to finish. In contrast, with the developed 2.5D modelling and the acceleration by a single GPU card, the Python code takes around 30 seconds to provide the same level of accuracy.

Table 7.3 A summary of the implemented REM modelling functions in different platforms

	Programming platform		
Functionality	MATLAB	C	Python
3D model + 3D source	✓	✓	
2D model + 3D source	✓	✓	✓
1D model + 3D source	✓		
the Earth-air interface	✓	✓	✓
VTI anisotropy	✓	✓	✓
TTI anisotropy	✓		
perfectly matched layers	✓		
CPU acceleration		✓	
GPU acceleration		✓	✓

7.5 Summary

I have extended the theory of REM to solve the 3D time-domain electric field problem with a dipole source in 1D, 2D, and 3D model space. The example run shows that the computational effort can be reduced by an order of magnitude for a 2.5D problem the loss of accuracy less than 1%. In addition, the required memory space is reduced accordingly.

I have implemented and tested different approaches to parallelize the code. The major computational tasks are the fast Fourier transforms and matrix dot products, which are highly suitable for GPU parallel computing. As a result, the GPU accelerated implementation

improves the performance by a factor of over 100, which demonstrates a successful application of GPU computing. The program is wrapped in Python for future use. The significant improvement in numerical efficiency generalizes the use of REM in large-scale, time-domain EM modelling or inversion problems.

Chapter 8

The Way Forward

Due to the time limit of my research, there are several interesting topics which have not been fully studied. This chapter discusses possible future research work. It consists of two parts. The first part suggests future development of REM functionalities that may be useful to further improve the forward modelling. The second part discusses the possible use of REM to undertake inversion of real-world CSEM data.

8.1 Improvements for Future REM Functionalities

Stoffa and Ziolkowski (2019) show the application of rapid expansion method (REM) to solving the 3D transient electric field in an isotropic conductive medium. I extend the theory and add a few more functionalities to the REM modelling algorithm as discussed in Chapter 4, 5, 6 and 7, including 1) the modelling of the air layer response; 2) the inclusion of vertical and tilted transverse isotropic anisotropy; 3) the application of perfectly matched layers (PML) in the Chebyshev domain; 4) the extension of REM to 2.5D modelling and 1D modelling; and 5) the acceleration of the code by GPU parallel computing. All the code has been written from scratch. We have access to the EM data collected from the Harding Field in the North Sea (refer to Ziolkowski et al. 2010), which can be a field dataset to prove the concept. Therefore, most of the synthetic models shown in my thesis are designed to consider a shallow marine CSEM environment to demonstrate the ability of REM. Due to the time limit of the project, there are more interesting topics found through my research which have not been fully studied. They should further broaden the use of REM in various other environments with more modelling options, if possible. Most of them have been discussed in the previous chapters. This section revisits the key aspects and gives recommendations for future REM functionalities.

8.1.1 Spatial discretization by adaptive grids

The current version of the REM code uses regular grids to discretize the 3D subsurface. The advantages and limitations of regular spatial sampling have been discussed in section 4.4 and 5.2.3. The Fourier pseudospectral estimation of spatial derivatives is very efficient, simple to implement, and very accurate, as demonstrated by the modelling results presented before. Nevertheless, there are certain situations where adaptive grids or irregular grids are preferable for a modelling problem. Those situations include 1) the modelling of the source region may require a denser grid sampling; 2) the numerical representation of a complex internal interface may require denser grid sampling; and 3) the truncation of the computational mesh may require coarser grid sampling so that a simple Dirichlet boundary condition can be valid. If a more advanced numerical boundary condition is available, such as PML, we may not need to vary the grid size in the boundary region. But we may still need the adaptive grids to handle the source region and the complex internal interfaces.

As stated before, the spatial discretization of the subsurface is completely independent of REM. REM only concerns the explicit time-stepping of the electric field by the Chebyshev polynomials. This process can be combined with any spatial discretization method. The theories derived in this thesis are completely transferable to a new spatial system. Adaptive grids could be an extra option in the REM modelling code in addition to regular grids.

There are a few options for implementing adaptive grids into the REM system. The closest form may be the work presented by Fornberg (1988). The author shows that by introducing a mapping function to the Fourier pseudospectral estimator, regular discretization can be transformed to the designed spatial system which locates the complex internal interfaces accurately. The theory is demonstrated by an elastic wave modelling example. Considering the REM case, the extra effort is to define and implement the mapping function during the Chebyshev recursion. The eigenvalues need to be updated accordingly based on the formulas given in chapter 5. A more complicated version than that is to implement an adaptive spectral element method to discretize the earth. The spectral element method has been demonstrated by, e.g., Komatitsch and Vilotte (1998) for seismic modelling, and by Zhou et al. (2017) for frequency-domain CSEM modelling. The spectral element methods maintain the high-order spatial accuracy and allows the numerical representation of complex interfaces. The adaptive mesh for the spectral element method has been shown by, e.g., Mavriplis (1994).

Finite-difference and finite-element methods are also well-known solutions to implement adaptive numerical grids. Extensive research studies have demonstrated the use of finite-difference grids (e.g., Commer and Newman 2004) and finite-element grids (e.g., Um et al. 2010) in time-domain CSEM modelling. Finite-order approximation of spatial derivatives may introduce numerical dispersion. Nevertheless, they are still broadly applied because

of their simplicity and to some extent their accuracy. One can always increase the order of spatial operator to increase the desired accuracy. For example, Mittet (2017) shows that the finite-difference operator of order 12 - 14 can reach similar accuracy to that obtained with a pseudospectral estimator, considering a single frequency component (45 Hz) in that example. Therefore finite-difference and finite-element methods remain interesting options to handle the spatial discretization as long as the numerical dispersion can be controlled below the required accuracy threshold.

REM can cope with any spatial discretization of the subsurface. It is an interesting topic to investigate which system works best with REM to implement irregular numerical grids.

8.1.2 Numerical boundary conditions

Two types of numerical boundary problems have been discussed in the thesis: the treatment of the Earth-air interface and the truncation of the computational mesh. The modelling of the air response is achieved by an upward continuation in the Chebyshev domain. The discussion in chapter 4 assumes a flat Earth-air interface because we are mainly considering a shallow marine CSEM problem. In land CSEM problems the air response can be removed during the processing step (e.g., Ziolkowski and Wright 2007). Alternatively the handling of the air layer with topography can be found in, e.g., Endo and Noguchi (2002) with a finite-difference solution; as well as in Börner et al. (2015) with a rational Krylov solution. Nevertheless, if the field study focuses on a marine problem, topography of the Earth-air interface can be neglected.

Two options have been tested to truncate the computational mesh in the Chebyshev domain: the Dirichlet boundary condition and the use of perfectly matched layers (PML). PML appears to be attractive. It improves the modelling results at the far offsets significantly, so that the simulation accuracy does not depend on the size of the model and the loss of the medium. Nevertheless, due to the limit of research time, the theory of PML has been developed only for an isotropic medium. Further research is recommended to extend the current Chebyshev-domain PML to consider anisotropic conductivity and the Earth-air interface. The inclusion of anisotropy should be straightforward. It is essentially deriving equations 6.28 - 6.33 again following the same procedure but using the conductivity tensor $\boldsymbol{\sigma}$. The inclusion of the air layer into PML is not that straightforward. By using the upward continuation we are assuming the electric field in the air obeys Laplace's equation. Therefore the PML formulas designed for Laplace's equation (e.g., Dedek et al. 2002) need to be transferred to the Chebyshev domain. Alternatively, a brute-force treatment of the air layer is to use a very small but practical conductivity value to represent the air. For example, Um et al. (2010) use 10^4 ohm-m. In that case the current PML equations can be used directly.

Nonetheless, unnecessary Chebyshev terms are then inevitable to time-step the field in the air, which reduces the numerical efficiency and may not be an elegant solution. Future work is needed.

8.1.3 The shallow source consideration

The shallow source problem has been discussed in section 4.4. The current REM code uses regular grids to discretize the subsurface. It can handle deep marine CSEM modelling problems and shallow marine CSEM modelling problems if the source rests on the seabed during the acquisition. For example, the Harding field data that we have access to are collected with source and receivers resting on the seabed during the acquisition (Ziolkowski et al. 2010). However, there is another type of survey, namely towed streamer EM as developed by Petroleum Geo-Services (PGS) and reported in Anderson and Mattson (2010). The towed streamer EM data are collected in the same way as towed streamer seismic data, with the electric source being towed approximately 10-20 m below the sea surface. Such a survey layout imposes problems for regular grids when the source needs to be located close to the Earth-air interface. Tests using 1D modelling by REM show that a source with depth 20-40 m requires the spatial interval to be approximately 2 m to propagate the field successfully. A grid spacing of 10 m shown in previous numerical examples is able to time-step the field with the source buried more than 80 m approximately below the sea surface. A source shallower than that will cause problems.

For time-domain EM modelling methods, the use of very fine grids is inevitable when modelling the field excited by a shallow source, no matter which spatial discretization method is used. The initial field needs to be calculated at an earlier time, otherwise the initial field will be truncated by the Earth-air interface and resulting in Gibbs oscillations. An earlier and sharper initial field means modelling a field with higher wavenumbers. Liu (1997) indicates the pseudospectral estimator requires at least two numerical grids per shortest wavelength. Mittet (2017) indicates the spatial sampling needs to be 4-5 grid points defined per shortest wavelength or above. These can be used as guidelines when considering the grid size in the source region.

The use of adaptive grids is definitely a potential solution for the shallow source problem, as discussed in section 8.1.1. Alternatively, one can band-limit the spatial frequencies of the Chebyshev terms during the iteration so that the regular spacing can meet the criteria in the source region. A third option is to band-limit the sharp variation of conductivity to mitigate the Gibbs phenomenon. The experiments of band-limiting the field and the model have been discussed in Mittet (2017). I personally recommend the adaptive grid solution since it seems to solve several problems at once.

A direct extension of my work to land CSEM problems requires more specific considerations. In principle, the surface source for land CSEM surveys can be treated as a very shallow source, which has already been discussed in the section above. The only concern is the numerical efficiency: how dense the numerical grids need to be to ensure the convergence of the Chebyshev recursion. Alternatively, one may want to model the EM field without the air response to reduce the computational effort. For example, if the earth's impulse response can be derived (e.g., Wright et al. 2002), and the air response can be removed during the data processing (e.g., Ziolkowski and Wright 2007), the forward modelling job then becomes similar to a deep-marine case, which is capable for the current REM code to undertake. For another example, if the air response has been avoided by measuring the shutting-off of a direct current source, the forward modelling job is again similar to the deep-marine case. However, the initial field needs to be solved analytically with the new source time function in order to initialize the recursion of the Chebyshev terms. Future work is needed.

8.2 Towards the Inversion of CSEM Data by REM

The ultimate goal of our REM forward modelling code is to undertake the inversion of CSEM field data, for instance, the Harding field data. During the last days of this project I have been trying to apply a stochastic method to invert the EM data based on the modelling by the REM code that we have developed. Nevertheless, due to the limitation of research time and computational resources, to the time point this thesis has been written up, I have not obtained solid inversion results that can prove the success of the stochastic inversion and the workflow. Therefore I discuss in this section the potential use of REM for a CSEM inverse problem, and regard this as another area that requires future work and research.

3D inversion examples to construct conductivity models from marine and land CSEM data have been given by, e.g., Commer and Newman (2008), Grayver et al. (2013), Oldenburg et al. (2013), and Zhdanov et al. (2014). A review of inversion algorithms and computational strategies can be found in Avdeev (2005) and Newman (2014). No matter which algorithms are used, the inversion that extracts a conductivity model from EM data can be characterized as a process of iterative forward modelling. An initial, made-up conductivity model is updated until its calculated electromagnetic response fits the data. Through the entire process the data are not changed. The goodness of fit is quantified by an objective function, where a typical L2-norm objective function can be written as

$$\phi(\mathbf{m}) = \frac{1}{2}\|\mathbf{W}(\mathbf{d} - F(\mathbf{m}))\|^2 + \mathbf{R}, \tag{8.1}$$

where $\mathbf{m}$ is the model vector containing all the conductivities and $\mathbf{d}$ is the data vector containing all the EM data; $F(\mathbf{m})$ is the forward modeller, denoting a non-linear process to calculate the synthetic data given a model $\mathbf{m}$; $\mathbf{W}$ is a weighting vector; and $\mathbf{R}$ is the regularization term to either stabilize the iteration process or to apply any designed model constraints (e.g., Constable et al. 1987). The best-fit model, that is, the model $\mathbf{m}$ which gives the minimum value of $\phi(\mathbf{m})$, is regarded as the subsurface model extracted from the data $\mathbf{d}$. Through this process, the accuracy of the forward modeller is essential. In our case, $F(\mathbf{m})$ is the forward modelling by REM. As discussed in the previous chapters, REM is a forward modeller with accuracy promised in both space and time, and therefore we expect the inversion with REM can lead us to a more accurate picture of the true subsurface.

There are two main types of method to find the minimum of $\phi(\mathbf{m})$: gradient-based methods and the stochastic methods. The possibility of combining them with REM are discussed in the following two subsections.

8.2.1 Gradient-based methods

Gradient-based methods minimize the objective function $\phi(\mathbf{m})$ based on its partial gradient with respect to $\mathbf{m}$. The gradient vector g is

$$g = \frac{\partial}{\partial m}\phi(\mathbf{m}) = (\frac{\partial}{\partial m_1}\phi, ..., \frac{\partial}{\partial m_M}\phi)^T, \tag{8.2}$$

where M denotes the length of the model vector. Given an initial model $\mathbf{m}_0$, a necessary condition to find a local minimum of $\phi(\mathbf{m})$ with respect to $\mathbf{m}_0$ is that the gradient vector approaches eventually to a zero vector, that is,

$$g = \mathbf{0}. \tag{8.3}$$

Since we are considering time-domain problems, the data are real numbers and the gradient vector can be derived as

$$g = \mathbf{J}^T\mathbf{W}(\mathbf{d} - F(\mathbf{m})) + \frac{\partial}{\partial m}\mathbf{R}, \tag{8.4}$$

where $\mathbf{J}^T(\mathbf{m})^T$ is the transpose of the sensitivity matrix

$$\mathbf{J}(\mathbf{m}) = \begin{pmatrix} \frac{\partial}{\partial m_1}F_1 & ... & \frac{\partial}{\partial m_M}F_1 \\ ... & ... & ... \\ \frac{\partial}{\partial m_1}F_N & ... & \frac{\partial}{\partial m_M}F_N \end{pmatrix}, \tag{8.5}$$

where N denotes the length of the data vector. Non-linear, gradient-based optimization methods update the model $\mathbf{m}$ at each iteration step

$$\mathbf{m}^{i+1} = \mathbf{m}^i + \delta\mathbf{m}^i, \tag{8.6}$$

and different algorithms use different ways to relate the updating direction of $\mathbf{m}$ to the gradient vector g to obtain $\delta\mathbf{m}^i$. Popular options can be, e.g., Gauss-Newton method, quasi-Newton method, and non-linear conjugate gradient method, etc. The comparison among those methods has been discussed by, e.g., Avdeev (2005) and Newman (2014). Most of the algorithms have been implemented in the *scipy.optimize* library with Python and the Python version REM code can therefore be used to formulate the objective function to be minimized. The only missing part is to derive the explicit solution of the sensitivity matrix $\mathbf{J}$ of the REM operator. One way to solve the matrix $\mathbf{J}$ is to use the adjoint-state method. It needs to find the adjoint operator of REM and to solve an extra linear system. That is, the total price is two times of forward modelling. The method has been explained by, e.g., Avdeev (2005), and Plessix (2006). Future work is required so that gradient-based optimization methods can be applicable with REM.

The appealing feature of gradient-based methods is that compared with global optimization methods, it converges very fast to a local minimum of the error surface, for instance, within 50 iterations. Considering the computational effort, it is almost always the choice when solving large-scale, 3D EM inversion problems, as shown in the papers listed above. Nevertheless, the limitation of a gradient-based method is also well-known. The minimum being found is a local minimum, closest to the initial model, and therefore the inversion results are highly dependent on the initial model. The 3D inversion itself is a highly non-unique problem, that is, different subsurface models can fit the data equally well. In that case, the high-dependency on the initial model means the inversion results can be easily biased. This is the reason that researchers are exploring global optimization methods in geophysical inversions (e.g., Sen and Stoffa 2013).

8.2.2 Global optimization trials

Global optimization methods are the group of optimization methods that aim to find the global minimum of the objective error function. They often use a computationally-massive random walk over the model space to provide the statistical probability to find the global minimum. Several famous groups of methods include, Monte Carlo methods, simulated annealing methods, and genetic algorithms, which have all been demonstrated successful by various seismic inversion studies (e.g., Sen and Stoffa 1991; Sen and Stoffa 1992; Martin

et al. 2012; Sen and Biswas 2017; Zhang et al. 2018). A comprehensive review of theory and applications of global optimization methods in geophysical inversion is given by Sen and Stoffa (2013).

During the last days of my Ph.D. project I have been trying to combine the simulated annealing method and REM to extract conductivities from EM data. Simulated annealing methods are attractive because of their statistical guarantee to find the global minimum, plus their ease of implementation. The theory is well explained in Ingber (1989), Ingber (1993), and Ingber et al. (2012), along with his powerful C-library implementation. The optimization process mimics a physical annealing process. At higher temperatures the model is perturbed with more freedom, as well as adopting a higher acceptance probability for the models that are considered worse than before. By accepting models that increases the objective error function, the algorithm avoids being trapped in a local minimum. The temperature is decreased following a designed annealing schedule through the optimization. As the temperature decreases, the algorithm reduces its search space and converges to a minimum. The geophysical applications of the method are given by, e.g., Sen and Stoffa (1991), Zhao et al. (1996), Ma (2002), and Jaysaval et al. (2019).

Jaysaval et al. (2019) demonstrate the success of applying a simulated annealing optimization to extract the resistivity model from CSEM data. Their work is probably the closest to the study that I want to do with REM. They show by using a very fast simulated annealing (VFSA) method, the subsurface resistive anomalies can be successfully distinguished from the background. What is more, the initial model can start from random numbers, and therefore the results are independent of the starting model. The forward modelling code is based on an implicit, frequency-domain method and it has been highly parallelized with MPI and OpenMP. One forward modelling iteration takes about 1.1 s using 20 CPU cores solving for 3 frequencies. The VFSA optimization solves 260 (20×13) model parameters with running 5000 iterations.

My tests with VFSA to extract the resistivity model follow the same idea, except that the forward modeller is replaced by the 2.5D version of the REM code implemented by myself. The 2D model consists of 1024×512 nodes in the x- and z-directions, and 32 k_y components in the strike wavenumber direction. The grid spacing is 10 m in both x- and z-directions, and therefore the 2D model represents roughly a 10 km by 5 km subsurface profile, which is similar to the size that the Harding field EM data can cover (see Ziolkowski et al. 2010). With such a model configuration, one forward modelling iteration by REM takes about 40 - 50 s to simulate the field up to 1 s, with a single K80 GPU being used. I tested the VFSA optimization with 2000 iterations, and it is able to reproduce a 1D synthetic resistivity model with 12 (1×12) model parameters, but it fails to reproduce a 2D synthetic model with 70

(10×7) model parameters. The entire computation takes more than 1 day (but less than 2 days) to finish on Eddie (The Edinburgh Compute and Data Facility Linux Compute Cluster), including the queue time. Since I do not have permission to run a task for more than 2 days on Eddie, the iterations of the VFSA optimization have not been improved significantly than 2000, given the current speed of the code.

Compared with the work by Jaysaval et al. (2019), one major limitation of my work is the speed of the current REM forward modeller. There is the fact that REM solves the full-bandwidth EM field which contains many more than 3 single frequencies, so it may lead to better quality inversion results. Nevertheless, the current speed is about 40 - 50 times slower than theirs, and therefore the speeding-up of the code is certainly one possible thing to improve the inversion results. In fact, the importance of numerical efficiency has been realized for a long time since interest in global optimization methods began, which leads to the development of the 2.5D theory and the GPU implementation. There are at least two ways to further improve the numerical efficiency. The first way is to improve the speed of the forward modeller directly. For example, the inclusion of adaptive grids may improve the efficiency since the model size can be reduced by using coarser grids in the boundary region. Second, one could investigate a parallel version of simulated annealing methods. As discussed in Chapter 7, the GPU acceleration prefers the computation to remain in the GPU, without any transfer between CPU and GPU, to maximize the speed. Therefore it is not easy to further parallelize one single forward modelling process. Nevertheless, the inversion algorithm, i.e., the perturbation of the model, can be further parallelized to allow a simultaneous search over the solution space. It is not difficult to implement. For example, I have written a Python file which uses *mpi*4*py* (a python library allowing the use of MPI) to construct a hybrid CPU-GPU computational system. Each forward modelling iteration is undertaken by a single GPU. The communication and the updating of the model are undertaken by multiple CPUs. Such a hybrid system allows the use of parallel global optimization methods, which may be an alternative way to interpret real-world CSEM data.

There are certainly other tricks to further improve the inversion results by VFSA. For example, the tuning of parameters, including the acceptance probability and the cooling schedule. The results will be convincing if we can combine REM and VFSA to interpret real-world data, e.g., the Harding field data. Future research is needed.

All the code files are available on Eddie, so that all the results shown in the thesis can be reproduced. They should also be helpful for future research.

8.3 Summary

I have discussed the recommended functionalities for future REM improvements. Spatially adaptive grids and the implementation of several numerical boundary conditions into a unified system should further generalize the use of REM in various environments. The consideration of a shallow source is a specific practical problem, and one recommended solution is to implement spatially adaptive grids.

The ultimate goal of the REM forward modeller is to extract the resistivity model from real-world CSEM data. Large-scale, 3D problems still require gradient-based methods for the consideration of numerical efficiency. In that case, the Jacobian matrix of the REM operator needs to be solved analytically. Alternatively, global optimization methods are found to be attractive if the computational effort is affordable, since those methods do not rely on the starting model and aim to find the global minimum. Current numerical trials suggest that future work is necessary to improve the numerical efficiency of the current REM modeller and to investigate the global optimization methods further, until we can demonstrate the workflow based on real-world CSEM data.

Chapter 9

Conclusion

The work described in this thesis explores various aspects of modelling the low-frequency, time-domain CSEM data by the rapid expansion method (REM). The use of the CSEM method for subsurface exploration is discussed as a complementary tool to the seismic method, with the focus on understanding subsurface electric resistivity. The interpretation of CSEM data relies on inversion, which is an iterative forward modelling process, to search for the model that best fits the data. It is essential that the forward modeller be accurate and efficient. REM is an explicit forward modelling method that solves the diffusive EM field based on a Chebyshev expansion of the matrix exponential operator in the domain of its eigenvalues. The method yields spectral accuracy in estimating temporal derivatives. In addition, the method only computes dot products among matrices during the modelling, which is highly preferable for parallel computing.

In this project I have developed several extensions to REM for the modelling of CSEM data, considering both the accuracy and efficiency of the method. As shown in Chapters 4, 5, 6 and 7, there are five main contributions of my research, pertaining to the Earth-air interface, anisotropy, absorbing numerical boundaries, 2.5D modelling and parallel implementation of the method. The key findings are revisited and summarized as below:

1. The inclusion of the Earth-air interface into an explicit time-domain EM modeller is often carried out by an upward continuation process, where the field in the air is determined explicitly by solving Laplace's equation based on the field on the surface. However, a direct upward continuation of the Chebyshev polynomials $\mathbf{Q}$ fails to produce stable modelling results because of the discontinuity of the field and the corresponding Gibbs phenomenon. The problem is solved by introducing another series of Chebyshev polynomials $\mathbf{P}$ pairing with $\mathbf{Q}$, or equivalently, decomposing the original one-step, second-order governing equation into two-step, first-order governing

equations. The Chebyshev polynomials **P** can be seen as the time derivative of the magnetic induction field decomposed in the Chebyshev domain. By using the upward continuation of **P**, the discontinuity problem can be avoided and the response from the Earth-air interface can be modelled accurately by the REM scheme.

2. Anisotropic conductivity can be included in the REM modelling by treating the conductivity as a tensor. Vertical transverse isotropic (VTI) anisotropy requires 2 parameters (vertical and horizontal conductivity) defined per node, whereas tilted transverse isotropic (TTI) anisotropy requires 4 parameters defined per node (normal and parallel conductivity, plus two rotation angles), to formulate the conductivity tensor. Eigenvalues of the propagation matrix including VTI and TTI anisotropy have been solved explicitly, whose values are important to ensure the convergence of the Chebyshev recursion. The inclusion of VTI anisotropy does not increase computational cost, whereas the TTI anisotropy requires the computation of two more matrix dot products per electric component for each iteration, to rotate the field forward and backward, to produce accurate results.

3. Conventional numerical boundary conditions for the Chebyshev domain are mainly Dirichlet boundary condition and periodic boundary condition. Their accuracy cannot be guaranteed if the numerical boundary is not far enough away from the source, i.e., if the field has not been attenuated enough when it hits the edge of the model. The problem has been solved by introducing perfectly matched layers (PML) acting as absorbing boundaries into the Chebyshev domain. To do so, a fictitious magnetic field is introduced to the Chebyshev domain, and the Chebyshev recursion has been re-arranged to a form similar to the coupled EM wave equations, so that time and frequency in the Chebyshev domain can be defined explicitly. Uniaxial PML formulas derived for EM waves have then been modified and extended to the Chebyshev domain. Numerical tests show the improvement by using PML is obvious, especially for the far-offset modelling results when the medium is less lossy. Other types of PML, or other EM wavefield modelling techniques can be transferred to the Chebyshev domain following a similar procedure, since now the Chebyshev time and frequency have been found and the recursion of the Chebyshev terms has been shown equivalent to the propagation of coupled EM wave fields.

4. The 2.5D modelling solves the 3D field but with a 2D model, which is interesting for the concern of numerical efficiency if the model containing only 2D structures is acceptable. I present the workflow for 2.5D diffusive EM modelling by REM. Assuming conductivity is invariant along the y-direction, the Chebyshev recursion is

carried out in the strike wavenumber domain (x, k_y, z) with k_y logarithmically spaced until the Nyquist. The initial field in the strike wavenumber domain has been solved analytically considering the field excited by two types of sources, an infinitesimal x-directed impulsive electric dipole, and a finite-length x-directed impulsive electric dipole. By comparing the 3D solution and the 2.5D solution for a 2D model, numerical tests show the computational effort can be reduced by an order of magnitude with the loss of accuracy less than 1%. The required memory space is reduced accordingly.

5. Several different parallel implementations of the method have been tested. The major computational tasks of REM are the fast Fourier transforms required by the pseudospectral evaluation of spatial derivatives, and matrix arithmetic operations during the iteration. These tasks are highly suitable for GPU parallel computing. By comparing the 2.5D modelling code for the same task, the GPU-accelerated C code running on a single K80 GPU is 100 times faster than the serial C code, and 20 times faster than the multi-threaded C code (parallelized with OpenMP) running with 16 CPU processors. For the time being, the memory space of GPU is still a limiting factor for it to undertake large-scale, 3D modelling jobs. Nevertheless, the memory of GPU is able to undertake 2.5D modelling jobs considering a real-world CSEM survey, and therefore preferable for 2D problems. The parallelization with CPUs can certainly improve the computational speed, but it results in a relatively low parallel efficiency compared with the GPU code.

Through my research, the REM modelling algorithms have been implemented in different programming languages with different functionalities. This is discussed in section 7.5 and listed in Table 7.3. The ultimate goal of a forward modeller is to undertake the inversion job of a field dataset. The final presentation of the REM modeller is a 2.5D modelling code written in CUDA C with GPU acceleration and wrapped in Python. The code is able to undertake a deep-marine CSEM modelling job, as well as a shallow-marine CSEM modelling job if the source is placed around the seabed. For example, considering a 2D shallow marine CSEM survey with size of 10 km $\times$ 5 km and the source placed 100 m below the sea surface, one forward modelling iteration by my REM code takes about 40 - 50 seconds to simulate the field up to 1 s. The accuracy has been demonstrated by many numerical tests presented in the thesis. This speed is fast enough if one aims to apply a gradient-based, local optimization to determine the subsurface conductivity. But it may not be fast enough for a global optimization method given the same computational resources and limit that I have.

Due to the time limit of the project, there are many interesting topics which have not been studied fully. The forward modelling code can be further studied either to include

more functionalities or to further improve numerical efficiency. The inversion of field data requires more research effort to demonstrate a complete process of the determination of subsurface resistivities from CSEM field data. These topics have been discussed in detail in Chapter 8. I am particularly interested in applying a global optimization method, such as simulated annealing methods, to interpret CSEM field data based on the REM algorithm. The global optimization method allows the extracted model independent of the initial model and therefore avoids the interpretation being trapped in a local minimum. The REM algorithm is an accurate, full-bandwidth EM modelling method which should bring us closer to the true subsurface model than a model with only two or three frequencies. The combination of these two should lead to a bright future. For the current implementation of the REM code, it still requires further improvement of numerical efficiency, or alternatively, more computational resources, to demonstrate the workflow based on a real-world CSEM dataset. More effort should be invested, to complete the study of the extraction of the subsurface resistivity model based on the time-domain CSEM data.

Appendix A

Eigenvalues of the propagation matrix

Appendix A shows the mathematical work to derive the eigenvalues of the propagation matrix with the inclusion of vertical transverse isotropic (VTI) and tilted transverse isotropic (TTI) anisotropy. The use of eigenvalues has been discussed in section 5.2.2, to ensure the convergence of the Chebyshev recursion with the inclusion of anisotropy.

A.1 solution to the eigenvalues

In the wavenumber domain the spatial derivatives ∂_x, ∂_y, and ∂_z are replaced by ik_x, ik_y, and ik_z, respectively, and the propagation matrix $\mathbf{G}$ is given as

$$\mathbf{G} = -\frac{1}{\mu_0}\begin{pmatrix} x_{11} & x_{12} & x_{13} \\ x_{21} & x_{22} & x_{23} \\ x_{31} & x_{32} & x_{33} \end{pmatrix}\begin{pmatrix} {k_y}^2+{k_z}^2 & -k_xk_y & -k_xk_z \\ -k_xk_y & {k_x}^2+{k_z}^2 & -k_yk_z \\ -k_xk_z & -k_yk_z & {k_x}^2+{k_y}^2 \end{pmatrix}, \tag{A.1}$$

where the elements x_{ij} correspond with the inverse of the conductivity tensor. With the conductivity tensor and the rotation matrix given in equations 5.5 and 5.6, the elements x_{ij}

are solved as

$$x_{11} = \frac{1}{\sigma_p}(\cos^2\theta\cos^2\phi + \sin^2\phi) + \frac{1}{\sigma_n}\sin^2\theta\cos^2\phi, \tag{A.2}$$

$$x_{22} = \frac{1}{\sigma_p}(\cos^2\theta\sin^2\phi + \cos^2\phi) + \frac{1}{\sigma_n}\sin^2\theta\sin^2\phi, \tag{A.3}$$

$$x_{33} = \frac{1}{\sigma_p}\sin^2\theta + \frac{1}{\sigma_n}\cos^2\theta, \tag{A.4}$$

$$x_{12} = x_{21} = (\frac{1}{\sigma_n} - \frac{1}{\sigma_p})\sin^2\theta\sin\phi\cos\phi, \tag{A.5}$$

$$x_{13} = x_{31} = (\frac{1}{\sigma_n} - \frac{1}{\sigma_p})\sin\theta\cos\theta\cos\phi, \tag{A.6}$$

$$x_{23} = x_{32} = (\frac{1}{\sigma_n} - \frac{1}{\sigma_p})\sin\theta\cos\theta\sin\phi. \tag{A.7}$$

I define $\mathbf{G} = -\mu_0^{-1}\mathbf{g}$, and the matrix $\mathbf{g}$ is therefore the product of the inverse conductivities and the wavenumbers, containing nine elements as

$$\mathbf{g} = \begin{pmatrix} g_{11} & g_{12} & g_{13} \\ g_{21} & g_{22} & g_{23} \\ g_{31} & g_{32} & g_{33} \end{pmatrix}. \tag{A.8}$$

The eigenvalues of a 3×3 matrix $\mathbf{g}$ satisfy

$$\begin{aligned} -\lambda^3 + \lambda^2(g_{11}+g_{22}+g_{33}) + \lambda(g_{31}g_{13}+g_{21}g_{12}+g_{32}g_{23}-g_{11}g_{22}-g_{22}g_{33}-g_{33}g_{11}) \\ +(g_{11}g_{22}g_{33}+g_{12}g_{23}g_{31}+g_{13}g_{21}g_{32}-g_{31}g_{22}g_{13}-g_{32}g_{23}g_{11}-g_{33}g_{21}g_{12}) = 0. \end{aligned} \tag{A.9}$$

In the isotropic case, zero is one of the eigenvalues of the propagation matrix. Therefore it is also one of the eigenvalues in the anisotropic case, that is, $\lambda_1 = 0$. This yields

$$g_{11}g_{22}g_{33} + g_{12}g_{23}g_{31} + g_{13}g_{21}g_{32} - g_{31}g_{22}g_{13} - g_{32}g_{23}g_{11} - g_{33}g_{21}g_{12} = 0. \tag{A.10}$$

The rest terms in equation A.9 are calculated as

$$\begin{aligned} g_{11}+g_{22}+g_{33} =& ({k_y}^2+{k_z}^2)x_{11} + ({k_x}^2+{k_z}^2)x_{22} + ({k_x}^2+{k_y}^2)x_{33} \\ & - 2k_xk_yx_{12} - 2k_xk_zx_{13} - 2k_yk_zx_{32}, \end{aligned} \tag{A.11}$$

and

$$\begin{aligned}
&g_{31}g_{13}+g_{21}g_{12}+g_{32}g_{23}-g_{11}g_{22}-g_{22}g_{33}-g_{33}g_{11}\\
=&-{k_z}^2({k_x}^2+{k_y}^2+{k_z}^2)(x_{11}x_{22}-x_{12}x_{12})-{k_x}^2({k_x}^2+{k_y}^2+{k_z}^2)(x_{22}x_{33}-x_{23}x_{23})\\
&-{k_y}^2({k_x}^2+{k_y}^2+{k_z}^2)(x_{11}x_{33}-x_{13}x_{13})+2k_yk_z({k_x}^2+{k_y}^2+{k_z}^2)(x_{11}x_{23}-x_{12}x_{13})\\
&+2k_xk_z({k_x}^2+{k_y}^2+{k_z}^2)(x_{13}x_{22}-x_{12}x_{23})+2k_xk_y({k_x}^2+{k_y}^2+{k_z}^2)(x_{12}x_{33}-x_{13}x_{23}).
\end{aligned} \tag{A.12}$$

The six quantities relating to the inverse conductivities are calculated and rearranged in the form of

$$x_{11}x_{22}-x_{12}x_{12}=\frac{1}{{\sigma_p}^2}+\frac{1}{\sigma_p}(\frac{1}{\sigma_n}-\frac{1}{\sigma_p})\sin^2\theta, \tag{A.13}$$

$$x_{22}x_{33}-x_{23}x_{23}=\frac{1}{{\sigma_p}^2}+\frac{1}{\sigma_p}(\frac{1}{\sigma_n}-\frac{1}{\sigma_p})(\sin^2\theta\sin^2\phi+\cos^2\theta), \tag{A.14}$$

$$x_{11}x_{33}-x_{13}x_{13}=\frac{1}{{\sigma_p}^2}+\frac{1}{\sigma_p}(\frac{1}{\sigma_n}-\frac{1}{\sigma_p})(\sin^2\theta\cos^2\phi+\cos^2\theta), \tag{A.15}$$

$$x_{11}x_{23}-x_{12}x_{13}=\frac{1}{\sigma_p}(\frac{1}{\sigma_n}-\frac{1}{\sigma_p})\sin\theta\cos\theta\sin\phi, \tag{A.16}$$

$$x_{13}x_{22}-x_{12}x_{23}=\frac{1}{\sigma_p}(\frac{1}{\sigma_n}-\frac{1}{\sigma_p})\sin\theta\cos\theta\cos\phi, \tag{A.17}$$

$$x_{12}x_{33}-x_{13}x_{23}=\frac{1}{\sigma_p}(\frac{1}{\sigma_n}-\frac{1}{\sigma_p})\sin^2\theta\sin\phi\cos\phi. \tag{A.18}$$

By combining equations from A.11 to A.18, the two non-zero eigenvalues of matrix **g** satisfy

$$\begin{aligned}
\lambda_2+\lambda_3=&\frac{2}{\sigma_p}({k_x}^2+{k_y}^2+{k_z}^2)+{k_x}^2(\frac{1}{\sigma_n}-\frac{1}{\sigma_p})(\sin^2\theta\sin^2\phi+\cos^2\theta)\\
&+{k_y}^2(\frac{1}{\sigma_n}-\frac{1}{\sigma_p})(\sin^2\theta\cos^2\phi+\cos^2\theta)+{k_z}^2(\frac{1}{\sigma_n}-\frac{1}{\sigma_p})\sin^2\theta\\
&-2k_yk_z(\frac{1}{\sigma_n}-\frac{1}{\sigma_p})\sin\theta\cos\theta\sin\phi-2k_xk_z(\frac{1}{\sigma_n}-\frac{1}{\sigma_p})\sin\theta\cos\theta\cos\phi\\
&-2k_xk_y(\frac{1}{\sigma_n}-\frac{1}{\sigma_p})\sin^2\theta\sin\phi\cos\phi,
\end{aligned} \tag{A.19}$$

and

$$\begin{aligned}\lambda_2\lambda_3 =&\frac{1}{\sigma_p}({k_x}^2+{k_y}^2+{k_z}^2)[\frac{1}{\sigma_p}({k_x}^2+{k_y}^2+{k_z}^2)+{k_x}^2(\frac{1}{\sigma_n}-\frac{1}{\sigma_p})(\sin^2\theta\sin^2\phi+\cos^2\theta)\\&+{k_y}^2(\frac{1}{\sigma_n}-\frac{1}{\sigma_p})(\sin^2\theta\cos^2\phi+\cos^2\theta)+{k_z}^2(\frac{1}{\sigma_n}-\frac{1}{\sigma_p})\sin^2\theta\\&-2k_yk_z(\frac{1}{\sigma_n}-\frac{1}{\sigma_p})\sin\theta\cos\theta\sin\phi-2k_xk_z(\frac{1}{\sigma_n}-\frac{1}{\sigma_p})\sin\theta\cos\theta\cos\phi\\&-2k_xk_y(\frac{1}{\sigma_n}-\frac{1}{\sigma_p})\sin^2\theta\sin\phi\cos\phi].\end{aligned} \tag{A.20}$$

Therefore the two non-zero eigenvalues are solved as

$$\lambda_2 =\frac{1}{\sigma_p}({k_x}^2+{k_y}^2+{k_z}^2), \tag{A.21}$$

$$\begin{aligned}\lambda_3 =&\frac{1}{\sigma_p}({k_x}^2+{k_y}^2+{k_z}^2)+{k_x}^2(\frac{1}{\sigma_n}-\frac{1}{\sigma_p})(\sin^2\theta\sin^2\phi+\cos^2\theta)\\&+{k_y}^2(\frac{1}{\sigma_n}-\frac{1}{\sigma_p})(\sin^2\theta\cos^2\phi+\cos^2\theta)+{k_z}^2(\frac{1}{\sigma_n}-\frac{1}{\sigma_p})\sin^2\theta\\&-2k_yk_z(\frac{1}{\sigma_n}-\frac{1}{\sigma_p})\sin\theta\cos\theta\sin\phi-2k_xk_z(\frac{1}{\sigma_n}-\frac{1}{\sigma_p})\sin\theta\cos\theta\cos\phi\\&-2k_xk_y(\frac{1}{\sigma_n}-\frac{1}{\sigma_p})\sin^2\theta\sin\phi\cos\phi.\end{aligned} \tag{A.22}$$

Equation A.22 can be rearranged to give a more compacted expression of λ_3, as shown in equation 5.9.

Appendix B

1-D and 2-D solutions by REM with 3-D source consideration

Appendix B shows the mathematical work to derive the initial electric field in the strike wavenumber domain (x, k_y, z) excited by an impulsive in-line dipole source with infinitesimal length and with a finite length. The analytic solution of the initial field allows the use of REM to solve the 3D electric field but with a 2D or 1D conductivity model, as discussed in section 7.2.

B.1 1-D and 2-D solutions by REM with 3-D source consideration

In some cases, the 3-D subsurface conductivity can be simplified to 2-D model space if one can assume the material properties are unchanged along the strike direction. The source (e.g., an electric dipole) emits a 3-D field, which yields a 2.5-D problem (e.g., Key and Ovall 2011). The main strategy of 2.5-D EM modelling is to convert the field along the strike direction to its wavenumber domain and solve a series of 2-D equations, and then convert the field back to the spatial domain. This is discussed in section 7.2.

Modelling by REM is flexible between the space and wavenumber domain, as the evolution of the field in the Chebyshev domain is independent of the domain. The updating of the terms can be carried out in the domains of (k_x, k_y, k_z), or (k_x, k_y, z), or (x, k_y, z) or (x, y, z), to simulate the field in a homogeneous, 1-D layered, 2-D, or 3-D model, respectively, with the propagation matrix $\mathbf{G}$ modified accordingly. To incorporate the 3-D source, the initial field needs to be solved analytically in the desired modelling domain.

Stoffa and Ziolkowski (2018) gives the space-domain solution for the electric field excited by an impulsive dipole. Considering an x-directed electric dipole located at the origin with coordinates $x = y = 0$, the strength of the initial electric field is solved as

$$E_x(x,y,z,t) = \frac{Ids\theta^3}{\pi^{3/2}\sigma t}\exp(-\theta^2 r^2)\big(1-\theta^2(y^2+z^2)\big), \tag{B.1}$$

$$E_y(x,y,z,t) = \frac{Ids\theta^5}{\pi^{3/2}\sigma t}\exp(-\theta^2 r^2)xy, \tag{B.2}$$

$$E_z(x,y,z,t) = \frac{Ids\theta^5}{\pi^{3/2}\sigma t}\exp(-\theta^2 r^2)xz, \tag{B.3}$$

where $\theta = (\frac{\mu_0\sigma}{4t})^{1/2}$ and $r = (x^2+y^2+z^2)^{1/2}$.

I use the Fourier transform pair as

$$E_x(x,k_y,z,t) = \int_{-\infty}^{+\infty} E_x(x,y,z,t)\exp(-ik_y y)dy, \tag{B.4}$$

and

$$E_x(x,y,z,t) = \frac{1}{2\pi}\int_{-\infty}^{+\infty} E_x(x,k_y,z,t)\exp(ik_y y)dk_y. \tag{B.5}$$

The objective is to transform the space-domain analytic solution to the wavenumber domains (x,k_y,z) and (k_x,k_y,z), to establish the initial electric field in the interested domain, and therefore allow the start of the REM modelling. I first solve the Fourier transform of the exponential component

$$\int_{-\infty}^{+\infty}\exp(-\theta^2 y^2)\exp(-ik_y y)dy = \frac{\sqrt{\pi}}{\theta}\exp\left(-\frac{{k_y}^2}{4\theta^2}\right), \tag{B.6}$$

and with the help of the Fourier transform derivative relation, the other exponential-related components can be solved as

$$\begin{aligned}
&\int_{-\infty}^{+\infty} y\exp(-\theta^2 y^2)\exp(-ik_y y)dy \\
&= \int_{-\infty}^{+\infty}\left(-\frac{1}{2\theta^2}\frac{\partial}{\partial y}\exp(-\theta^2 y^2)\right)\exp(-ik_y y)dy \\
&= -\frac{ik_y}{2\theta^2}\frac{\sqrt{\pi}}{\theta}\exp\left(-\frac{{k_y}^2}{4\theta^2}\right) \\
&= -\frac{ik_y\sqrt{\pi}}{2\theta^3}\exp\left(-\frac{{k_y}^2}{4\theta^2}\right),
\end{aligned} \tag{B.7}$$

and

$$\begin{aligned}
&\int_{-\infty}^{+\infty} y^2 \exp(-\theta^2 y^2)\exp(-ik_y y)dy \\
=&\int_{-\infty}^{+\infty}\left(\frac{1}{4\theta^4}\frac{\partial^2}{\partial y^2}\exp(-\theta^2 y^2)+\frac{1}{2\theta^2}\exp(-\theta^2 y^2)\right)\exp(-ik_y y)dy \\
=&(-\frac{{k_y}^2}{4\theta^4}+\frac{1}{2\theta^2})\frac{\sqrt{\pi}}{\theta}\exp\left(-\frac{{k_y}^2}{4\theta^2}\right) \\
=&(-\frac{{k_y}^2\sqrt{\pi}}{4\theta^5}+\frac{\sqrt{\pi}}{2\theta^3})\exp\left(-\frac{{k_y}^2}{4\theta^2}\right).
\end{aligned} \tag{B.8}$$

With the results showing in equations B.6 to B.8, it is straightforward to transform the electric field from the (x,y,z) domain to the (x,k_y,z) domain. The three electric field components are solved as

$$E_x(x,k_y,z,t)=\frac{Ids}{4\pi\sigma t}\exp(-\theta^2(x^2+z^2)-\frac{{k_y}^2}{4\theta^2})(-4\theta^4 z^2+2\theta^2+{k_y}^2), \tag{B.9}$$

$$E_y(x,k_y,z,t)=-i\frac{Ids\theta^2}{2\pi\sigma t}\exp(-\theta^2(x^2+z^2)-\frac{{k_y}^2}{4\theta^2})xk_y, \tag{B.10}$$

$$E_z(x,k_y,z,t)=\frac{Ids\theta^4}{\pi\sigma t}\exp(-\theta^2(x^2+z^2)-\frac{{k_y}^2}{4\theta^2})xz. \tag{B.11}$$

Equations B.9, B.10 and B.11 give the analytic solution of the (x,k_y,z) domain electric field excited by an x-directed impulsive electric dipole. The solution allows the start of the REM modelling in the (x,k_y,z) domain.

Equations B.9, B.10 and B.11 can be further transformed to the horizontal wavenumber domain (k_x,k_y,z), to consider a 1-D model space with 3-D dipole source. Similarly to equations B.6, B.7 and B.8, the x-related exponential terms can be transformed to its wavenumber domain as

$$\int_{-\infty}^{+\infty}\exp(-\theta^2x^2)\exp(-ik_x x)dx=\frac{\sqrt{\pi}}{\theta}\exp\left(-\frac{{k_x}^2}{4\theta^2}\right), \tag{B.12}$$

$$\int_{-\infty}^{+\infty}x\exp(-\theta^2x^2)\exp(-ik_x x)dx=-\frac{ik_x\sqrt{\pi}}{2\theta^3}\exp\left(-\frac{{k_x}^2}{4\theta^2}\right), \tag{B.13}$$

and the three electric field components are solved as

$$E_x(k_x,k_y,k_z,t)=\frac{Ids}{4\pi^{1/2}\sigma t\theta}\exp(-\frac{{k_x}^2}{4\theta^2}-\frac{{k_y}^2}{4\theta^2}-\theta^2z^2)(-4\theta^4z^2+2\theta^2+{k_y}^2), \tag{B.14}$$

$$E_y(k_x,k_y,z,t) = -\frac{Ids}{4\pi^{1/2}\sigma t\theta}\exp(-\frac{{k_x}^2}{4\theta^2}-\frac{{k_y}^2}{4\theta^2}-\theta^2z^2)k_xk_y, \tag{B.15}$$

$$E_z(k_x,k_y,z,t) = -i\frac{Ids\theta}{2\pi^{1/2}\sigma t}\exp(-\frac{{k_x}^2}{4\theta^2}-\frac{{k_y}^2}{4\theta^2}-\theta^2z^2)k_xz. \tag{B.16}$$

Equations B.14, B.15 and B.16 give the analytic solution of the (k_x,k_y,z) domain electric field excited by an x-directed impulsive electric dipole. The solution allows the start of the REM modelling in the (k_x,k_y,z) domain.

Considering the bipole source (a dipole with finite length), Ziolkowski and Taylor (2010) solve the initial field based on an integration of equations 3.36 to 3.38 along the x-direction. Considering an x-directed bipole source locating from X_1 to X_2 on the x-axis, the space-domain electric field is solved as

$$\begin{aligned}E_x(x,y,z,t) = \frac{I\theta^2}{2\pi\sigma t}\exp(-\theta^2(y^2+z^2))(\theta^2(y^2+z^2)-1)[\mathrm{erf}(\theta(x-X_2))\\ -\mathrm{erf}(\theta(x-X_1))],\end{aligned} \tag{B.17}$$

$$E_y(x,y,z,t) = \frac{I\theta^3y}{2\pi^{3/2}\sigma t}\exp(-\theta^2(y^2+z^2))(e^{-\theta^2(x-X_2)^2}-e^{-\theta^2(x-X_1)^2}), \tag{B.18}$$

$$E_z(x,y,z,t) = \frac{I\theta^3z}{2\pi^{3/2}\sigma t}\exp(-\theta^2(y^2+z^2))(e^{-\theta^2(x-X_2)^2}-e^{-\theta^2(x-X_1)^2}). \tag{B.19}$$

With the results showing in equations B.6 and B.7, the bipole source excited electric field is solved in the (x,k_y,z) domain as

$$\begin{aligned}E_x(x,k_y,z,t) = \frac{I}{8\pi^{1/2}\sigma t\theta}\exp(-\theta^2z^2-\frac{{k_y}^2}{4\theta^2})(4\theta^4z^2-2\theta^2-{k_y}^2)[\mathrm{erf}(\theta(x-X_2))\\ -\mathrm{erf}(\theta(x-X_1))],\end{aligned} \tag{B.20}$$

$$E_y(x,k_y,z,t) = -i\frac{Ik_y}{4\pi\sigma t}\exp(-\theta^2z^2-\frac{{k_y}^2}{4\theta^2}))(e^{-\theta^2(x-X_2)^2}-e^{-\theta^2(x-X_1)^2}), \tag{B.21}$$

$$E_z(x,k_y,z,t) = \frac{Iz\theta^2}{2\pi\sigma t}\exp(-\theta^2z^2-\frac{{k_y}^2}{4\theta^2}))(e^{-\theta^2(x-X_2)^2}-e^{-\theta^2(x-X_1)^2}). \tag{B.22}$$

Equations B.20, B.21 and B.22 give the analytic solution of the (x,k_y,z) domain electric field excited by an x-directed impulsive electric bipole. The solution allows the start of the REM modelling in the (x,k_y,z) domain.

Appendix C

Published papers

Appendix C attaches the published papers from my research work. The first paper discusses the inclusion of the Earth-air interface and the inclusion of anisotropy into REM, which is a summary of the work shown in Chapters 4 and 5. The second paper discusses the similarity of REM to coupled EM wave equations, and shows the solution of numerical boundary problems in the Chebyshev domain by perfectly matched layers (PML).

GEOPHYSICS, VOL. 84, NO. 5 (SEPTEMBER-OCTOBER 2019); P. E323–E335, 12 FIGS.
10.1190/GEO2018-0143.1

Time evolution of the electric field using the rapid expansion method with pseudospectral evaluation of spatial derivatives — Part 2: Inclusion of anisotropy and the earth-air interface

Yikuo Liu[1], Anton Ziolkowski[1], and Paul L. Stoffa[2]

ABSTRACT

We have evaluated an extension of the 3D 3C rapid-expansion method for time-domain electromagnetic modeling with pseudospectral evaluation of spatial derivatives that includes anisotropic conductivity and the earth-air interface. We found that transverse isotropic anisotropy can be included in the modeling with the manipulation of the conductivity tensor. We model the response of the earth-air interface by using the upward continuation of the time derivative of the magnetic induction. All three electric field components are collocated with the electric conductivities and are modeled independently and simultaneously with spectral accuracy in space and time. Numerical tests against the analytical solution for a half-space and spectral methods for 1D anisotropic layered earth models demonstrate the excellent accuracy of this approach.

INTRODUCTION

Carcione (2006) introduces a Chebyshev algorithm to solve the 2D electromagnetic (EM) problem for a magnetic source in conductive media, accurate to the Nyquist frequency in space and time. Stoffa and Ziolkowski (2019), here referred to as paper 1, extend the 2D numerical scheme of Carcione (2006) to the 3D full-space EM diffusion problem in conductive media with an impulsive electric dipole source. The code is parallelized, leading to computational efficiency. We extend the work of paper 1 to include anisotropy and the earth-air interface.

The electrical resistivity of a rock is normally direction dependent, and is therefore anisotropic. Electrical anisotropy is an important property that influences the interpretation of controlled-source electromagnetic (CSEM) measurements, and it is normal. For example, the grouping together of thin isotropic rock layers of different isotropic resistivities can be treated as macroanisotropy at the numerical scale (Edwards et al., 1984). We extend the work described in paper 1 and present a pseudospectral (PS) method to solve the fully anisotropic 3D EM field in conductive media in the time domain. Compared with the conventional finite difference (FD) solution (e.g., Wang and Hohmann, 1993; Commer and Newman, 2004), there are two clear advantages: (1) The estimation of spatial and temporal derivatives has infinite order of accuracy and (2) all three electric field components are collocated at the same position so that the material properties are not altered during modeling. Averaging the material property is, however, a standard treatment in staggered grids used by FD methods. It results in ambiguous definitions of boundaries and creates transition layer effects (Feise et al., 2004).

The earth-air interface is an important boundary. The propagation of the EM field in the earth is essentially a diffusive process, whereas in the air the EM field travels as waves with the speed of light. The huge difference of velocity leads to a difficulty for time-domain methods. Oristaglio and Hohmann (1984) solve this problem in an FD scheme by treating the EM field in the air as a potential field that satisfies Laplace's equation. The air field is determined instantaneously and explicitly from the EM field on the surface, by upward continuation. However, to our knowledge, due to the natural difference between the FD and PS methods, there is no such PS example that models the response from the earth-air interface for a diffusional time scale. An empirical approximation is to set the resistivity of air to a large value, e.g., 10^4 ohm-m (Um et al., 2010). The accuracy of this approximation decreases with increasing offset. It may also introduce unnecessary time steps. We show that the response of the earth-air interface can be modeled with the rapid-expansion method (REM) via upward continuation of the time derivative of the magnetic induction.

Manuscript received by the Editor 19 February 2018; revised manuscript received 12 April 2019; published ahead of production 27 June 2019; published online 16 September 2019.
[1]University of Edinburgh, School of Geosciences, Edinburgh, UK. E-mail: yikuo.liu@ed.ac.uk; anton.ziolkowski@ed.ac.uk.
[2]University of Texas at Austin, Institute for Geophysics and Department of Geological Sciences, Jackson School of Geosciences, Austin, Texas, USA. E-mail: stoffa@ig.utexas.edu.

We first extend the work of paper 1 to derive the solution of 3D full-space EM diffusion by REM in anisotropic medium. We then describe how we include the earth-air interface. We demonstrate the accuracy of the code by comparing the modeling results with the analytical solution of a half-space and then with the published EMmod code (Hunziker et al., 2015) for 1D layered vertical transverse isotropic (VTI) media. We show its ability to handle tilted transverse isotropic (TTI) conductivities, and its robustness to the presence of 3D sharp material contrasts, to demonstrate the usefulness of this approach.

THEORY

In conductive media in which the displacement current can be neglected, the electric field $\mathbf{E}(x, y, z, t)$ satisfies the diffusion equation

$$\frac{\partial}{\partial t}\mathbf{E} = -\frac{1}{\mu_0}\boldsymbol{\sigma}^{-1}\nabla\times\nabla\times\mathbf{E} - \boldsymbol{\sigma}^{-1}\frac{\partial}{\partial t}\mathbf{J_s}, \tag{1}$$

where $\mathbf{E}$ is the vector consisting of three electric wavefield components $\mathbf{E}(x, y, z, t) = (E_x, E_y, E_z)^T$ with units in V/m, μ_0 is the magnetic permeability of free space ($\mu_0 = 4\pi\times10^{-7}$ H/m), $\mathbf{J_s}$(A/m^2) is the source current density, and $\boldsymbol{\sigma}$(S/m) is the conductivity tensor

$$\boldsymbol{\sigma} = \begin{pmatrix} \sigma_{xx} & \sigma_{xy} & \sigma_{xz} \\ \sigma_{yx} & \sigma_{yy} & \sigma_{yz} \\ \sigma_{zx} & \sigma_{zy} & \sigma_{zz} \end{pmatrix}. \tag{2}$$

We define a right-handed Cartesian coordinate system to discretize the model, in which $z = 0$ m is the earth-air interface and z is positive downward.

3D solution by REM

Equation 1 can be written in the form

$$\frac{\partial}{\partial t}\mathbf{E} = \mathbf{G}\mathbf{E} + \mathbf{s}, \tag{3}$$

where $\mathbf{s}$ is the source term and $\mathbf{G}$ is the propagation matrix containing all of the spatial derivatives and the anisotropic conductivities. Paper 1 shows how to solve equation 3 in an isotropic full space with an impulsive electric dipole source $t = 0$. The numerical workflow proceeds in the following way:

1) Obtain an initial field condition by solving equation 3 analytically at an appropriate initial time. Because the source is impulsive, the source term is absent $t > 0$.
2) In the absence of sources, the evolution of the electric field follows an exponential operator, which can be evaluated using the Chebyshev expansion of exp(x). The initial field is the first Chebyshev term. The following terms are obtained using the recurrence relation for Chebyshev polynomials.
3) Step 2 is repeated until the number of terms reaches a sufficient degree for convergence, and the choice of the degree is related to the eigenvalue of the propagation matrix.
4) All of the Chebyshev terms are weighted and summed together to reconstruct the electric field in the time domain.

Inclusion of anisotropy

The propagation matrix $\mathbf{G}$ needs to be evaluated at every step in the Chebyshev recursion:

$$\begin{aligned}\mathbf{G} &= -\frac{1}{\mu_0}\boldsymbol{\sigma}^{-1}\mathbf{D} \\ &= -\frac{1}{\mu_0}\begin{pmatrix} \sigma_{xx} & \sigma_{xy} & \sigma_{xz} \\ \sigma_{yx} & \sigma_{yy} & \sigma_{yz} \\ \sigma_{zx} & \sigma_{zy} & \sigma_{zz} \end{pmatrix}^{-1}\begin{pmatrix} -(\partial_y^2+\partial_z^2) & \partial_y\partial_x & \partial_z\partial_x \\ \partial_x\partial_y & -(\partial_x^2+\partial_z^2) & \partial_z\partial_y \\ \partial_x\partial_z & \partial_y\partial_z & -(\partial_x^2+\partial_y^2) \end{pmatrix},\end{aligned} \tag{4}$$

where $\mathbf{D}$ is the matrix containing all of the spatial derivatives and $\boldsymbol{\sigma}^{-1}$ is the inverse of the conductivity tensor. Matrix $\mathbf{D}$ is evaluated in the wavenumber domain as a PS method accompanied with 3D forward and inverse fast Fourier transform (IFFT), as described in paper 1. The matrix $\boldsymbol{\sigma}^{-1}$ is implemented in the space domain considering the spatial and directional variation of conductivities.

The electric field components $\{E_x, E_y, E_z\}$ are defined at the same positions as the conductivity tensor $\boldsymbol{\sigma}$. Therefore, the current density $\mathbf{J}$ and the electric field $\mathbf{E}$ are connected directly via $\boldsymbol{\sigma}$, and the inclusion of anisotropy is straightforward without any interpolation or averaging. Steps 1–4 of the numerical workflow discussed above do not change. However, to include transverse isotropic anisotropy, the inverse of $\boldsymbol{\sigma}$ is modified as

$$\boldsymbol{\sigma}^{-1} = \mathbf{R}^T\begin{pmatrix} \sigma_p & 0 & 0 \\ 0 & \sigma_p & 0 \\ 0 & 0 & \sigma_n \end{pmatrix}^{-1}\mathbf{R}, \tag{5}$$

where σ_p and σ_n are the conductivities parallel and normal to the transverse isotropic plane, respectively, and $\mathbf{R}$ is the rotation matrix

$$\mathbf{R} = \begin{pmatrix} \cos\theta\cos\varphi & \cos\theta\sin\varphi & -\sin\theta \\ -\sin\varphi & \cos\varphi & 0 \\ \sin\theta\cos\varphi & \sin\theta\sin\varphi & \cos\theta \end{pmatrix}, \tag{6}$$

with its elements defined by two Euler angles, the strike φ and the dip θ, to describe the rotation of the Cartesian coordinate system to the tilted coordinate system, in which the transverse isotropic anisotropy can be described by a diagonal matrix (Jaysaval et al., 2016). For the isotropic and the VTI cases, $\mathbf{R}$ is an identity matrix with $\varphi = \theta = 0$ and $\boldsymbol{\sigma}$ reduces to a diagonal matrix with two values $\{\sigma_p, \sigma_n\}$ defined per node. Up to this point, the inclusion of anisotropy does not increase the computational cost. For a TTI case, extra computation is needed to carry out the forward and backward rotation of the coordinates.

By substituting equations 5 and 6 into equation 4 and evaluating the spatial derivatives in the wavenumber domain, the eigenvalues of the propagation matrix $\mathbf{G}$ are solved as (see Appendix A)

$$\lambda_1 = 0, \tag{7}$$

$$\lambda_2 = -\frac{1}{\mu_0\sigma_p}(k_x^2 + k_y^2 + k_z^2), \tag{8}$$

and

$$\lambda_3 = -\frac{1}{\mu_0\sigma_p}(k_x \sin\theta\cos\varphi + k_y \sin\theta\sin\varphi + k_z\cos\theta)^2 - \frac{1}{\mu_0\sigma_n}[(k_x \sin\theta\sin\varphi - k_y \sin\theta\cos\varphi)^2 + (k_x\cos\theta - k_z\sin\theta\cos\varphi)^2 + (k_y\cos\theta - k_z\sin\theta\sin\varphi)^2]. \quad (9)$$

Therefore, the eigenvalues are on the negative real axis, and the system is stable with the inclusion of anisotropy. When $\sigma_p = \sigma_n$ and $\varphi = \theta = 0$, the expression of λ_3 is simplified to the same as λ_2, and they are actually the eigenvalues of the isotropic propagation matrix as given in paper 1. In an anisotropic case, the maximum absolute eigenvalue should consider the spatial variation as well as the directional variation of the conductivity. Defining quantity a as the maximum value of the inverse of the parallel and normal conductivities times μ_0^{-1}, that is, $a = \max((1/\mu_0\sigma_p), (1/\mu_0\sigma_n))$, the absolute value of λ_3 always satisfies the inequality

$$|\lambda_3| \le a[(k_x \sin\theta\cos\varphi + k_y \sin\theta\sin\varphi + k_z\cos\theta)^2 + (k_x \sin\theta\sin\varphi - k_y \sin\theta\cos\varphi)^2 + (k_x\cos\theta - k_z\sin\theta\cos\varphi)^2 + (k_y\cos\theta - k_z\sin\theta\sin\varphi)^2] = a(k_x^2 + k_y^2 + k_z^2), \quad (10)$$

and the right side value of equation 10 is also always greater than or equal to $|\lambda_2|$. The maximum wavenumber components are the Nyquist wavenumbers, which for grid spacings Δx, Δy, and Δz are $k_x = \pi/\Delta x$, $k_y = \pi/\Delta y$, and $k_z = \pi/\Delta z$. Therefore, the maximum absolute eigenvalue b (refer to paper 1) is given as

$$b = a\pi^2\left(\frac{1}{\Delta x^2} + \frac{1}{\Delta y^2} + \frac{1}{\Delta z^2}\right). \quad (11)$$

This expression is similar to that given in paper 1, but now it accounts for transverse isotropic anisotropy. Because the value of a takes the maximum between $(\mu_0\sigma_p)^{-1}$ and $(\mu_0\sigma_n)^{-1}$, the expression for b derived in equation 11 is always sufficiently large to ensure convergence and accuracy. Alternatively, one can calculate the eigenvalues from equations 8 and 9 based on the knowledge of σ_p, σ_n, φ, and θ, to decide the order of the Chebyshev terms. Another choice is to observe the value of $I_k(bt)$, as discussed in paper 1.

Inclusion of the earth-air interface

Wang and Hohmann (1993) and Commer and Newman (2004) present a finite-difference implementation of the earth-air interface in 3D EM modeling. Given that the air conductivity is zero, under the quasistatic approximation the magnetic fields and its time derivative obey Laplace's equation:

$$\frac{\partial^2}{\partial x^2}\mathbf{A} + \frac{\partial^2}{\partial y^2}\mathbf{A} + \frac{\partial^2}{\partial z^2}\mathbf{A} = 0, \quad (12)$$

where $\mathbf{A}$ is a vector field that could be the magnetic induction $\mathbf{B}$ or its time derivative $\dot{\mathbf{B}}$. Any component of $\mathbf{A}$ at any height in the air can be instantaneously determined by the continuation of its surface field, following the solution of equation 12 in the horizontal wavenumber domain, as

$$\tilde{A}_n(k_x, k_y, z<0) = \tilde{A}_n(k_x, k_y, z=0)\exp\left(\sqrt{k_x^2 + k_y^2}\,z\right), \quad (13)$$

where subscript n denotes the x-, y-, or z-component and $\tilde{A}_n$ denotes the field after a 2D Fourier transform along the horizontal axes. Wang and Hohmann (1993) use the continuation of field $\mathbf{B}$, and Commer and Newman (2004) use the continuation of field $\dot{\mathbf{B}}$. Because the field in the air is explicitly determined from the field on the surface, it avoids a direct simulation of the air field, which would require many tiny time steps and is computationally too onerous.

Our implementation of the earth-air interface in REM follows a similar idea. However, in the case of REM, we have found that direct continuation of the Chebyshev terms $\mathbf{Q}$ fails to produce accurate and stable results. The Chebyshev terms $\mathbf{Q}$, as part of $\mathbf{E}$, share the same continuity conditions as the electric field. During the simulation, the vertical electric component E_z and its Chebyshev terms Q_z are discontinuous across the earth-air interface. This leads to two difficulties in applying upward continuation: (1) A direct modification of Q_z intensifies the Gibbs phenomenon and eventually generates a nonphysical source on the boundary, and (2) calculation of $\mathbf{Q}$ exactly on the surface is problematic because of the discontinuity.

We have found that these problems are avoided if we use the continuation of the time derivative of the magnetic induction $\dot{\mathbf{B}}$. Faraday's law states that $\dot{\mathbf{B}}$ is the negative of the curl of $\mathbf{E}$. To exploit the use of $\dot{\mathbf{B}}$, we introduce the Chebyshev pairs $\mathbf{Q}$ and $\mathbf{P}$, where the Chebyshev term $\mathbf{P}$ satisfies Faraday's law:

$$\mathbf{P} = -\nabla\times\mathbf{Q}, \quad (14)$$

and $\mathbf{P}$ has the same relation to $\mathbf{Q}$ as $\dot{\mathbf{B}}$ does to $\mathbf{E}$. By taking the curl of equation 3 and following the same modeling procedure, the magnetic induction time derivative $\dot{\mathbf{B}}$ can be written as a weighted summation of Chebyshev terms $\mathbf{P}$. As can be shown by mathematical induction, the field $\mathbf{P}$ shares the same continuity condition with the field $\dot{\mathbf{B}}$. In the air layer, in which the conductivity is zero, they both propagate their information instantaneously without any decay.

We first look at the vertical component $\dot{B}_z$ and its Chebyshev term P_z, which has the largest magnitude when the source is a horizontal dipole. The term B_z is continuous across the earth-air interface. Therefore, P_z is also continuous, which allows it to be interpolated at the surface and supports the continuation of it into the air, as shown in equation 13. The horizontal components of a potential field satisfying equation 12 can be calculated from its vertical component on the same horizontal plane (e.g., Macnae 1984; Wang and Hohmann, 1993), and P_x and P_y can be obtained from P_z as

$$\tilde{P}_x(k_x, k_y, z) = -\frac{ik_x}{\sqrt{k_x^2 + k_y^2}}\tilde{P}_z(k_x, k_y, z) \quad (15)$$

and

$$\tilde{P}_y(k_x, k_y, z) = -\frac{ik_y}{\sqrt{k_x^2 + k_y^2}}\tilde{P}_z(k_x, k_y, z), \qquad (16)$$

where $\tilde{P}_x$, $\tilde{P}_y$, and $\tilde{P}_z$ are the fields P_x, P_y, and P_z after a 2D Fourier transform along the horizontal axes. Therefore, the modeling of P_x and P_y can also benefit from P_z. The air is included as a special layer through the modeling. We use at least two nodes to define the air layer. It is simulated together with the earth grids under the REM structure except that for each Chebyshev term, the values in the air layer need to be updated explicitly by the upward continuation.

Inclusion of the earth-air interface in REM is summarized as follows. For each Chebyshev term $\mathbf{Q}$, whenever the propagation matrix $\mathbf{G}$ needs to be applied, we replace this one step, double-curl computation with a two-step, single-curl computation, to implement the upward continuation in REM. Because the single-curl computation evaluates the first-order derivative, we need to use a staggered Fourier method to keep the phase continuity at the Nyquist wavenumber. For example, a phase-shift operator $\exp(\pm ik_z\Delta z/2)$ is applied when computing the z-derivative. All of the modifications are made during step 2 of the full space simulation and are summarized below:

2.1) Apply the phase shift operator $\mathbf{D}^{\pm}$ to the electric field $\tilde{\mathbf{Q}}$ and compute the curl of it in the wavenumber domain. The obtained Chebyshev term $\tilde{\mathbf{P}}$ is staggered to $\tilde{\mathbf{Q}}$ and corresponds to the time derivative of the magnetic induction $\dot{\mathbf{B}}$.

2.2) Take the surface field of $\tilde{P}_z$ and update the values of $\tilde{\boldsymbol{P}}$ in the air layer, where $\tilde{P}_z$ is updated by the upward continuation (equation 13) and $\tilde{P}_x$ and $\tilde{P}_y$ are obtained from $\tilde{P}_z$ (equations 15 and 16).

2.3) Apply another phase shift operator $\mathbf{D}^{\mp}$ to the updated $\tilde{\mathbf{P}}$ and compute the curl of it, and multiply the result by $-\mu_0^{-1}\boldsymbol{\sigma}^{-1}$.

For the earth grids, the combination of steps 2.1–2.3 is equivalent to computing the propagation matrix $\mathbf{G}$ (equation 4), without violating any results discussed in the previous sections, except now the earth-air interface has been included by the addition of an air layer. Note that, although $\tilde{\mathbf{Q}}$ and $\tilde{\mathbf{P}}$ are staggered, $\tilde{\mathbf{Q}}$ and $\boldsymbol{\sigma}$ are always defined at the same position, which supports the inclusion of anisotropy as discussed before. Steps 1, 3, and 4 remain unchanged for the half-space simulation. The additional cost mainly comes from the required forward and inverse Fourier transforms. The process of upward continuation can also be parallelized if necessary (Commer and Newman, 2004).

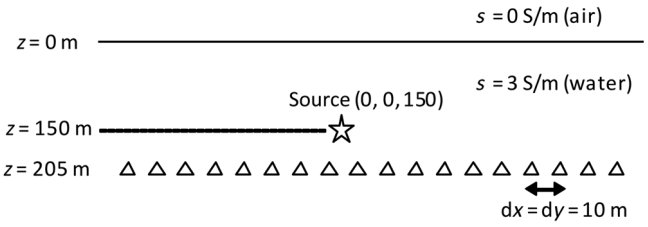

Figure 1. Model configuration: a homogeneous half-space model. The air-water interface is defined as $z = 0$ m. The node spacing is 10 m and is arranged such that the first layer of nodes is 5 m below the air-water interface. The dipole source is located 150 m below the air-water interface in the center with coordinates $x = y = 0$. The receivers are located 55 m below the source, on nodes.

NUMERICAL EXAMPLES

In this section, we present numerical tests to demonstrate the accuracy and sensitivity of the REM solution. First, we check our code in a homogeneous half-space against the analytical solution given by Slob et al. (2010). Then, we add VTI layers to the half-space and check the solution against the published 1D EMmod modeling code (Hunziker et al., 2015). Finally, we test the performance of the REM when TTI anisotropy and 3D resistive anomalies are present.

We have written the algorithm in a parallel FORTRAN code (see paper 1) and an alternative MATLAB code. For the tests below with synthetic data and computationally small models, we show the results from the MATLAB code, running on a desktop machine with a single processor (3.20 GHz). The model is constructed using $128 \times 128 \times 128$ nodes. The initial field is built with $t_0 = 10^{-3}$ s after some preliminary tests.

Homogeneous half-space

We set the conductivity of the medium to be 3 S/m to consider a marine CSEM case. Figure 1 shows the model configuration, with the earth-air interface at $z = 0$, the nodes in the earth are at $z = 5$, 15, 25 m, etc. As shown in paper 1, the x-directed dipole is not at a node and is placed at $z = 150$ m below the air-water interface in the center of the model with coordinates $x = y = 0$ m. The receivers are located 55 m below the source; that is, the receivers are on nodes. The grid spacing is 10 m along each direction, and we use nine grids (nodes) to represent the air layer.

Figure 2 examines the half-space modeling results in the spatial domain. The absolute amplitudes of three electric components are compared with the explicit Green's tensors given by Slob et al. (2010) along all of the inline receivers with coordinate $y = 5$ m. The REM results show excellent agreement with the analytical solution. For a duration of 60 ms, the sum of relative difference along 128 grids is calculated as 0.75% for E_x, 0.75% for E_y, and 1.08% for E_z. This level of accuracy is similar to the 2D full-space example shown in Carcione (2006). The magnitude of E_x is usually larger than the magnitudes of E_y and E_z, and the inline electric field is usually more robust in the presence of actual or numerical noise.

The airwave refers to the electric field refracted at the earth-air interface, traveling through the air at the speed of light and propagating vertically downward into the earth. We calculate the airwave using the analytic solution (Slob et al., 2010) and show it in dashed lines in Figure 2 to compare the strength of it with the total electric field at different time points. Because the source and the receivers are buried in the conductive medium, the total field is the airwave and the direct field plus scattering of both.

Figure 3 compares the half-space modeling results in the time domain. We use 90 time samples distributed logarithmically from 0.001 to 0.5 s. Because the electric field in time is reconstructed from the Chebyshev terms, we have the flexibility to choose a linear or a logarithmic time scale and the computational cost depends only on the maximum time of the response. The three receivers shown below are located on the same inline $y = 5$ m, but with three different source-receiver offsets 105, 255, and 405 m, respectively, in the x-direction, considering the near, mid, and far offsets. The REM solution fits well with the analytical solution, which again demonstrates the accuracy of this method. If we move the receiver further away from the source, the accuracy starts to decrease as the effect of numerical boundaries becomes more severe. For a model using the Dirichlet boundary

condition or periodic boundary condition, distortions from the boundaries are inevitable. For these boundary conditions, the model needs to be sufficiently large for a given propagation time.

The results of Figure 2 (time duration 60 ms) use $M = 340$ Chebyshev terms, and the results of Figure 3 (time duration 500 ms) use $M = 1000$. The required number of Chebyshev terms is propor-

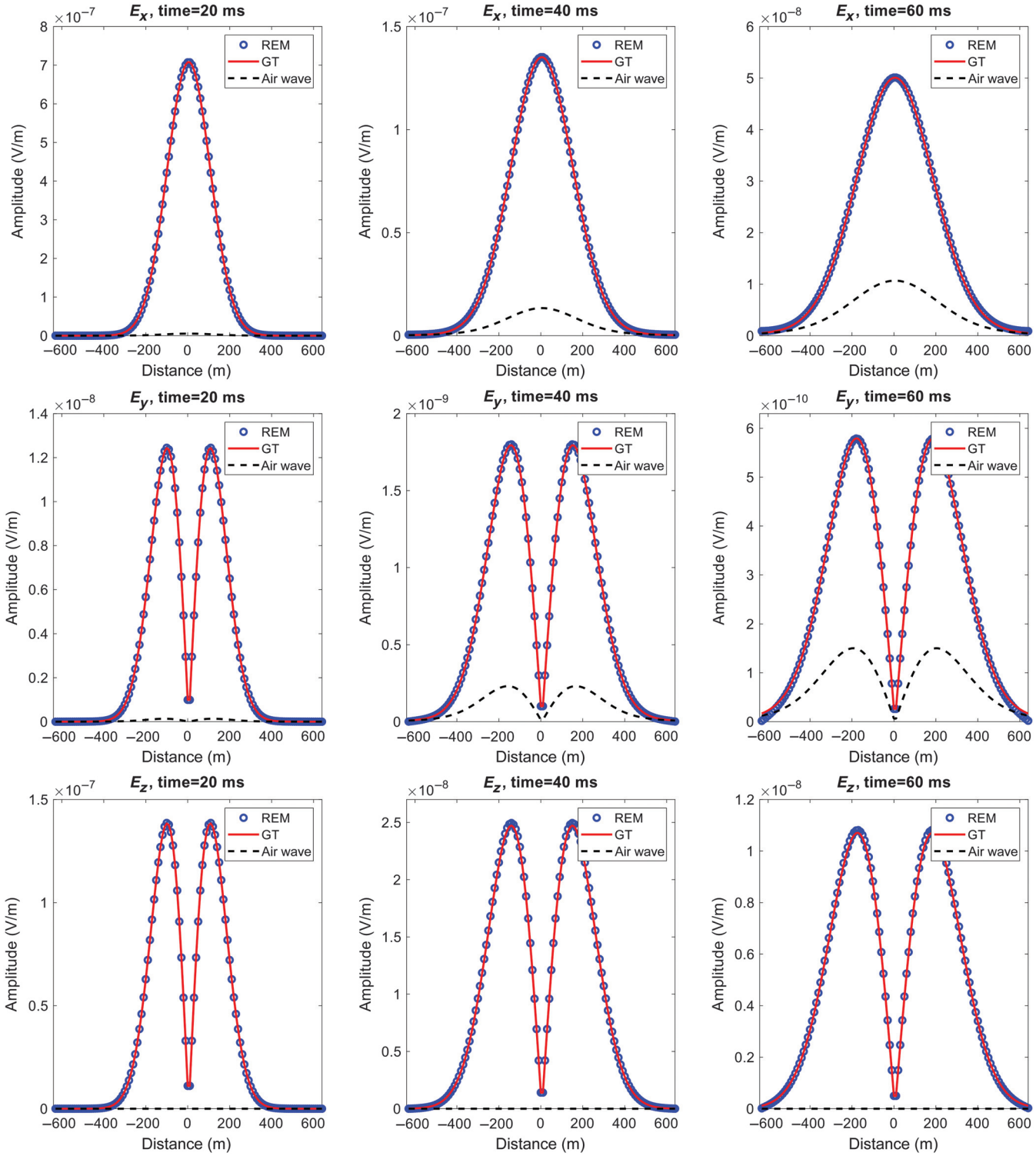

Figure 2. Homogeneous half-space results: comparison of the absolute amplitude of three electric components in the space domain. The REM solutions are denoted by the circles, and the Green's tensors (analytical solution) are denoted by the solid lines. The airwave (analytic solution) is shown in the dashed lines. From left to right shows the field of 20, 40, and 60 ms after constructing the initial field. The source (0, 0, 150) m is located in the center of the horizontal plane and 150 m below the air-water interface. The inline receivers are located 55 m below the source with coordinate $y = 5$ m.

tional to the square root of the maximum time. And we have the option to use a logarithmic time scale to save storage (because we only update the Chebyshev terms). This shows the advantage of this method in long time EM modeling. The execution time took approximately 300 s for the first example and 1800 s for the second example with a single processor.

Layered half-space with VTI and TTI anisotropy

Then, we include anisotropy in the modeling. We first check the accuracy of the REM solution in 1D VTI models against EMmod (Hunziker et al., 2015). EMmod simulates the 3D EM field in a 1D earth in the frequency-wavenumber domain, and it is transformed back to space through a Hankel transformation. We need to select several frequencies and transform the results back to the time domain via an IFFT. Because the solution is constructed in a 1D model, it does not suffer from the boundary problems like the 3D methods.

We show two examples. First, we put sediments beneath a water layer, as illustrated in Figure 4a. To consider a more realistic situation than the isotropic assumption, we consider mild VTI anisotropy. The vertical ρ_v and horizontal ρ_h resistivities of the sediments are defined as 2 and 1 ohm-m, respectively, with VTI anisotropy $\lambda = \sqrt{\rho_v/\rho_h} = \sqrt{2}$. The dipole source is located 150 m below the air-water interface, and the receivers are located just above the seabed.

Figure 5 compares the inline electric field in the time domain. The EMmod results consist of 250 time samples linearly distributed from 2 to 500 ms, and we use the same logarithmic time sampling (90 samples from 1 to 500 ms) for REM. In general, the REM results show good agreement with the exact solution. At the near offset (105 m), the mismatch at early times (before 0.01 s) is essentially due to the mismatch of the time sampling. REM uses 33 time samples to capture the first peak before 0.01 s, whereas we use 5 time samples with EMmod. For these parameters, the early-time, sharp variation of the electric field is better characterized by the REM results. The very accurate near-offset, early-time modeling results should lead to a confident estimate of the shallow conductivity in the inversion, which is fundamental to the further inversion of deeper sections. A slight divergence of the curves can be observed for far-offset (405 m) results. Compared with the half-space model, the late-time, far-offset divergence indicates that distortions from the numerical boundaries arrive earlier in this case because the diffusive speed in the sediment layer is faster. In contrast, the 1D solution is free of numerical boundary problems.

Then, we insert a 100 m thick, isotropic 1D resistor into the anisotropic sediments at 100 m beneath the seabed, as shown in Figure 4b. The same time-domain comparison is made and shown in Figure 6. The near-offset results still show excellent agreement. The mid- and far-offset results are accurate at early times, but they suffer more severe boundary distortion at late times and toward the edge of the model. The maximum signal at any distance d arrives at time $t = \mu\sigma d^2/4$ (Carcione, 2006), and for the resistive layer with $\sigma = 0.02$ S/m it takes only 2.6 ms for the diffusive field to travel from the center to the edge. A time recording of 500 ms is clearly beyond the ability of this 1 km size model. However, in real 3D problems, the boundary effect can be efficiently attenuated with two factors: (1) resistors are usually 3D bodies with finite size surrounded by conductive sediments in which the diffusion can be slowed down and attenuated and (2) a much larger model is often used in CSEM modeling and such effects can be moved out to later times and larger distances.

Up to this point, we have examined the REM solutions with the amplitudes shown on a linear scale, so that any differences can be clearly observed. In some cases, however, it is the order of magnitude that needs to be determined rather than the amplitude itself. Therefore, it is common to compare the modeling results on a logarithmic scale (e.g., Wang and Hohmann, 1993; Commer and Newman, 2004). Figure 7 shows the results of Figure 6 on a logarithmic scale. The maximum relative difference is approximately 11% on the linear-scale amplitude, calculated at the peak values of the far-offset results. The same amount of difference reduces to 0.6% after taking the base 10 logarithm of the amplitudes. Although contaminated with numerical reflections from the boundaries, the REM results show good

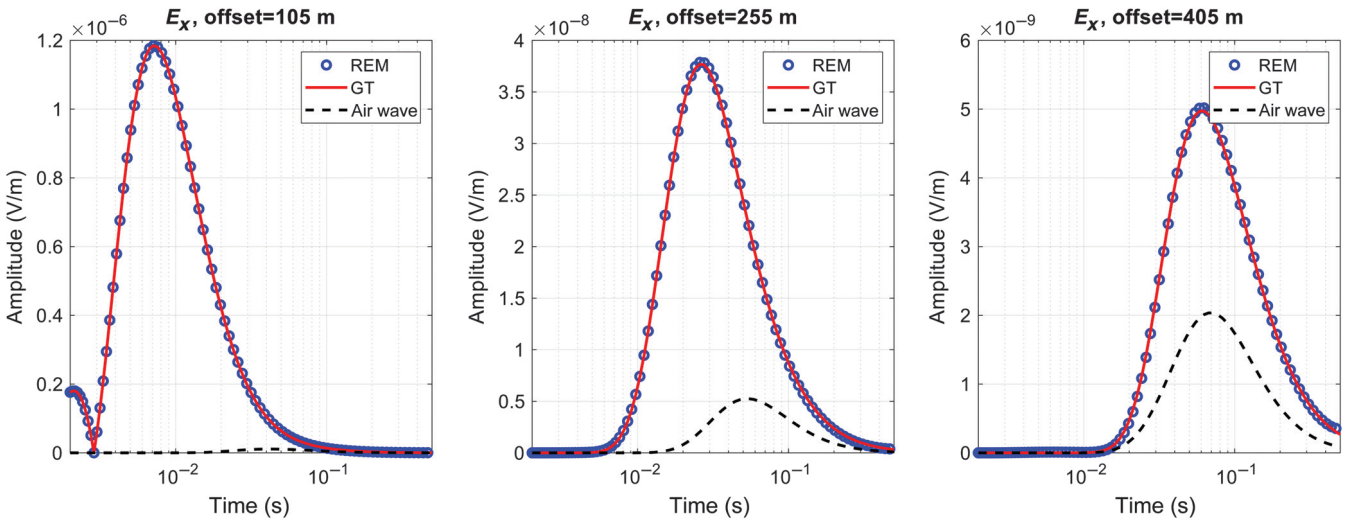

Figure 3. Homogeneous half-space results: comparison of the absolute amplitude of the inline electric field in the time domain. The REM solutions are denoted by the circles, and the Green's tensors (analytical solution) are denoted by the solid lines. The airwave (analytic solution) is shown in the dashed lines. From left to right, the graphs show the responses at inline receivers ($y = 5$ m) with offsets of 105, 255, and 405 m in the x-direction, respectively. The source is located in the center of the horizontal plane and 150 m below the air-water interface.

agreement with the calibration code in terms of determining the order of magnitude.

We rotate the transverse isotropic plane of the anisotropic sediments 30° clockwise around the y-axis, considering a TTI anisotropy case (strike $\varphi = 0°$, dip $\theta = 30°$) as shown in Figure 4c. We show snapshots of the Chebyshev terms Q_x in Figure 8 to compare the VTI and TTI example. The tilt of the propagation of the wavefield is clearly observed in the TTI sediments. Reflections from the air-water interface and the water-sediments interface can also be distinguished in both cases. Numerical dispersion is hardly observed. The change of amplitude is plotted in Figure 9, comparing the inline electric field at the same receiver position. The amplitude change is noticeable in

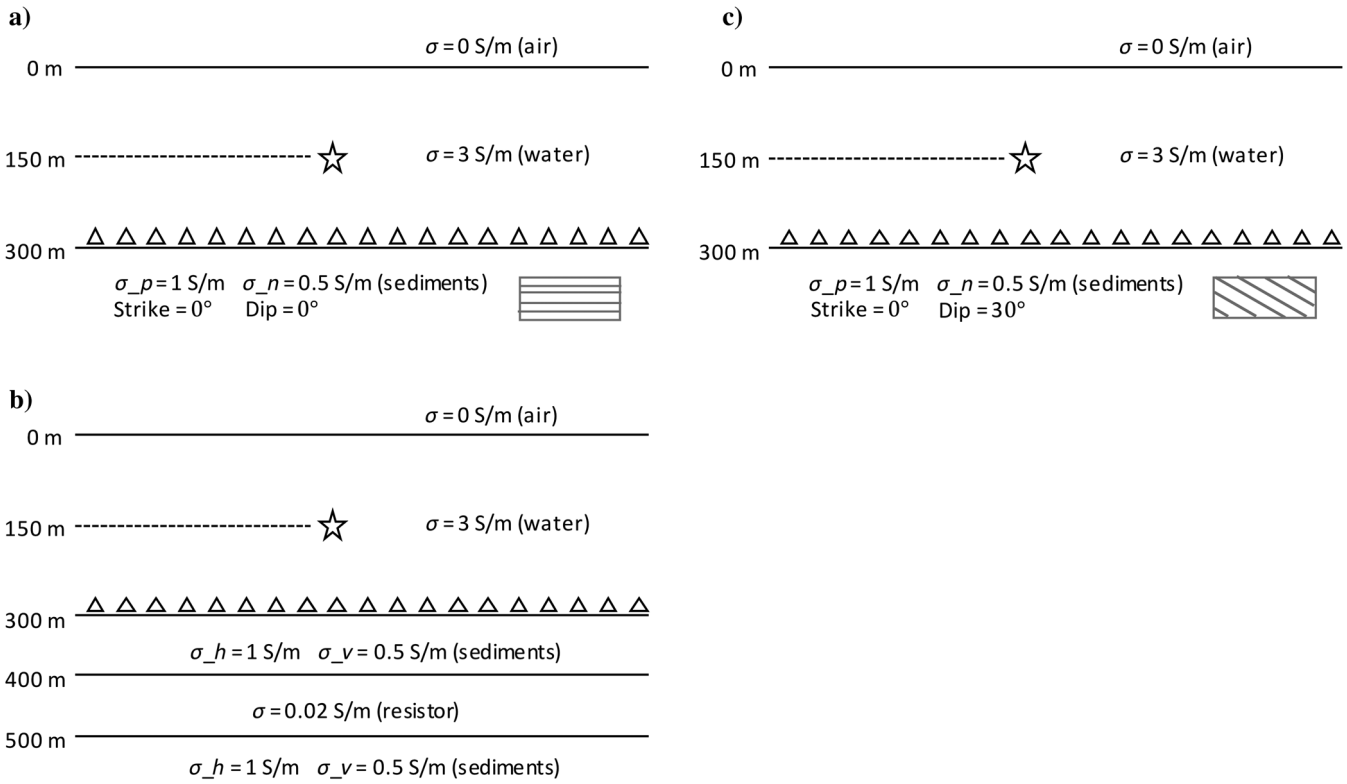

Figure 4. Model configuration: layered anisotropic half-space. The 1D model consists of a 300 m thick water layer beneath the air, and a layer of (a) VTI anisotropic sediments, (b) VTI anisotropic sediments plus a 100 m thick resistive layer, and (c) TTI sediments with a 30° dip.

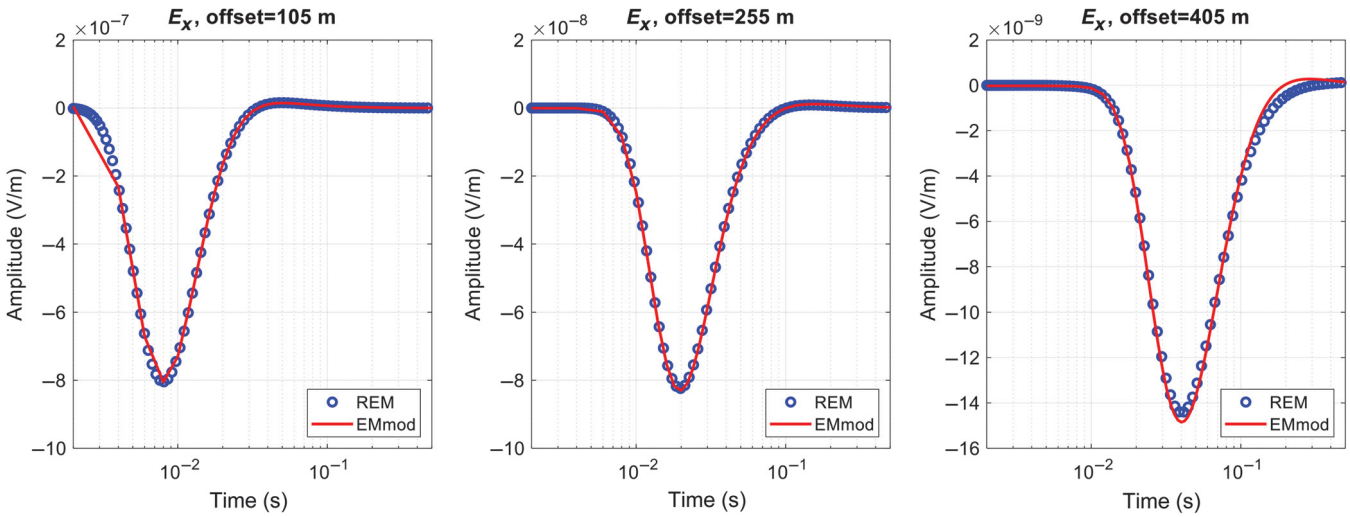

Figure 5. Layered half-space with VTI anisotropy: comparison of the inline electric field in the time domain. The REM and EMmod solutions are denoted by the circles and solid lines. From left to right, the graphs show the responses at crossline receivers ($x = 5$ m) with offsets in the y-direction of 105, 255, and 405 m, respectively. The model configuration is illustrated in Figure 4a.

the mid and far offsets in which the scattered field has a relatively higher contribution than the direct field. These examples demonstrate the ability of REM to handle VTI and TTI types of conductivity.

Finally, we test our code with 3D variations of conductivity with a sharp material contrast (a factor of 50). A $200 \times 200 \times 100$ m block, with an anomalous conductivity, is inserted into the background model of Figure 4a. We consider a resistive case (0.02 S/m) and a conductive case (50 S/m). The resulting new models are shown in Figure 10a and 10b, respectively. Figures 11 and 12 show the x-z plane snapshots of the inline electric field when the 3D anomalies are included. Sharp variations of the conductivity lead to velocity contrasts of the propagating field, and the boundaries of the anomalous block in both situations are imaged very well by the variation of the electric field when traveling through it, especially the vertical boundaries. Nonphysical noise is hardly seen with the presence of sharp material contrasts. This example demonstrates the ability of REM to handle 3D problems.

DISCUSSION

The PS REM method is an explicit method that solves the time evolution of the diffusive electric field. Compared with implicit methods, explicit methods are attractive in terms of their simplicity and robustness in the presence of large conductivity contrasts. An explicit method is also found to be reliable to produce accurate results over a large dynamic time range (Commer and Newman, 2004). The major drawback of the explicit method is the stringent stability condition, which leads to a high computational effort. The Chebyshev approach, however, is an efficient and attractive explicit method for two reasons. First, the number of evaluations of the propagation matrix required by REM is much fewer than the second-order finite difference in time. For example, considering the 3D example shown in Figure 10a with a minimum conductivity of 0.02 S/m, the maximum diffusion time step by finite differences (Potter, 1973) is $\Delta t = \mu\sigma\Delta x^2/4 \approx 6.28 \times 10^{-7}$ s, and a simulation of 1 s requires the matrix $\mathbf{G}$ to be evaluated for $t/\Delta t \approx 1.59 \times 10^6$ times. However, the Chebyshev approach requires approximately 1.7×10^5 evaluations of $\mathbf{G}$, which is about an order of magnitude cheaper. And this efficiency further increases with the length of simulation time. Thus, it is beneficial for long-time simulations. Second, the Chebyshev method does not require the computation of inner products, which is highly beneficial in parallel computing. This is the advantage of the proposed method over the Krylov approach (Carcione, 2006).

We deliberately used a small model that would fit into a standard desktop or laptop machine and compute in a reasonable time, to demonstrate that the method is practical to use. There are edge effects that lead to small errors in the far-offset results. One solution to that is to move to a bigger machine and extend the model size. An alternative solution is to add perfectly matched layers (PMLs). As shown in paper 1, the Chebyshev terms are essentially waves in the Chebyshev domain, and the PML designed for EM waves should be well-suited to the Chebyshev terms to eliminate edge effects.

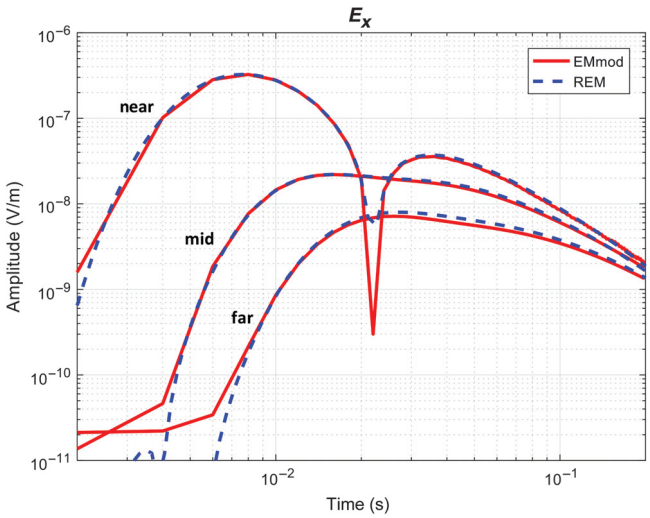

Figure 7. Comparison of the inline electric field with amplitude in logarithmic scale. The same EMmod and REM results of Figure 8 are now compared on a logarithmic scale, shown by the solid and dashed lines.

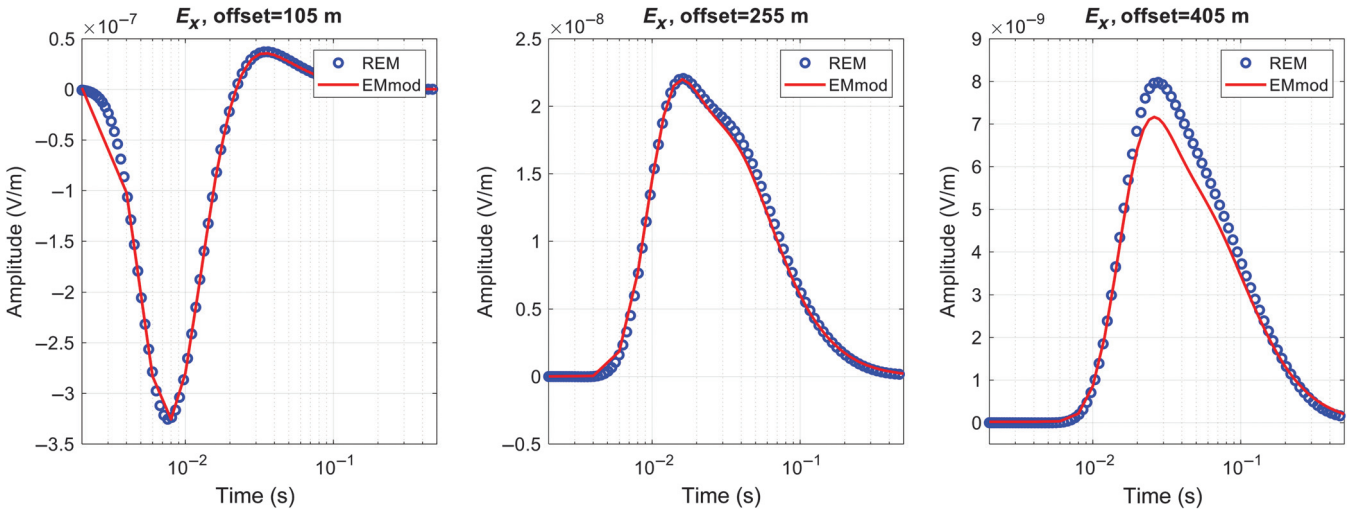

Figure 6. Layered half-space with VTI anisotropy and resistor: comparison of the inline electric field in the time domain. The REM and EMmod solutions are denoted by the circles and solid lines. From left to right, the graphs show the responses at inline receivers ($y = 5$ m) with offsets in the x-direction of 105, 255, and 405 m, respectively. The model configuration is illustrated in Figure 4b.

We use regular spacing because of the numerical efficiency of the FFT and we can apply the PS method to obtain accurate spatial derivatives. In some situations, however, this may not be the best parameterization of the model. Certain model configurations pose problems for regular grids and irregular grids may be more appropriate. Paper 1 mentions the towed streamer and towed shallow

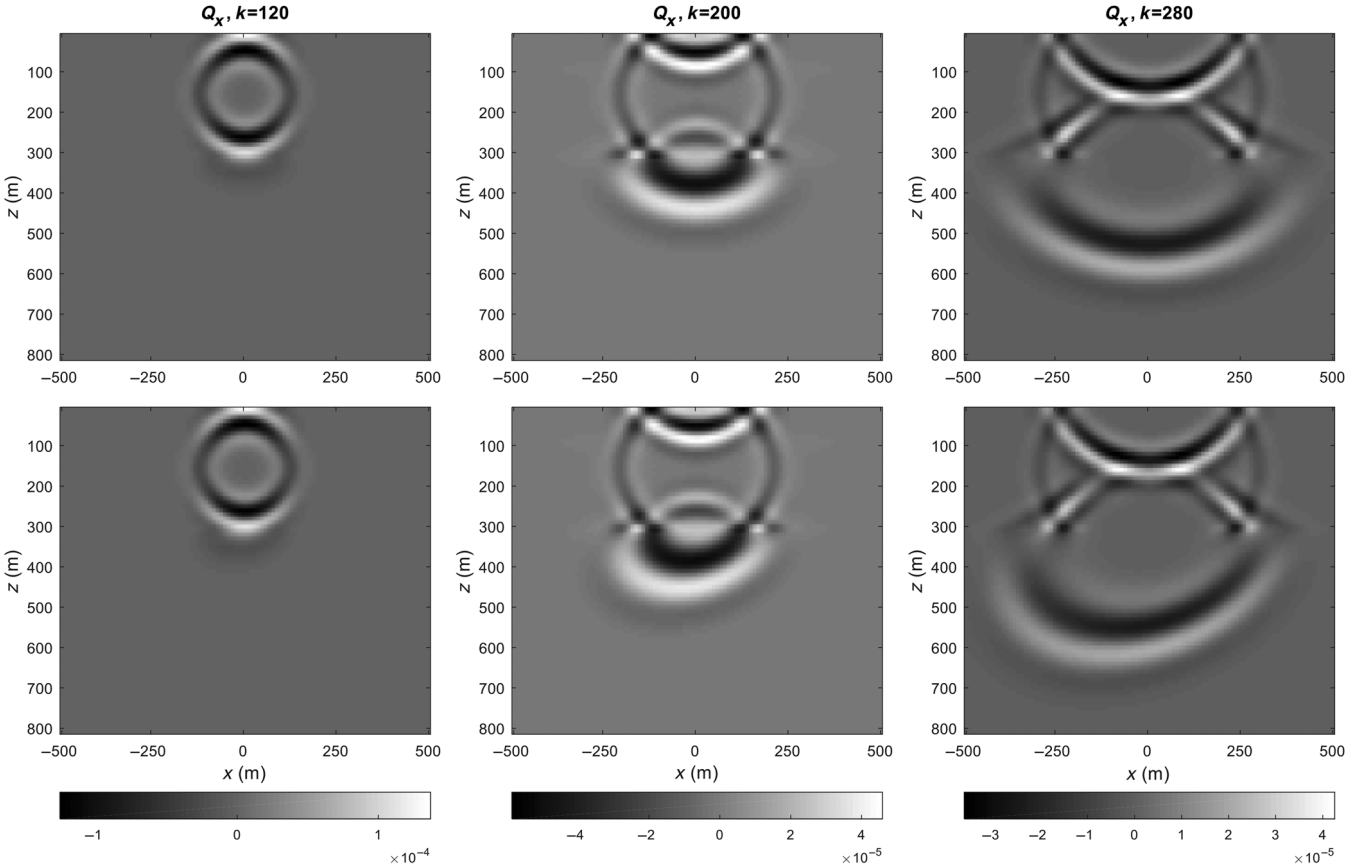

Figure 8. Snapshots of Q_x. The x-z plane locates on $y = 5$ m. The model configurations are shown in Figure 4a and 4c, for the top and bottom row, to consider the VTI and the TTI sediments, respectively. From left to right, the graphs show the snapshots of the 120th, the 200th, and the 280th Chebyshev term of the x-component electric field, respectively.

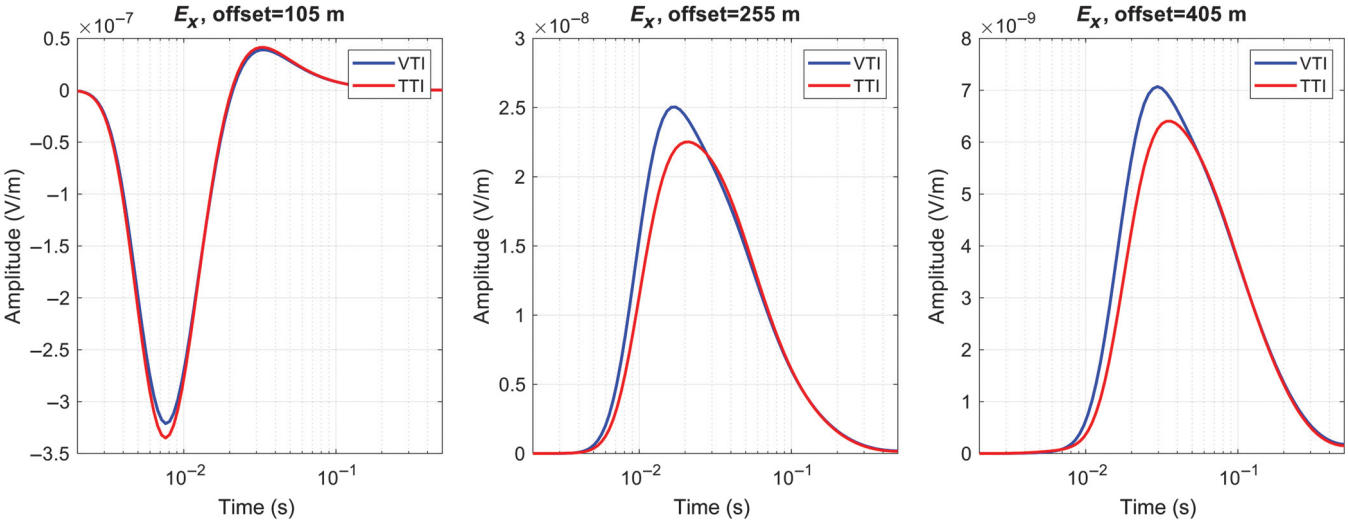

Figure 9. Layered half-space with VTI and TTI anisotropy: comparison of the inline electric field in the time domain. The solutions in the VTI and TTI case are denoted by the black and gray lines, respectively. From left to right, the graphs show the responses at inline receivers ($y = 5$ m) with offsets in the x-direction of 105, 255, and 405 m, respectively. The model configurations are illustrated in Figure 4a and 4c.

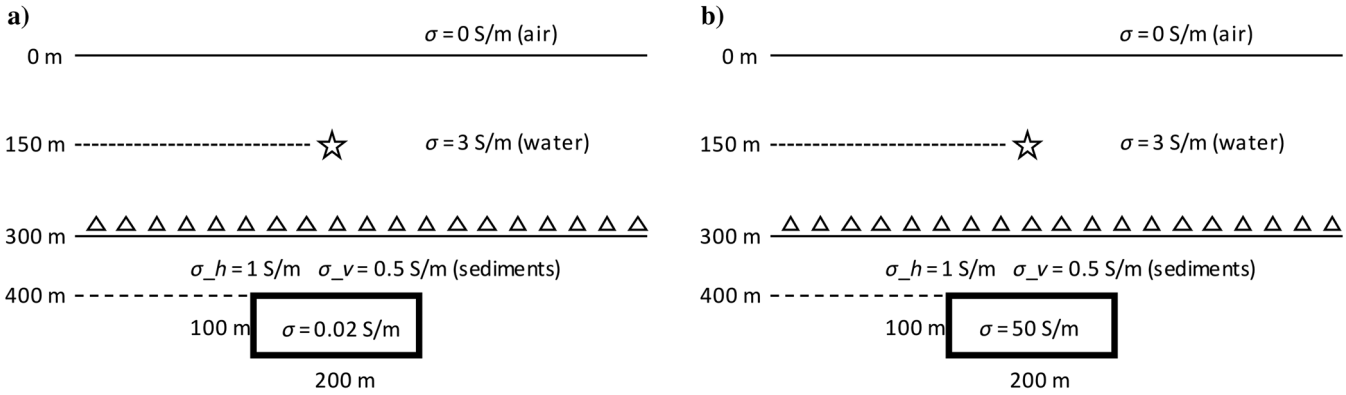

Figure 10. Model configuration: layered half-space with VTI anisotropic sediments and a 3D resistivity anomaly. The 3D anomalous block has a size of $200 \times 200 \times 100$ m. It is put into the background model as shown in Figure 4a, with its center right below the dipole source. The anomalous conductivities are (a) 0.02 S/m and (b) 50 S/m, respectively, to consider the presence of a 3D resistor and a 3D conductor.

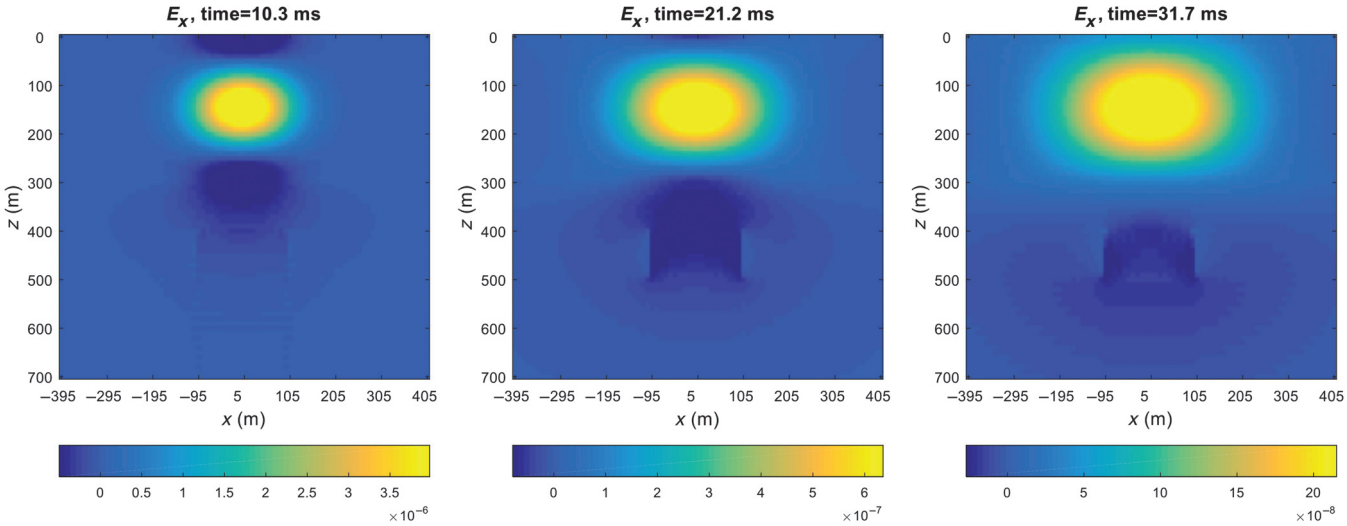

Figure 11. Test of the presence of a 3D resistor: wavefield snapshots. From left to right, the graphs show the x-component snapshots on the x-z plane ($y = 5$ m) at time 10.3, 21.2, and 31.7 ms. The model configuration is illustrated in Figure 9a.

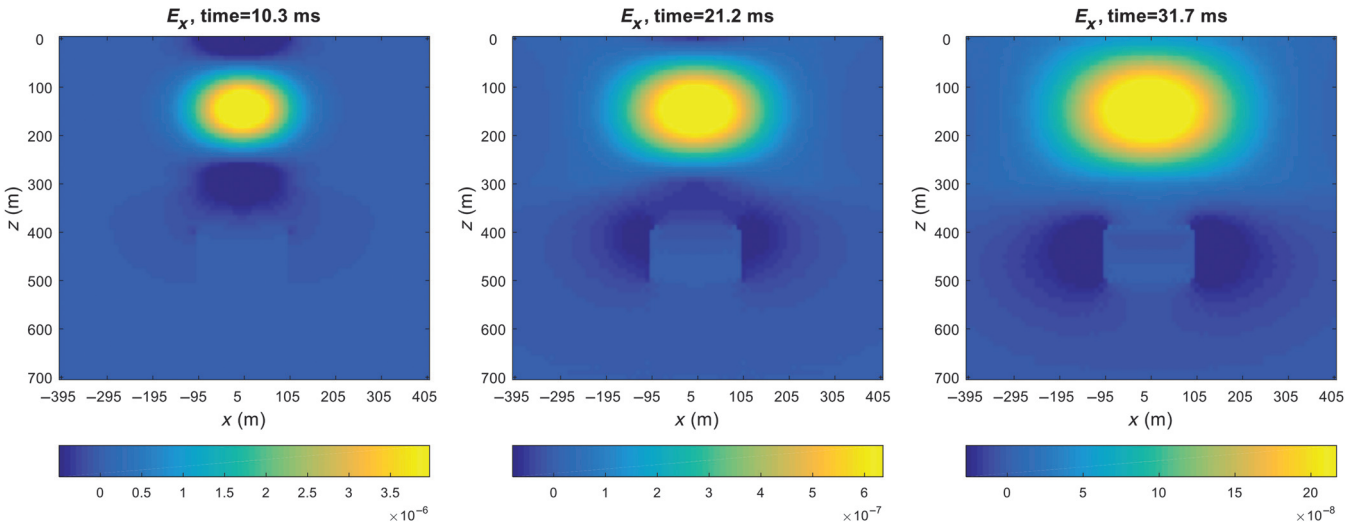

Figure 12. Test of the presence of a 3D conductor: wavefield snapshots. From left to right, the graphs show the x-component snapshots on the x-z plane ($y = 5$ m) at time 10.3, 21.2, and 31.7 ms. The model configuration is illustrated in Figure 9b.

source system for marine EM surveying (Anderson and Mattsson, 2010). Tests using 1D modeling by REM show that a source with depth 20–40 m requires the spatial interval to be approximately 2 m to propagate the field successfully. For an explicit time-domain modeling method, the use of very fine grids is inevitable when modeling a shallow source, no matter what modeling method is used: finite difference, finite element, or REM. We emphasize that the problem of spatial sampling has nothing to do with REM, which is concerned only with the time-stepping component of the evolution. REM can doubtless cope with irregular grids: An eigenvalue analysis will be required for the limiting case, and the time stepping interval will be determined by the lowest resistivity (fastest speed) and the smallest spatial grid block.

CONCLUSION

We have presented two extensions of the PS REM method to solve the 3D diffusive electric field in the time domain. (1) Any type of anisotropy can be included in the modeling with the manipulation of the conductivity tensor. (2) The response from the earth-air interface is modeled using the upward continuation of the time derivative of the magnetic induction. Numerical tests against 1D spectral methods have demonstrated the excellent accuracy of this method.

This algorithm has several appealing features. First, the estimation of partial derivatives has spectral accuracy in space and time. This is a clear advantage over low-order approximations of derivatives. Second, time evolution by the Chebyshev approach is efficient and flexible, and it is well-suited to parallel computing. Third, all field components are sampled at the same location as the conductivity. The interface of material properties is exactly defined half-way between the grids without any averaging or transition layer. This is another advantage over the conventional Yee's grid used by FD methods. Finally, the inclusion of various types of anisotropy in the modeling is straightforward.

ACKNOWLEDGMENTS

We thank the assistant editor J. Shragge, reviewer R. Mittet, and two anonymous reviewers, who all provided very constructive comments and suggestions that greatly improved the paper.

DATA AND MATERIALS AVAILABILITY

The paper contains only synthetic data calculated using algorithms described in the paper or using published code, as detailed in the paper.

APPENDIX A

EIGENVALUES OF THE PROPAGATION MATRIX

In the wavenumber domain, the spatial derivatives ∂_x, ∂_y, and ∂_z are replaced by ik_x, ik_y, and ik_z, respectively, and the propagation matrix $\mathbf{G}$ is given as

$$\mathbf{G}=-\frac{1}{\mu_0}\begin{pmatrix} x_{11} & x_{12} & x_{13} \\ x_{21} & x_{22} & x_{23} \\ x_{31} & x_{32} & x_{33} \end{pmatrix}\begin{pmatrix} k_y^2+k_z^2 & -k_xk_y & -k_xk_z \\ -k_xk_y & k_x^2+k_z^2 & -k_yk_z \\ -k_xk_z & -k_yk_z & k_x^2+k_y^2 \end{pmatrix}, \tag{A-1}$$

where the elements x_{ij} correspond with the inverse of the conductivity tensor. With the rotation matrix and the conductivity tensor given in equations 5 and 6, the elements x_{ij} are solved as

$$x_{11}=\frac{1}{\sigma_p}(\cos^2\theta\cos^2\varphi+\sin^2\varphi)+\frac{1}{\sigma_n}\sin^2\theta\cos^2\varphi, \tag{A-2}$$

$$x_{22}=\frac{1}{\sigma_p}(\cos^2\theta\sin^2\varphi+\cos^2\varphi)+\frac{1}{\sigma_n}\sin^2\theta\sin^2\varphi, \tag{A-3}$$

$$x_{33}=\frac{1}{\sigma_p}\sin^2\theta+\frac{1}{\sigma_n}\cos^2\theta, \tag{A-4}$$

$$x_{12}=x_{21}=\left(\frac{1}{\sigma_n}-\frac{1}{\sigma_p}\right)\sin^2\theta\,\sin\,\varphi\,\cos\,\varphi, \tag{A-5}$$

$$x_{13}=x_{31}=\left(\frac{1}{\sigma_n}-\frac{1}{\sigma_p}\right)\sin\,\theta\,\cos\,\theta\,\cos\,\varphi, \tag{A-6}$$

$$x_{32}=x_{23}=\left(\frac{1}{\sigma_n}-\frac{1}{\sigma_p}\right)\sin\,\theta\,\cos\,\theta\,\sin\,\varphi. \tag{A-7}$$

Let us define $\mathbf{G}=-\mu_0^{-1}\mathbf{g}$, and the matrix $\mathbf{g}$ is therefore the product of the inverse conductivities and the wavenumbers containing nine elements as

$$\mathbf{g}=\begin{pmatrix} g_{11} & g_{12} & g_{13} \\ g_{21} & g_{22} & g_{23} \\ g_{31} & g_{32} & g_{33} \end{pmatrix}. \tag{A-8}$$

The eigenvalues of a 3×3 matrix $\mathbf{g}$ satisfy

$$\begin{aligned}&-\lambda^3+\lambda^2(g_{11}+g_{22}+g_{33})+\lambda(g_{31}g_{13}+g_{21}g_{12}\\&\quad+g_{32}g_{23}-g_{11}g_{22}-g_{22}g_{33}-g_{11}g_{33})+\\&(g_{11}g_{22}g_{33}+g_{12}g_{23}g_{31}+g_{13}g_{21}g_{32}-g_{31}g_{22}g_{13}\\&\quad-g_{32}g_{23}g_{11}-g_{33}g_{21}g_{12})=0.\end{aligned} \tag{A-9}$$

In the isotropic case, zero is one of the eigenvalues of the propagation matrix. Therefore, it is also one of the eigenvalues in the anisotropic case, that is, $\lambda_1=0$. This yields

$$\begin{aligned}&g_{11}g_{22}g_{33}+g_{12}g_{23}g_{31}+g_{13}g_{21}g_{32}-g_{31}g_{22}g_{13}\\&\quad-g_{32}g_{23}g_{11}-g_{33}g_{21}g_{12}=0.\end{aligned} \tag{A-10}$$

The rest terms in equation A-9 are calculated as

$$g_{11}+g_{22}+g_{33}=(k_y^2+k_z^2)x_{11}+(k_x^2+k_z^2)x_{22}+(k_x^2+k_y^2)x_{33}-2k_xk_yx_{12}-2k_xk_zx_{13}-2k_yk_zx_{32} \quad \text{(A-11)}$$

and

$$\begin{aligned}&g_{31}g_{13}+g_{21}g_{12}+g_{32}g_{23}-g_{11}g_{22}-g_{22}g_{33}-g_{11}g_{33}\\&=-k_z^2(k_x^2+k_y^2+k_z^2)(x_{11}x_{22}-x_{12}x_{12})\\&\quad-k_x^2(k_x^2+k_y^2+k_z^2)(x_{22}x_{33}-x_{23}x_{23})\\&-k_y^2(k_x^2+k_y^2+k_z^2)(x_{11}x_{33}-x_{13}x_{13})\\&\quad+2k_yk_z(k_x^2+k_y^2+k_z^2)(x_{11}x_{23}-x_{12}x_{13})\\&+2k_xk_z(k_x^2+k_y^2+k_z^2)(x_{13}x_{22}-x_{12}x_{23})\\&\quad+2k_xk_y(k_x^2+k_y^2+k_z^2)(x_{12}x_{33}-x_{13}x_{23}).\end{aligned} \quad \text{(A-12)}$$

The six quantities relating to the inverse conductivities are calculated and rearranged in the form of

$$x_{11}x_{22}-x_{12}x_{12}=\frac{1}{\sigma_p^2}+\frac{1}{\sigma_p}\left(\frac{1}{\sigma_n}-\frac{1}{\sigma_p}\right)\sin^2\theta, \quad \text{(A-13)}$$

$$x_{22}x_{33}-x_{23}x_{23}=\frac{1}{\sigma_p^2}+\frac{1}{\sigma_p}\left(\frac{1}{\sigma_n}-\frac{1}{\sigma_p}\right)(\sin^2\theta\sin^2\varphi+\cos^2\theta), \quad \text{(A-14)}$$

$$x_{11}x_{33}-x_{13}x_{13}=\frac{1}{\sigma_p^2}+\frac{1}{\sigma_p}\left(\frac{1}{\sigma_n}-\frac{1}{\sigma_p}\right)(\sin^2\theta\cos^2\varphi+\cos^2\theta), \quad \text{(A-15)}$$

$$x_{11}x_{23}-x_{12}x_{13}=\frac{1}{\sigma_p}\left(\frac{1}{\sigma_n}-\frac{1}{\sigma_p}\right)\sin\theta\cos\theta\sin\varphi, \quad \text{(A-16)}$$

$$x_{13}x_{22}-x_{12}x_{23}=\frac{1}{\sigma_p}\left(\frac{1}{\sigma_n}-\frac{1}{\sigma_p}\right)\sin\theta\cos\theta\cos\varphi, \quad \text{(A-17)}$$

$$x_{12}x_{33}-x_{13}x_{23}=\frac{1}{\sigma_p}\left(\frac{1}{\sigma_n}-\frac{1}{\sigma_p}\right)\sin^2\theta\sin\varphi\cos\varphi. \quad \text{(A-18)}$$

By combining equations from A-11 to A-18, the two nonzero eigenvalues of matrix **g** satisfy

$$\begin{aligned}\lambda_2+\lambda_3=&\frac{2}{\sigma_p}(k_x^2+k_y^2+k_z^2)+k_x^2\left(\frac{1}{\sigma_n}-\frac{1}{\sigma_p}\right)(\sin^2\theta\sin^2\varphi+\cos^2\theta)\\&+k_y^2\left(\frac{1}{\sigma_n}-\frac{1}{\sigma_p}\right)(\sin^2\theta\cos^2\varphi+\cos^2\theta)+k_z^2\left(\frac{1}{\sigma_n}-\frac{1}{\sigma_p}\right)\sin^2\theta\\&-2k_yk_z\left(\frac{1}{\sigma_n}-\frac{1}{\sigma_p}\right)\sin\theta\cos\theta\sin\varphi\\&-2k_xk_z\left(\frac{1}{\sigma_n}-\frac{1}{\sigma_p}\right)\sin\theta\cos\theta\cos\varphi\\&-2k_xk_y\left(\frac{1}{\sigma_n}-\frac{1}{\sigma_p}\right)\sin^2\theta\sin\varphi\cos\varphi\end{aligned} \quad \text{(A-19)}$$

and

$$\begin{aligned}\lambda_2\lambda_3=&\frac{1}{\sigma_p}(k_x^2+k_y^2+k_z^2)\left[\frac{1}{\sigma_p}(k_x^2+k_y^2+k_z^2)\right.\\&+k_x^2\left(\frac{1}{\sigma_n}-\frac{1}{\sigma_p}\right)(\sin^2\theta\sin^2\varphi+\cos^2\theta)\\&+k_y^2\left(\frac{1}{\sigma_n}-\frac{1}{\sigma_p}\right)(\sin^2\theta\cos^2\varphi+\cos^2\theta)+k_z^2\left(\frac{1}{\sigma_n}-\frac{1}{\sigma_p}\right)\sin^2\theta\\&-2k_yk_z\left(\frac{1}{\sigma_n}-\frac{1}{\sigma_p}\right)\sin\theta\cos\theta\sin\varphi\\&-2k_xk_z\left(\frac{1}{\sigma_n}-\frac{1}{\sigma_p}\right)\sin\theta\cos\theta\cos\varphi\\&\left.-2k_xk_y\left(\frac{1}{\sigma_n}-\frac{1}{\sigma_p}\right)\sin^2\theta\sin\varphi\cos\varphi\right].\end{aligned} \quad \text{(A-20)}$$

Therefore, the two nonzero eigenvalues are solved as

$$\lambda_2=\frac{1}{\sigma_p}(k_x^2+k_y^2+k_z^2) \quad \text{(A-21)}$$

and

$$\begin{aligned}\lambda_3=&\frac{1}{\sigma_p}(k_x^2+k_y^2+k_z^2)+k_x^2\left(\frac{1}{\sigma_n}-\frac{1}{\sigma_p}\right)(\sin^2\theta\sin^2\varphi+\cos^2\theta)\\&+k_y^2\left(\frac{1}{\sigma_n}-\frac{1}{\sigma_p}\right)(\sin^2\theta\cos^2\varphi+\cos^2\theta)+k_z^2\left(\frac{1}{\sigma_n}-\frac{1}{\sigma_p}\right)\sin^2\theta\\&-2k_yk_z\left(\frac{1}{\sigma_n}-\frac{1}{\sigma_p}\right)\sin\theta\cos\theta\sin\varphi\\&-2k_xk_z\left(\frac{1}{\sigma_n}-\frac{1}{\sigma_p}\right)\sin\theta\cos\theta\cos\varphi\\&-2k_xk_y\left(\frac{1}{\sigma_n}-\frac{1}{\sigma_p}\right)\sin^2\theta\sin\varphi\cos\varphi.\end{aligned} \quad \text{(A-22)}$$

Equation A-22 can be rearranged to give a compacted expression of λ_3, as shown in the main section of the paper.

REFERENCES

Anderson, C., and J. Mattsson, 2010, An integrated approach to marine electromagnetic surveying using a towed streamer and source: First Break, **28**, 71–75.

Carcione, J. M., 2006, Geophysical software and algorithms: A spectral numerical method for electromagnetic diffusion: Geophysics, **71**, no. 1, I1–I9, doi: 10.1190/1.2159050.

Commer, M., and G. Newman, 2004, A parallel finite-difference approach for 3D transient electromagnetic modeling with galvanic sources: Geophysics, **69**, 1192–1202, doi: 10.1190/1.1801936.

Edwards, R. N., D. C. Nobes, and E. Gomez-Trevino, 1984, Offshore electrical exploration of sedimentary basins: The effects of anisotropy in horizontally isotropic layered media: Geophysics, **49**, 566–576, doi: 10.1190/1.1441691.

Feise, M. W., J. B. Schneider, and P. J. Bevelacqua, 2004, Finite-difference and pseudospectral time-domain methods applied to backward-wave metamaterials: IEEE Transactions on Antennas and Propagation, **52**, 2955–2962, doi: 10.1109/TAP.2004.835274.

Hunziker, J., J. Thorbecke, and E. Slob, 2015, The electromagnetic response in a layered vertical transverse isotropic medium: A new look at an old problem: Geophysics, **80**, no. 1, F1–F18, doi: 10.1190/geo2013-0411.1.

Jaysaval, P., D. V. Shantsev, S. K. Ryhove, and T. Bratteland, 2016, Fully anisotropic 3-D EM modelling on a Lebedev grid with a multigrid preconditioner: Geophysical Journal International, **207**, 1554–1572, doi: 10.1093/gji/ggw352.

Macnae, J. C., 1984, Survey design for multicomponent electromagnetic systems: Geophysics, **49**, 265–273, doi: 10.1190/1.1441658.

Oristaglio, M. L., and G. W. Hohmann, 1984, Diffusion of electromagnetic fields into a two-dimensional earth: A finite-difference approach: Geophysics, **49**, 870–894, doi: 10.1190/1.1441733.

Potter, D., 1973, Computational physics: John Wiley and Sons.

Slob, E., J. Hunziker, and W. A. Mulder, 2010, Green's tensors for the diffusive electric field in a VTI half-space: Progress in Electromagnetics Research, **107**, 1–20, doi: 10.2528/PIER10052807.

Stoffa, P. L., and A. Ziolkowski, 2019, Time evolution of the electric field using the rapid expansion method (REM) with pseudo-spectral evaluation of spatial derivatives — Part 1: Geophysics, **84**, no. 5, 1–11, doi: 10.1190/GEO2018-0179.1.

Um, E. S., J. M. Harris, and D. L. Alumbaugh, 2010, 3D time-domain simulation of electromagnetic diffusion phenomena: A finite-element electric-field approach: Geophysics, **75**, no. 4, F115–F126, doi: 10.1190/1.3473694.

Wang, T., and G. W. Hohmann, 1993, A finite-difference, time-domain solution for three-dimensional electromagnetic modeling: Geophysics, **58**, 797–809, doi: 10.1190/1.1443465.

GEOPHYSICS, VOL. 85, NO. 1 (JANUARY-FEBRUARY 2020); P. E15–E26, 11 FIGS.
10.1190/GEO2018-0753.1

Application of perfectly matched layers in 3D transient controlled-source electromagnetic modeling by the rapid expansion method

Yikuo Liu[1]

ABSTRACT

I have developed an extension of the rapid expansion method (REM) for 3D time-domain controlled-source electromagnetic modeling that includes perfectly matched layers (PMLs) as the absorbing boundary. The REM solves the time-domain electric field by a weighted summation of the Chebyshev polynomials. The results are free of temporal dispersion and accurate to the Nyquist frequency, yet the domain of Chebyshev polynomials lacks an accurate absorbing boundary. I find that by introducing a fictitious magnetic field in the Chebyshev domain, the recursion of the Chebyshev polynomials obeys a discrete coupled wave equation, which shares a similarity with the propagation of EM waves in a lossless medium. The time and frequency components in the Chebyshev domain are derived based on the eigenvalues of the propagation matrix, and the PML theory designed for EM waves can be extended to the Chebyshev domain in a straightforward way. Numerical tests against analytical solution and spectral methods show an excellent agreement after PML solves the boundary problem in the Chebyshev domain, which demonstrates the accuracy of the REM algorithm and the usefulness of the PML absorbing boundary.

INTRODUCTION

The transient controlled-source electromagnetic (CSEM) method has been developed for exploration for subsurface fluids, including hydrocarbons (e.g., Strack, 1992; Wright et al., 2002; Ziolkowski et al., 2007). Inversion of CSEM data requires the ability to model the 3D transient electric field accurately, given a known conductivity model. Most existing time-domain modeling schemes use finite-difference or finite-element methods (e.g., Wang and Hohmann, 1993; Commer and Newman, 2004; Um et al., 2010). Low-order approximations of temporal derivatives have finite accuracy and may introduce numerical errors and dispersion (e.g., Adhidjaja and Hohmann, 1989). To address this issue, Tal-Ezer (1986) proposes a spectral method for hyperbolic equations based on a Chebyshev expansion of the time operator. The time evolution of the wavefield is integrated by a summation of the Chebyshev terms in the domain of the eigenvalues of the propagation matrix, and it is called the rapid expansion method (REM) by Kosloff et al. (1989). The accuracy of REM has been demonstrated in 2D and 3D time-domain seismic modeling (Tal-Ezer et al., 1987, 1990; Muir et al., 1992; Pestana and Stoffa, 2010) and in 2D and 3D time-domain EM modeling (De Raedt et al., 2003; Carcione, 2006; Liu et al., 2018; Stoffa and Ziolkowski, 2018). The results are free of temporal discretization errors and are accurate to the Nyquist frequency. Most of these authors use the Fourier pseudospectral (PS) method to evaluate the spatial derivatives in the wavenumber domain. The applications and advantages of the PS method have been widely discussed in previous studies such as Fornberg (1987, 1988).

There is a potential issue in this approach, however, that may degrade the accuracy of the REM results: the lack of an accurate and efficient absorbing boundary condition (ABC). For instance, De Raedt et al. (2003) show that the Chebyshev method can be orders of magnitude more efficient than finite-difference time-stepping methods; however, "FDTD methods can easily handle absorbing boundary conditions but at present, there is no guarantee that the Chebyshev polynomial approximation will still be accurate in these circumstances." One possible solution is to manually reduce the amplitude of the Chebyshev terms in the surrounding strips of the mesh (e.g., Tal-Ezer et al., 1987; Carcione, 2006). These boundaries are absorbing, but there are numerical reflections generated by the manual damping, which can degrade the accuracy of the modeling. Alternatively, one can avoid the use of absorbing boundaries by increasing the size of the simulation model. It can be a more practical option in modeling diffusive EM fields because the diffusive EM fields decay naturally in a conductive medium (e.g., Wang and Hohmann, 1993; Commer and Newman, 2004). However, the appearance

Manuscript received by the Editor 1 November 2018; revised manuscript received 23 July 2019; published ahead of production 14 September 2019; published online 22 November 2019.
[1]University of Edinburgh, School of Geosciences, Edinburgh, UK. E-mail: yikuo.liu@ed.ac.uk (corresponding author).

of a less-lossy (resistive) medium makes the results less reliable if we are unable to truncate the Chebyshev terms in space.

Therefore, a more advanced ABC is required to solve the boundary problem related to the Chebyshev method. One option is to exploit the use of the perfectly matched layer (PML) in the Chebyshev domain. PML is a well-established ABC technique in time- and frequency-domain EM modeling and is often considered the most effective one to attenuate the EM fields. It was proposed by Berenger (1994), with the idea of matching the impedance of the absorbing layer to make it reflectionless. Gedney (1996) shows that PML can be implemented by introducing uniaxial anisotropic material in the absorbing region. Alternatively, Chew and Weedon (1994) apply the PML absorbing boundary with a modified set of Maxwell's equations as the EM field is stretched in complex coordinates. More advanced versions of PML are further developed, such as complex frequency-shifted PML (Kuzuoglu and Mittra, 1996) and convolutional PML (Roden and Gedney, 2000), to optimize its efficiency in an arbitrary medium and improve the absorption of evanescent waves. It has been a popular choice to truncate finite-difference grids, as shown by recent studies of 3D magnetotelluric modeling (de la Kethulle de Ryhove and Mittet, 2014) and 3D CSEM modeling (Hu et al., 2017; Li et al., 2018).

I show that the PML technique can be extended to the Chebyshev domain to simulate the 3D time-domain electric field by REM. By transforming the time-domain electric field to the Chebyshev domain, the Chebyshev terms follow a one-step, second-order wave equation. I introduce a fictitious magnetic field in the Chebyshev domain and modify the original governing equation to a set of two-step, first-order wave equations. The new simulation of the Chebyshev terms is very similar to the propagation of EM waves in a lossless medium. The PML technique can be applied to the Chebyshev terms in a straightforward way, and attenuates the Chebyshev terms close to the boundary and therefore correct the electric field so that the boundary problem in the Chebyshev method can be solved.

I first review the work of Stoffa and Ziolkowski (2018) to describe the solution of the 3D electric field by REM. Then, I introduce a fictitious field in the Chebyshev domain and describe the modification of the governing equation. I show how the theory of PML based on EM wave modeling can be applied to the Chebyshev terms of the electric field. Finally, I demonstrate the accuracy of the method and the usefulness of absorbing boundary by two numerical examples.

THEORY

In conductive media where the displacement current can be neglected, the electric field $\mathbf{E}(x, y, z, t)$ satisfies the diffusion equation:

$$\frac{\partial}{\partial t}\mathbf{E} = -\frac{1}{\mu_0}\boldsymbol{\sigma}^{-1}\nabla\times\nabla\times\mathbf{E} - \boldsymbol{\sigma}^{-1}\frac{\partial}{\partial t}\mathbf{J}_\mathbf{s}, \tag{1}$$

where $\mathbf{E}$ is the vector consisting of three electric wavefield components $\mathbf{E}(x, y, z, t) = (E_x, E_y, E_z)^T$ with units V/m, μ_0 is the magnetic permeability of free space ($\mu_0 = 4\pi\times10^{-7}$ H/m), $\mathbf{J}_\mathbf{s}(\mathrm{A/m^2})$ is the source current density, and $\boldsymbol{\sigma}(\mathrm{S}/m)$ is the conductivity tensor.

3D solution by REM

The solution of equation 1 by REM has been discussed in Stoffa and Ziolkowski (2018). They consider an isotropic subsurface with an impulsive electric dipole source. Equation 1 can be written in the following form:

$$\frac{\partial}{\partial t}\mathbf{E} = \mathbf{G}\mathbf{E} + \mathbf{s}, \tag{2}$$

where $\mathbf{s}$ is the source term and $\mathbf{G}$ is the propagation matrix containing all the spatial derivatives and the conductivities:

$$\mathbf{G} = -\frac{1}{\mu_0\sigma}\begin{pmatrix} -(\partial_y^2+\partial_z^2) & \partial_y\partial_x & \partial_z\partial_x \\ \partial_x\partial_y & -(\partial_x^2+\partial_z^2) & \partial_z\partial_y \\ \partial_x\partial_z & \partial_y\partial_z & -(\partial_x^2+\partial_y^2) \end{pmatrix}. \tag{3}$$

Because the source is impulsive, immediately after the impulse there is no source but there is an initial field. The relaxation of the electric field follows an exponential operator

$$\mathbf{E}(t) = \mathbf{E}_0\exp(\mathbf{G}t), \tag{4}$$

where $\mathbf{E}_0$ defines the initial field. The exponential term $\mathbf{E}_0\exp(\mathbf{G}t)$ is numerically evaluated by a Chebyshev expansion truncated to order M

$$\mathbf{E}(t) \approx \sum_{k=0}^{M} b_k\mathbf{Q}_k, \tag{5}$$

where $\mathbf{Q}_k$ denotes the kth Chebyshev term, and the weights b_k are given by

$$b_k = c_k\ \exp(-bt)I_k(bt), \tag{6}$$

where $c_0 = 1$, $c_k = 2$, for $k \geq 1$, I_k is the modified Bessel function, and b is the maximum absolute eigenvalue of the propagation matrix $\mathbf{G}$. The choice of M in equation 5 is related to the value of b to ensure the convergence (Carcione, 2006; Stoffa and Ziolkowski, 2018). The Chebyshev terms are updated by the recursion relation as

$$\mathbf{Q}_0 = \mathbf{E}_0, \tag{7}$$

$$\mathbf{Q}_1 = \mathbf{F}\mathbf{E}_0, \tag{8}$$

$$\mathbf{Q}_{k+1} = 2\mathbf{F}\mathbf{Q}_k - \mathbf{Q}_{k-1}, \tag{9}$$

with the numerical operator $\mathbf{F}$ defined as

$$\mathbf{F} = \frac{1}{b}\mathbf{G} + \mathbf{I}, \tag{10}$$

where $\mathbf{I}$ is the identity matrix.

The numerical structure of the modeling code exactly follows equations 7–9 to obtain the required Chebyshev terms. The electric field is obtained by a weighted summation of the Chebyshev terms, as shown in equation 5.

Introducing a fictitious magnetic field

Stoffa and Ziolkowski (2018) find that, by combing equations 3, 9, and 10, the updating of Chebyshev terms can be written in the following form:

$$\frac{\mathbf{Q}_{k+1}-2\mathbf{Q}_k+\mathbf{Q}_{k-1}}{\Delta p^2}=-\frac{1}{\mu\sigma}\nabla\times\nabla\times\mathbf{Q}_k, \tag{11}$$

where $\Delta p=\sqrt{2/b}$ is the equivalent "time" step in the Chebyshev domain with dimensions of the square root of time. This equation is a discrete wave equation. For a numerical problem with node spacing Δx, Δy, and Δz, the Chebyshev time step Δp is a constant value:

$$\Delta p=\frac{1}{\pi}\left(\frac{2\mu_0\sigma_{\min}}{\Delta x^{-2}+\Delta y^{-2}+\Delta z^{-2}}\right)^{\frac{1}{2}}, \tag{12}$$

where $\sigma_{\min}$ denotes the minimum conductivity in the model.

I define $\mathbf{Q}$ as the Chebyshev electric field and p as the Chebyshev time. I introduce another field $\mathbf{L}$, such that

$$\mu\frac{\mathbf{L}_{k+1/2}-\mathbf{L}_{k-1/2}}{\Delta p}=-\nabla\times\mathbf{Q}_k, \tag{13}$$

$$\sigma\frac{\mathbf{Q}_{k+1}-\mathbf{Q}_k}{\Delta p}=\nabla\times\mathbf{L}_{k+1/2}. \tag{14}$$

By taking the curl of equation 13 and replacing the curl of $\mathbf{L}$ by the form of equation 14, the combination of equations 13 and 14 is equivalent to equation 11, except that in equation 11, I use $\{\mathbf{Q}_k,\mathbf{Q}_{k-1}\}$ to update $\mathbf{Q}_{k+1}$, but now in equations 13 and 14, I use $\{\mathbf{Q}_k,\mathbf{L}_{k-1/2}\}$ to update $\{\mathbf{Q}_{k+1},\mathbf{L}_{k+1/2}\}$. The fields $\{\mathbf{Q},\mathbf{L}\}$ propagating in the Chebyshev domain are exactly like the fields $\{\mathbf{E},\mathbf{H}\}$ propagating in a vacuum where the first-order time derivative has been dropped and EM fields propagate as waves. The numerical simulation of $\{\mathbf{Q},\mathbf{L}\}$ is exactly a finite-difference scheme, which is derived based on the Chebyshev recursion relation. For the initial field $k=0$, I use

$$\mu\frac{\mathbf{L}_{1/2}}{\Delta p/2}=-\nabla\times\mathbf{Q}_0, \tag{15}$$

$$\sigma\frac{\mathbf{Q}_1-\mathbf{Q}_0}{\Delta p}=\nabla\times\mathbf{L}_{1/2}, \tag{16}$$

and again equations 15 and 16 give $\mathbf{Q}_1=-b^{-1}\mu\sigma^{-1}\nabla\times\nabla\times\mathbf{Q}_0+\mathbf{Q}_0$, which is equivalent to the Chebyshev relation given in equation 8. Therefore, the modeling of the diffusive field $\mathbf{E}$ becomes a wave-based scheme in the Chebyshev domain and any EM wave modeling technique should be easily extended and applied to the Chebyshev terms $\{\mathbf{Q},\mathbf{L}\}$.

Inclusion of PML in the Chebyshev domain

Chew and Weedon (1994) show that PML can be implemented in the model by stretching the coordinates in the complex domain. The modified Maxwell's equations are

$$i\omega\mu\tilde{\mathbf{H}}=-[\mathbf{s}^{-1}]\nabla\times\tilde{\mathbf{E}}, \tag{17}$$

$$i\omega\varepsilon\tilde{\mathbf{E}}=[\mathbf{s}^{-1}]\nabla\times\tilde{\mathbf{H}}, \tag{18}$$

where the tilde symbol denotes the fields in the frequency domain and $[\mathbf{s}^{-1}]$ denotes the coordinate stretching tensor that consists of complex numbers. In the main body of the model, there is no PML and $\mathbf{s}$ is an identity matrix; the coordinates are not stretched and the governing equations are Maxwell's equations. In the PML region, the complex tensor $\mathbf{s}$ is designed to match the impedance of the medium but the inclusion of the imaginary part makes the medium lossy to absorb energy.

In this paper, I consider an isotropic case. The Chebyshev pairs $\{\mathbf{Q},\mathbf{L}\}$ in the stretched coordinates are defined as

$$i\upsilon\mu\tilde{\mathbf{L}}=-[\mathbf{s}^{-1}]\nabla\times\tilde{\mathbf{Q}}, \tag{19}$$

$$i\upsilon\sigma\tilde{\mathbf{Q}}=[\mathbf{s}^{-1}]\nabla\times\tilde{\mathbf{L}}, \tag{20}$$

where υ is the angular frequency in the Chebyshev frequency domain that corresponds to the Chebyshev time p and σ is the conductivity of the medium. With reference to Berenger (2002), I similarly define the complex coordinate stretching factors as

$$s_d=\kappa_d+\frac{\eta_d}{\alpha_d+i\upsilon\sigma}, \tag{21}$$

where $d=x$, y, or z denotes the direction, $\eta\geq 0$ controls the loss in the PML region, $\alpha\geq 0$ controls the shift of the frequency-dependent component, and $\kappa\geq 1$ acts as a scaling factor.

Equations 19–21 are the governing equations to implement a general form of PML in the Chebyshev domain. In this paper, I show the application of uniaxial PML. Other types of PML can be similarly used by varying the corresponding terms in equations 19–21. Following the derivation in Gedney (1996), the curl operator in the stretched coordinates is written as

$$[\mathbf{s}^{-1}]\nabla\times=\begin{bmatrix}0 & -\frac{s_x}{s_y}\frac{1}{s_z}\frac{\partial}{\partial z} & \frac{s_x}{s_z}\frac{1}{s_y}\frac{\partial}{\partial y}\\ \frac{s_y}{s_x}\frac{1}{s_z}\frac{\partial}{\partial z} & 0 & -\frac{s_y}{s_z}\frac{1}{s_x}\frac{\partial}{\partial x}\\ -\frac{s_z}{s_x}\frac{1}{s_y}\frac{\partial}{\partial y} & \frac{s_z}{s_y}\frac{1}{s_x}\frac{\partial}{\partial x} & 0\end{bmatrix}, \tag{22}$$

with $\kappa=1$ and $\alpha=0$ in the stretching factors s_x, s_y, and s_z. I take the L_x component as an example to derive its numerical solution. Combining equations 19, 21, and 22, the L_x component in the Chebyshev frequency domain is written as

$$i\upsilon\tilde{L_x}\left(1+\frac{\eta_x}{i\upsilon\sigma}\right)^{-1}\left(1+\frac{\eta_y}{i\upsilon\sigma}\right)\left(1+\frac{\eta_z}{i\upsilon\sigma}\right)=-\frac{1}{\mu}\left[-\frac{\partial\tilde{Q}_y}{\partial z}+\frac{\partial\tilde{Q}_z}{\partial y}\right]. \tag{23}$$

The Fourier transform derivative relation can be extended to the Chebyshev domain as

$$\frac{\partial}{\partial p}L_x=\frac{1}{2\pi}\int_{-\infty}^{+\infty}i\upsilon\tilde{L_x}\exp(i\upsilon p)d\upsilon. \tag{24}$$

Converting equation 23 into the Chebyshev time domain, and transforming the frequency-dependent terms into the corresponding derivatives and integrals with respect to p, yields

$$\frac{\partial}{\partial p}L_x+\frac{\eta_y+\eta_z}{\sigma}L_x+\int_{-\infty}^{p}\frac{\eta_y\eta_z}{\sigma^2}L_x(\tau)d\tau=$$
$$-\frac{1}{\mu}\left[-\frac{\partial Q_y}{\partial z}+\frac{\partial Q_z}{\partial y}\right]-\frac{1}{\mu}\int_{-\infty}^{p}\frac{\eta_x}{\sigma}\left[-\frac{\partial Q_y(\tau)}{\partial z}+\frac{\partial Q_z(\tau)}{\partial y}\right]d\tau. \quad (25)$$

The components of **L** and **Q** are collocated in space and staggered in the Chebyshev time. I use the central difference to calculate the derivative with respect to p, which is consistent with the governing equations 13 and 14, such that

$$\frac{\partial}{\partial p}L_{x,k}=\frac{L_{x,k+\frac{1}{2}}-L_{x,k-\frac{1}{2}}}{\Delta p}. \quad (26)$$

Equation 25 can be approximated numerically as

$$\left(1+\frac{\eta_y+\eta_z}{2\sigma}\Delta p\right)L_{x,k+\frac{1}{2}}=-\frac{\Delta p}{\mu}\left[-\frac{\partial Q_{y,k}}{\partial z}+\frac{\partial Q_{z,k}}{\partial y}\right]$$
$$+\left(1-\frac{\eta_y+\eta_z}{2\sigma}\Delta p\right)L_{x,k-\frac{1}{2}}$$
$$-\frac{\eta_y\eta_z}{\sigma^2}\sum_{k'=1}^{k'=k}L_{x,k'-\frac{1}{2}}\Delta p^2-\frac{\eta_x}{\mu\sigma}\sum_{k'=0}^{k'=k}\left[-\frac{\partial Q_{y,k'}}{\partial z}+\frac{\partial Q_{z,k'}}{\partial y}\right]\Delta p^2, \quad (27)$$

and equation 27 is the one that is used to update L_x in the PML region. If $\eta_x=\eta_y=\eta_z=0$, equation 27 reduces to the normal equation, which is used to update the field in the main section. Other components $\{L_y, L_z, Q_x, Q_y, Q_z\}$ can be worked out following a similar procedure. The corresponding equations are given in Appendix A.

The interface between the interior region and the PML region is reflectionless; however, there is still an apparent reflection from the outer boundary of the model. For a PML layer with thickness δ and decay factor $\eta(\rho)$, with ρ denoting the distance from the PML-interior interface, the apparent reflection is a function of the incident angle θ, solved by Berenger (1994),

$$R(\theta)=\exp\left(-\frac{2\cos\theta}{\sigma c}\int_0^{\delta}\eta(\rho)d\rho\right), \quad (28)$$

where $c=(\mu\sigma)^{-1/2}$ is the propagation speed in the Chebyshev space domain. For numerical consideration, the value of $\eta(\rho)$ needs to be tapered gradually from its maximum to zero toward the PML-interior interface:

$$\eta(\rho)=\eta_{\max}\left(\frac{\rho}{\delta}\right)^m, \quad (29)$$

where m can be either 2 or 3. As pointed out by Berenger (2002), $m=3$ has a better absorption on the evanescent region, whereas $m=2$ has a better absorption on the propagating region. I use $m=2$. Substituting equation 29 into 28, the apparent reflection is

$$R(\theta)=\exp\left(-\frac{2\delta\cos\theta}{m+1}\frac{\eta_{\max}}{\sigma c}\right). \quad (30)$$

The value of $R(\theta)$ can be used to measure the effectiveness of the absorption. By increasing the decay factor $\eta_{\max}$, the predicted reflection error $R(\theta)$ will continuously decrease. However, there is a lower bound for the realizable $R(\theta)$ in the discrete space because the numerical discretization error increases with the decay factor $\eta_{\max}$. For example, Gedney (1996) finds that for a 10-node PML, the minimum error occurs when $R(0)\approx e^{-16}$ and for a five-cell PML, the minimum error occurs when $R(0)\approx e^{-8}$. The optimal choice of $R(0)$ is problem-dependent and controlled by $\eta_{\max}$. I use a modified optimal formulation for $\eta_{\max}$ similar to that in Pan et al. (2012) and Li et al. (2018),

$$\eta_{\max}(x,y,z)=w\frac{(m+1)\sigma(x,y,z)}{\delta\Delta p}, \quad (31)$$

where w is a constant that determines the magnitude of $\eta_{\max}$ and $R(\theta)$. The inclusion of Δp makes the scale of w less problem-dependent and easier to tune. For an EM modeling problem with node spacing of 20 m, varying w from 1 to 100 gives the normal incidence reflection $R(0)$ varying from approximately e^{-1} to e^{-40}, which should cover most of the desired range of $R(0)$.

NUMERICAL EXAMPLES

I present two numerical examples to demonstrate the use of PML in REM modeling. First, I check the code in a homogeneous whole space, against the analytical solution given by Slob et al. (2010). Then, I add resistive layers to the model and check the solution against the published 1D modeling code called EMmod (Hunziker et al., 2015). The analytical solution and the semianalytical 1D modeling method are free of boundary problems. I compare the 3D modeling results with and without PML, to demonstrate the correctness of the developed theory and to discuss the improvements of the results by improving the absorbing boundary.

The algorithm is written in a parallel C code and in an alternative MATLAB code. For the tests below with synthetic data and computationally small models, I show the results from the MATLAB code, running on a desktop machine with a single processor (3.20 GHz). The model cube is constructed with 128 nodes along each of the x-, y-, and z-directions, with 14 nodes on each side working as the PML absorbing boundary. Therefore, the main section of the cube has $100\times100\times100$ nodes, excluding the absorbing boundaries. The node spacing is 10 m. The x-directed dipole source is located 200 m below the PML region, and the inline receivers are located 145 m below the source on the nodes (Figure 1a). I use a maximum decay factor $\eta_{\max}$ with $w=25$ such that the apparent reflection at normal incidence is approximately $R(0)\approx e^{-19}$.

I first compare the snapshots of Q_x in the homogeneous whole space (Figure 1a). Because **Q** and **L** are waves in the Chebyshev domain, it is a good place to observe the appearance of any numerical reflections from the boundary.

When PML is turned off, the modeling of REM uses the periodic boundary condition. This is because the spatial derivatives in the propagation matrix **G** are evaluated in the wavenumber domain and the periodicity of the fast Fourier transform (FFT) makes the field periodic. Figure 2 shows the propagation of Q_x in an

x-z slice. The upgoing wave generated from the source and shown on the top of the 80th Chebyshev term eventually appears at the bottom of the model and interacts with the downgoing wave as shown in the 280th Chebyshev term. The upgoing wave proves that a problem certainly exists. Then, PML is turned on and the new snapshots of Q_x are shown in Figure 3. The upgoing wave has vanished in the 180th and 280th Chebyshev terms because the medium is infinite and the wave keeps propagating out of the model. No numerical reflection is observed from the boundary.

The effect of PML is also checked along the horizontal directions. The x-y horizontal slices of Q_x are compared in Figures 4 and 5, without and with PML applied, respectively. The periodicity of the field is observed again by comparing the 180th and the 380th Chebyshev term. The energy is trapped in the model without absorbing boundaries. If Dirichlet boundary condition is used, we can expect pseudoreflections from the numerical boundary instead of periodicity problems. In any case, the boundary effects are clearly illustrated in the Chebyshev domain. When turning on the PML, the scattered energy becomes almost invisible, as shown in Figure 5. The comparisons of the horizontal and vertical slices of Q_x show that PML is absorbing and reflectionless in all three directions.

The time-domain response of the electric field is a weighted sum of the Chebyshev terms, and the wave-like characteristics are smoothed out by the modified Bessel function (equation 5). Therefore, we cannot observe an extra arrival corresponding to the upgoing wave. What we can observe is a slight mismatch of the long tails of the

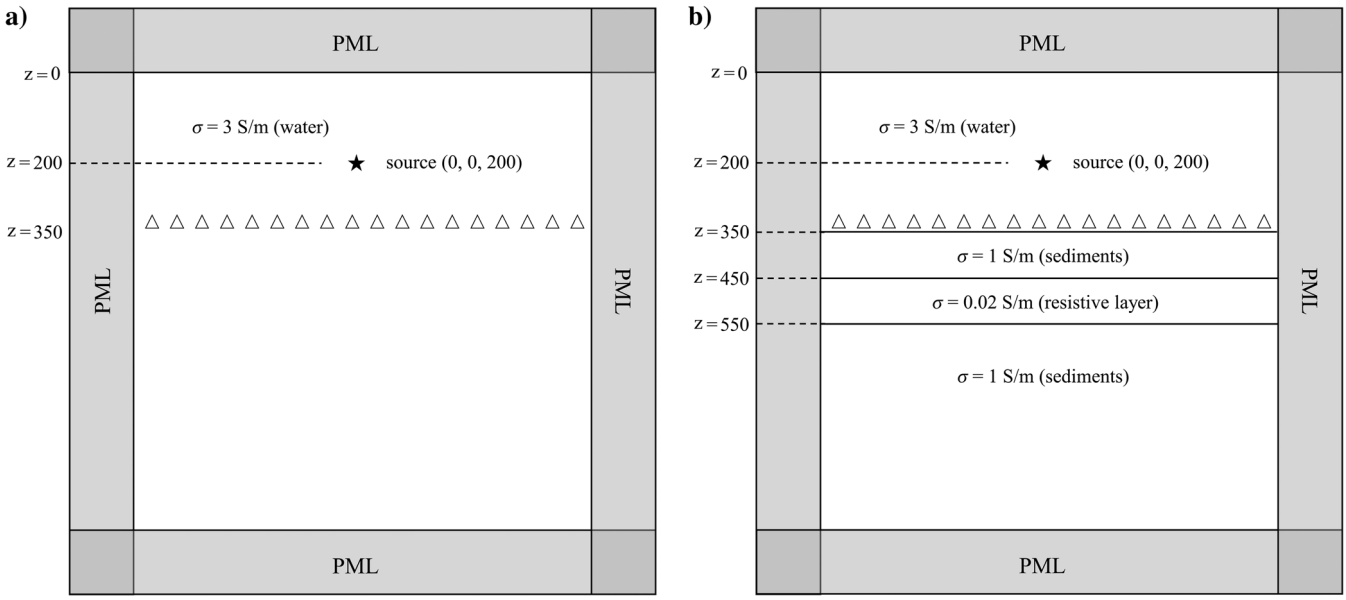

Figure 1. Configuration of the model. PML is implemented with 14 nodes on each side along the x-, y-, and z-directions. The x-directed dipole source is located 200 m below the PML region in the center with coordinates $x = y = 0$. The inline receivers ($y = 5$ m) are 145 m below the source on the nodes. The node spacing is 10 m. (a) A homogeneous model. (b) A 1D layered model.

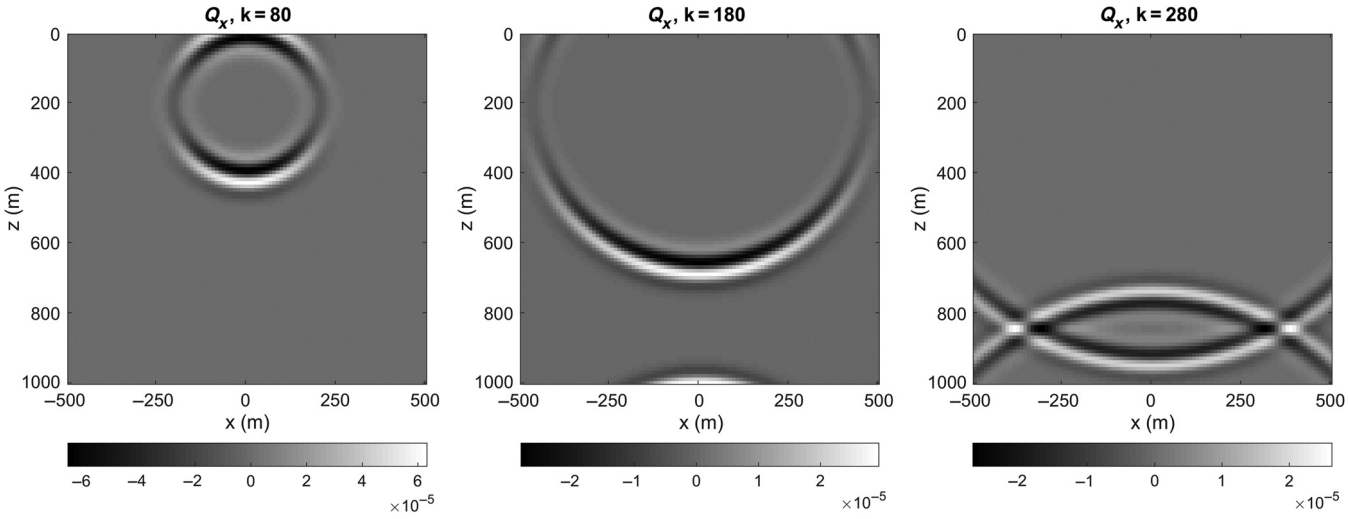

Figure 2. Snapshots of Q_x. The x-z plane is located on $y = 5$ m. The model configuration is shown in Figure 1a. PML is OFF. The PML region is not shown.

curves at the far offset and late times, as shown in Figure 6. After turning on the PML, the mismatch vanishes and the REM results show excellent agreement with the analytical solution in Figure 7.

The electric field in the conductive medium is naturally attenuative, and in some cases, the decay of the field itself is strong enough to absorb the numerical reflections from the boundary. However, the extent of the decay certainly depends on the conductivity of the medium. A resistive layer with a smaller conductivity gives a faster diffusive speed and less attenuation of the field, and under such circumstance, the boundary problem can be severe. To demonstrate this, I insert layers into the previous model, with $\sigma = 1$ S/m representing sediments and $\sigma = 0.02$ S/m representing a potential resistive target (Figure 1b). The Chebyshev terms Q_x are compared in Figure 8. The horizontal axis is the inline offset, and the vertical axis is the Chebyshev order k of the term Q_x. By presenting in this way, the Chebyshev terms can be analyzed in a way similar to seismic data. Without PML, the appearance of linear noise and periodic multiples is observed when the order k is greater than 4000. Due to the weighting by the modified Bessel function (equation 6), this section has a relatively greater contribution in the late time response rather than the early times. The amplitude of E_x, as examined in Figure 9, shows a clear difference from the calibration curve, in the peak value and in the long tail. The relative misfit increases toward the edge of the model.

Linear noise and periodic multiples are generated due to the periodicity of the field, and the boundary effect in this example has a severe impact on E_x because the resistive layer gives relatively little attenuation. After including PML, as shown in Figure 8, the unwanted signals are almost invisible in the high-order Q_x terms. As a result, the amplitude of E_x, as examined in Figure 10, shows excellent agreement with the calibration curve. The relative difference calculated at the far-offset receiver is shown in Figure 11.

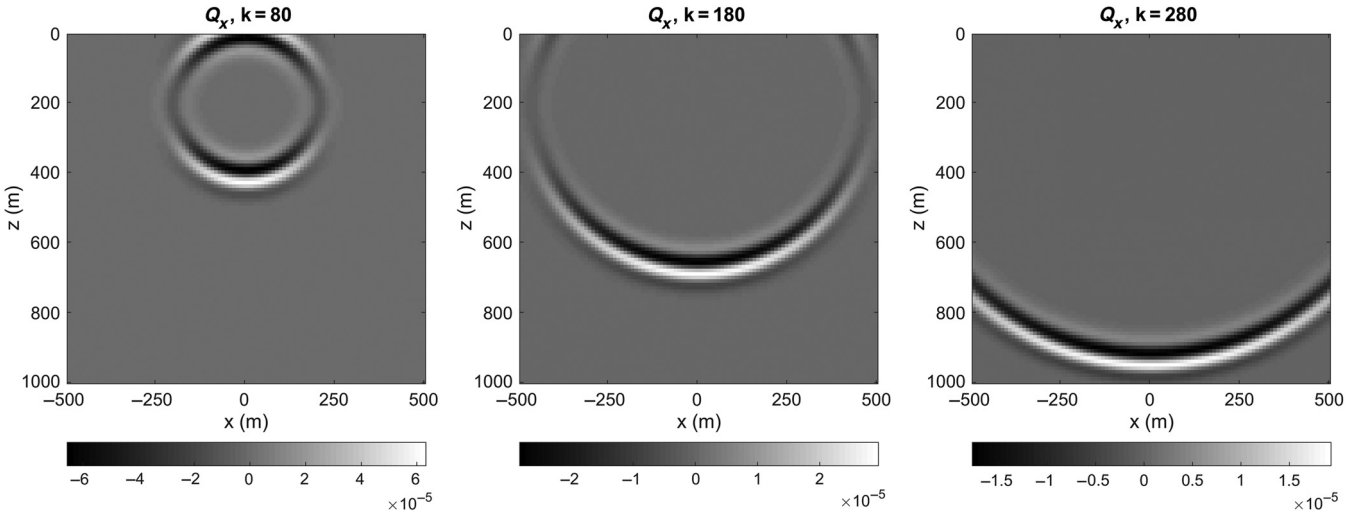

Figure 3. Snapshots of Q_x. The x-z plane is located on $y = 5$ m. The model configuration is shown in Figure 1a. PML is ON. The PML region is not shown.

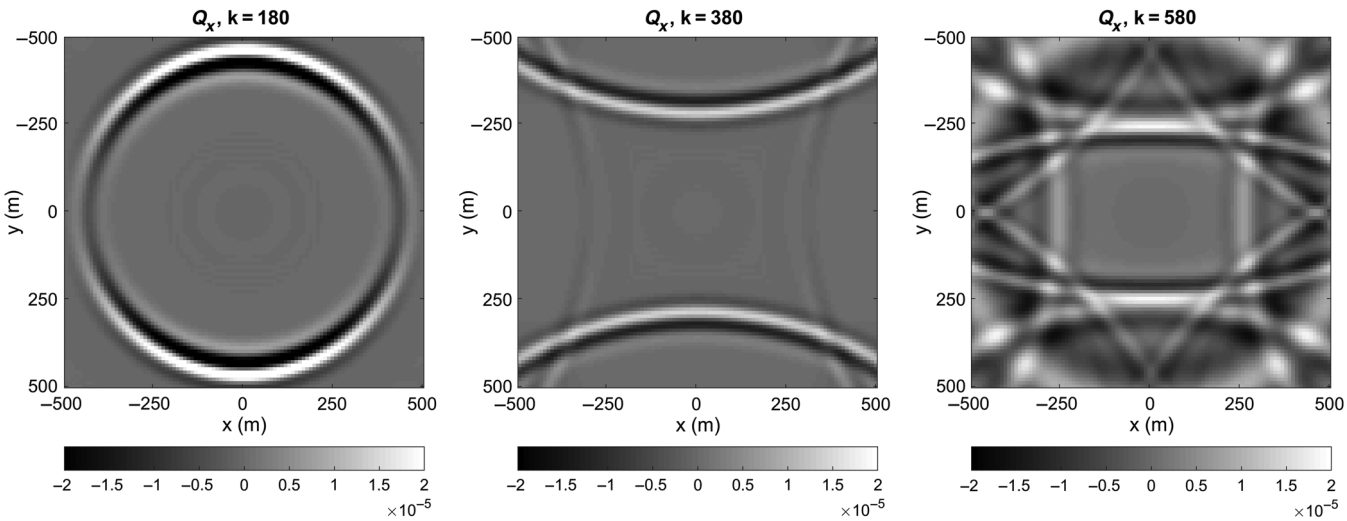

Figure 4. Snapshots of Q_x. The x-y receiver plane is located on $z = 345$ m, 145 m below the source. The model configuration is shown in Figure 1a. PML is OFF. The PML region is not shown.

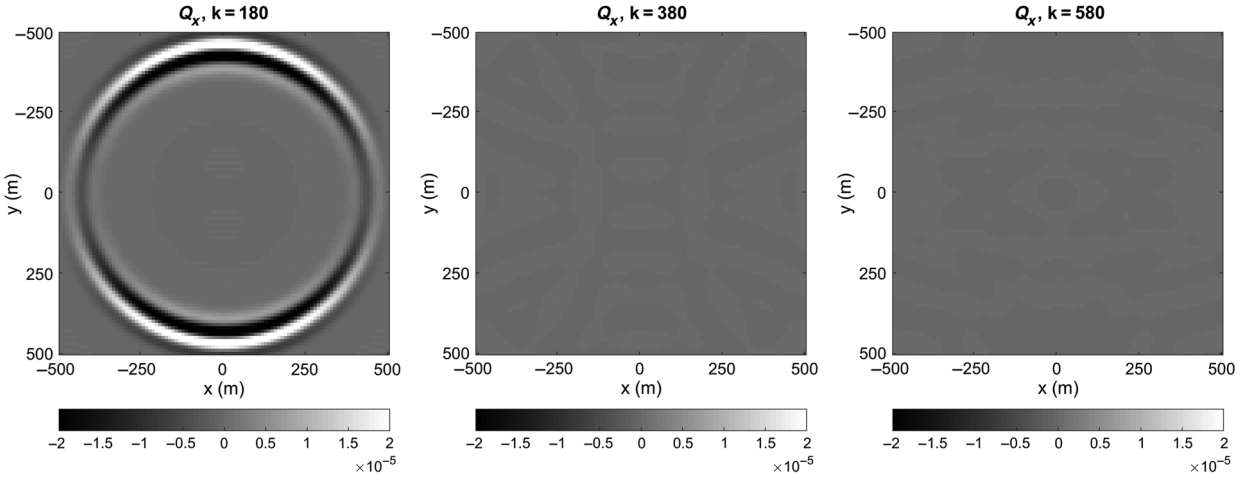

Figure 5. Snapshots of Q_x. The x-y receiver plane is located on $z = 345$ m, 145 m below the source. The model configuration is shown in Figure 1a. PML is ON. The PML region is not shown.

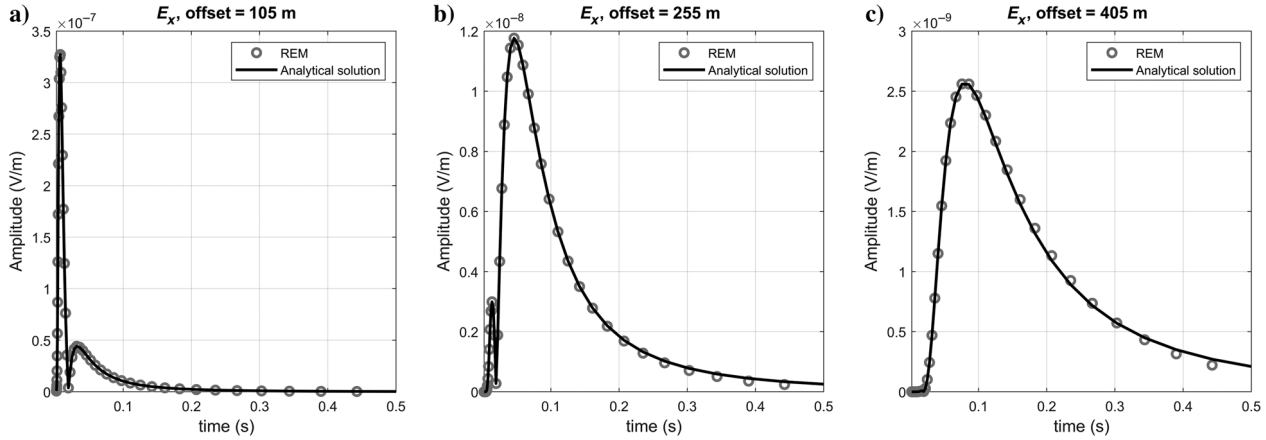

Figure 6. Comparison of the inline electric field in the time domain. The model configuration is shown in Figure 1a. PML is OFF. The REM and analytical solution are denoted by the circles and solid lines, respectively. (a-c) The absolute amplitude of E_x at inline receivers ($y = 5$ m) with offsets in the x-direction of 105 m (20%), 255 m (50%), and 405 m (80%), respectively.

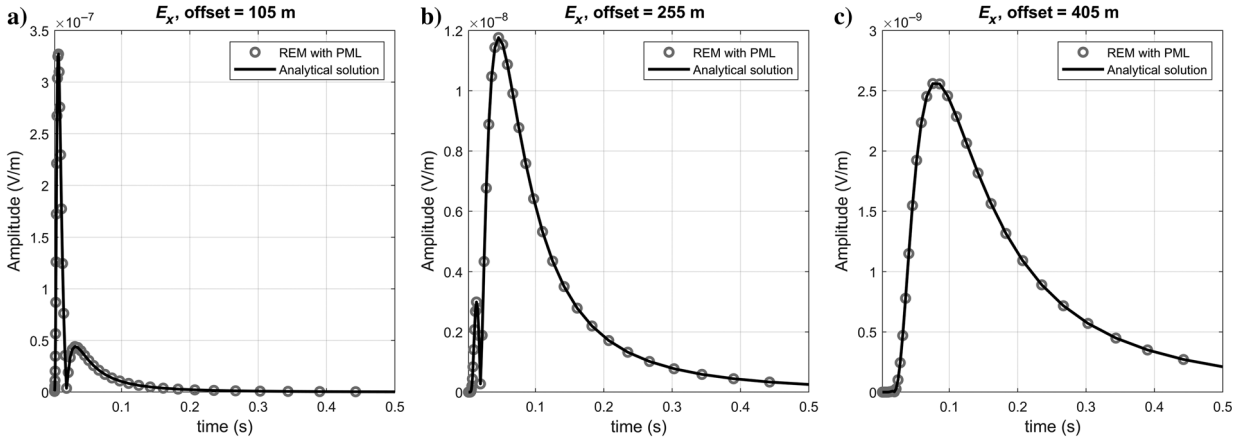

Figure 7. Comparison of the inline electric field in the time domain. The model configuration is shown in Figure 1a. PML is ON. The REM and analytical solution are denoted by the circles and solid lines, respectively. (a-c) The absolute amplitude of E_x at inline receivers ($y = 5$ m) with offsets in the x-direction of 105 m (20%), 255 m (50%), and 405 m (80%), respectively.

For the homogeneous case, the relative differences between the analytical solution and the REM results reduce to less than 0.1% after incorporating PML, apart from the difference in tiny amplitudes at very early times. For the 1D layered model, the relative differences between the EMmod and the REM results are approximately 0.1%–1% for most of the simulation time, slightly larger than in the homogeneous case. The numerical error inevitably increases due to the direct implementation of internal interfaces (Mittet, 2017). The EMmod results also exhibit some numerical errors, as shown by the oscillation observed at the near-offset receiver (Figure 10). This may be due to the discrete Hankel transformation from the wavenumber to the space domain, as discussed in Hunziker et al. (2015), as well as the FFT and the spline interpolation managed by myself to match the results at the same time point. Nevertheless, the excellent agreement between the modeling responses delivers a convincing result that demonstrates the accuracy of the Chebyshev method when PML solves the boundary problem.

The number of nodes in the PML region can vary from a few to approximately 20 nodes. Figure 11 shows the change in the relative difference when the thickness of the PML is reduced from 14 nodes to 10 nodes and 6 nodes, respectively. For the 6-node PML, the maximum relative difference increases to approximately 0.5% for the

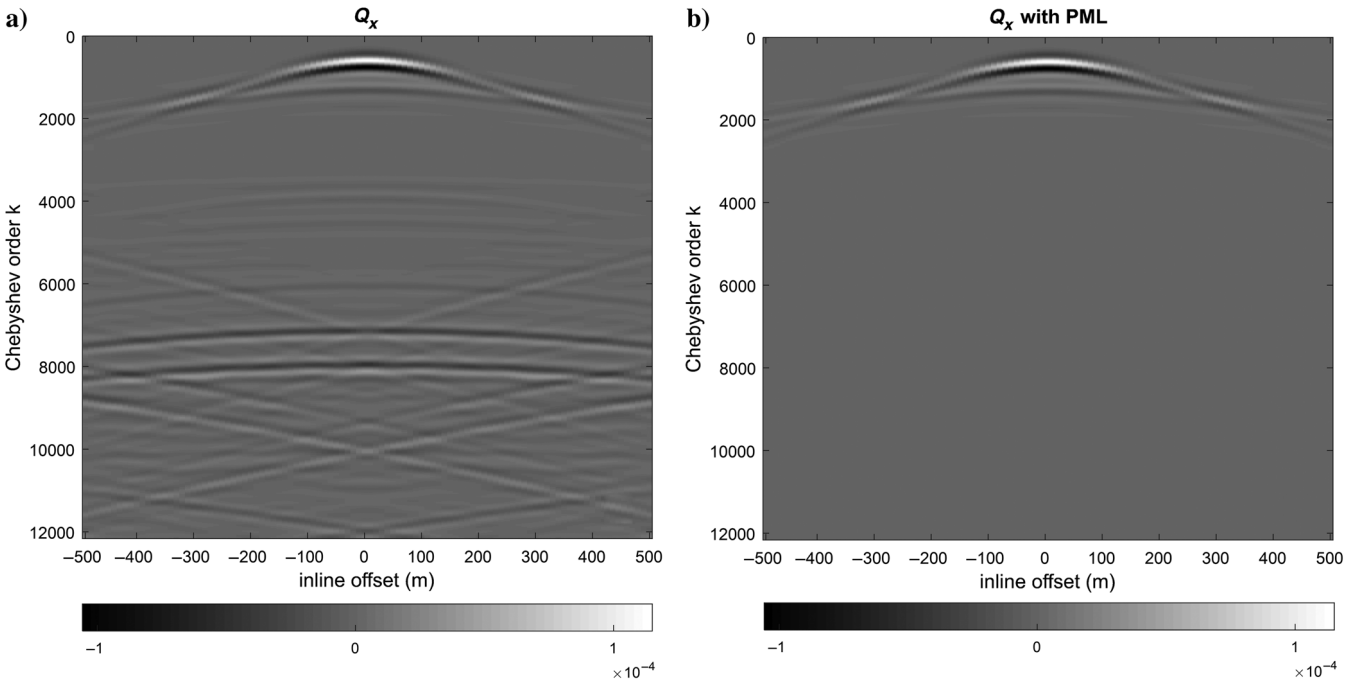

Figure 8. Comparison of Q_x in the 1D layered model. The receiver line is located on $y = 5$ m and $z = 345$ m. Chebyshev terms Q_x are sampled at every 10 terms. (a and b) The Chebyshev terms Q_x with PML turning OFF and turning ON, respectively.

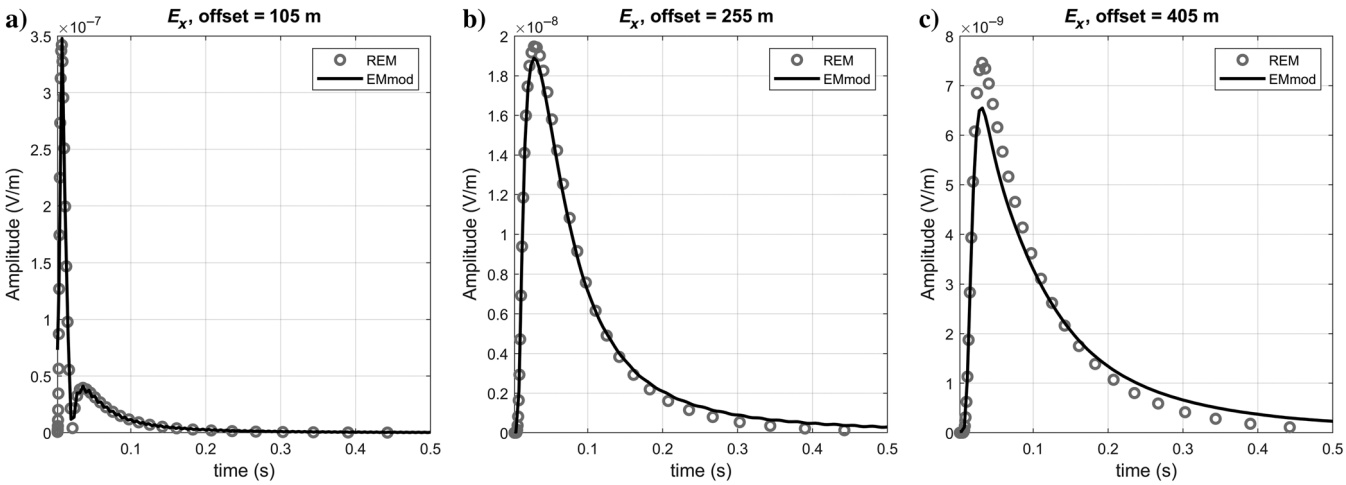

Figure 9. Comparison of the inline electric field in the time domain. The model configuration is shown in Figure 1b. PML is OFF. The REM and EMmod solution are denoted by circles and solid lines, respectively. (a-c) The absolute amplitude of E_x at inline receivers ($y = 5$ m) with offsets in the x-direction of 105 m (20%), 255 m (50%), and 405 m (80%), respectively.

homogeneous model and to approximately 4% for the 1D layered model. This level of accuracy may be practically acceptable in some cases. For the purpose of comparison, the values of $\eta_{\max}$ are kept the same for all three PMLs. Better performance may be achieved for the thinner PMLs after tuning the optimal parameter for each case. A thinner PML usually requires a smaller decay factor to balance the apparent reflection and the discretization error (Gedney, 1996).

DISCUSSION

I have demonstrated the inclusion of PML in an isotropic case. To include the earth-air interface and anisotropic conductivity in the REM modeling, see Liu et al. (2018). The earth-air interface can be included by the upward continuation of the field **L**. Anisotropy can be included by the manipulation of the conductivity tensor. The use of PML gives several advantages. First, the accuracy of the modeling results, especially at far offsets, becomes more reliable and it no longer depends on the size of the simulation and the loss in the medium. Second, the computational cost can be reduced because of the truncation of the simulation region. Finally, for joint inversion of seismic and CSEM data (e.g., Hu et al., 2009), a good absorbing boundary condition such as PML avoids enlarging the EM model, which is more convenient for grid matching of the two data sets.

The application of PML only requires modeling the time evolution of the electric field in the Chebyshev domain. The evaluation of the spatial derivatives at every step is, however, independent of that. At some times, one may want to use the finite-element or finite-difference method for the consideration of the geometry or the computational cost. Under such cases, the theory developed in this paper can be directly transferred to a finite-element or finite-difference

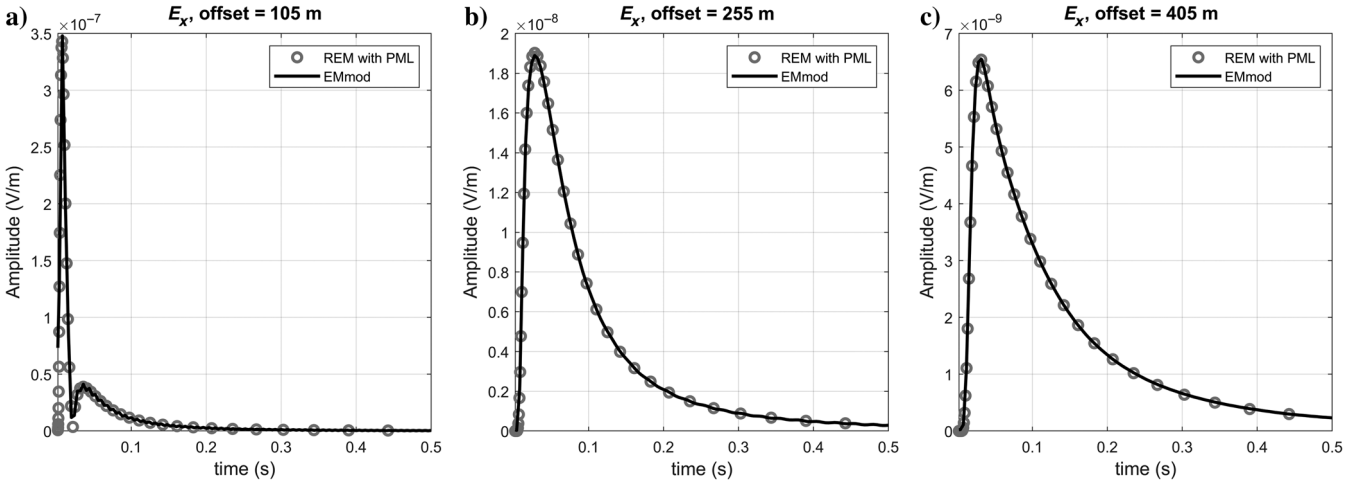

Figure 10. Comparison of the inline electric field in the time domain. The model configuration is shown in Figure 1b. PML is ON. The REM and EMmod solution are denoted by the circles and solid lines, respectively. (a-c) The absolute amplitude of E_x at inline receivers ($y = 5$ m) with offsets in the x-direction of 105 m (20%), 255 m (50%), and 405 m (80%), respectively.

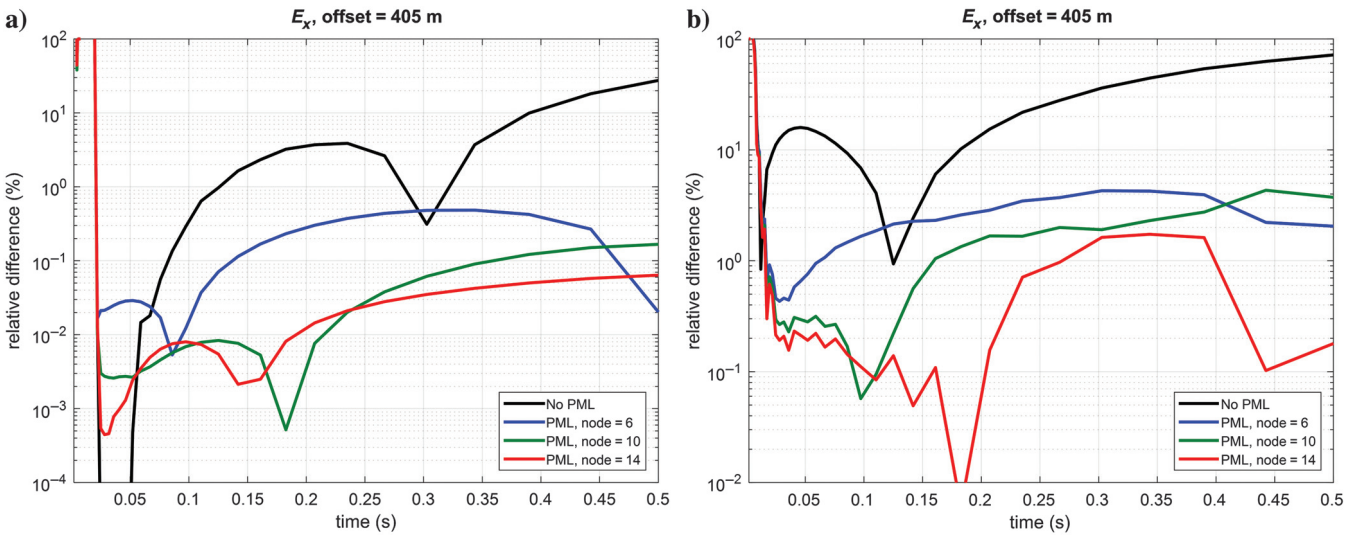

Figure 11. Relative difference of the inline electric field in the time domain. (a and b) The relative difference calculated at the far-offset receiver ($x = 405$ m) for the homogeneous model (Figure 1a) and for the 1D layered model (Figure 1b), respectively. The calibration methods are the analytical solution (Slob et al., 2010) and the semianalytical solution EMmod (Hunziker et al., 2015), respectively. Four cases are considered: REM modeling without PML and REM modeling with 6, 10, and 14 nodes acting as the PML region.

time-domain modeling to include PML as the absorbing boundary. The only change is to evaluate the propagation matrix **G** in the space domain, instead of the wavenumber domain.

The simulation of the time-domain electric field exactly follows a coupled wave equation in the Chebyshev domain. The similarity between the Chebyshev pair and the EM wave is discussed in the "Theory" section. I have shown that PML can be applied to modeling the diffusive EM field in the Chebyshev domain. Other EM wavefield modeling techniques could be similarly transferred if necessary.

CONCLUSION

I have presented an extension of the pseudospectral REM method to solve the 3D diffusive electric field in the time domain. The original decoupled, one-step governing equation is modified to a coupled, two-step governing equation by introducing a fictitious magnetic field in the Chebyshev domain. The Chebyshev terms of the diffusive electric field exhibit similarities with EM wave propagation in a lossless medium, and EM wave modeling techniques can be transferred to the Chebyshev domain in a straightforward way.

I have shown a successful application of PML as absorbing boundaries in REM modeling. PML is directly implemented in the Chebyshev domain to attenuate the Chebyshev terms in the absorbing region. The boundary effects are almost invisible in the waves propagating in the Chebyshev domain. The modeling results of the electric field show excellent agreement with the calibration code after turning on PML, which demonstrates the accuracy of the algorithm. The improvement of the far-offset results is clear, which demonstrates the usefulness of PML.

ACKNOWLEDGMENTS

The author thanks A. Ziolkowski for his constructive discussions and suggestions. The author thanks R. Mittet, two anonymous reviewers, associate editor, and J. Shragge for their useful comments that have greatly helped to improve the paper.

DATA AND MATERIALS AVAILABILITY

Data associated with this research are available and can be obtained by contacting the corresponding author.

APPENDIX A

INCLUSION OF PML IN THE CHEBYSHEV DOMAIN

The derivations of the modeling of components $\{L_y, L_z, Q_x, Q_y, Q_z\}$ in the PML region are listed in this appendix. By expanding equations 17 and 18 with the complex coordinate-stretching factors, the components $\{L_y, L_z, Q_x, Q_y, Q_z\}$ satisfy equations A-1–A-5 in the Chebyshev frequency domain:

$$i\upsilon\tilde{L}_y\left(1+\frac{\eta_y}{i\upsilon\sigma}\right)^{-1}\left(1+\frac{\eta_x}{i\upsilon\sigma}\right)\left(1+\frac{\eta_z}{i\upsilon\sigma}\right)=-\frac{1}{\mu}\left[-\frac{\partial\tilde{Q}_z}{\partial x}+\frac{\partial\tilde{Q}_x}{\partial z}\right], \tag{A-1}$$

$$i\upsilon\tilde{L}_z\left(1+\frac{\eta_z}{i\upsilon\sigma}\right)^{-1}\left(1+\frac{\eta_x}{i\upsilon\sigma}\right)\left(1+\frac{\eta_y}{i\upsilon\sigma}\right)=-\frac{1}{\mu}\left[-\frac{\partial\tilde{Q}_x}{\partial y}+\frac{\partial\tilde{Q}_y}{\partial x}\right], \tag{A-2}$$

$$i\upsilon\tilde{Q}_x\left(1+\frac{\eta_x}{i\upsilon\sigma}\right)^{-1}\left(1+\frac{\eta_y}{i\upsilon\sigma}\right)\left(1+\frac{\eta_z}{i\upsilon\sigma}\right)=\frac{1}{\sigma}\left[-\frac{\partial\tilde{L}_y}{\partial z}+\frac{\partial\tilde{L}_z}{\partial y}\right], \tag{A-3}$$

$$i\upsilon\tilde{Q}_y\left(1+\frac{\eta_y}{i\upsilon\sigma}\right)^{-1}\left(1+\frac{\eta_x}{i\upsilon\sigma}\right)\left(1+\frac{\eta_z}{i\upsilon\sigma}\right)=\frac{1}{\sigma}\left[-\frac{\partial\tilde{L}_z}{\partial x}+\frac{\partial\tilde{L}_x}{\partial z}\right], \tag{A-4}$$

$$i\upsilon\tilde{Q}_z\left(1+\frac{\eta_z}{i\upsilon\sigma}\right)^{-1}\left(1+\frac{\eta_x}{i\upsilon\sigma}\right)\left(1+\frac{\eta_y}{i\upsilon\sigma}\right)=\frac{1}{\sigma}\left[-\frac{\partial\tilde{L}_x}{\partial y}+\frac{\partial\tilde{L}_y}{\partial x}\right]. \tag{A-5}$$

These components are then converted to the Chebyshev time domain, as given in equations A-6–A-10.

$$\frac{\partial}{\partial p}L_y+\frac{\eta_x+\eta_z}{\sigma}L_y+\int_{-\infty}^{p}\frac{\eta_x\eta_z}{\sigma^2}L_y(\tau)d\tau=$$
$$-\frac{1}{\mu}\left[-\frac{\partial Q_z}{\partial x}+\frac{\partial Q_x}{\partial z}\right]-\frac{1}{\mu}\int_{-\infty}^{p}\frac{\eta_y}{\sigma}\left[-\frac{\partial Q_z(\tau)}{\partial x}+\frac{\partial Q_x(\tau)}{\partial z}\right]d\tau, \tag{A-6}$$

$$\frac{\partial}{\partial p}L_z+\frac{\eta_x+\eta_y}{\sigma}L_z+\int_{-\infty}^{p}\frac{\eta_x\eta_y}{\sigma^2}L_z(\tau)d\tau=$$
$$-\frac{1}{\mu}\left[-\frac{\partial Q_x}{\partial y}+\frac{\partial Q_y}{\partial x}\right]-\frac{1}{\mu}\int_{-\infty}^{p}\frac{\eta_z}{\sigma}\left[-\frac{\partial Q_x(\tau)}{\partial y}+\frac{\partial Q_y(\tau)}{\partial x}\right]d\tau, \tag{A-7}$$

$$\frac{\partial}{\partial p}Q_x+\frac{\eta_y+\eta_z}{\sigma}Q_x+\int_{-\infty}^{p}\frac{\eta_y\eta_z}{\sigma^2}Q_x(\tau)d\tau=$$
$$\frac{1}{\sigma}\left[-\frac{\partial L_y}{\partial z}+\frac{\partial L_z}{\partial y}\right]+\frac{1}{\sigma}\int_{-\infty}^{p}\frac{\eta_x}{\sigma}\left[-\frac{\partial L_y(\tau)}{\partial z}+\frac{\partial L_z(\tau)}{\partial y}\right]d\tau, \tag{A-8}$$

$$\frac{\partial}{\partial p}Q_y+\frac{\eta_x+\eta_z}{\sigma}Q_y+\int_{-\infty}^{p}\frac{\eta_x\eta_z}{\sigma^2}Q_y(\tau)d\tau=$$
$$\frac{1}{\sigma}\left[-\frac{\partial L_z}{\partial x}+\frac{\partial L_x}{\partial z}\right]+\frac{1}{\sigma}\int_{-\infty}^{p}\frac{\eta_y}{\sigma}\left[-\frac{\partial L_z(\tau)}{\partial x}+\frac{\partial L_x(\tau)}{\partial z}\right]d\tau, \quad \text{(A-9)}$$

$$\frac{\partial}{\partial p}Q_z+\frac{\eta_x+\eta_y}{\sigma}Q_z+\int_{-\infty}^{p}\frac{\eta_x\eta_y}{\sigma^2}Q_z(\tau)d\tau=$$
$$\frac{1}{\sigma}\left[-\frac{\partial L_x}{\partial y}+\frac{\partial L_y}{\partial x}\right]+\frac{1}{\sigma}\int_{-\infty}^{p}\frac{\eta_z}{\sigma}\left[-\frac{\partial L_x(\tau)}{\partial y}+\frac{\partial L_y(\tau)}{\partial x}\right]d\tau. \quad \text{(A-10)}$$

The numerical approximations are given in equations A-11–A-15, which are the equations used in the PML region to update **Q** and **L**:

$$\left(1+\frac{\eta_x+\eta_z}{2\sigma}\Delta p\right)L_{y,k+\frac{1}{2}}=-\frac{\Delta p}{\mu}\left[-\frac{\partial Q_{z,k}}{\partial x}+\frac{\partial Q_{x,k}}{\partial z}\right]$$
$$+\left(1-\frac{\eta_x+\eta_z}{2\sigma}\Delta p\right)L_{y,k-\frac{1}{2}}$$
$$-\frac{\eta_x\eta_z}{\sigma^2}\sum_{k'=1}^{k'=k}L_{y,k'-\frac{1}{2}}\Delta p^2-\frac{\eta_y}{\mu\sigma}\sum_{k'=0}^{k'=k}\left[-\frac{\partial Q_{z,k'}}{\partial x}+\frac{\partial Q_{x,k'}}{\partial z}\right]\Delta p^2, \quad \text{(A-11)}$$

$$\left(1+\frac{\eta_x+\eta_y}{2\sigma}\Delta p\right)L_{z,k+\frac{1}{2}}=-\frac{\Delta p}{\mu}\left[-\frac{\partial Q_{x,k}}{\partial y}+\frac{\partial Q_{y,k}}{\partial x}\right]$$
$$+\left(1-\frac{\eta_x+\eta_y}{2\sigma}\Delta p\right)L_{z,k-\frac{1}{2}}$$
$$-\frac{\eta_x\eta_y}{\sigma^2}\sum_{k'=1}^{k'=k}L_{z,k'-\frac{1}{2}}\Delta p^2-\frac{\eta_z}{\mu\sigma}\sum_{k'=0}^{k'=k}\left[-\frac{\partial Q_{x,k'}}{\partial y}+\frac{\partial Q_{y,k'}}{\partial x}\right]\Delta p^2, \quad \text{(A-12)}$$

$$\left(1+\frac{\eta_y+\eta_z}{2\sigma}\Delta p\right)Q_{x,k+1}=\frac{\Delta p}{\sigma}\left[-\frac{\partial L_{y,k+\frac{1}{2}}}{\partial z}+\frac{\partial L_{z,k+\frac{1}{2}}}{\partial y}\right]$$
$$+\left(1-\frac{\eta_y+\eta_z}{2\sigma}\Delta p\right)Q_{x,k}$$
$$-\frac{\eta_y\eta_z}{\sigma^2}\sum_{k'=0}^{k'=k}Q_{x,k'}\Delta p^2+\frac{\eta_x}{\sigma^2}\sum_{k'=0}^{k'=k}\left[-\frac{\partial L_{y,k'+\frac{1}{2}}}{\partial z}+\frac{\partial L_{z,k'+\frac{1}{2}}}{\partial y}\right]\Delta p^2, \quad \text{(A-13)}$$

$$\left(1+\frac{\eta_x+\eta_z}{2\sigma}\Delta p\right)Q_{y,k+1}=\frac{\Delta p}{\sigma}\left[-\frac{\partial L_{z,k+\frac{1}{2}}}{\partial x}+\frac{\partial L_{x,k+\frac{1}{2}}}{\partial z}\right]$$
$$+\left(1-\frac{\eta_x+\eta_z}{2\sigma}\Delta p\right)Q_{y,k}$$
$$-\frac{\eta_x\eta_z}{\sigma^2}\sum_{k'=0}^{k'=k}Q_{y,k'}\Delta p^2+\frac{\eta_y}{\sigma^2}\sum_{k'=0}^{k'=k}\left[-\frac{\partial L_{z,k'+\frac{1}{2}}}{\partial x}+\frac{\partial L_{x,k'+\frac{1}{2}}}{\partial z}\right]\Delta p^2, \quad \text{(A-14)}$$

$$\left(1+\frac{\eta_x+\eta_y}{2\sigma}\Delta p\right)Q_{z,k+1}=\frac{\Delta p}{\sigma}\left[-\frac{\partial L_{x,k+\frac{1}{2}}}{\partial y}+\frac{\partial L_{y,k+\frac{1}{2}}}{\partial x}\right]$$
$$+\left(1-\frac{\eta_x+\eta_y}{2\sigma}\Delta p\right)Q_{z,k}$$
$$-\frac{\eta_x\eta_y}{\sigma^2}\sum_{k'=0}^{k'=k}Q_{z,k'}\Delta p^2+\frac{\eta_z}{\sigma^2}\sum_{k'=0}^{k'=k}\left[-\frac{\partial L_{x,k'+\frac{1}{2}}}{\partial y}+\frac{\partial L_{y,k'+\frac{1}{2}}}{\partial x}\right]\Delta p^2. \quad \text{(A-15)}$$

REFERENCES

Adhidjaja, J. I., and G. W. Hohmann, 1989, A finite-difference algorithm for the transient electromagnetic response of a three-dimensional body: Geophysical Journal International, **98**, 233–242, doi: 10.1111/j.1365-246X.1989.tb03348.x.

Berenger, J. P., 1994, A perfectly matched layer for the absorption of electromagnetic waves: Journal of Computational Physics, **114**, 185–200, doi: 10.1006/jcph.1994.1159.

Berenger, J. P., 2002, Application of the CFS PML to the absorption of evanescent waves in waveguides: IEEE Microwave and Wireless Components Letters, **12**, 218–220, doi: 10.1109/LMWC.2002.1010000.

Carcione, J. M., 2006, Geophysical software and algorithms: A spectral numerical method for electromagnetic diffusion: Geophysics, **71**, no. 1, I1–I9, doi: 10.1190/1.2159050.

Chew, W. C., and W. H. Weedon, 1994, A 3-D perfectly matched medium from modified Maxwell's equations with stretched coordinates: Microwave and Optical Technology Letters, **7**, 599–604, doi: 10.1002/(ISSN)1098-2760.

Commer, M., and G. Newman, 2004, A parallel finite-difference approach for 3D transient electromagnetic modeling with galvanic sources: Geophysics, **69**, 1192–1202, doi: 10.1190/1.1801936.

de la Kethulle de Ryhove, S., and R. Mittet, 2014, 3D marine magnetotelluric modeling and inversion with the finite-difference time-domain method: Geophysics, **79**, no. 6, E269–E286, doi: 10.1190/geo2014-0110.1.

De Raedt, H., K. Michielsen, J. S. Kole, and M. T. Figge, 2003, Solving the Maxwell equations by the Chebyshev method: A one-step finite-difference time-domain algorithm: IEEE Transactions on Antennas and Propagation, **51**, 3155–3160, doi: 10.1109/TAP.2003.818809.

Fornberg, B., 1987, The pseudospectral method: Comparisons with finite differences for the elastic wave equation: Geophysics, **52**, 483–501, doi: 10.1190/1.1442319.

Fornberg, B., 1988, The pseudospectral method: Accurate representation of interfaces in elastic wave calculations: Geophysics, **53**, 625–637, doi: 10.1190/1.1442497.

Gedney, S. D., 1996, An anisotropic perfectly matched layer-absorbing medium for the truncation of FDTD lattices: IEEE Transactions on Antennas and Propagation, **44**, 1630–1639, doi: 10.1109/8.546249.

Hu, W., A. Abubakar, and T. M. Habashy, 2009, Joint electromagnetic and seismic inversion using structural constraints: Geophysics, **74**, no. 6, R99–R109, doi: 10.1190/1.3246586.

Hu, Y., G. Egbert, Y. Ji, and G. Fang, 2017, A novel CFS-PML boundary condition for transient electromagnetic simulation using a fictitious wave domain method: Radio Science, **52**, 118–131, doi: 10.1002/2016RS006160.

Hunziker, J., J. Thorbecke, and E. Slob, 2015, The electromagnetic response in a layered vertical transverse isotropic medium: A new look at an old problem: Geophysics, **80**, no. 1, F1–F18, doi: 10.1190/geo2013-0411.1.

Kosloff, D., A. Q. Filho, E. Tessmer, and A. Behle, 1989, Numerical solution of the acoustic and elastic wave equations by a new rapid expansion method: Geophysical Prospecting, **37**, 383–394, doi: 10.1111/j.1365-2478.1989.tb02212.x.

Kuzuoglu, M., and R. Mittra, 1996, Frequency dependence of the constitutive parameters of causal perfectly matched anisotropic absorbers: IEEE Microwave and Guided Wave Letters, **6**, 447–449, doi: 10.1109/75.544545.

Li, G., Y. Li, B. Han, and Z. Liu, 2018, Application of the perfectly matched layer in 3-D marine controlled-source electromagnetic modeling: Geophysical Journal International, **212**, 333–344, doi: 10.1093/gji/ggx382.

Liu, Y., A. Ziolkowski, and P. L. Stoffa, 2018, Time evolution of the electric field using the rapid expansion method: Inclusion of the free surface and anisotropy: 80th Annual International Conference and Exhibition, EAGE, Extended Abstracts, Tu E 13.

Mittet, R., 2017, On the internal interfaces in finite-difference schemes: Geophysics, **82**, no. 4, T159–T182, doi: 10.1190/geo2016-0477.1.

Muir, F., J. Dellinger, J. Etgen, and D. Nichols, 1992, Modeling elastic fields across irregular boundaries: Geophysics, **57**, 1189–1193, doi: 10.1190/1.1443332.

Pan, G., A. Abubakar, and T. M. Habashy, 2012, An effective perfectly matched layer design for acoustic fourth-order frequency-domain finite difference scheme: Geophysical Journal International, **188**, 211–222, doi: 10.1111/j.1365-246X.2011.05244.x.

Pestana, R. C., and P. L. Stoffa, 2010, Time evolution of the wave equation using rapid expansion method: Geophysics, **75**, no. 4, T121–T131, doi: 10.1190/1.3449091.

Roden, J. A., and S. D. Gedney, 2000, Convolutional PML (CPML): An efficient FDTD implementation of the CFS-PML for arbitrary media: Microwave and Optical Technology Letters, **27**, 334–339, doi: 10.1002/(ISSN)1098-2760.

Slob, E., J. Hunziker, and W. A. Mulder, 2010, Green's tensors for the diffusive electric field in a VTI half-space: Progress in Electromagnetics Research, **107**, 1–20, doi: 10.2528/PIER10052807.

Stoffa, P. L., and A. Ziolkowski, 2018, Time evolution of the electric field using the rapid expansion method (REM) with pseudo-spectral evaluation of spatial derivatives: 80th Annual International Conference and Exhibition, EAGE, Extended Abstracts, Tu E 12.

Strack, K.-M., 1992, Exploration with deep transient electromagnetics: Elsevier Science Publ. Co. Inc.

Tal-Ezer, H., 1986, Spectral methods in time for hyperbolic problems: SIAM Journal of Numerical Analysis, **23**, 11–26, doi: 10.1137/0723002.

Tal-Ezer, H., J. M. Carcione, and D. Kosloff, 1990, An accurate and efficient scheme for wave propagation in linear viscoelastic media: Geophysics, **55**, 1366–1379, doi: 10.1190/1.1442784.

Tal-Ezer, H., D. Kosloff, and Z. Koren, 1987, An accurate scheme for seismic forward modeling: Geophysical Prospecting, **35**, 479–490, doi: 10.1111/j.1365-2478.1987.tb00830.x.

Um, E. S., J. M. Harris, and D. L. Alumbaugh, 2010, 3D time-domain simulation of electromagnetic diffusion phenomena: A finite-element electric-field approach: Geophysics, **75**, no. 4, F115–F126, doi: 10.1190/1.3473694.

Wang, T., and G. W. Hohmann, 1993, A finite-difference, time-domain solution for three-dimensional electromagnetic modeling: Geophysics, **58**, 797–809, doi: 10.1190/1.1443465.

Wright, D., A. Ziolkowski, and B. Hobbs, 2002, Hydrocarbon detection and monitoring with a multichannel transient electromagnetic (MTEM) survey: The Leading Edge, **21**, 852–864, doi: 10.1190/1.1508954.

Ziolkowski, A., B. Hobbs, and D. Wright, 2007, Multitransient electromagnetic demonstration survey in France: Geophysics, **72**, no. 4, F197–F209, doi: 10.1190/1.2735802.

References

Abdellah, M., Saleh, S., Eldeib, A., and Shaarawi, A. (2012). High performance multi-dimensional (2d/3d) fft-shift implementation on graphics processing units (gpus). In *2012 Cairo International Biomedical Engineering Conference (CIBEC)*, pages 171–174. IEEE.

Adhidjaja, J. I. and Hohmann, G. W. (1989). A finite-difference algorithm for the transient electromagnetic response of a three dimensional body. *Geophysical Journal International*, 98:233–242.

Amestoy, P. R., Duff, I. S., L'Excellent, J.-Y., and Koster, J. (2001). A fully asynchronous multifrontal solver using distributed dynamic scheduling. *SIAM Journal on Matrix Analysis and Applications*, 23(1):15–41.

Amundsen, L., Løseth, L., Mittet, R., Ellingsrud, S., and Ursin, B. (2006). Decomposition of electromagnetic fields into upgoing and downgoing components. *Geophysics*, 71(5):G211–G223.

Anderson, C. and Mattson, J. (2010). An integrated approach to marine electromagnetic surveying using a towed streamer and source. *First Break*, 28(5).

Aristodemou, E. and Thomas-Betts, A. (2000). Dc resistivity and induced polarisation investigations at a waste disposal site and its environments. *Journal of Applied Geophysics*, 44(2-3):275–302.

Aruliah, D. A. and Ascher, U. M. (2002). Multigrid preconditioning for krylov methods for time-harmonic maxwell's equations in three dimensions. *SIAM Journal on Scientific Computing*, 24(2):702–718.

Avdeev, D. B. (2005). Three-dimensional electromagnetic modelling and inversion from theory to application. *Surveys in Geophysics*, 26(6):767–799.

Bale, R. A. (2002). Staggered grids for 3d pseudospectral modeling in anisotropic elastic media. *Calgary CREWES Res. Rep*, 14:1–14.

Bannister, P. (1984). New simplified formulas for elf subsurface-to-subsurface propagation. *IEEE Journal of Oceanic Engineering*, 9(3):154–163.

Berenger, J. P. (1994). A perfectly matched layer for the absorption of electromagnetic waves. *J. Comput. Phys.*, 114:185–200.

Berenger, J. P. (2002). Application of the cfs pml to the absorption of evanescent waves in waveguides. *IEEE Microw. Wirel. Compon. Lett.*, 12(6):218–220.

Bhattacharya, P. (2012). *Direct current geoelectric sounding: Principles and interpretation*, volume 9. Elsevier.

Börner, R.-U., Ernst, O. G., and Güttel, S. (2015). Three-dimensional transient electromagnetic modelling using rational krylov methods. *Geophysical Journal International*, 202(3):2025–2043.

Briggs, W. L., Henson, V. E., and McCormick, S. F. (2000). *A multigrid tutorial*. SIAM.

Carcione, J. M. (2006). Geophysical software and algorithms: A spectral numerical method for electromagnetic diffusion. *Geophysics*, 71:11–19.

Carcione, J. M., Kosloff, D., and Kosloff, R. (1988). Wave propagation simulation in a linear viscoelastic medium. *Geophysical Journal International*, 95(3):597–611.

Chave, A. D. (2009). On the electromagnetic fields produced by marine frequency domain controlled sources. *Geophysical Journal International*, 179(3):1429–1457.

Chave, A. D., Constable, S. C., and Edwards, R. N. (1991). Electrical exploration methods for the seafloor. In *Electromagnetic Methods in Applied Geophysics: Volume 2, Application, Parts A and B*, pages 931–966. Society of Exploration Geophysicists.

Cheesman, S., Edwards, R., and Chave, A. (1987). On the theory of sea-floor conductivity mapping using transient electromagnetic systems. *Geophysics*, 52(2):204–217.

Chew, W. C. and Weedon, W. H. (1994). A 3-d perfectly matched medium from modified maxwell's equations with stretched coordinates. *Microwave Opt. Tech. Lett.*, 7:599–604.

Collino, F. and Tsogka, C. (2001). Application of the perfectly matched absorbing layer model to the linear elastodynamic problem in anisotropic heterogeneous media. *Geophysics*, 66(1):294–307.

Commer, M., Hoversten, G. M., and Um, E. S. (2015). Transient-electromagnetic finite-difference time-domain earth modeling over steel infrastructure. *Geophysics*, 80(2):E147–E162.

Commer, M. and Newman, G. (2004). A parallel finite-difference approach for 3d transient electromagnetic modelling with galvanic sources. *Geophysics*, 69:1192–1202.

Commer, M. and Newman, G. A. (2008). New advances in three-dimensional controlled-source electromagnetic inversion. *Geophysical Journal International*, 172(2):513–535.

Connell, D. (2011). *A comparison of marine time-domain and frequency-domain controlled source electromagnetic methods*. PhD thesis, UC San Diego.

Constable, S. (2010). Ten years of marine csem for hydrocarbon exploration. *Geophysics*, 75(5):75A67–75A81.

Constable, S. and Cox, C. (1996). Marine controlled-source electromagnetic sounding: 2. the pegasus experiment. *Journal of Geophysical Research: Solid Earth*, 101(B3):5519–5530.

Constable, S. C., Parker, R. L., and Constable, C. G. (1987). Occam's inversion: A practical algorithm for generating smooth models from electromagnetic sounding data. *Geophysics*, 52:289–300.

Corrêa, G. J., Spiegelman, M., Carbotte, S., and Mutter, J. C. (2002). Centered and staggered fourier derivatives and hilbert transforms. *Geophysics*, 67(5):1558–1563.

Courant, R., Friedrichs, K., and Lewy, H. (1928). Über die partiellen differenzengleichungen der mathematischen physik. *Mathematische annalen*, 100(1):32–74.

Cox, C., Constable, S., Chave, A., and Webb, S. (1986). Controlled-source electromagnetic sounding of the oceanic lithosphere. *Nature*, 320(6057):52–54.

Davis, T. A. (2006). *Direct methods for sparse linear systems*. SIAM.

Davydycheva, S., Druskin, V., and Habashy, T. (2003). An efficient finite-difference scheme for electromagnetic logging in 3d anisotropic inhomogeneous mediafinite-difference scheme in anisotropic media. *Geophysics*, 68(5):1525–1536.

de Hoop, A. T. (1996). A general correspondence principle for time-domain electromagnetic wave and diffusion fields. *Geophysical Journal International*, 127(3):757–761.

de la Kethulle de Ryhove, S. and Mittet, R. (2014). 3d marine magnetotelluric modeling and inversion with the finite-difference time-domain method. *Geophysics*, 79(6):E269–E286.

Dedek, L., Dedkova, J., and Valsa, J. (2002). Optimization of perfectly matched layer for laplace's equation. *IEEE transactions on magnetics*, 38(2):501–504.

Druskin, V. (1988). A spectral semi-discrete method for numerical solution of 3-d non-stationary problems in electrical prospecting. *Phys. Sol. Earth*, 24:641–648.

Druskin, V. and Knizhnerman, L. (1994). Spectral approach to solving three-dimensional maxwell's diffusion equations in the time and frequency domains. *Radio Science*, 29(4):937–953.

Druskin, V., Knizhnerman, L., and Zaslavsky, M. (2009). Solution of large scale evolutionary problems using rational krylov subspaces with optimized shifts. *SIAM Journal on Scientific Computing*, 31(5):3760–3780.

Druskin, V., Lieberman, C., and Zaslavsky, M. (2010). On adaptive choice of shifts in rational krylov subspace reduction of evolutionary problems. *SIAM Journal on Scientific Computing*, 32(5):2485–2496.

Druskin, V. L., Knizhnerman, L., and Lee, P. (1999). New spectral lanczos decomposition method for induction modeling in arbitrary 3-d geometry. *Geophysics*, 64(3):701–706.

Du Fort, E. and Frankel, S. (1953). Stability conditions in the numerical treatment of parabolic differential equations. *Mathematical Tables and other aids to computation*, 7(43):135–152.

Edwards, R. and Chave, A. (1986). A transient electric dipole-dipole method for mapping the conductivity of the sea floor. *Geophysics*, 51(4):984–987.

Edwards, R., Nobes, D., and Gomez-Trevino, E. (1984). Offshore electrical exploration of sedimentary basins: The effects of anisotropy in horizontally isotropic, layered media. *Geophysics*, 49(5):566–576.

Ellingsrud, S., Eidesmo, T., Johansen, S., Sinha, M., MacGregor, L., and Constable, S. (2002). Remote sensing of hydrocarbon layers by seabed logging (sbl): Results from a cruise offshore angola. *The Leading Edge*, 21:972–982.

Ellis, M., Sinha, M., and Parr, R. (2009). Investigations into the discrepancies between electro-magnetic and borehole derived resistivities in overburden sediment. In *71st EAGE Conference and Exhibition incorporating SPE EUROPEC 2009*.

Endo, M. and Noguchi, K. (2002). Three-dimensional modeling considering the topography for the case of the time-domain electromagnetic method. In *Methods in Geochemistry and Geophysics*, volume 35, pages 85–107. Elsevier.

Engelmark, F., Mattsson, J., McKay, A., and Du, Z. (2014). Towed streamer em comes of age. *First Break*, 32(4).

Fanavoll, S., Gabrielsen, P. T., and Ellingsrud, S. (2014). Csem as a tool for better exploration decisions: Case studies from the barents sea, norwegian continental shelf. *Interpretation*, 2(3):SH55–SH66.

Feise, M. W., Schneider, J. B., and Bevelacqua, P. J. (2004). Finite-difference and pseudospectral time-domain methods applied to backward-wave metamaterials. *IEEE transactions on antennas and propagation*, 52(11):2955–2962.

Fornberg, B. (1987). The pseudospectral method: Comparisons with finite differences for the elastic wave equation. *Geophysics*, 52:483–501.

Fornberg, B. (1988). The pseudospectral method: accurate representation of interfaces in elastic wave calculations. *Geophysics*, 53(5):625–637.

Frigo, M. and Johnson, S. G. (2005). The design and implementation of fftw3. *Proceedings of the IEEE*, 93(2):216–231.

Gedney, S. D. (1996). An anisotropic perfectly matched layer-absorbing medium for the truncation of fdtd lattices. *IEEE Trans. Antennas Propag.*, 44:1630–1639.

Grayver, A. V., Streich, R., and Ritter, O. (2013). Three-dimensional parallel distributed inversion of csem data using a direct forward solver. *Geophysical Journal International*, 193(3):1432–1446.

Gutknecht, M. H. (1993). Variants of bicgstab for matrices with complex spectrum. *SIAM journal on scientific computing*, 14(5):1020–1033.

Helwig, S., Myer, D., Key, K., El Kaffas, A., Wu, X., Eide, K., and Frafjord, Ø. (2018). A comparison between time domain and frequency domain inversion of vertical-vertical csem data. In *80th EAGE Conference and Exhibition 2018*, volume 2018, pages 1–5. European Association of Geoscientists & Engineers.

Helwig, S. L., El Kaffas, A. W., Holten, T., Frafjord, Ø., and Eide, K. (2013). Vertical dipole csem: technology advances and results from the snøhvit field. *First break*, 31(4).

Hesthaven, J. S., Gottlieb, S., and Gottlieb, D. (2007). *Spectral methods for time-dependent problems*, volume 21. Cambridge University Press.

Holten, T., Flekkøy, E. G., Måløy, K. J., and Singer, B. (2009). Vertical source and receiver csem method in time-domain. In *SEG Technical Program Expanded Abstracts 2009*, pages 749–753. Society of Exploration Geophysicists.

Hördt, A., Blaschek, R., Kemna, A., and Zisser, N. (2007). Hydraulic conductivity estimation from induced polarisation data at the field scale—the krauthausen case history. *Journal of Applied Geophysics*, 62(1):33–46.

Hördt, A. and Müller, M. (2000). Understanding lotem data from mountainous terrain. *Geophysics*, 65(4):1113–1123.

Houck, R. T., Ciucivara, A., and Hornbostel, S. (2015). Accuracy and effectiveness of three-dimensional controlled source electromagnetic data inversions. *Geophysics*, 80(2):E83–E95.

Hu, W., Abubakar, A., and Habashy, T. M. (2009). Joint electromagnetic and seismic inversion using structural constraints. *Geophysics*, 74(6):R99–R109.

Hu, Y., Egbert, G., Ji, Y., and Fang, G. (2017). A novel cfs-pml boundary condition for transient electromagnetic simulation using a fictitious wave domain method. *Radio Science*, 52(1):118–131.

Hunziker, J., Slob, E., and Mulder, W. (2011). Effects of the airwave in time-domain marine controlled-source electromagnetics. *Geophysics*, 76:F251–F261.

Hunziker, J., Thorbecke, J., and Slob, E. (2015). The electromagnetic response in a layered vertical transverse isotropic medium: A new look at an old problem. *Geophysics*, 80:F1–F18.

Ingber, L. (1989). Very fast simulated re-annealing. *Mathematical and computer modelling*, 12(8):967–973.

Ingber, L. (1993). Simulated annealing: Practice versus theory. *Mathematical and computer modelling*, 18(11):29–57.

Ingber, L., Petraglia, A., Petraglia, M. R., Machado, M. A. S., et al. (2012). Adaptive simulated annealing. In *Stochastic global optimization and its applications with fuzzy adaptive simulated annealing*, pages 33–62. Springer.

Jaysaval, P., Datta, D., Sen, M. K., Arnulf, A. F., Denel, B., and Williamson, P. (2019). 5 d controlled-source electromagnetic inversion using very fast simulated annealing algorithm. In *SEG Technical Program Expanded Abstracts 2019*, pages 1060–1064. Society of Exploration Geophysicists.

Jaysaval, P., Shantsev, D. V., Ryhove, S. K., and Bratteland, T. (2016). Fully anisotropic 3-d em modelling on a lebedev grid with a multigrid pre-conditioner. *Geophysical Journal International*, 207:1554–1572.

Key, K. (2009). 1d inversion of multicomponent, multifrequency marine csem data: Methodology and synthetic studies for resolving thin resistive layers. *Geophysics*, 74(2):F9–F20.

Key, K. and Ovall, J. (2011). A parallel goal-oriented adaptive finite element method for 2.5-d electromagnetic modelling. *Geophysical Journal International*, 186:137–154.

King, R. W., Owens, M., and Wu, T. T. (2012). *Lateral electromagnetic waves: theory and applications to communications, geophysical exploration, and remote sensing*. Springer Science & Business Media.

Knizhnerman, L., Druskin, V., and Zaslavsky, M. (2009). On optimal convergence rate of the rational krylov subspace reduction for electromagnetic problems in unbounded domains. *SIAM Journal on Numerical Analysis*, 47(2):953–971.

Koldan, J., Puzyrev, V., de la Puente, J., Houzeaux, G., and Cela, J. M. (2014). Algebraic multigrid preconditioning within parallel finite-element solvers for 3-d electromagnetic modelling problems in geophysics. *Geophysical Journal International*, 197(3):1442–1458.

Komatitsch, D. and Vilotte, J.-P. (1998). The spectral element method: an efficient tool to simulate the seismic response of 2d and 3d geological structures. *Bulletin of the seismological society of America*, 88(2):368–392.

Kong, F., Johnstad, S., Røsten, T., and Westerdahl, H. (2008). A 2.5 d finite-element-modeling difference method for marine csem modeling in stratified anisotropic media. *Geophysics*, 73(1):F9–F19.

Kosloff, D., Filho, A. Q., Tessmer, E., and Behle, A. (1989). Numerical solution of the acoustic and elastic wave equations by a new rapid expansion method. *Geophysical Prospecting*, 37:383–394.

Kuzuoglu, M. and Mittra, R. (1996). Frequency dependence of the constitutive parameters of causal perfectly matched anisotropic absorbers. *IEEE Microwave and Guided wave letters*, 6(12):447–449.

Lebedev, V. I. (1964). Difference analogies of orthgonal decompositions of basic differential operators and some boundary value problems. i. *Soviet Computational Mathematics and Mathematical Physics*, 4:449–465.

Lee, K. and Morrison, H. F. (1985). A numerical solution for the electromagnetic scattering by a two-dimensional inhomogeneity. *Geophysics*, 50(3):466–472.

Lee, K. H., Liu, G., and Morrison, H. F. (1989). A new approach to modeling the electromagnetic response of conductive media. *Geophysics*, 54(9):1180–1192.

Lee, K. H. and Xie, G. (1993). A new approach to imaging with low-frequency electromagnetic fields. *Geophysics*, 58(6):780–796.

Lee, T. J. and Uchida, T. (2005). Electromagnetic traveltime tomography: Application for reservoir characterization in the lost hills oil field, california. *Geophysics*, 70(3):G51–G58.

Li, G. and Li, Y. (2017). Joint inversion for transmitter navigation and seafloor resistivity for frequency-domain marine csem data. *Journal of Applied Geophysics*, 136:178–189.

Li, G., Li, Y., Han, B., and Liu, Z. (2018). Application of the perfectly matched layer in 3-d marine controlled-source electromagnetic modeling. *Geophysical Journal International*, 212:333–344.

Li, H., Xue, G.-Q., and Zhao, P. (2017). A new imaging approach for dipole–dipole time-domain electromagnetic data based on the q-transform. *Pure and Applied Geophysics*, 174(10):3939–3953.

Li, Y. and Key, K. (2007). 2d marine controlled-source electromagnetic modeling: Part 1—an adaptive finite-element algorithm. *Geophysics*, 72(2):WA51–WA62.

Liu, Q. (1997). The pstd algorithm: A time-domain method requiring only two cells per wavelength. *Microwave and optical technology letters*, 15(3):158–165.

Liu, Q. H. (1999). Pml and pstd algorithm for arbitrary lossy anisotropic media. *IEEE microwave and guided wave letters*, 9(2):48–50.

Liu, Y. (2019). Application of perfectly matched layers in 3d transient controlled-source electromagnetic modeling by the rapid expansion method. *Geophysics*, 85(1):E15–E26.

Liu, Y., Hagdorn, M., and Ziolkowski, A. (2019a). Gpu-accelerated transient electro-magnetic modelling. In *81st EAGE Conference and Exhibition 2019*.

Liu, Y. and Yin, C. (2014). 3d anisotropic modeling for airborne em systems using finite-difference method. *Journal of Applied Geophysics*, 109:186–194.

Liu, Y., Ziolkowski, A., and Stoffa, P. L. (2019b). Time evolution of the electric field using the rapid expansion method (rem) with pseudo-spectral evaluation of spatial derivatives: Part ii inclusion of anisotropy and the earth-air interface. *Geophysics*, 84(5):1–55.

Loseth, L. O., Pedersen, H. M., Ursin, B., Amundsen, L., and Ellingsrud, S. (2006). Low-frequency electromagnetic fields in applied geophysics: Waves or diffusion? *Geophysics*, 71:W29–W40.

Løseth, L. O., Wiik, T., Olsen, P. A., and Hansen, J. O. (2014). Detecting skrugard by csem—prewell prediction and postwell evaluation. *Interpretation*, 2(3):SH67–SH77.

Ma, X.-Q. (2002). Simultaneous inversion of prestack seismic data for rock properties using simulated annealing. *Geophysics*, 67(6):1877–1885.

Macnae, J. C. (1984). Survey design for multicomponent electromagnetic systems. *Geophysics*, 49:265–273.

Madsen, K. (2006). Modelling study of airwave contribution to the csem signal. In *68th EAGE Conference and Exhibition incorporating SPE EUROPEC 2006*.

Martin, J., Wilcox, L. C., Burstedde, C., and Ghattas, O. (2012). A stochastic newton mcmc method for large-scale statistical inverse problems with application to seismic inversion. *SIAM Journal on Scientific Computing*, 34(3):A1460–A1487.

Mattsson, J., Hall, G., Björnemo, E., McKay, A., Ronaess, M., and Anderson, C. (2012). Error analysis and capability modelling for towed streamer electromagnetics. *First Break*, 30(8).

Mavriplis, C. (1994). Adaptive mesh strategies for the spectral element method. *Computer methods in applied mechanics and engineering*, 116(1-4):77–86.

Mittet, R. (2010). High-order finite-difference simulations of marine csem surveys using a correspondence principle for wave and diffusion fields. *Geophysics*, 75(1):F33–F50.

Mittet, R. (2017). On the internal interfaces in finite-differences schemes. *Geophysics*, 82:T159–T182.

Mittet, R. and Berre, L. (2018). Data-driven initial-model estimation with application to marine csem data. In *SEG Technical Program Expanded Abstracts 2018*, pages 893–897. Society of Exploration Geophysicists.

Mittet, R. and Schaug-Pettersen, T. (2008). Shaping optimal transmitter waveforms for marine csem surveys. *Geophysics*, 73(3):F97–F104.

Mulder, W. (2006). A multigrid solver for 3d electromagnetic diffusion. *Geophysical prospecting*, 54(5):633–649.

Mulder, W. A., Wirianto, M., and Slob, E. C. (2008). Time-domain modeling of electromagnetic diffusion with a frequency-domain code. *Geophysics*, 73(1):F1–F8.

Nabighian, M. (1987). Electromagnetic methods in applied geophysics (vol. 1). *Theory. Soc. Explor. Geophys., Tulsa, OK*.

Nabighian, M. N. (1991). *Electromagnetic Methods in Applied Geophysics: Volume 2, Application, Parts A and B: Volume 2, Application, Parts A and B*. Society of Exploration Geophysicists.

Nauta, M., Okoniewski, M., and Potter, M. (2013). Fdtd method on a lebedev grid for anisotropic materials. *IEEE Transactions on Antennas and Propagation*, 61(6):3161–3171.

Nekut, A. and Spies, B. R. (1989). Petroleum exploration using controlled-source electromagnetic methods. *Proceedings of the IEEE*, 77(2):338–362.

Newman, G. A. (2014). A review of high-performance computational strategies for modeling and imaging of electromagnetic induction data. *Surveys in Geophysics*, 35(1):85–100.

Nickolls, J. and Dally, W. J. (2010). The gpu computing era. *IEEE micro*, 30(2):56–69.

Nordskag, J. I. and Amundsen, L. (2007). Asymptotic airwave modeling for marine controlled-source electromagnetic surveying. *Geophysics*, 72(6):F249–F255.

Oldenburg, D. W., Haber, E., and Shekhtman, R. (2013). Three dimensional inversion of multisource time domain electromagnetic data. *Geophysics*, 78(1):E47–E57.

Oristaglio, M. L. and Hohmann, G. W. (1984). Diffusion of electromagnetic fields into a two-dimensional earth: A finite-difference approach. *Geophysics*, 49:870–894.

Pan, G. A. A. and Habashy, T. M. (2012). An effective perfectly matched layer design for acoustic fourth-order frequency-domain finite difference scheme. *Geophysical Journal International*, 188:211–222.

Pestana, R. C. and Stoffa, P. L. (2010). Time evolution of the wave equation using rapid expansion method. *Geophysics*, 75:T121–T131.

Plessix, R.-E. (2006). A review of the adjoint-state method for computing the gradient of a functional with geophysical applications. *Geophysical Journal International*, 167(2):495–503.

Potter, D. (1973). Computational physics.

Raedt, H. D., Michielsen, K., Kole, J. S., and Figge, M. T. (2003). Solving the maxwell equations by the chebyshev method: A one-step finite-difference time-domain algorithm. *IEEE Transactions on Antennas and Propagation*, 51(11):3155–3160.

Rein, A., Hoffmann, R., and Dietrich, P. (2004). Influence of natural time-dependent variations of electrical conductivity on dc resistivity measurements. *Journal of hydrology*, 285(1-4):215–232.

Roden, J. A. and Gedney, S. D. (2000). Convolution pml (cpml): An efficient fdtd implementation of the cfs–pml for arbitrary media. *Microwave and optical technology letters*, 27(5):334–339.

Schaller, A., Streich, R., Drijkoningen, G., Ritter, O., and Slob, E. (2018). A land-based controlled-source electromagnetic method for oil field exploration: An example from the schoonebeek oil field. *Geophysics*, 83(2):WB1–WB17.

Sen, M. K. and Biswas, R. (2017). Transdimensional seismic inversion using the reversible jump hamiltonian monte carlo algorithm. *Geophysics*, 82(3):R119–R134.

Sen, M. K. and Stoffa, P. L. (1991). Nonlinear one-dimensional seismic waveform inversion using simulated annealing. *Geophysics*, 56(10):1624–1638.

Sen, M. K. and Stoffa, P. L. (1992). Rapid sampling of model space using genetic algorithms: examples from seismic waveform inversion. *Geophysical Journal International*, 108(1):281–292.

Sen, M. K. and Stoffa, P. L. (2013). *Global optimization methods in geophysical inversion*. Cambridge University Press, second edition.

Seran, E., Godefroy, M., Pili, E., Michielsen, N., and Bondiguel, S. (2017). What we can learn from measurements of air electric conductivity in 222rn-rich atmosphere. *Earth and Space Science*, 4(2):91–106.

Singer, B. S. and Atramonova, S. (2013). Vertical electric source in transient marine csem: Effect of 3d inhomogeneities on the late time response. *Geophysics*, 78(4):E173–E188.

Slob, E., Hunziker, J., and Mulder, W. A. (2010). Green's tensors for the diffusive electric field in a vti half-space. *Progress In Electromagnetics Research*, 107:1–20.

Srnka, L. J., Carazzone, J. J., Ephron, M. S., and Eriksen, E. A. (2006). Remote reservoir resistivity mapping. *The Leading Edge*, 25(8):972–975.

Stoffa, P. and Ziolkowski, A. (2018). Time evolution of the electric field using the rapid expansion method (rem) with pseudo-spectral evaluation of spatial derivatives. *80th EAGE Conference and Exhibition*, EAGE:Expanded Abstract.

Stoffa, P. L. and Ziolkowski, A. (2019). Time evolution of the electric field using the rapid expansion method (rem) with pseudo-spectral evaluation of spatial derivatives part i. *Geophysics*, 84(5):1–43.

Streich, R. (2016). Controlled-source electromagnetic approaches for hydrocarbon exploration and monitoring on land. *Surveys in geophysics*, 37(1):47–80.

Tal-Ezer, H. (1986). Spectral methods in time for hyperbolic problems. *SIAM Journal of Numerical Analysis*, 23:11–26.

Tal-Ezer, H. (1989). Spectral methods in time for parabolic problems. *SIAM Journal of Numerical Analysis*, 26:1–11.

Tal-Ezer, H., Carcione, J. M., and Kosloff, D. (1990). An accurate and efficient scheme for wave propagation in linear viscoelastic media. *Geophysics*, 55(10):1366–1379.

Tal-Ezer, H., Kosloff, D., and Koren, Z. (1987). An accurate scheme for seismic forward modelling. *Geophysical Prospecting*, 35:479–490.

Ten Kroode, F., Bergler, S., Corsten, C., de Maag, J. W., Strijbos, F., and Tijhof, H. (2013). Broadband seismic data—the importance of low frequencies. *Geophysics*, 78(2):WA3–WA14.

Um, E. S., Harris, J. M., and Alumbaugh, D. L. (2010). 3d time-domain simulation of electromagnetic diffusion phenomena: A finite-element electric-field approach. *Geophysics*, 75(4):F115–F126.

Van der Vorst, H. A. (1992). Bi-cgstab: A fast and smoothly converging variant of bi-cg for the solution of nonsymmetric linear systems. *SIAM Journal on scientific and Statistical Computing*, 13(2):631–644.

Vozoff, K. (1972). The magnetotelluric method in the exploration of sedimentary basins. *Geophysics*, 37(1):98–141.

Wait, J. (1966). Fields of a horizontal dipole over a stratified anisotropic half-space. *IEEE Transactions on Antennas and Propagation*, 14:790–792.

Wang, B. (2006). 2d and 3d potential-field upward continuation using splines. *Geophysical Prospecting*, 54(2):199–209.

Wang, T. and Fang, S. (2001). 3-d electromagnetic anisotropy modelling using finite differences. *Geophysics*, 66:1386–1398.

Wang, T. and Hohmann, G. W. (1993). A finite-difference, time-domain solution for three-dimensional electromagnetic modelling. *Geophysics*, 58:797–809.

Wannamaker, P. E., Hohmann, G. W., and Ward, S. H. (1984). Magnetotelluric responses of three-dimensional bodies in layered earths. *Geophysics*, 49(9):1517–1533.

Ward, S. H. and Hohmann, G. W. (1987). Electromagnetic theory for geophysical applications. In Nabighian, M. N., editor, *Electromagnetic Methods in Applied Geophysics*, volume 1. Society of Exploration Geophysicists, Tulsa, U.S.A.

Weir, G. J. (1980). Transient electromagnetic fields about an infinitesimally long grounded horizontal electric dipole on the surface of a uniform half-space. *Geophysical Journal of the Royal Astronomical Society*, 61:41–56.

Weiss, C. J. and Newman, G. A. (2002). Electromagnetic induction in a fully 3-d anisotropic earth. *Geophysics*, 67:1104–1114.

Werthmüller, D. (2009). Inversion of multi-transient em data from anisotropic media.

Werthmüller, D. (2014). Bayesian estimation of resistivities from seismic velocities.

Werthmüller, D. (2017). An open-source full 3d electromagnetic modeler for 1d vti media in python: empymod. *Geophysics*, 82(6):WB9–WB19.

Werthmüller, D., Ziolkowski, A., and Wright, D. (2013). Background resistivity model from seismic velocities. *Geophysics*, 78:E213–E223.

Wesseling, P. (1995). Introduction to multigrid methods.

Wilson, A. J. (1997). *The equivalent wavefield concept in multichannel transient electromagnetic surveying*. PhD thesis, University of Edinburgh.

Wright, D. (2015). Quantifying the effect of the air/water interface in marine active source em. *Journal of Applied Geophysics*, 118:92–105.

Wright, D., Ziolkowski, A., and Hobbs, B. (2002). Hydrocarbon detection and monitoring with a multicomponent transient electromagnetic (mtem) survey. *The Leading Edge*, 21(9):852–864.

Wright, D. A., Ziolkowski, A. M., and Hobbs, B. A. (2005). Detection of subsurface resistivity contrasts with application to location of fluids. US Patent 6,914,433.

Yee, K. (1966). Numerical solution of initial boundary value problems involving maxwell's equations in isotropic media. *IEEE Transactions on antennas and propagation*, 14(3):302–307.

Zhang, X., Curtis, A., Galetti, E., and De Ridder, S. (2018). 3-d monte carlo surface wave tomography. *Geophysical Journal International*, 215(3):1644–1658.

Zhao, L.-S., Sen, M. K., Stoffa, P., and Frohlich, C. (1996). Application of very fast simulated annealing to the determination of the crustal structure beneath tibet. *Geophysical Journal International*, 125(2):355–370.

Zhdanov, M. S. (2010). Electromagnetic geophysics: Notes from the past and the road ahead. *Geophysics*, 75(5):75A49–75A66.

Zhdanov, M. S., Endo, M., Cox, L. H., Čuma, M., Linfoot, J., Anderson, C., Black, N., and Gribenko, A. V. (2014). Three-dimensional inversion of towed streamer electromagnetic data. *Geophysical Prospecting*, 62(3):552–572.

Zhou, Y., Zhuang, M., Shi, L., Cai, G., Liu, N., and Liu, Q. H. (2017). Spectral-element method with divergence-free constraint for 2.5-d marine csem hydrocarbon exploration. *IEEE Geoscience and Remote Sensing Letters*, 14(11):1973–1977.

Ziolkowski, A., Hobbs, B. A., and Wright, D. (2007). Multitransient electromagnetic demonstration survey in france. *Geophysics*, 72(4):F197–F209.

Ziolkowski, A., Parr, R., Wright, D., Nockles, V., Limond, C., Morris, E., and Linfoot, J. (2010). Multi-transient electromagnetic repeatability experiment over the north sea harding field. *Geophysical Prospecting*, 58:1159–1176.

Ziolkowski, A. and Slob, E. (2019). *Introduction to Controlled-source Electromagnetic Methods: Detecting Subsurface Fluids*. Cambridge University Press.

Ziolkowski, A. and Stoffa, P. L. (2019). Equivalent wave field of diffusive controlled source electromagnetic (csem) data. In *SEG Technical Program Expanded Abstracts 2019*, pages 1080–1084. Society of Exploration Geophysicists.

Ziolkowski, A. and Taylor, D. (2010). Impulsive bipole current source. *PGS Internal Report*.

Ziolkowski, A. and Wright, D. (2007). Removal of the airwave in shallow-marine transient em data. In *SEG Technical Program Expanded Abstracts 2007*, pages 534–538. Society of Exploration Geophysicists.

Ziolkowski, A. and Wright, D. (2012). The potential of the controlled source electromagnetic method: A powerful tool for hydrocarbon exploration, appraisal, and reservoir characterization. *IEEE Signal Processing Magazine*, 29(4):36–52.

Ziolkowski, A., Wright, D., and Mattsson, J. (2011). Comparison of pseudo-random binary sequency and square-wave transient controlled-source electromagnetic data over the peon gas discovery, norway. *Geophysical Prospecting*, 59:1114–1131.